ULTRASONIC SCATTERING FROM VOLUMETRIC FLAWS IN STRUCTURAL MATERIALS AND THEIR CHARACTERISATION

by

JICHENG YANG

Thesis Submitted for the Degree of

Doctor of Philosophy

Department of Mechanical Engineering

UNIVERSITY COLLEGE LONDON

January 1992

TO My Parents

ABSTRACT

This thesis is a theoretical and experimental study of ultrasonic scattering from volumetric flaws in structural materials and ultrasonic inversion techniques for nondestructive characterisation of such flaws.

For forward scattering problems, the Method Of Optimal Truncation (MOOT) is studied. A large general purposed computer model is developed based on MOOT. The computer model can be used to simulate ultrasonic scattering from different shapes and sizes of voids, with only minor changes. Numerical results for a number of voids are presented in both the frequency and time domains to provide understanding of basic physical mechanism of scattering by volumetric flaws. The simulated forward scattering data are also used to test a new inversion technique developed in this study.

A new ultrasonic inversion technique is developed for determining the geometrical features of a volumetric flaw in structural materials, by the inversion of the backscattered ultrasonic signal using the area function formula. The area function formula is derived from a weak scattering approximation, the Born approximation, but it is shown that the area function sizing technique works well for voids which are clearly strong scatterers. The technique extracts the flaw size from the shape of the area function which is evaluated from the backscattering signal. Unlike most of other ultrasonic inversion schemes, this technique has the advantage that it does not require the determination of the flaw centroid (zero-of-time problem). The technique is tested by the inversion of the numerical and experimental scattering data for estimating the sizes of a number of flaws. The results show very good agreement between the true sizes and the estimated sizes.

The experimental work is carried out on simulated defects in the immersion and contact modes. Several techniques for processing experimental signals are investigated, including deconvolution techniques.

ACKNOWLEDGEMENTS

I would like to thank my supervisor Dr. L. J. Bond for his supervision, encouragement and his comments on the drafts of this thesis.

I wish to thank the Education Section of the Chinese Embassy, London, and the British Council for all their support, financially and administratively.

I am grateful to Dr. Nader Saffari for many helpful discussions. I also wish to thank all my colleagues in Ultrasonics Group, including Ioannis Tsironis, Amit Som and Peter Albach for their support.

Finally, I owe special thanks to my parents and my wife for their love and understanding throughout my Ph.D program.

CONTENTS

LIST OF FIGURES

LIST OF TABLES

Chapter 1.
INTRODUCTION

1.1 Statement of the Problem

The presence of voids and inclusions is a serious threat to the integrity of many structural materials. Crack initiation at the boundary of such flaws is a common occurrence. Detection and sizing of imperfections such as these is thus of great importance. For example, there is interest in the reliable detection and characterisation of volumetric scatterers in the size range of 10 to 1000 μm in critical components such as turbine disc [Bond, 1989b].

This thesis is a theoretical and experimental study of ultrasonic scattering from volumetric flaws in structural materials and ultrasonic inversion techniques for nondestructive characterisation of such flaws.

Nondestructive Evaluation (NDE) may be defined as the determination of the serviceability of a component on the basis of nondestructive measurements [Thompson and Wadley, 1989]. The development of fracture mechanics has made it possible to predict the serviceability of parts containing flaws of known size. This requires nondestructive testing technique to characterize flaws quantitatively, i.e. to determine the size, geometric shape, material properties, etc. [Thompson and Thompson, 1985].

Ultrasonics is one of the most commonly used NDE methods. When a propagation ultrasonic wave interacts with a flaw in the material, the scattered waves contain rich information about the flaw. These scattered waves can be monitored and used for characterisation of the flaw. There are actually three separate stages of this characterisation process. The first stage is flaw detection - the determination that a signal received is actually from a flaw. The

second stage is flaw classification - the identification of a flaw as crack-like or volumetric. The third stage is flaw characterisation - estimating the size, shape, orientation and material properties of the flaw. This thesis will be concerned with only one aspect of the flaw characterisation problem, reconstructing the geometric features of volumetric flaws in structural materials. The focus will be on developing a new ultrasonic inverse scattering methodology for sizing volumetric flaws. Attention is also paid to developing a numerical model simulating elastic wave interactions with volumetric flaws. The numerical model is used to generate forward scattering data to provide understanding of scattering mechanism and to test the inversion technique.

1.2 Contributions

There are four major accomplishments of this study:

(1) The development of a new ultrasonic inverse scattering technique (the area function sizing scheme) for sizing volumetric flaws. The method is shown to have some attractive advantages over the existing inversion techniques, such as inverse Born approximation.

(2) Successful applications of this method experimentally to several simple shaped flaws, and numerically to some regular and irregular shaped flaws.

(3) Development of a large computer model based on the idea of the method of optimal truncation (MOOT) [Visscher, 1980a,b]. The computer model can be used to simulate ultrasonic scattering from different shaped voids, with only minor changes according to the size and shape of the void considered.

(4) Calculation of the far-field backscattering responses from several irregular shaped voids in both the frequency domain and the time domain.

Parts of the research results from this study have been presented at two international conferences and the contributions are published in the corresponding proceedings:

(1) J. Yang and L. J. Bond, "Reconstruction of Volumetric Flaws Using Ultrasonic Backscattering Data", Ultrasonics International 91, Le Touquet, France, July 1-4, 1991, Butterworth-Heinemann (In press).

(2) J. Yang and L. J. Bond "Ultrasonic Sizing of Voids Using Area Functions", 18th Review of Progress in Quantitative Non-Destructive Evaluation, Brunswick, Maine, USA, July 29 - August 2, 1991, Vol. 11, Plenum Press, New York (In press).

A paper summarising this study has been submitted to a journal:
J. Yang and L. J. Bond, "Ultrasonic Technique for Sizing Voids by Using Area Functions", IEE Proceedings Part A (Submitted).

1.3 Thesis Structure

There are six chapters in this thesis.

Chapter 1 is an introduction in which the problem is stated, and the contributions of this study are outlined.

Chapter 2 is a brief review, discussing some basic concepts and terms for elastic waves in solids, as well as some methods dealing with ultrasonic

forward and inverse scattering problems.

Chapter 3 contains a brief theoretical derivation of MOOT and discussions about numerical convergence and accuracy for this method. The simulated backscattering responses from some non-spherical voids are also presented in this chapter.

In Chapter 4, a new inversion sizing scheme, the area function sizing technique, is developed. Bandwidth requirements of this sizing scheme are discussed in this chapter. Some numerical results from application of this technique to regular and irregular shaped voids are presented.

Chapter 5 gives experimental sizing results for several simple flaws using the area function sizing method. The experimental procedures and signal processing techniques are discussed.

Chapter 6 gives conclusions of this study and some suggestions for future work.

Chapter 2

REVIEW OF THE BACKGROUND TO THE PRESENT STUDY

2.1 Introduction

This chapter deals with the background material related to this study. Section 2.2 briefly reviews a few basic properties of elastic wave propagation in solids. Section 2.3 discusses the problems of forward scattering from isolated volumetric flaws. Inverse scattering techniques for flaw characterisation are reviewed in section 2.4.

The study is confined to elastic, homogeneous and isotropic media. Since the fundamental aspects of elastic wave propagation and scattering have been presented in many classic books [Auld, 1973; Graff, 1975; Hudson, 1980] and review papers [Thompson and Wadley, 1989; Pao, 1983], the following review has been kept as concise as possible.

2.2 Elastic Waves in Solids

An elastic medium can remain in equilibrium under a shearing stress. When the force is applied for a short time period or is changing rapidly the effect on the medium is considered in terms of stress propagation. Suppose that x_i describes the Cartesian coordinates of a material point in an elastic medium and that u_i describes the displacement of the point from its equilibrium position. Then in linear regime, in the absence of any body force, the equations of motion have the form:

$$\rho \frac{\partial^2 u_i}{\partial t^2} = \frac{\partial T_{ij}}{\partial x_j} \qquad (2\text{-}1)$$

where ρ is the density of the material, and T_{ij} is the mechanical stress tensor. For stresses which do not cause permanent deformation of the solid, the stress-

strain relation is governed by Hooke's law:

$$T_{ij} = C_{ijkl}\varepsilon_{kl} \tag{2-2}$$

with summation over the repeated subscripts k and l, where C_{ijkl} are the elements of the fourth-rank elastic stiffness tensor, and ε_{kl} are the elements of the second-rank elastic strain tensor:

$$\varepsilon_{kl} = \frac{1}{2}\left(\frac{\partial u_k}{\partial x_l} + \frac{\partial u_l}{\partial x_k}\right) \tag{2-3}$$

The combination of equations (2-1) to (2-3) leads to the elastic wave equation

$$(\lambda + \mu)u_{j,ji} + \mu u_{i,jj} = \rho \ddot{u}_i \tag{2-4a}$$

which can then be expressed in vector form,

$$(\lambda+2\mu)\nabla\nabla\cdot\vec{u} - \mu\nabla\times\nabla\times\vec{u} = \rho\frac{\partial^2\vec{u}}{\partial t^2} \tag{2-4b}$$

where λ and μ are its Lamé elastic constants which are related to the independent elements of the elastic constant tensor:

$$\begin{aligned}\lambda &= C_{11} - 2C_{44}\\ \mu &= C_{44}\end{aligned} \tag{2-5}$$

It is possible to obtain a simpler set of wave equations by introducing the scalar and vector potentials ϕ and $\vec{H}$ such that

$$\begin{aligned}\vec{u} &= \nabla\phi + \nabla\times\vec{H}\\ \nabla\cdot\vec{H} &= 0\end{aligned} \tag{2-6}$$

If equation (2-6) is substituted into equation (2-4), the following equations are obtained

$$(\lambda + 2\mu)\nabla^2\phi + \rho\frac{\partial^2\phi}{\partial t^2} = 0 \tag{2-7}$$

$$\mu\nabla^2\vec{H} + \rho\frac{\partial^2\vec{H}}{\partial t^2} = 0 \tag{2-8}$$

They have plane-wave solutions

$$\phi = \phi_0 e^{(i\vec{\kappa}\cdot\vec{r} - i\omega t)} \tag{2-9}$$

$$\vec{H} = \vec{H}_0 e^{(i\vec{\beta}\cdot\vec{r} - i\omega t)} \tag{2-10}$$

where ϕ and $\vec{H}$ correspond to longitudinal and transverse waves, and $\vec{\kappa}$ and $\vec{\beta}$ represent the wave vectors for longitudinal and transverse waves respectively. The directions of the wave vectors are the same with the wave propagation directions, and their values are

$$\begin{aligned} k &= \frac{\omega}{c} \\ \beta &= \frac{\omega}{c_t} \end{aligned} \tag{2-11}$$

where c and c_t are the longitudinal and transverse wave velocities respectively. They are related to the material properties as

$$\begin{aligned} c &= \sqrt{(\lambda + 2\mu)/\rho} \\ c_t &= \sqrt{\mu/\rho} \end{aligned} \tag{2-12}$$

2.3 Forward Scattering from Isolated Volumetric Flaws

For nondestructive testing applications, we are interested in the entire process of elastic wave generation, propagation, scattering and detection. This

section is limited to consideration of elastic wave interactions with (scattering by) isolated flaws.

It has been realized that meaningful flaw characterisation is possible only when the basic physical mechanism of scattering by discontinuities is understood [Fitting and Adler, 1977]. This requires strong theoretical foundations in elastic wave scattering by flaws. The topic of elastic wave propagation and scattering has produced a vast volume of literature across many fields of study which range from geophysics and seismology - where waves interact with features with dimensions of up to a few kilometres - to microwave electronics where interaction is with features that are a fraction of a millimetre [Saffari, 1986]. This section is intended to give a brief review of the theoretical and numerical treatments of elastic eave interactions with volumetric defects, quoting some key references.

A general starting point is often the decomposition of the total elastic displacement field, $\vec{u}$, into an incident field, $\vec{u}_o$, and a scattered field, $\vec{u}_s$,

$$\vec{u} = \vec{u}_o + \vec{u}_s \tag{2-13}$$

For an isolated inhomogeneity embedded in an otherwise isotropic and homogeneous medium, the far-field scattered ultrasonic field can be described by [Gubernatis *et al*, 1977a]

$$\vec{u}_s = \vec{A}_l \frac{e^{ik|\vec{r}|}}{|\vec{r}|} + \vec{B}_t \frac{e^{i\beta|\vec{r}|}}{|\vec{r}|} \tag{2-14}$$

where $\vec{r}$ is the position vector measured from the coordinates centre, $\vec{A}_l$ is the amplitude vector of the scattering longitudinal wave and $\vec{B}_t$ is that of the scattering transverse wave.

The forward scattering problem is to obtain $\vec{A}_l$ and $\vec{B}_t$ with given incident waves and for the known properties of the host and scatterer materials. The

scattering and diffraction of any type is a difficult problem in mathematical physics. Virtually all the theoretical work that has been done with elastic waves has simplified the problem.

In the following discussions, the methods of solution for the forward scattering problem are categorized in six groups, namely (1) exact solutions, (2) integral formalism, (3) ray theory, (4) transition matrix methods, (5) boundary integral equation or boundary element methods, and (6) numerical modelling methods [Harker, 1988; Pao, 1983]. However, this is by no means an attempt to cover all the existing methods.

2.3.1 Exact solutions

It is desirable to get exact solutions in elastic wave scattering problem, but very few problems can be solved exactly. Only the problems of scattering from spherical and cylindrical scatterers have exact solutions [Pao, 1983].

Ying and Truell [1956], Johnson and Truell [1965] studied longitudinal and transverse waves incident on a spherical obstacle (including an elastic sphere, a rigid sphere and a spherical cavity) in an isotropically elastic medium. They explicitly evaluated expressions for the scattering cross-section in the Rayleigh regime. The general solutions are described in terms of an infinite series of linear equations. To get numerical results this series must be truncated. Ying and Truell [1956] series solutions are used in this study to simulate backscattering from spherical voids and inclusions.

White [1958] examined scattering from an infinite cylindrical scatterer, both theoretically and experimentally. Similar to the case of spherical scatterer, an infinite series of linear equations is obtained by theoretical treatment.

2.3.2 Integral formalism

The exact scattering solutions do not, unfortunately, generalize to more complex flaw shapes. For such problems, integral equation approaches and numerical techniques have been used extensively [Harker, 1988].

Figure 2.1 shows a general scattering situation from volumetric flaws. The integral equation describing the scattering from an isolated inhomogeneity was given by Gubernatis *et al* [1977a] as

$$u_i^s(\vec{r}) = u_i^o(\vec{r}) + \delta\rho\omega^2 \int_V g_{im}(\vec{r}-\vec{r}')u_m(\vec{r}')dV_1 + \delta C_{jklm}\int_V g_{ij,k}(\vec{r}-\vec{r}')u_{l,m}(\vec{r}')dV_1 \qquad (2\text{-}15)$$

where $\Delta\rho$ and ΔC_{ijkl} are the changes in density and elastic stiffness constant between host and scatterer, *ijkl* are direction indices, $g(\vec{r}-\vec{r}')$ is the Green's function at $\vec{r}$ due to a point source at $\vec{r}'$, u_m is the displacement field at $\vec{r}'$, and the integral is over the flaw volume V_1 in the space V containing the scatterer. u_i^s is the total scattered field and u_i^o is the incident field, and ω is the angular frequency of the incident wave.

In some problems, it is more convenient to rewrite equation (2-15) as a surface integral. The surface integral formulation for scattering can be found in many books and papers [Harker, 1988; Thompson and Wadley, 1989].

For most of flaw shapes, equation (2-15) is usually solved by approximation methods. For example, Kirchhoff approximation [Freedman, 1962] and Born approximation [Gubernatis *et al*, 1977b] are commonly used.

a) The Kirchhoff approximation

The essence of the Kirchhoff approximation is that values and gradients

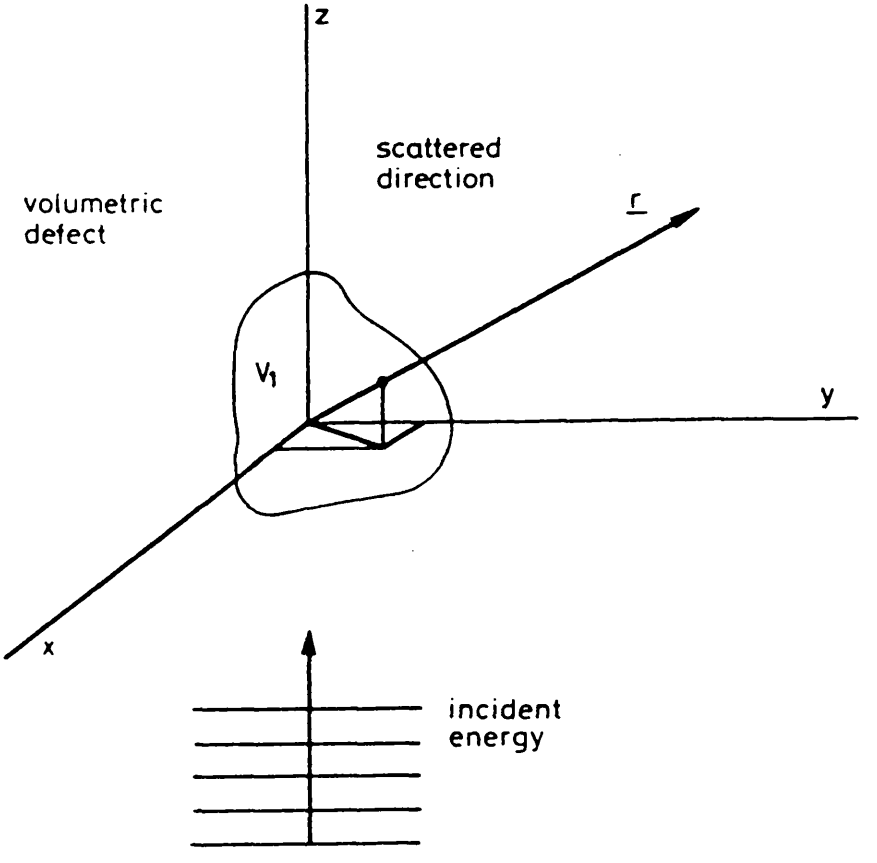

Figure 2.1 A general scattering situation from volumetric flaws (after Chaloner and Bond [1987])

of the displacements are determined by the incident field, and that the incident field is non-zero only in regions which would be insonified in a geometric ray picture [Harker, 1988]. The scattered field is then calculated by performing the surface integral over the region of the scattering surface outside a sharply defined shadow zone. The approximation is more accurate at high frequency and near specular angles.

The elastodynamic Kirchhoff approximation has been applied by Brind *et al* [1984] and Adler and Achenbach [1980] to scattering by a cylindrical cavity and by a crack. Brind *et al* [1984] have also developed a hybrid theory where creeping waves are explicitly incorporated in high frequency far-field integral solution.

b) The Born approximation

This is a weak scattering approximation where elastic properties of the scatterer differ only slightly from those of the host material, and thus the scattering is weak and the total wave-field is dominated by the incident wave [Gubernatis, *et al* 1977b]. The first Born approximation is perhaps the simplest among all the approximation methods. It is the first term in an iteration perturbation series, that is, the incident (unperturbed) wave field is substituted for the unknown wave-field inside the scatterer. Thus the approximation only partially accounts for diffraction and scattering. Gubernatis *et al* [1977b] applied this approximation theory to elastic wave scattering, giving the theoretical formulas in the frequency domain. The time domain Born approximation was later reported by Richardson and Rose [1982]. The time domain Born approximation is studied in more detail in chapter 4 of this thesis, where a new inversion sizing scheme is developed based on this approximation.

Considerable numerical and experimental work has shown that good

agreement has been obtained using the Born approximation with strong scatterers in various elastic media in the backscattering directions [Addison *et al*, 1982; Chaloner, 1987]. Gubernatis *et al* [1977b] investigated the validity of the Born approximation to strong scatterers by comparing it with exact results for spherical scatterers. They concluded that for voids in elastic media the Born approximation describes the scattering well for $ka \leq 1$ (where k represents the wave number, and a represents the radius of the flaw or more generally the size of the flaw) and when the scattering is viewed in the backscattering directions. For elastic inclusions, however, where the properties of scatterer and host differed by 20-40%, the Born approximation is surprisingly good for all angles and even at short wavelengths [Gubernatis *et al*, 1977b].

The Distorted Wave Born Approximation (DWBA) [Tittmann *et al*, 1983] is an extension of the Born approximation. The basic idea upon which the DWBA is based is that any general shaped scatterer is represented by the combination of a spherical scatterer and a remainder function. The exact solution for a spherical scatterer can be calculated using the Ying and Truell [1956] model, and the remainder is regarded as a perturbation. It is assumed that the displacement field in the remainder volume is the same as in the sphere. The method is therefore expected to be good for near-spheres and weak scatterers. The approximation results from the DWBA and the experimental results were compared and shown good agreement [Tittmann *et al*, 1983].

The Born approximation was extended by Gubernatis [1979] to the quasistatic approximation and the extended quasistatic approximation. The distinguishing feature of these approximations is the replacement of the actual strain field inside the scatterer volume by a strain field based on the one found in the static problem. Gubernatis [1979] showed that the extended quasistatic approximation is in excellent agreement with exact result for values of ka up to about unity.

2.3.3 Geometric Ray Theory

Geometric acoustics is the acoustic analogue of geometric optics. The geometric ray theory for the scattering of acoustic waves by a smooth body was developed by Levy and Keller [1959]. A full exposition of this method is contained in the monograph by Achenbach *et al* [1982].

Geometric acoustics makes the generalization by treating every point on wave-front as part of a plane wave. It assumes that rays and wave-fronts are always perpendicular to each other, even in complicated cases where the material properties vary from point to point, so that the rays are not straight [Harker, 1988]. A geometric ray connects a source and a receiver by the path of minimum travel time of a wave. The amplitude of the wave decays as it radiates from the source, and the decay rate can be calculated in terms of the length of the ray [Pao, 1983]. Geometric ray theory is only valid at high frequency limit.

2.3.4 *T*-matrix Methods

The developments of this method have been reported in the proceedings of a special conference [Varadan and Varadan, 1980] and many other publications [Waterman, 1976; Varadan and Pao, 1976; etc.]. Varadan and Varadan [1988] gave a comprehensive list of publications on this topic.

The essence of the *T*-matrix method is that the incident and the scattered waves are expanded in terms of an infinite series of orthogonal basis wave functions. The unknown scattering coefficients are related to the known incident wave coefficients by an infinite matrix *T*. The scattered fields are then described in terms of a set of the basis functions and coefficients.

In practice, the *T*-Matrix calculation must always be truncated and the approximation is made better by increasing the number of terms in the expansion. The accuracy of this simple truncation may be assessed by comparing the results obtained with those arising from the solution with an extra term in the series. Larger flaw size to wavelength ratios (i.e. larger *ka*) require a larger number of terms, which means that because of limitations of computer word-length and computing time, there is an upper bound on the *ka* range which can be treated. Also, since the *T*-Matrix method involves a partial wave expansion, the method cannot be used in practice for very short wavelength (large *ka*) incident wave [Visscher, 1980b; Albach, 1989]. The *T*-matrix approach has primarily been employed for axisymmetric scatterers when the wavelength is comparable to the flaw dimension.

Visscher [1980a,b] developed a method called the Method Of Optimal Truncation (MOOT), a least squares boundary residual method originally proposed for electromagnetic scattering [Davies, 1973], giving general approaches of the construction of the *T*-matrix. He has given several optimal truncation approaches which minimize the boundary condition errors due to the truncation of the infinite series. He has applied MOOT to the calculation of scattering from various scatterers, including spheroidal voids and inclusions.

MOOT is used in this study to simulate ultrasonic scattering from regular and irregular shaped voids. Chapter 4 gives more details of the theory and applications of MOOT.

2.3.5 Boundary Integral Equation or Boundary Element Methods

This technique is similar to the *T*-Matrix method in that this technique involves the solution of an integral equation, which in this case is obtained by dividing the surface of the scatterer into elements each of which then has an

associated unknown displacement [Manolis and Beskos, 1988]. This technique is increasingly used and has already been used for scattering by arbitrarily shaped voids and also a range of both volumetric [Rizzo *et al*, 1985] and surface features [Albach, 1989; Sanchez-Sesma, 1987]. The major limitations appear to be due to the complexity which can be encountered in the formulation of the initial equations and then solution of the equation set involved. [Bond, 1989a]

2.3.6 Numerical Modelling Methods

In practical applications of elastic wave scattering to nondestructive evaluation, one frequently wants to treat complicated geometrical situations, which are not amenable to analytic treatment. In these cases, one can choose to use a completely numerical approach such as a finite difference or a finite element method.

The finite difference method has been successfully applied to the solution of many physical problems that were previously analytically intractable, including problems in NDE [Saffari, 1988]. The basic idea of the finite difference method is to replace the differential form of the wave equation by a discrete set of equations in which the displacements (or other values of the field) are defined only on the points of intersection of a grid. The partial derivatives in the wave equation are approximated to a given accuracy. Recently, the applications of this method have been widely reported [Saffari and Bond 1987; Bond, 1982]. A review was given by Bond [1982], in which he showed that a finite difference method is best suited for modelling the scattering problem in the resonance region where the scatterer dimensions are of the same order as the wavelength.

The finite element method is relatively new and has not been as widely

applied to nondestructive testing wave propagation problems as the finite difference method. However, there are some publications about the applications of this method, e.g. Tsao *et al* [1983], Datta and Shah [1982]. The most recent review of finite difference and finite element methods was given by Bond [1989a].

In summary, exact solutions are only available for particular simple geometrical shapes (e.g. sphere). The Born approximation is valid for small, weak scatterers at low frequency with $ka \leq 1$. The Kirchhoff approximation and geometric ray theory are applicable at high frequency. For general cases, in the intermediate region where ka is of unity, the T-matrix methods, the finite difference and finite element methods are most suitable. The properties of the various numerical methods considered are summarised as Table 2.1 which was compiled from Bond [1989a].

Table 2.1 Comparison of various techniques applied to ultrasonic wave propagation and scattering (after Bond [1989a])

Technique.	Analytical methods	Finite differences	Elastic Kirchhoff	Born Approx.	Geometrical theory of diffraction	T-Matrix.	BIE or BEM.
Property.							
ka restriction.	ka<< 1 ka>> 1	0.1< ka <20	ka>>1	ka <1	ka >>1	0<ka<15	0 <ka< 6
Field region	Far	Near or Far	Far	Far	.Far	Either	Near or Far
Dimension	3-D	2-D (3-D)	3-D	3-D	2.5-D	3-D	Most 3-D
Shape of scatterer	circle, cylinder sphere.	limited (square.) *	small surface slope.	good range **	crack-like	ellipsoidal cavity.	Arbitrary.
Included material	restricted	most ***	**	weak	X	***	Strong or weak
Mode conversion	**	***	***	**	*	***	***
Incident wave.	plane or spherical	arbitrary 2-D	plane or spherical	**	**	**	Arbitrary
Short pulse.	**	***	*	+	*	X	FFT used.
Multiple scattering. (2 Body)	+	***	+	+	*	**	**.

Rating system: *** Very good, ** Good, * Copes, + poor, X Very Poor. (Temple [1987])

2.4 Inverse Scattering Techniques for Flaw Characterisation and Sizing

In this section, the development of the inverse scattering techniques for characterisation of volumetric flaws is reviewed, following the most recent review paper by Thompson and Wadley [1989]. A very important class of techniques based on the formation of images is not considered since their implementation and interpretation does not depend on explicit knowledge of the principles of forward scattering models [Thompson and Wadley, 1989]. The inverse scattering techniques can be divided into three groups, which can be roughly categorized by the ratio of flaw size to wavelength.

2.4.1 High frequency or large flaws ($ka>>1$)

When the wavelength is small with respect to the size of the scatterer, the scattering can be considered to be the superposition of energy travelling along various ray paths. In measurements of the scattering from smooth objects it has been found that specular reflections, creeping rays propagating around the periphery of the object, and rays propagating through the interior of the object make major contributions to the received signals and that the time and amplitudes of these rays can be used in sizing and identifying the material of the flaw [Thompson and Wadley, 1989]. The ideas have been applied to the problems of sizing inclusions in ceramics [Chou *et al.*, 1980] and voids and inclusions in metals [Gruber, 1980]. Figure 2.2 was compiled from Chou *et al* [1980], showing wave forms backscattered from various flaws in Si_3N_4 and identifying the arrivals with various ray paths. However, experiments indicate that the creeping ray may be highly damped by the surface roughness of naturally occurring flaws [Cohen-Tenoudji *et al*, 1981], and the robustness of sizing techniques based on these ray paths may not be as great as desired for naturally occurring flaws. Moreover, in many practical cases, material attenuation may preclude the use of sufficiently high frequencies to allow the

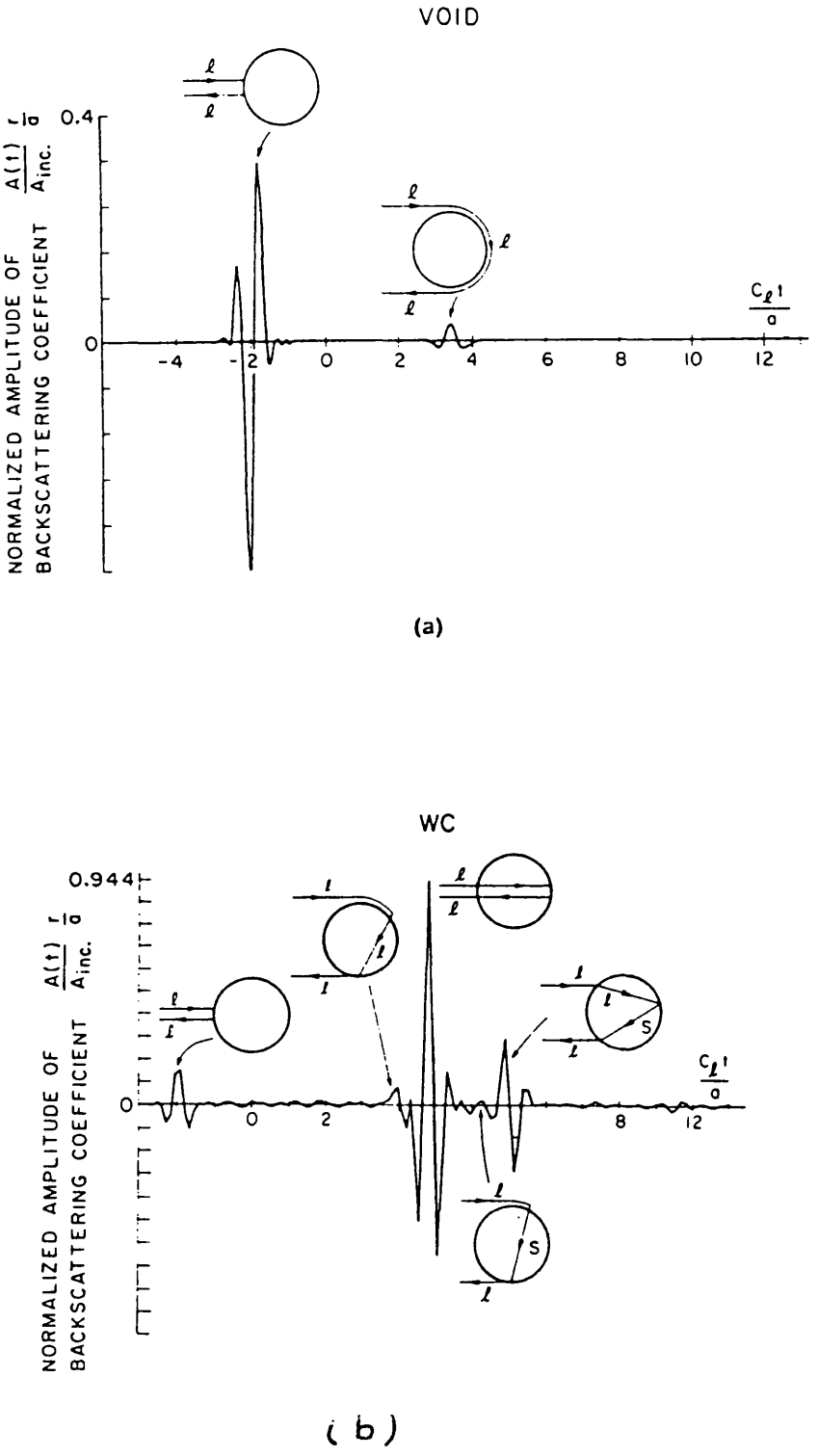

Figure 2.2 Backscattered waveforms in the time domain from spherical scatterers in Si_3N_4; (a) Void; (b) WC [Chou et al, 1980].

various signals to be resolved in time.

2.4.2 Mid-frequency or intermediate size flaws ($ka \approx 1$)

When the wavelength is medial with respect to the flaw size, the scattered waves contain rich information about the scatterer. Many inverse scattering solutions in this regime have been developed for reconstructing the shapes of volumetric flaws. The one that has received most investigation in quantitative nondestructive evaluation is the Inverse Born Approximation (IBA), which has been reviewed in detail by Rose [1989].

The IBA was derived from the assumption that the flaw is a weakly scattering, three-dimensional discontinuity [Rose and Krumhansl, 1979]. It is a reconstruction algorithm consisting of an inverse Fourier transform of the scattering amplitudes measured at appropriate angles and frequencies. Although the IBA is based on the weak scattering assumption, it has been found to accurately predict the size of voids and to be fairly robust in the presence of noise and limited bandwidth [Elsley and Addison, 1980].

If one assumes spherical symmetry of a scatterer, only a one-dimensional inverse transform is required, and the algorithm can be simplified greatly. In fact, much of attention has been given to the 1-D case [Rose, 1989]. For ellipsoidal defects, the 1-D IBA algorithm can still be used. In that case 1-D algorithm has been shown to reconstruct the front-surface tangent plane distance [Rose *et al*, 1982]. The tangent plane distance corresponds to the distance from the flaw centroid to a plane, perpendicular to the propagation direction and tangent to that surface of the flaw, nearest the transducer. Figure 2.3 shows the tangent plane distance. A transformation is then required to convert plots of the front-surface tangent plane distances to the true flaw boundary. The experimental reconstructions of the shapes of ellipsoidal voids

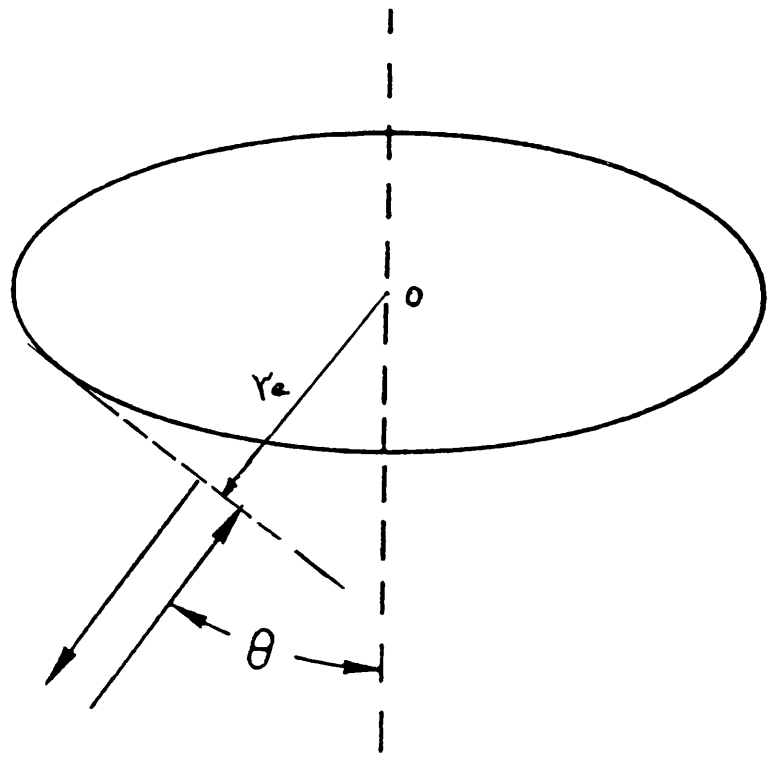

Figure 2.3 The tangent plane distance for the ellipsoidal scatterer

and naturally occurring inclusions in aircraft engine turbine have been successfully accomplished [Addison *et al*, 1982; Hsu *et al*, 1984]. The 1-D IBA has been found to require a bandwidth of $0.5 \leq ka \leq 2.5$ [Rose, 1989; Chaloner, 1988].

The full three-dimensional form of the IBA has been studied less extensively. It has been reported that the algorithm can exactly determine the shape of convex defects from perfect backscattering data [Rose and Opsal, 1983].

The major advantages of the 1-D IBA approach can be summarized as: (1) sizing information can be obtained from band-limited data containing relatively long wavelengths; (2) the dimension measured lies along the line of propagation of the ultrasonic beam. However, there are a number of difficulties concerning experimental implementation of the algorithm. Most notably, the algorithm requires the time origin in the time domain signal to be at the flaw centroid. This can in principle be determined from the low frequency phase characteristic of the scattered signals, but practical implementation is made difficult by a number of factors, including the absence of low frequency energy in many commercially available transducers. Attempts have been made to restore the lost low frequency information by extrapolation [Koo *et al*, 1990; Koo, 1987]. There are also attempts to use the IBA without explicitly determining the flaw centroid. One of them is an empirical method called "Born again" or "Born Radius/Zero-of-Time Shift Domain (BR/ZOTSD) method" [Bond *et al*, 1988; Addison *et al*, 1982; Chaloner, 1988; Bond *et al*, 1987]. The method involves applying the IBA algorithm for a large number of time-shifts. A pattern is therefore produced, from which the radius of the flaw can be obtained.

Kogan *et al* [1985] also developed an algorithm related to the IBA,

based on the zeros of the ultrasonic scattering amplitude. The method is based on the observation that, for a wide class of flaws, the zeros in the real and imaginary parts of the frequency domain scattering amplitude occur at characteristic frequencies which depend on the flaw size. The method is simpler than the inverse Born algorithm because the flaw sizes are extracted directly from the characteristic frequencies. This method employs the same input data as the IBA and has certain common limitations.

The another inverse algorithm which has received considerable attention is the Physical Optics Far Field Inverse Scattering (POFFIS) algorithm [Bleistein and Cohen, 1979 and 1980]. POFFIS was derived as an inverse solution to the scattering from voids, as described by the physical optics approximation. The algorithm also consists of the evaluation of the inverse Fourier transform of measured scattered fields. However, instead of reconstructing the characteristic function of the flaw as in the IBA, the normal derivative of this function, i.e., the flaw edge, is reconstructed. Langenberg *et al* [1982] compared several inverse scattering algorithms based on synthetic data, and found POFFIS applicable to a wide range of flaw shapes. As implied by the term "physical optics", POFFIS is a high frequency method working in the frequency range of $3 \leq ka \leq 7$. However, in the applications, the algorithm has been found to work well down to frequencies as low as 1.2 ka, below which undersizing occurs.

Cohen-Tenoudji and Tittmann [1982] formulated an inversion algorithm based on the Kirchhoff approximation, where the output is the length of the illuminated flaw region in the direction of the ultrasonic illumination. The algorithm was shown to be useful in the $1 \leq ka \leq 4$ range for the construction of an image.

2.4.3 Low frequency or small flaws ($ka<<1$)

When the wavelength is large with respect to the size of the scatterer, a detailed reconstruction of the flaw size is impossible. However, It has been found that a considerable amount of information about the flaw geometry exists in this long wavelength region [Richardson, 1978; Kohn *et al*, 1979]. Tittmann *et al* [1980] have applied probabilistic inversion methods to experimental data to determine the size, shape, and orientation of a spheroidal void in a titanium alloy.

Chapter 3
NUMERICAL SIMULATION OF ULTRASONIC SCATTERING FROM NON-SPHERICAL VOIDS

3.1 Introduction

This chapter reports numerical modelling work used to generate forward scattering data to test the inversion technique which is described in the next chapter, as well as to provide understanding of basic physical mechanism in scattering by voids.

In this chapter, the Method Of Optimal Truncation (MOOT), a least squares boundary residual method which was originally proposed for electromagnetic scattering [Davies, 1973] and then introduced to elastic wave scattering [Visscher, 1980a,b], is studied. MOOT has been investigated and used by many scientists, and it has been found to be efficient, versatile and reliable. A large computer model based on the idea of MOOT and the numerical results are reported in this chapter. The computer model can be used to simulate ultrasonic scattering from different shaped voids, with only minor changes according to the size and shape of the void considered.

The structure of this chapter is as follows. Section 3.2 describes the theory of MOOT; Section 3.3 discusses numerical convergency and accuracy; In Section 3.4, numerical scattering results from several non-spherical voids are given, and their features are explained; finally, discussions of the results are given in Section 3.5.

3.2 Theory of Method Of Optimal Truncation (MOOT)

The detailed theoretical treatments of MOOT can be found in many

publications [Visscher, 1980a,b; Opsal and Visscher, 1985; Visscher, 1981]. Here, the analysis given by Visscher [1980a,b] is followed to give a brief analysis and the derivation of MOOT.

Figure 3.1 depicts the scattering geometry. The wave function (displacement of the medium from its equilibrium position) for elastic waves is considered as time harmonic

$$\vec{u}(\vec{r},t) = \vec{u}(\vec{r})\, e^{-i\omega t} \tag{3-1}$$

where $\vec{u}$ represents the displacement of the medium, and $\vec{r}$ is the position.

The basic idea of MOOT is to decompose the wave function,$\vec{u}$, into its partial-wave components $\vec{u}_{plm}$ [Visscher, 1981],

$$\vec{u}_{1lm} = k^{-1}\nabla\varphi_{lm} \tag{3-2}$$

$$\vec{u}_{2lm} = \vec{r}\times\nabla\psi_{lm} \tag{3-3}$$

$$\vec{u}_{3lm} = \beta^{-1}\nabla\times\vec{u}_{2lm} \tag{3-4}$$

where the first index specifies polarization: p=1 represents the longitudinal wave, p=2 and 3 represent the transverse waves, and φ and ψ are solutions of Helmholtz's equation

$$(\nabla^2 + k^2)\varphi = 0, \quad (\nabla^2 + \beta^2)\psi = 0 \tag{3-5}$$

They are

$$\begin{aligned} \varphi_{lm} &= z_l(kr)Y_{lm}(\theta,\phi) \\ \psi_{lm} &= z_l(\beta r)Y_{lm}(\theta,\phi) \end{aligned} \tag{3-6}$$

where Y_{lm} is a spherical harmonic function, θ and ϕ are the polar and azimuthal angles, and z_l is a spherical Bessel function. Outside flaw, in scattered wave $\vec{u}_s$,

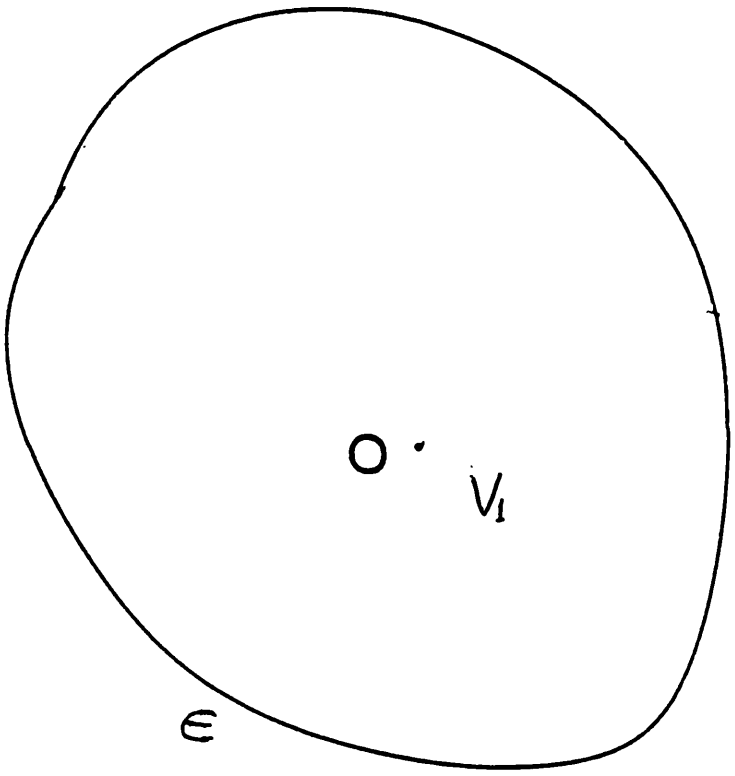

Figure 3.1 Scattering geometry. The scatterer occupies the volume V_1, and ϵ represents the surface of the scatterer.

the outgoing spherical Hankel function, $z_l=h_l^{(1)}$, should be chosen. Inside flaw, in incident wave $\vec{u}_o$, the regular spherical Bessel function, $z_l=j_l$, should be chosen [Opsal and Visscher, 1985].

In the scattering problem, it is natural to divide the displacement into incident and scattered parts $\vec{u}_o$ and $\vec{u}_s$, as shown in equation (2-13)

$$\vec{u}=\vec{u}_o+\vec{u}_s \tag{2-13}$$

$\vec{u}_s$ and $\vec{u}_o$ can be expanded in terms of the basis functions $\vec{u}_{plm}$ [Visscher, 1981],

$$\vec{u}_s=\sum_{plm} a_{plm}\vec{u}_{plm}^{+} \tag{3-7}$$

$$\vec{u}_o=\sum_{plm} d_{plm}\vec{u}_{plm}^{-} \tag{3-8}$$

where the "+" means $z_l=h_l^{(1)}$, and the "-" means $z_l=j_l$.

The expansion of a vectorial plane wave with arbitrary polarisation in terms of spherical vector wave functions can be found in Morse and Feshbach [1953], and in many publications [Varadan and Pao, 1976; Visscher, 1980a,b; Albach, 1989]. Here only the expansion of the incident longitudinal wave is considered. Assume the incident longitudinal plane wave has a wave vector $\vec{k}_o$ with a unit amplitude

$$\vec{u}_o=\hat{e}_o e^{i\vec{k}_o\cdot\vec{r}} \tag{3-9}$$

where $\hat{e}_o$ is the polarisation of the plane wave. The expansion of $\vec{u}_o$ in terms of spherical vector function $\vec{u}_{1lm}^{-}$ is given as [Visscher; 1980b]

$$\vec{u}_o=4\pi\sum_{l,m} i^{(l-1)}Y_{lm}^{*}(\theta_o,\phi_o)\vec{u}_{1lm}^{-} \tag{3-10}$$

where θ_o and ϕ_o are the polar and azimuthal angles of $\vec{k}_o$. So, the coefficients

d_{1lm} for the incident longitudinal wave are

$$\begin{aligned} d_{1lm} &= 4\pi i^{(l-1)} Y^*_{lm}(\theta_o, \phi_o) \\ d_{2lm} &= 0 \\ d_{3lm} &= 0 \end{aligned} \tag{3-11}$$

To obtain the scattering coefficients a_{plm} (equation (3-7)), equation (2-13) needs to be solved. To solve this equation, the boundary conditions constraining $\vec{u}$ on the flaw surface must be satisfied. For a void, the free surface boundary conditions apply, namely

$$\vec{t}(\vec{r}) = \overleftrightarrow{T} \cdot \hat{n} = 0, \quad \vec{r} \; is \; on \in \tag{3-12}$$

where $\vec{t}$ is the surface traction which is a vector with dimensions of force per unit area, $\overleftrightarrow{T}$ is the stress tensor, $\hat{n}$ is the outward unit normal to the void surface, and $\in$ represents the void surface. Equation (3-12) can be expressed in vector notation as

$$\vec{t} = 2\mu(\hat{n} \cdot \nabla)\vec{u} + \mu \hat{n} \times (\nabla \times \vec{u}) + \lambda \hat{n} \nabla \cdot \vec{u} = 0 \tag{3-13}$$

The total surface traction is naturally divided into two parts, $\vec{t}_o$ due to the incident wave and $\vec{t}_s$ due to the scattered waves, and they are decomposed into their partial-wave basis components $\vec{t}_{plm}$

$$\begin{aligned} \vec{t} &= \vec{t}_o + \vec{t}_s \\ &= \sum_{plm} d_{plm} \vec{t}^{\,-}_{plm} + \sum_{plm} a_{plm} \vec{t}^{\,+}_{plm} \end{aligned} \tag{3-14}$$

Equation (3-14) is substituted into equation (3-12) to satisfy the free surface boundary conditions

$$\sum_{plm} [d_{plm} \vec{f}^{-}_{plm}(\vec{r}_\epsilon) + a_{plm} \vec{f}^{+}_{plm}(\vec{r}_\epsilon)] = 0 \qquad (3\text{-}15)$$

where $\vec{r}_\epsilon$ represents the position vector on the void surface.

Now, a set of functions $[\vec{f}_j]$, j=1, 2, ···, ∞, is introduced, which is complete on the void surface. If equation (3-15) is multiplied by $\vec{f}^{*}_j(\vec{r}_\epsilon)$ (where "*" means the conjugate), and integrated over ϵ, it becomes [Visscher, 1980a]

$$\sum_{plm} \left[d_{plm} \int_\epsilon \vec{f}_j^{\,*} \cdot \vec{f}^{-}_{plm} dS + a_{plm} \int_\epsilon \vec{f}_j^{\,*} \cdot \vec{f}^{+}_{plm} dS \right] = 0 \qquad (3\text{-}16)$$

which can be written in matrix form as

$$Q^{-} d + Q^{+} a = 0 \qquad (3\text{-}17)$$

where

$$\begin{aligned} Q^{-}_{j,plm} &= \int_\epsilon \vec{f}_j^{\,*} \cdot \vec{f}^{-}_{plm} dS \\ Q^{+}_{j,plm} &= \int_\epsilon \vec{f}_j^{\,*} \cdot \vec{f}^{+}_{plm} dS \end{aligned} \qquad (3\text{-}18)$$

In a computer calculation, it is impossible to introduce complete sets $[\vec{f}_j]$ because they must always be truncated, i.e. j=1, 2, ···, L, with L finite. If $L \rightarrow \infty$, the matrix equation (equation (3-17)) is completely equivalent to the stress free boundary conditions, and the solutions will not depend on the choice of the complete set $[\vec{f}_j]$. When L is finite, as it must be in practice, an error is encountered in satisfying the boundary conditions, and the set $[\vec{f}_j]_L$ must be chosen very carefully. MOOT optimizes the approximate solution by a least squares minimization of that error. The result of that minimization for a void scatterer is [Visscher, 1980a,b; Opsal and Visscher, 1985; Opsal, 1981]

$$\vec{f}_j = \vec{t}^{+}_{plm} \tag{3-19}$$

This result is used in this study. If equation (3-19) is substituted into equation (3-18), then the results are

$$\begin{aligned} Q^{+}_{plm,\,p'l'm'} &= \int_{\epsilon} \vec{t}^{+\,*}_{plm} \cdot \vec{t}^{+}_{p'l'm'}\, dS \\ Q^{-}_{plm,\,p'l'm'} &= \int_{\epsilon} \vec{t}^{+\,*}_{plm} \cdot \vec{t}^{-}_{p'l'm'}\, dS \end{aligned} \tag{3-20}$$

As discussed before, the matrices are always truncated:

$l = 0, 1, 2, \cdots, l_{max},$

$m = -l, (-l + 1), \cdots, l,$

so the rank of the matrices is

$$3(1 + 3 + 5 + \cdots + 2l_{max} + 1) = 3(l_{max}+1)^2 = L$$

where "3" is because p has three values.

Consideration is now restricted to axially symmetric voids, to obtain an important computation simplification. Without further loss of generality, it is assumed that the axis of symmetry to be along the z axis. By careful inspection using the properties of spherical harmonic functions, it is found that [Visscher, 1980a,b]

$$\begin{aligned} Q^{+}_{plm,\,p'l'm'} &= \int_{\epsilon} \vec{t}^{+\,*}_{plm} \cdot \vec{t}^{+}_{p'l'm'}\, dS = 0 \\ Q^{-}_{plm,\,p'l'm'} &= \int_{\epsilon} \vec{t}^{+\,*}_{plm} \cdot \vec{t}^{-}_{p'l'm'}\, dS = 0 \end{aligned} \quad , \; if \quad m \neq m' \tag{3-21}$$

So, both Q^{+} and Q^{-} are block-diagonal matrices which can be rearranged as

$$Q = \begin{bmatrix} Q^{(0)} & 0 & \cdot & 0 & 0 \\ 0 & Q^{(1)} & \cdot & \cdot & 0 \\ \cdot & \cdot & \cdot & \cdot & \cdot \\ 0 & \cdot & \cdot & \cdot & 0 \\ 0 & \cdot & \cdot & \cdot & Q^{(l_{max})} \end{bmatrix} \tag{3-22}$$

and

$$Q^{(m)}=\begin{bmatrix} Q_{1mn,1mn} & \cdot & Q_{1mn,1l_{max}m} & \cdot & Q_{1mn,3l_{max}m} \\ \cdot & \cdot & \cdot & \cdot & \cdot \\ Q_{1l_{max}m,1mn} & \cdot & \cdot & \cdot & \cdot \\ \cdot & \cdot & \cdot & \cdot & \cdot \\ Q_{3l_{max}m,1mn} & \cdot & \cdot & \cdot & Q_{3l_{max}m,3l_{max}m} \end{bmatrix} \tag{3-23}$$

where Q represents either Q^- or Q^+, and the rank of $Q^{(m)}$ is $3(l_{max}-m+1)$.

Equation (3-17) can then be solved through a set of smaller rank equations

$$Q^{-(m)}d^{(m)} + Q^{+(m)}a^{(m)} = 0 \tag{3-24}$$

where

$$d^{(m)}=\begin{bmatrix} d_{1mn} \\ \cdot \\ d_{1l_{max}m} \\ 0 \\ \cdot \\ 0 \end{bmatrix} \tag{3-25}$$

$$a^{(m)}=\begin{bmatrix} a_{1mn} \\ \cdot \\ a_{1l_{max}m} \\ a_{2mn} \\ \cdot \\ a_{3l_{max}m} \end{bmatrix} \tag{3-26}$$

By inspection of the matrix elements using the properties of the spherical harmonic function, one can find that both Q^- and Q^+ satisfy [Visscher, 1980b]

$$Q_{pl-m,\,p'l-m} = (-1)^{p-p'} Q_{plm,\,p'lm} \tag{3-27}$$

This means that there is no need to solve the equations for negative m separately. Once the equations for positive m have been solved, the coefficients, a_{plm}, for negative m can be obtained from those for positive m,

$$a_{pl-m} = (-1)^{(p+m+1)} a_{plm} \tag{3-28}$$

Far-field results

Once a_{plm} have been calculated, the amplitudes of the scattered waves can be obtained immediately. In the area of non-destructive evaluation, the far-field results are usually of interest. Here only the scattered longitudinal wave in the far-field is considered. From equation (3-2), the displacement vector for the scattered longitudinal wave is given by

$$\begin{aligned} \vec{u}_s(\vec{r}) &= \sum_{1lm} a_{1lm} \vec{u}^{+}_{1lm} \\ &= k^{-1} \sum_{lm} a_{1lm} \nabla \varphi^{+}_{lm}(\vec{r}) \\ &= k^{-1} \sum_{lm} a_{1lm} \nabla h_l^{(1)}(kr) Y_{lm}(\theta,\phi) \end{aligned} \tag{3-29}$$

For large arguments, the spherical Hankel functions $h_j^{(1)}(kr)$ have the following asymptotic property

$$h_l^{(1)}(kr) \simeq (-i)^{l+1}\frac{e^{ikr}}{kr} \tag{3-30}$$

Thus, in the far-field, when the argument kr is large, the scattered longitudinal wave can be regarded as outgoing spherical wave, and its amplitude can be found as the radial component of the scattered displacement vector

$$\left[\vec{u}_s(\vec{r})\right]_r = \hat{e}_r k^{-1}\sum_{lm} a_{1lm}\frac{\partial h_l^{(1)}(kr)}{\partial r}Y_{lm}(\theta,\phi) \tag{3-31}$$

Using equation (3-30) and a recursion formula of the Bessel functions,

$$z_l'(x) = -z_{l+1}(x) + \frac{lz_l(x)}{x}\ , \tag{3-32}$$

to process equation (3-31), one obtains

$$\begin{aligned}\left[\vec{u}_s(\vec{r})\right]_r &\simeq \frac{e^{ikr}}{r}\hat{e}_r\sum_{lm}\left(\frac{(-i)^l}{k} + \frac{l(-i)^{(l+1)}}{k^2 r}\right)a_{1lm}Y_{lm}(\theta,\phi) \\ &\simeq \frac{e^{ikr}}{r}\vec{A}_l\end{aligned} \tag{3-33}$$

where $\vec{A}_l$ is the longitudinal scattering amplitude, also defined in equation (2-14), and

$$\vec{A}_l \simeq \hat{e}_r\sum_{lm}\left(\frac{(-i)^l}{k} + \frac{l(-i)^{(l+1)}}{k^2 r}\right)a_{1lm}Y_{lm}(\theta,\phi) \tag{3-34}$$

In the far-field,

$$r\to\infty,\quad \frac{l(-i)^{(l+1)}}{k^2 r}\to 0 \tag{3-35}$$

So, $\vec{A}_l$ can be approximated as

$$\vec{A}_l \simeq \hat{e}_r k^{-1}\sum_{lm}(-i)^l a_{1lm}Y_{lm}(\theta,\phi) \tag{3-36}$$

The differential cross-section for longitudinal wave, $d\sigma_l/d\Omega$, (where $d\Omega$ is the differential element of solid angle), is defined as the scattered longitudinal power per unit solid angle divided by the incident power per unit area. With a unit amplitude for the incident longitudinal wave, the differential cross-section is related to A_l by the following equation [Gubernatis *et al*, 1977a]

$$\begin{aligned}\frac{d\sigma_l}{d\Omega} &= |A_l|^2 \\ &= k^{-2}\left|\sum_{lm}(-i)^l a_{1lm} Y_{lm}(\theta,\phi)\right|^2\end{aligned} \tag{3-37}$$

The total longitudinal cross section, σ_l, is defined as the ratio of the average longitudinal power flux scattered into all directions to the average intensity of the incident fields [Gubernatis *et al*, 1977a]. It is simply the integration of $d\sigma_l/d\Omega$ over all angles. From equation (3-37)

$$\begin{aligned}\sigma_l &= \int \frac{d\sigma_l}{d\Omega} d\Omega \\ &= k^{-2}\sum_{lm}|a_{1lm}|^2\end{aligned} \tag{3-38}$$

When the convergence of the method is considered the following two quantities are considered [Opsal and Visscher, 1985]: (1) the total longitudinal cross-section, σ_l, expressed as equation (3-38), and (2) the normalized boundary residual,

$$J/J_0 = \frac{\int_\epsilon |\vec{r}|^2 dS}{\int_\epsilon |\vec{r}_o|^2 dS} = \frac{\int_\epsilon |(\vec{r}_o + \vec{r}_s)|^2 dS}{\int_\epsilon |\vec{r}_o|^2 dS} \tag{3-39}$$

3.3 Implementation, Numerical Convergence and Accuracy

Based on the above theoretical analysis of MOOT, a computer program has been developed to calculate ultrasonic wave scattering from axially symmetric voids. As a test case, a 4:3 oblate void in titanium (c=6.20 *km/s*, c_t=3.125 *km/s*) is used to discuss the implementation of the computer program and the numerical convergency and accuracy. The void is shown as figure 3.2, where *a:b=4:3* and *a=0.22 mm*. Oblate voids are important since they serve as models for volumetric flaws found in structural applications. Numerical results for several other voids are presented in Section 3.4.

The main parts of the program are listed below.

(1) Calculation of the surface traction components, $\vec{t}_{plm}$, on the surface of the void. The formulas for these calculations can be found in many classic books and papers [Pao and Mow, 1973; Visscher, 1980b]. These formulas are included in Appendix 3A. Appendix 3B contains Bessel functions and spherical harmonic functions, and their properties, which are essential for the evaluation of these formulas.

(2) Evaluation of Q matrix elements. After the surface traction components have been calculated, a n-point Gauss-Legendre quadrature scheme [Press *et al*, 1986] is used to evaluate the surface integral (equation (3-20)) to get the matrix elements.

(3) Solving linear system, equation (3-24), to obtain partial-wave coefficients a_{plm}.

(4) Calculation of the scattering amplitude, $\vec{A}_l$, from a_{plm} using equation (3-36).

There are two most important parameters influencing accuracy and

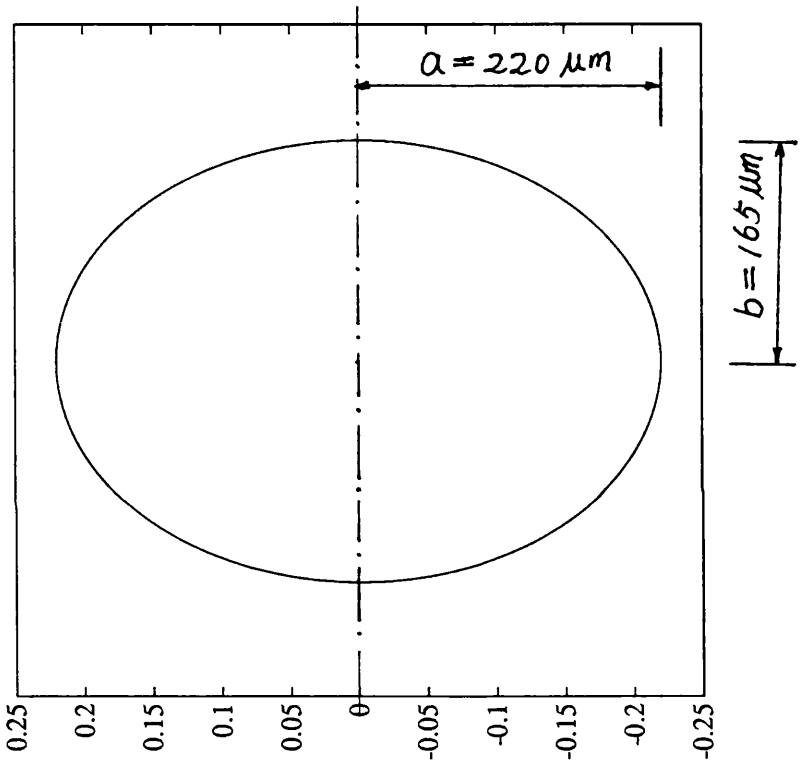

Figure 3.2 Backscattering from a 4:3 oblate void.

computing time. One is the number of the integration points (n) taken in the Gauss-Legendre numerical integration scheme. Another parameter is the truncation limit (l_{max}) which determines the ranks of the matrices.

Larger n leads to more accurate matrix elements. But, because of the limitation of computing time, n cannot be made too large. It is determined in practice by trial and error. Figure 3.3 demonstrates the effect of changing n on the total longitudinal scattering cross-section, σ_l, for the 4:3 oblate void with ka=2.2 and incident polar angle $\theta_o=\pi/4$. It is seen that σ_l converges rapidly when n>8. Similarly, figure 3.4 shows the same data for a higher incident frequency (ka=6.6). σ_l is seen to converge rapidly when n>12.

Figure 3.5 displays the effect of increasing l_{max} on σ_l for the 4:3 oblate void with $\theta_o=\pi/4$ and ka=2.2. σ_l converges rapidly when l_{max}>3, especially when l_{max}>5. Figure 3.6 shows the same data for a higher incident frequency (ka=6.6). Comparing these two figures, one can see that σ_l converges faster for lower incident frequency.

The satisfactory convergence of the total longitudinal cross section itself cannot conclude that the solutions for the scattering problem are close to the correct ones. However, the boundary residual (equation (3-39) is a conclusive criteria to assess the accuracy of the numerical scattering results for voids. The boundary condition for a void is that $\vec{t}$=0 on $\in$ (the surface of the void). If $\vec{t}_s$ is an exact scattering solution, J/J_o equals zero. If and only if J/J_o is small, then the solution for displacements, surface tractions, amplitudes, etc., is close to the correct one. Smaller J/J_o means more accurate solution.

To illustrate the effect of changing l_{max} on accuracy and to display the

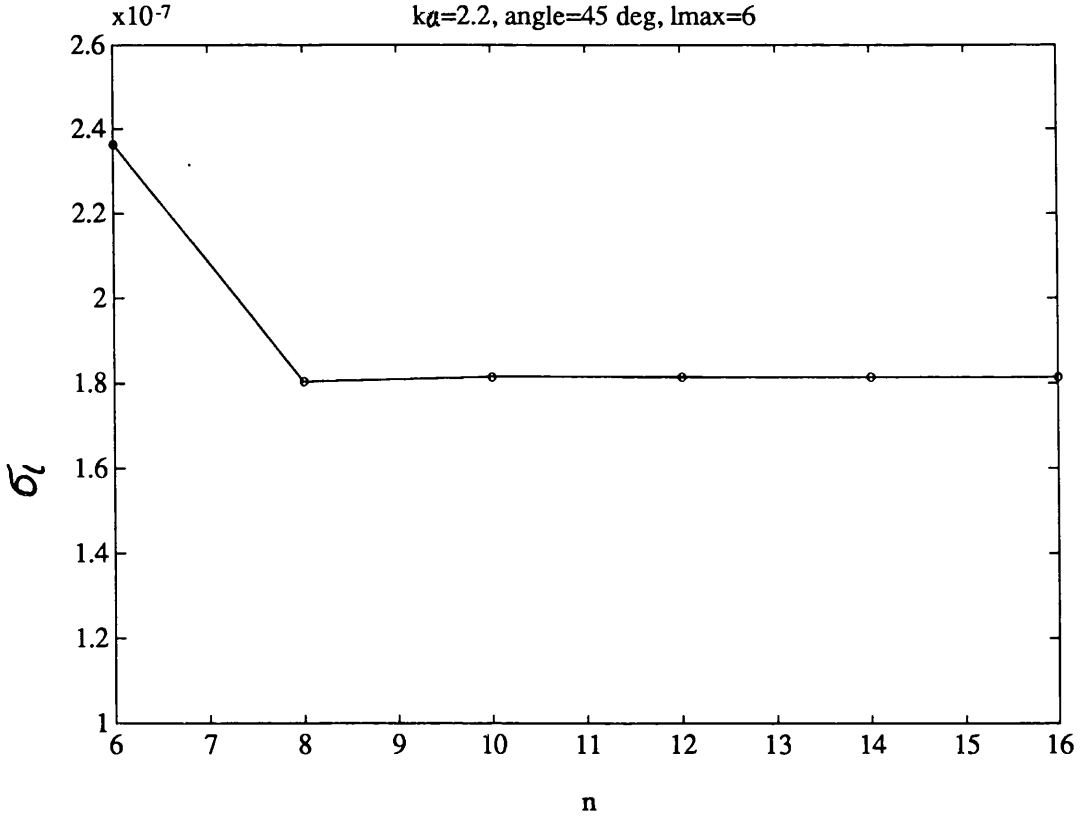

Figure 3.3 Total longitudinal cross section for $\theta_o=\pi/4$ and ka=2.2.

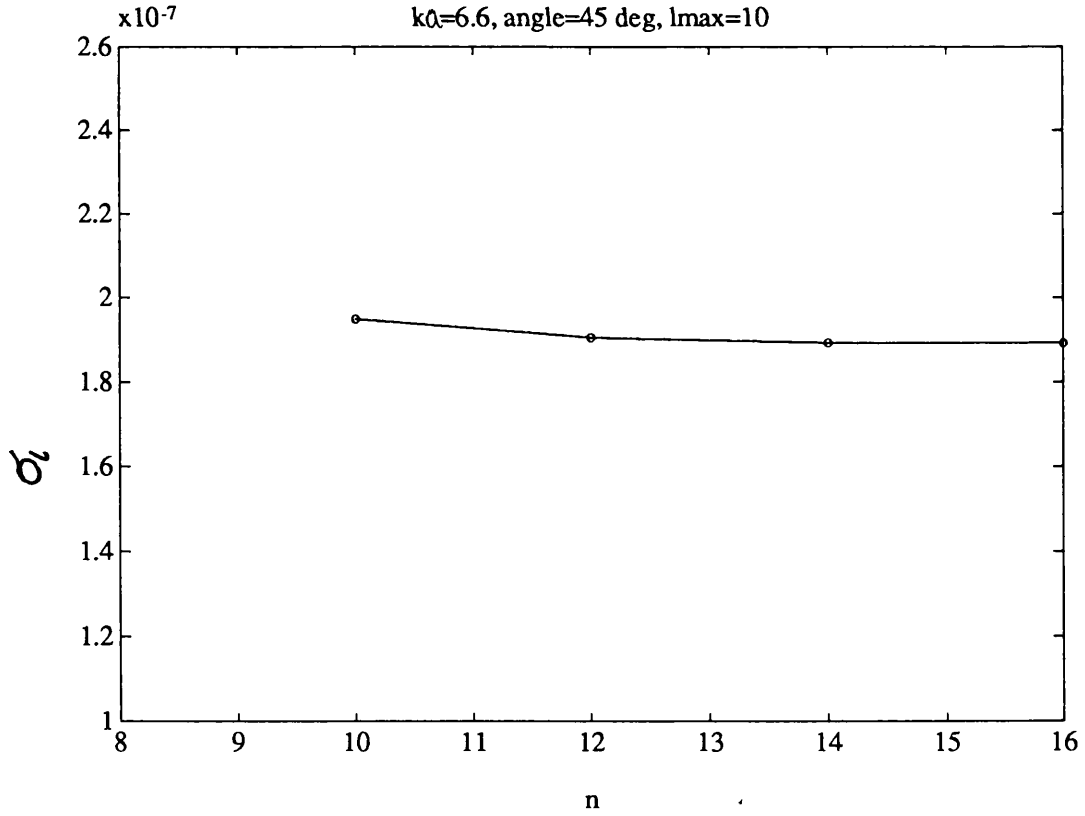

Figure 3.4 Same as figure 3.3, but ka=6.6.

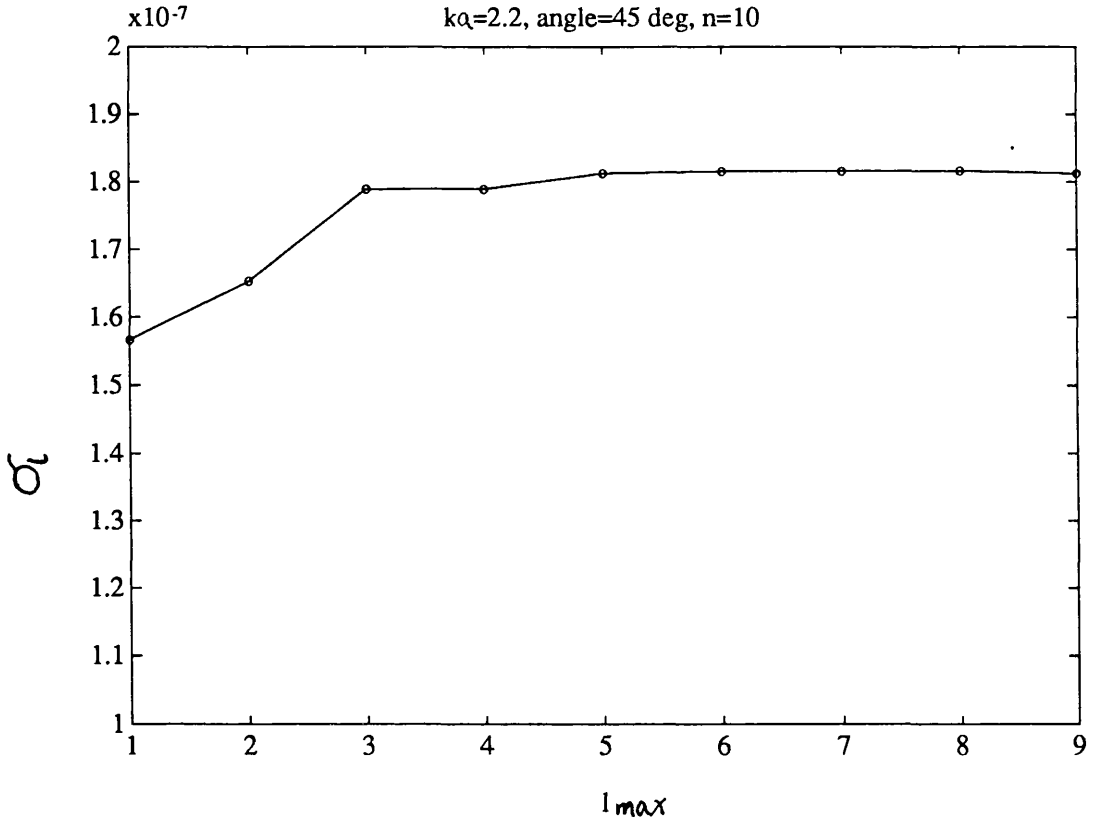

Figure 3.5 σ_l over l_{max} for $\theta_o=\pi/4$ and ka=2.2.

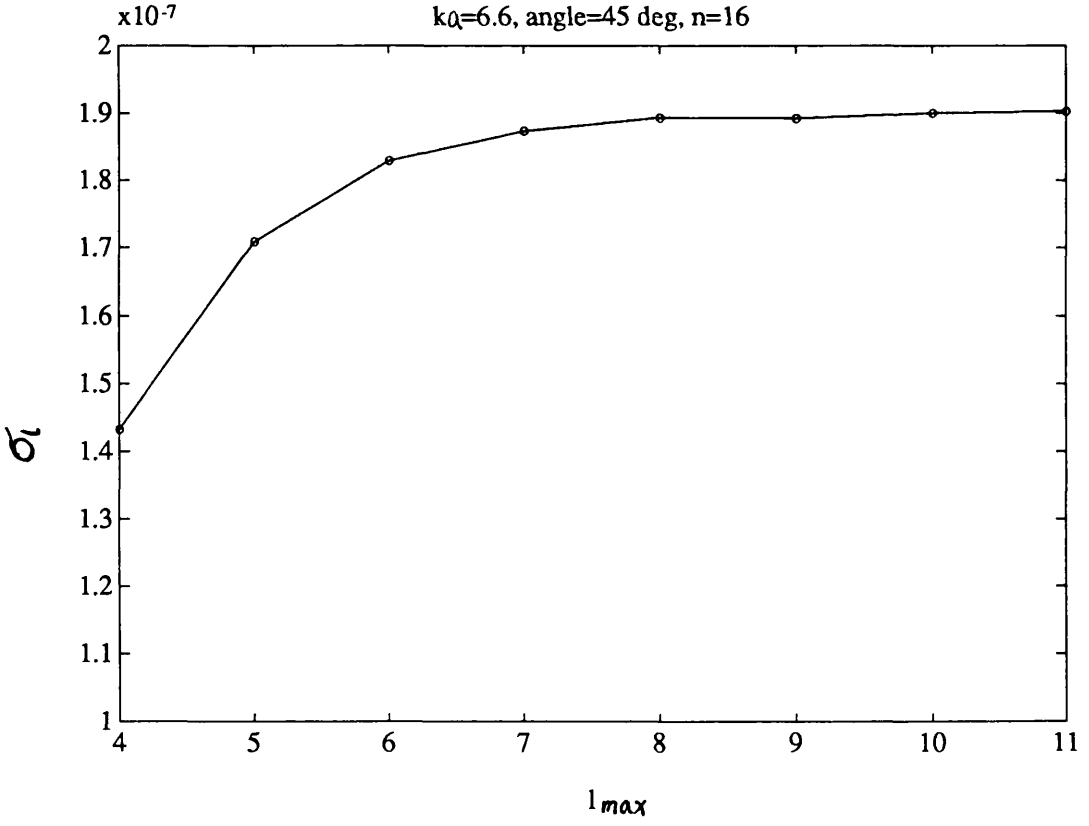

Figure 3.6 Same as figure 3.5, but ka=6.6.

convergence properties of J/J_o, J/J_o has been calculated for the 4:3 oblate void with $\theta_o=\pi/4$. Figure 3.7a shows how J/J_o converges for ka=2.2. Figure 3.7b shows the same data for a shorter incident wavelength (ka=6.6). It can be seen from these two figures that the boundary residual for a higher frequency converges more slowly. Results presented by Opsal and Visscher [1985] also showed that the solution for the scatterer with a larger aspect ratio converges more slowly than the solution for the scatter with a smaller aspect ratio.

According to the above discussion about the effects of changing the number of integration points (n) and the truncation limit (l_{max}) on accuracy and convergency of the solution, the computer program has been designed in such a way that for lower frequencies and scatterers with smaller aspect ratios, smaller n and l_{max} are used. For higher frequencies and scatterers with larger aspect ratios, larger n and l_{max} are selected.

The computer program has been run to simulate the scattering from several regular and irregular shaped voids. The results are shown below and compared with the published results if available.

3.4 Numerical results for Several Voids

The voids considered here include a 4:3 oblate void, a 2:1 oblate void, an ovate void and two overlapping voids.

3.4.1 A 4:3 oblate void

The void is shown as figure 3.2. Figure 3.8a displays the backscattering amplitudes, A_l^*, for six incident directions. With the incident polar angle increasing from 0 to $\pi/2$, A_l^* becomes smaller and smaller, as expected by intuition, because the encountered cross-sectional area becomes smaller and

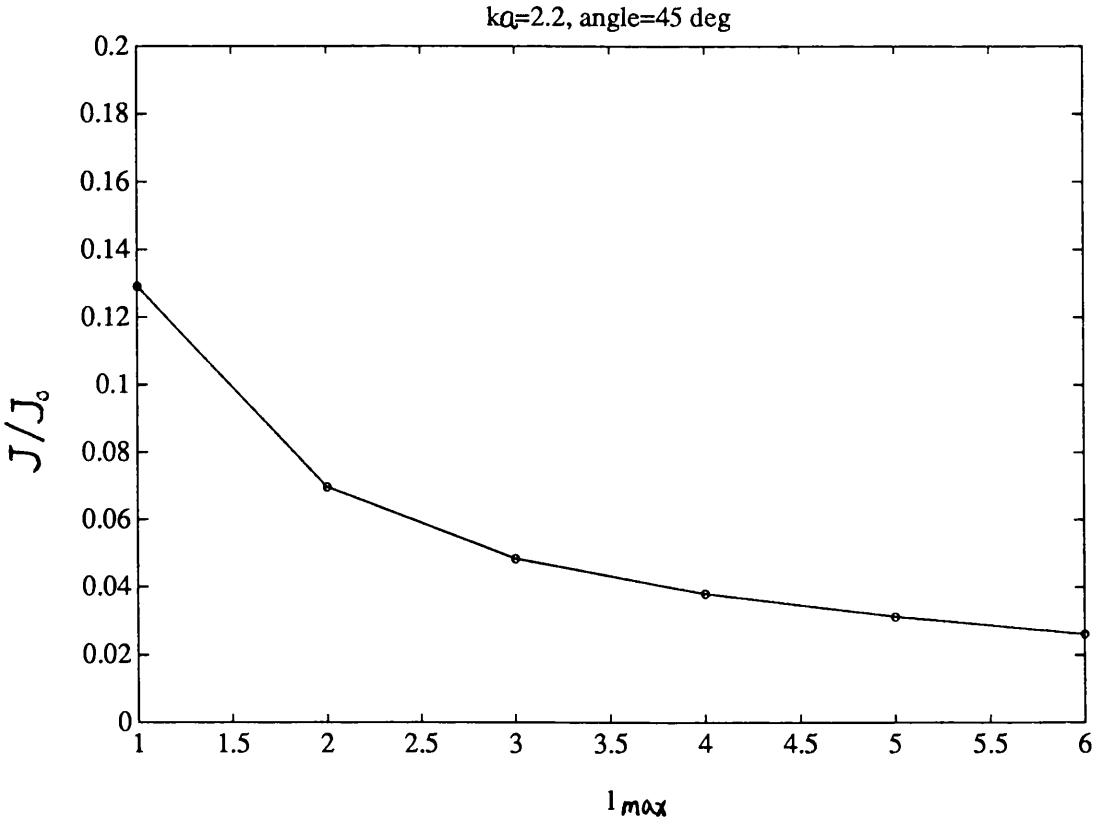

Figure 3.7a Normalized Boundary residual J/J_o over l_{max} for $\theta_o=\pi/4$ and ka=2.2

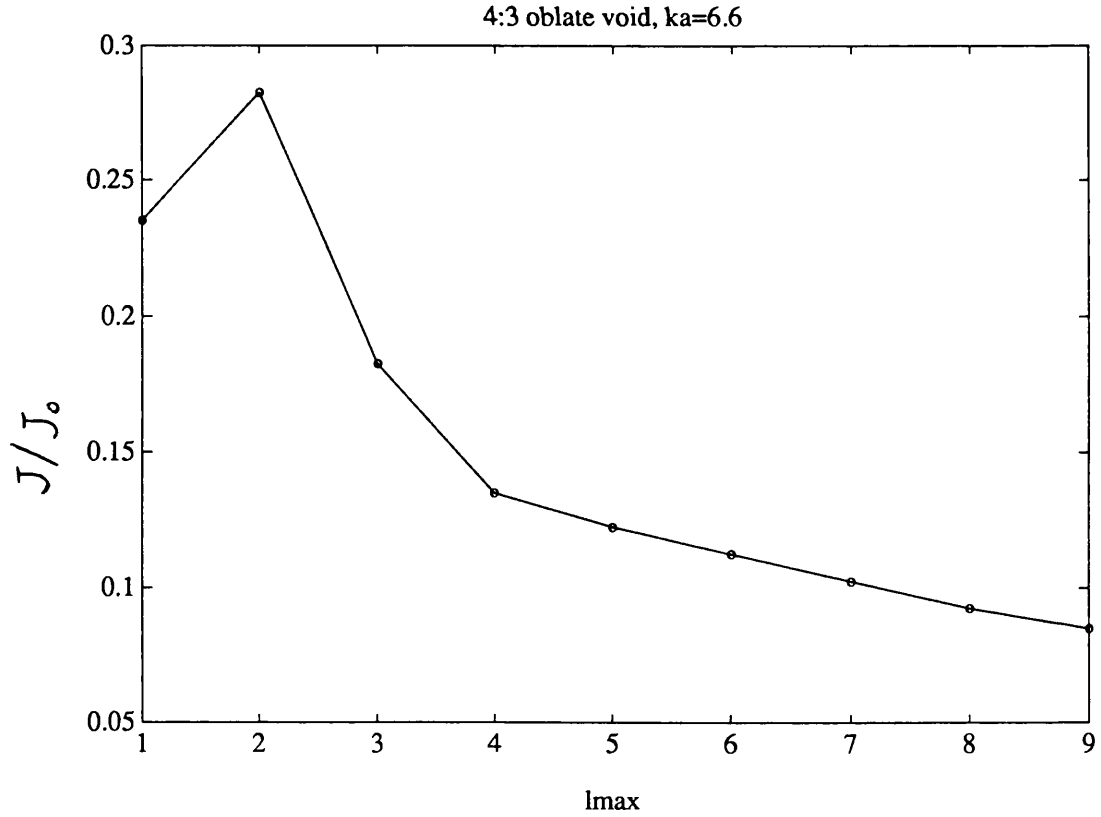

Figure 3.7b Boundary residual over l_{max} for $\theta_o=\pi/4$ and ka=6.6.

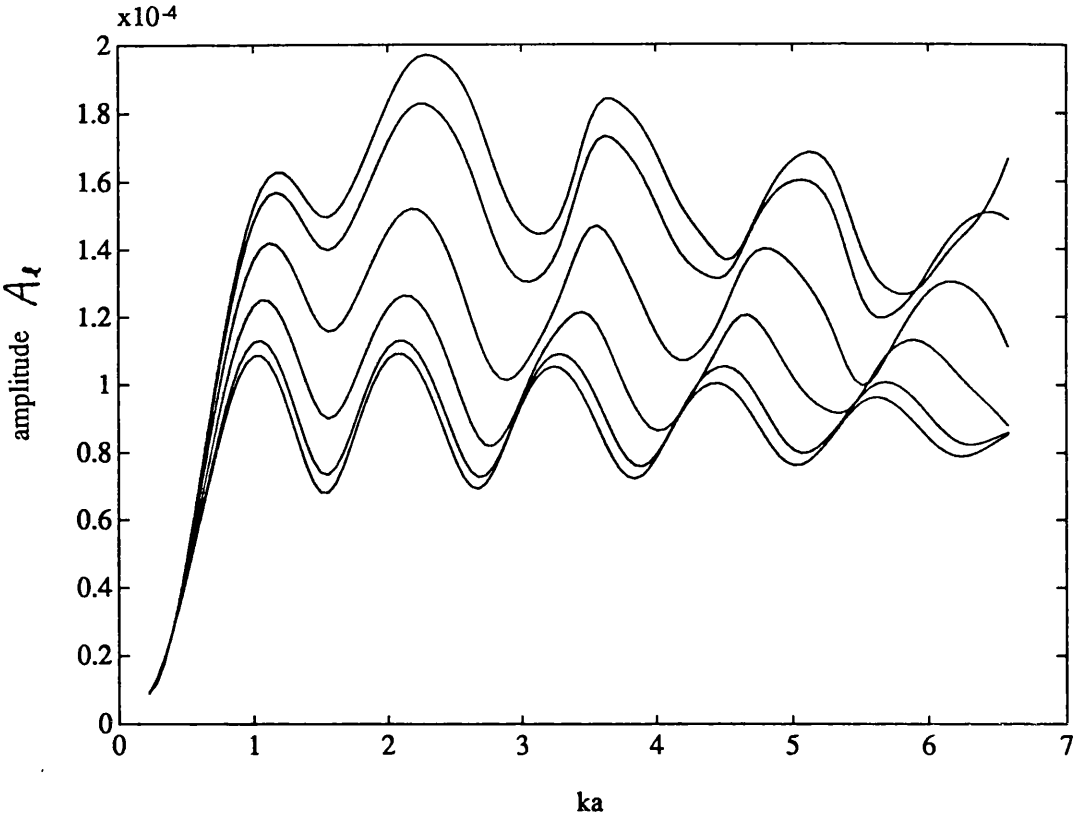

Figure 3.8a Backscattering amplitude from a 4:3 (220:165 μm) oblate void

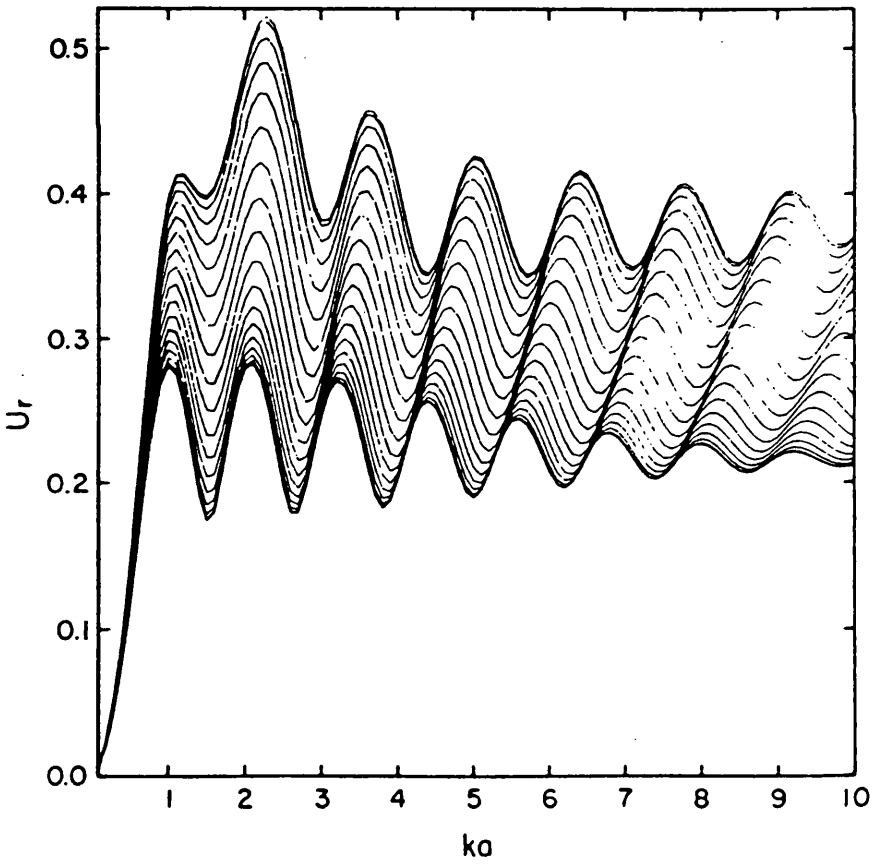

Figure 3.8b Backscattering amplitude from a 4:3 spheroidal void, published by Opsal and Visscher [1985]

smaller. Figure 3.8b shows the scattering results from a 4:3 oblate void published by Opsal and Visscher [1985] who used a method called Augmented MOOT which is more complicated and more accurate. Comparing figure 3.8a with figure 3.8b, one can find that the scattering features, such as the *ka* values where the peaks and valleys occur, peak ratios for different incident directions, are almost identical. Since the scattering amplitudes were normalized in different ways for these two figures, they are not compared.

Figure 3.9a shows the backscattering amplitude in the frequency domain at a single direction (θ_o=0.2π). Figure 3.9b shows the time-domain response at that direction. This was obtained by taking a Fourier transform of the data in figure 3.9a. The Fourier transform was performed simply using the signal processing software, MATLAB.

As the frequency domain response is limited to a certain frequency range, the time domain response is also limited to the same frequency range. A cosine bell window function is introduced in the Fourier transform to avoid Gibbs oscillations in the time domain response due to cut-off of some frequency information [Zhang and Bond, 1989; Papoulis, 1977].

Some features of figures 3.9a and 3.9b can be qualitatively and quantitatively understood. Part of the incident wave is specularly reflected from the front surface, and part is bent around the void (creeping wave) and excites a reflected plane wave on the other side of the void in the backward direction to interfere with the specular part. These are shown as figure 3.10. One can clearly see from figure 3.9b that a main pulse reflected from the front surface of the void and a further weak pulse, corresponding to the creeping wave, arriving at a time τ later. The oscillating pattern in the frequency domain corresponds to the interference between these two signals. These features are very similar to the scattering features from a spherical void which were

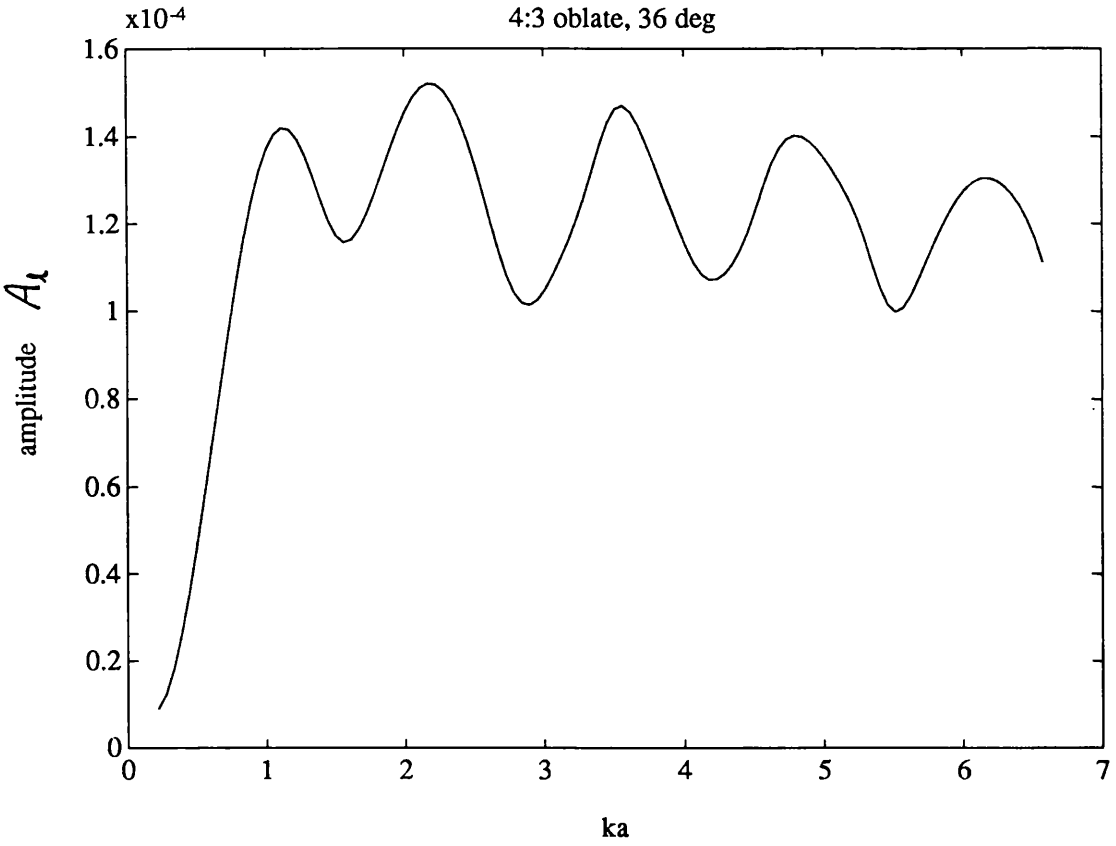

Figure 3.9a The frequency domain backscattering amplitude at θ_o=0.2π

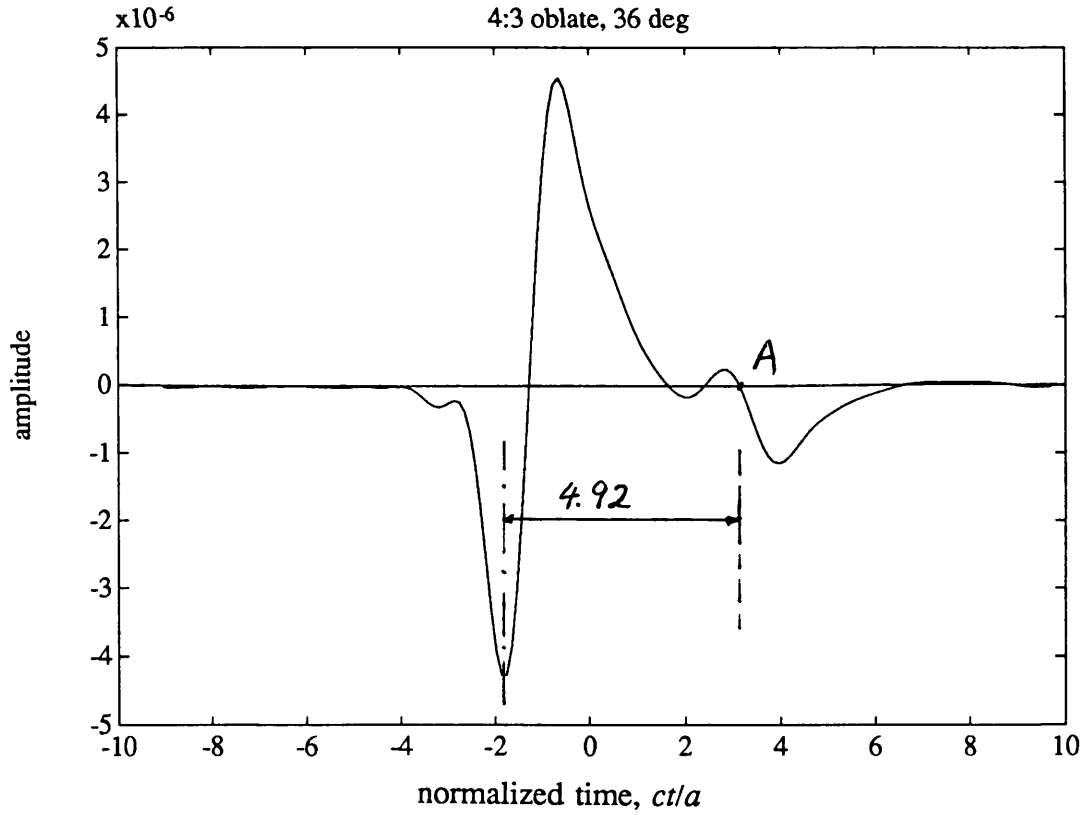

Figure 3.9b The time domain backscattering response at θ_o=0.2π

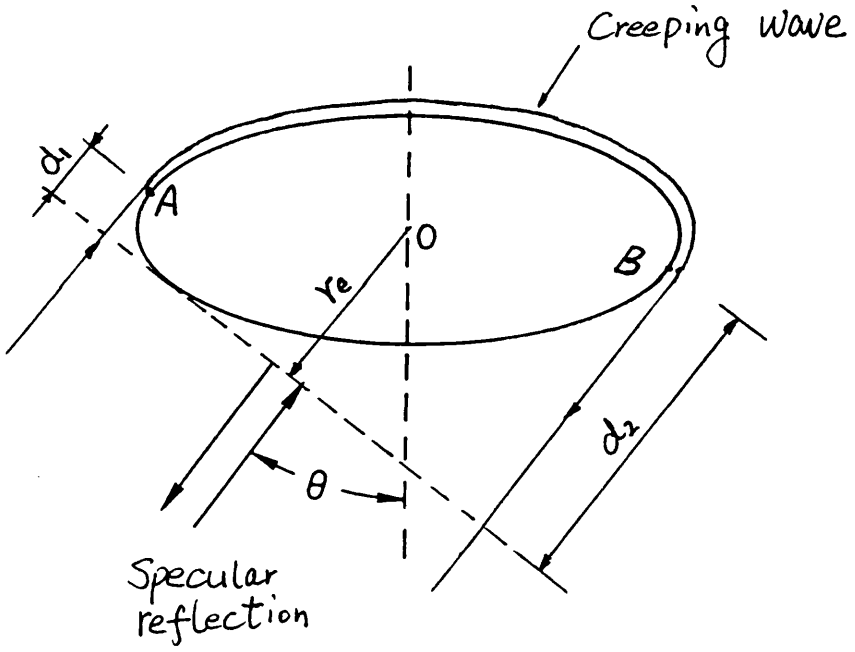

Figure 3.10 The specular reflection, the creeping wave, and the tangent plane distance r_e

discussed by Gruber [1980] and Kino [1987].

From the paths for the specular reflection and the creeping wave indicated in figure 3.10, the transit time, τ, between these two waves (for a spheroidal void) can be estimated as

$$\tau = 2r_e/c + 2Ea/c_c \qquad (3\text{-}40)$$

where c_c represents the creeping wave velocity which is about $0.87c$ in titanium [Gruber, 1980; Zhang and Bond, 1989], and $2Ea$ is the distance the creeping wave has to creep, halfway around the void. (E is the complete elliptic integral of the second kind, and $E=1.38$ for a 4:3 spheroid.) r_e is the tangent plane distance shown in figure 3.10, $2r_e$ is equal to the distance (d_1+d_2) indicated in figure 3.10. At $\theta_o=0.2\pi$, $r_e=0.845a$, thus, $\tau=4.86a/c$ is obtained from equation (3-40).

As pointed out by Zhang and Bond [1989], in the time domain response there is spreading in the wave packet following the front surface reflection and in the creeping wave components. As neither of these is a simple delta function, the determination of the arrival time for the creeping wave leaves to some debate. In this study, the zero crossing point (A) (see figure 3.9b) is used as the arrival time for the creeping wave, following Zhang and Bond [1989] 's suggestion. The transit time thus measured from figure 3.9b is $4.92\pm0.04\ a/c$, which is very close to the transit time obtained from equation (3-40).

3.4.2 A 2:1 oblate void

The void considered here is a 2:1 (*a:b=252:126* μm) oblate void in titanium. Figure 3.11 shows the frequency domain backscattering responses for three incident directions: θ_o=0, $\pi/4$, and $\pi/2$. The results are compared with the results published by Opsal and Visscher [1985], shown as figure 3.12. The scattering patterns compare well, especially at lower frequencies when $ka<4$. The discrepancies may be due to that Opsal and Visscher used a modified MOOT which is more accurate than MOOT used here, especially when the aspect ratio of the scatterer is large or the frequency is high.

Figures 3.13a-c show the time domain responses at these three directions obtained from Fourier transforming the data in figure 3.11. The simple physical arguments used to explain the scattering from the 4:3 oblate void can be employed here in the same way to analyze the scattering features.

The transit time, τ, between the specular response and the creeping wave can be calculated from equation (3.40). For *a:b*=2:1, E=1.21. τ is different for each direction, as r_e is different. Table 3.1 lists τ for these three directions. The transit times measured from the numerical results in figures 3.13a - 3.13c agree with this analysis very well.

Table 3.1 Transit time between the specular response and the creeping wave for the 2:1 oblate void

θ_o	r_e *(a)*	τ *(a/c)* by analysis	τ *(a/c)* measured from calculations
0	0.50	3.78	3.60±0.04
$\pi/4$	0.79	4.36	4.28±0.04
$\pi/2$	1.00	4.78	4.74±0.04

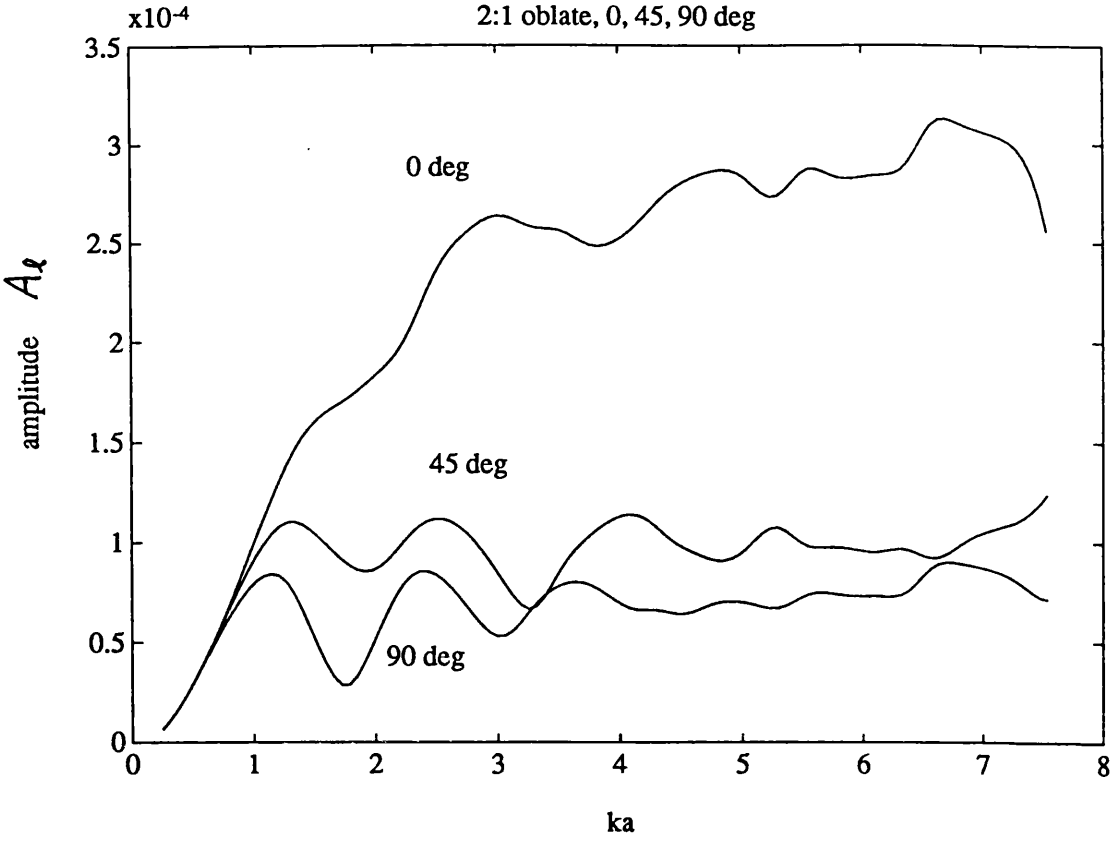

Figure 3.11 Backscattering amplitudes from the 2:1 oblate void at three directions.

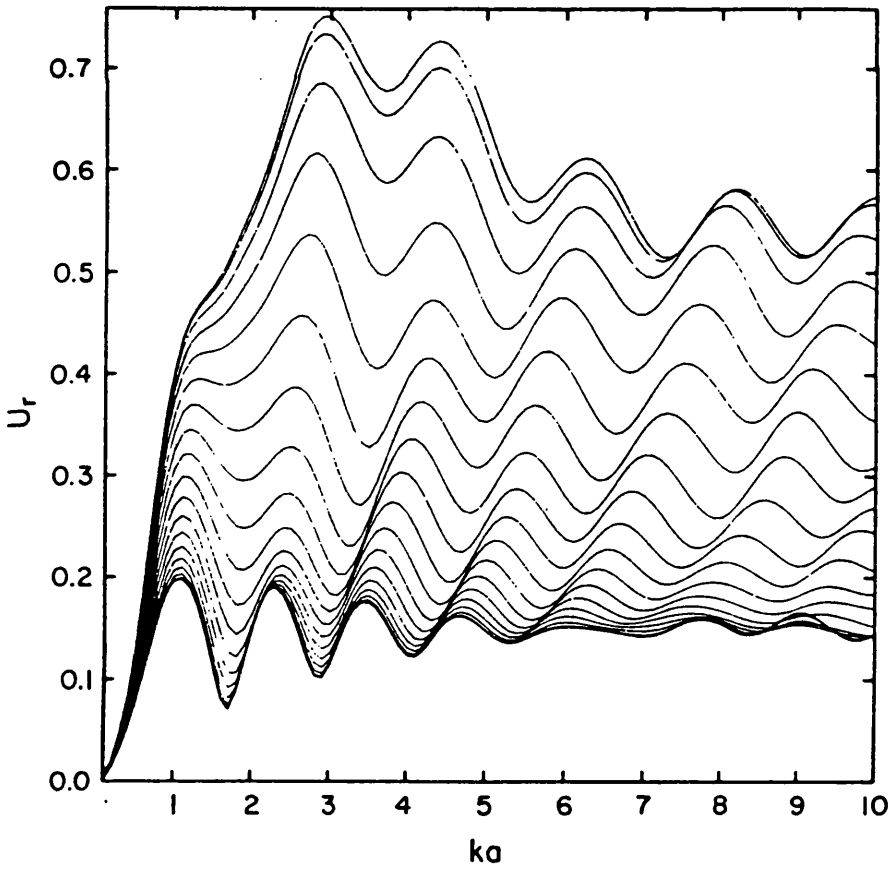

Figure 3.12 Backscattering from a 2:1 oblate void, by Opsal and Visscher [1985]

(a)

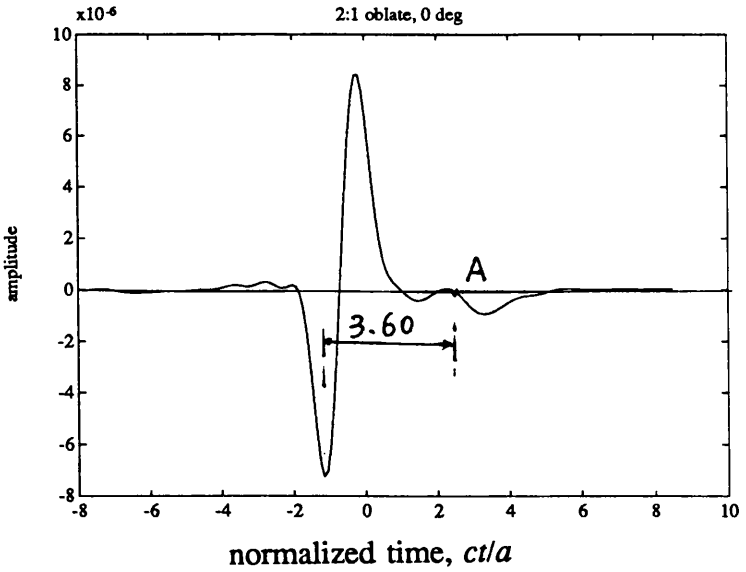

(b)

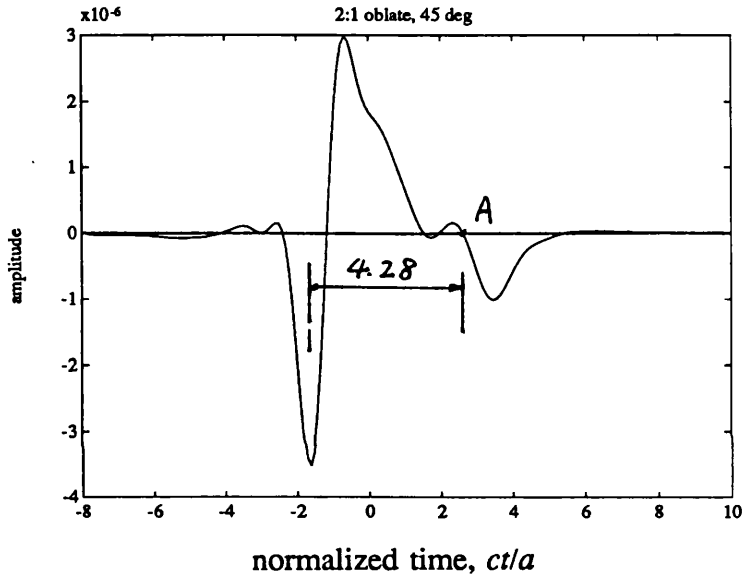

(c)

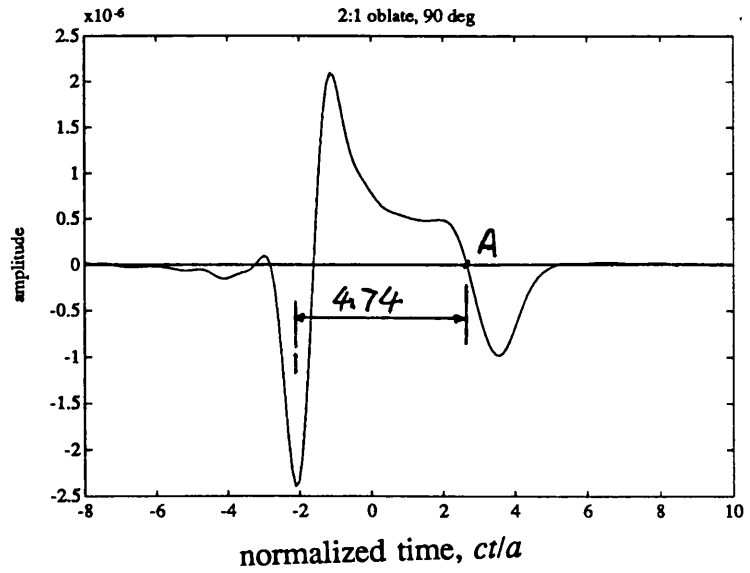

Figure 3.13 The time domain responses from the 2:1 oblate void at three directions (a) $\theta_o=0$; (b) $\theta_o=\pi/4$; (c) $\theta_o=\pi/2$.

3.4.3 An ovate void

The shape and dimensions of the void are shown as figure 3.14. It consists of a half 4:3 oblate and a half 3:4 prolate. It is axially symmetric, but not centrally symmetric. Some examples of backscattering from this void are shown in figures 3.15-3.17.

Figure 3.15a shows the scattering situation at $\theta_o=0$, indicating the specular reflection and the creeping wave path. Figures 3.15b and 3.15c show the frequency domain and time domain responses. As in the case of oblate void, part of the incident wave is specularly reflected by the front surface, and part of the incident wave incites a longitudinal creeping wave at the shadow boundary (point *A*). The creeping wave travels along the circumference away from the point *A* and excites a reflected longitudinal wave on the other side of the void (point *B*). From figure 3.15a, for $\theta_o=0$, the transit time (τ) between, the specular reflection and the creeping wave can be estimated as

$$\tau = 2b/c + 2Ea/c_c = 5.84a/c \qquad (3\text{-}41)$$

where *2Ea* is the distance the creeping wave has to creep, as indicated in figure 3.15a.

Figures 3.16a-c show the scattering results when the incident angle θ_o is $\pi/2$. The transit time should be

$$\tau = 2a/c + E(a+b)/c_c = 5.70a/c \qquad (3\text{-}42)$$

where *E(a+b)* is the distance the creeping wave has to creep, as indicated in figure 3.16a.

Similarly, figures 3.17a-c show the scattering results when the incident angle $\theta_o=\pi$. In this case, the transit time is

$$\tau = 2d/c + 2Eb/c_c = 5.73a/c \qquad (3\text{-}43)$$

where $2Eb$ is the distance the creeping wave has to creep, as indicated in figure 3.17a.

All the transit times measured from figures 15c, 16c and 17c are compared with the above predictions in Table 3.2. The agreements are satisfactory.

Table 3.2 Transit time between the specular response and the creeping wave for the ovate void

θ_o	r_e (a)	τ (a/c) by analysis	τ (a/c) measured from calculations
0	1.33	5.84	5.85±0.06
$\pi/2$	1.00	5.70	5.67±0.06
π	0.75	5.73	5.76±0.06

There are no published results available to compare for this case. Ovate voids are important, because they can serve as more generalized models than spheroidal voids for volumetric flaws found in structural materials.

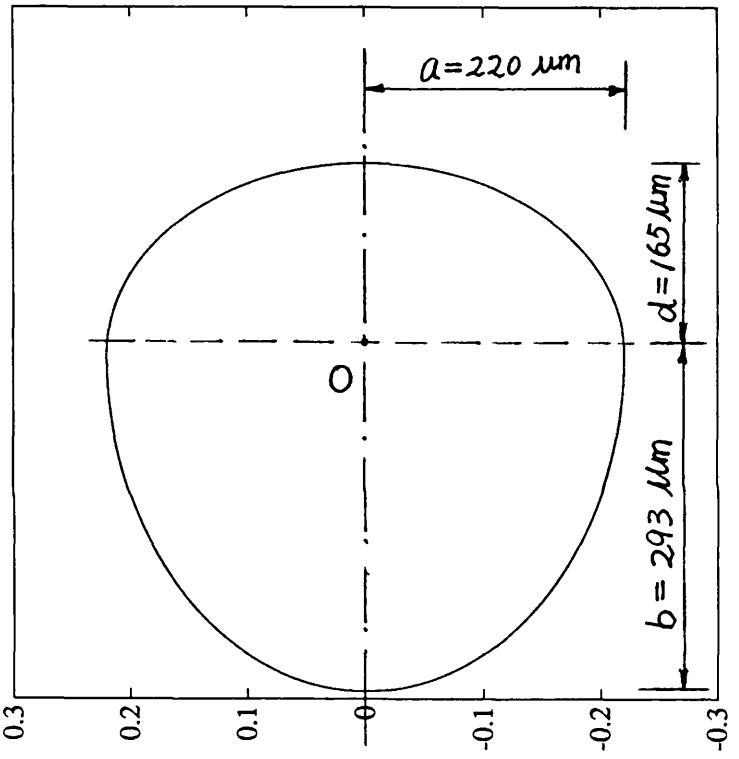

Figure 3.14 Backscattering from an ovate void.

(a)

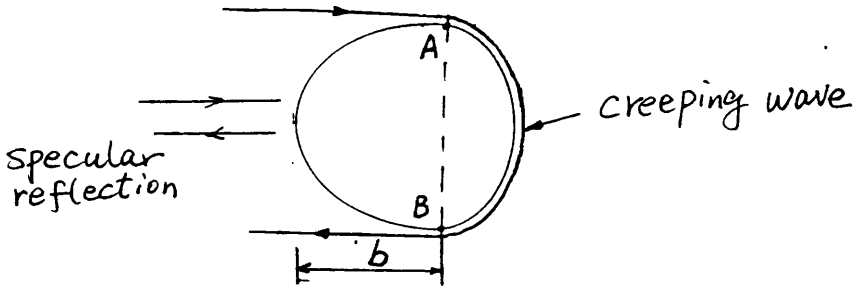

(b)

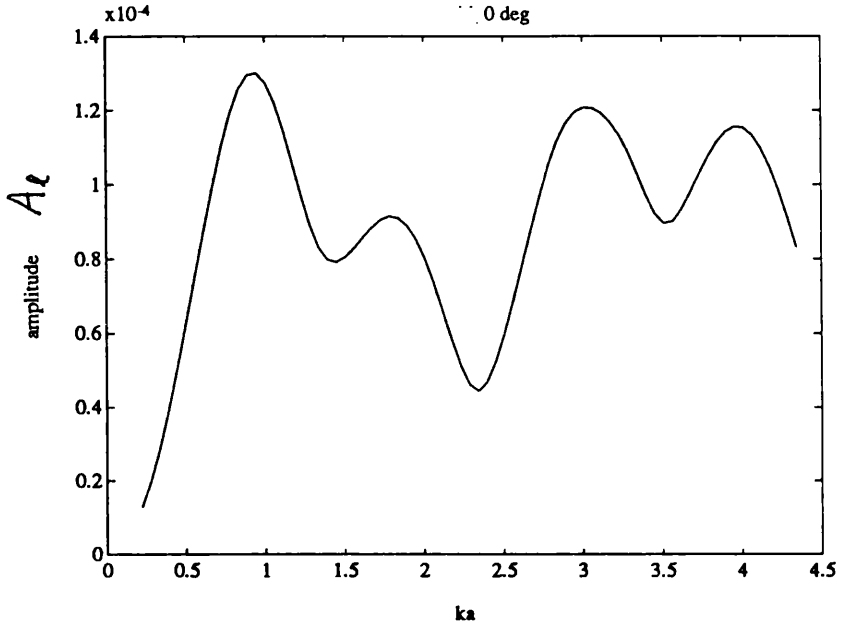

(c)

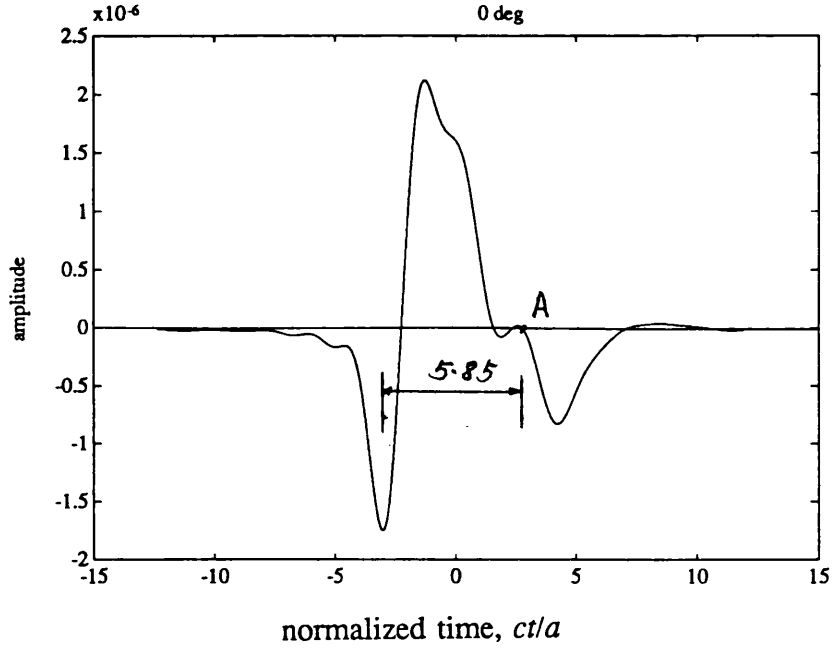

Figure 3.15 Backscattering from the ovate void at θ_o=0. (a) the front surface reflection and the creeping wave; (b) the frequency domain amplitude; (c) the time domain response.

(a)

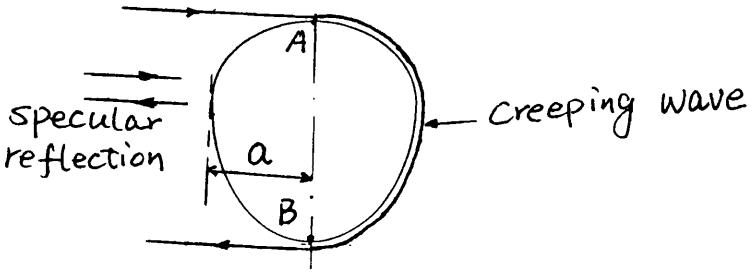

(b)

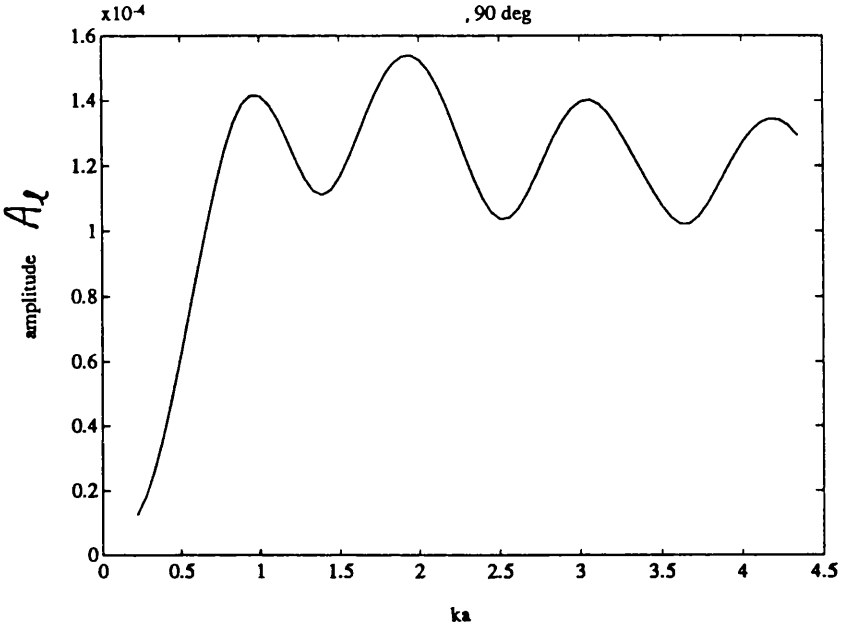

(c)

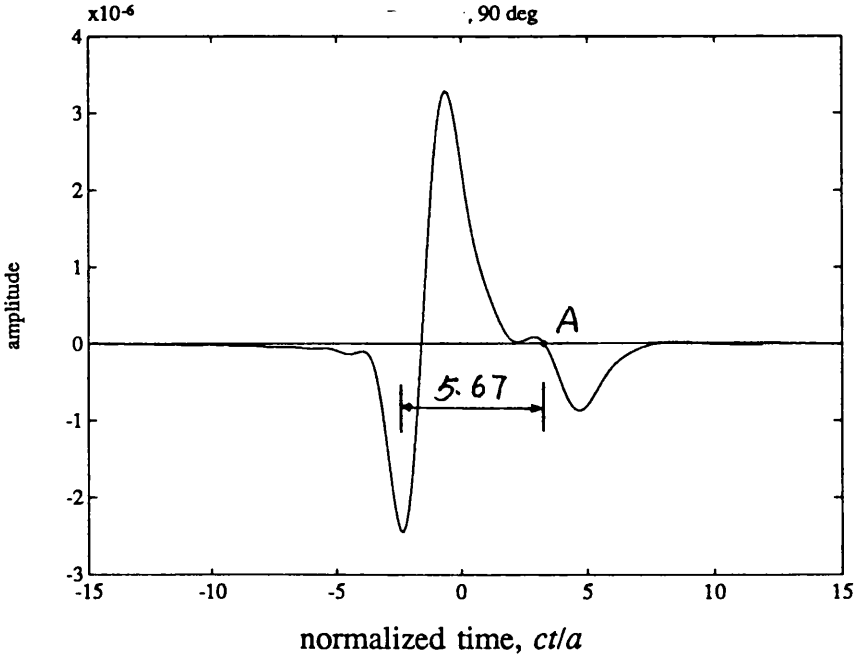

Figure 3.16 Backscattering from the ovate void at $\theta_o=\pi/2$ (a) the front surface reflection and the creeping wave (b) the frequency domain amplitude; (c) the time domain response.

(a)

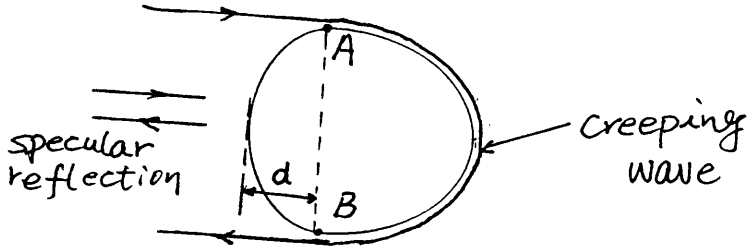

(b)

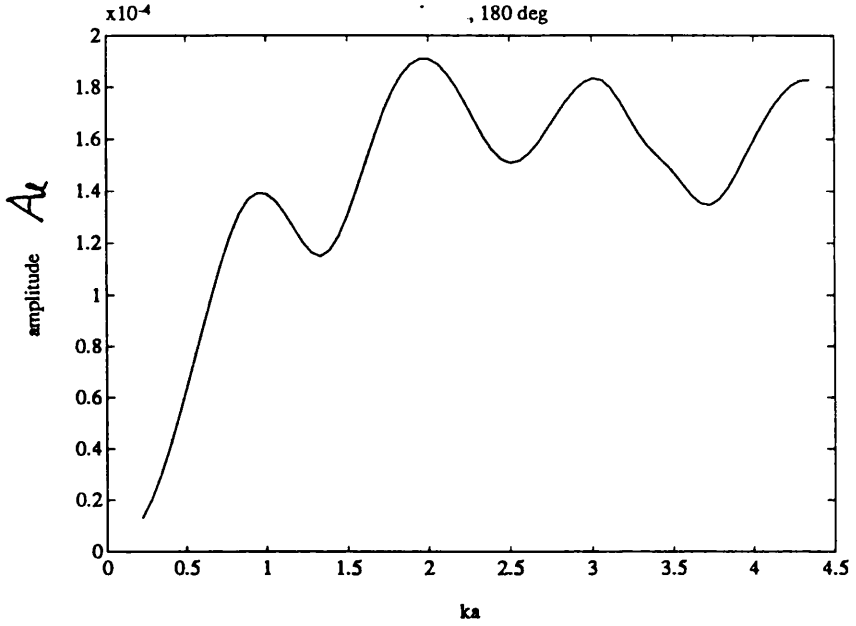

(c)

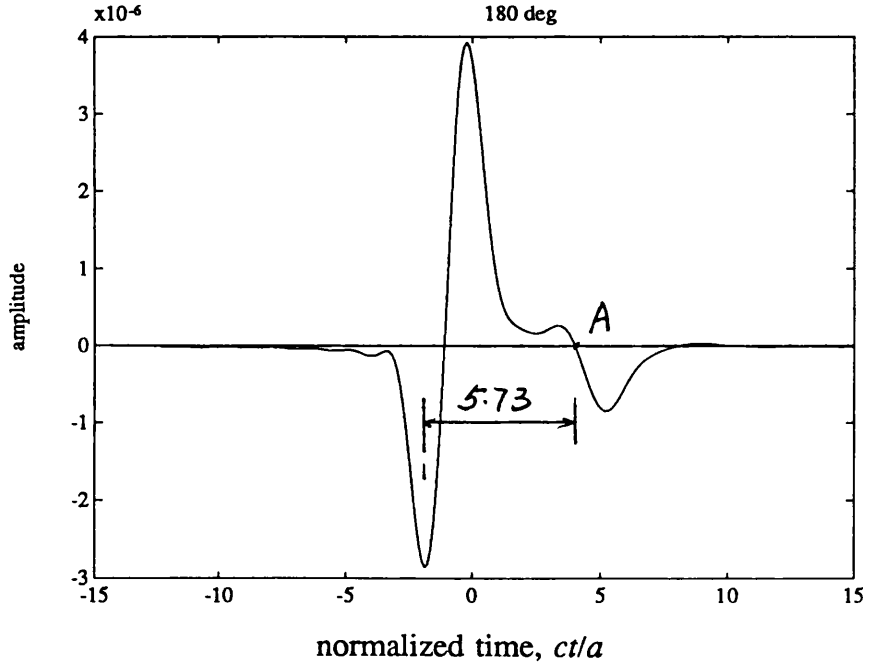

Figure 3.17 Backscattering from the ovate void at $\theta_o=\pi$. (a) the front surface reflection and the creeping wave (b) the frequency domain amplitude; (c) the time domain response.

3.4.4 Two overlapping spherical voids

The void considered here consists of two overlapping spherical voids, one half the radius of the other, with its centre on the surface of the large sphere. Figure 3.18 illustrates its shape and dimensions. The radius of the large sphere is 200 μm, and the radius of the small sphere is 100 μm. Figures 3.19 to 3.22 show the simulated backscattering results at some incident directions: θ_o=0, $\pi/2$, $2\pi/3$, and π. (At $\theta_o=2\pi/3$, the incident wave reaches the two voids at the same time.) Opsal and Visscher [1985] studied the same shaped void. Their frequency domain results are also shown in these figures.

Figures 3.19(a), 3.20(a), 3.21(a), 3.22(a) represent the calculated scattering amplitudes obtained from this study in the frequency domain. Figures 3.19(b), 3.20(b), 3.21(b), 3.22(b) are the results by Opsal and Visscher [1985]. It can be seen from these two groups of figures that at each incident direction, the scattering patterns predicted by these two studies are very similar.

Figures 3.19(c), 3.20(c), 3.21(c) and 3.22(c) are the time domain responses obtained from this study. Some features of the responses can still be explained by the model of a front surface specular reflection followed by a creeping wave. Figures 3.19(d), 3.20(d), 3.21(d) and 3.22(d) indicate the specular reflections and possible paths for the creeping waves. The specular reflections and the creeping waves are well observed in the time domain responses. Quantitative analysis of the transit times between the specular reflections and the creeping waves is made difficult by the complicity of the shape of the void.

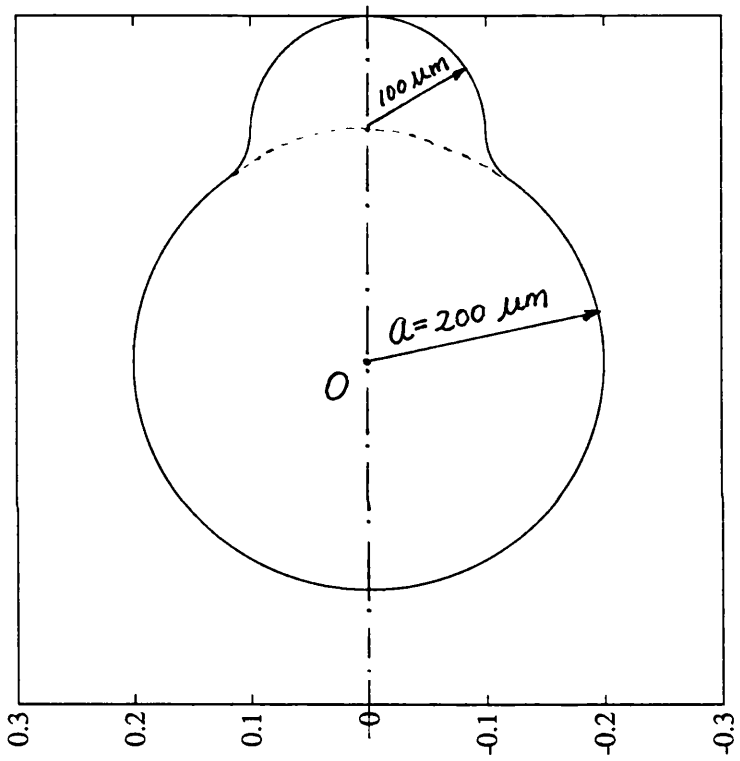

Figure 3.18 Backscattering from two overlapping spherical voids

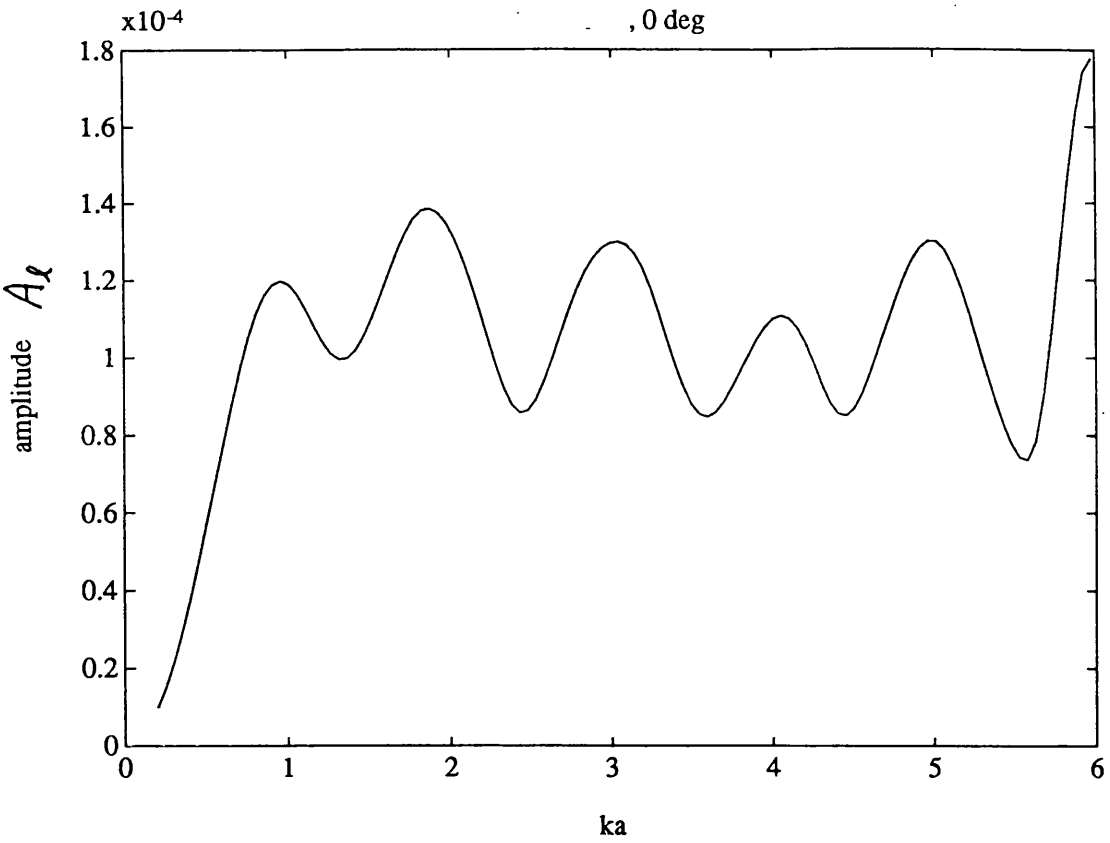

Figure 3.19 Backscattering from the two overlapping voids at θ_o=0. (a) the frequency domain amplitude obtained from this study

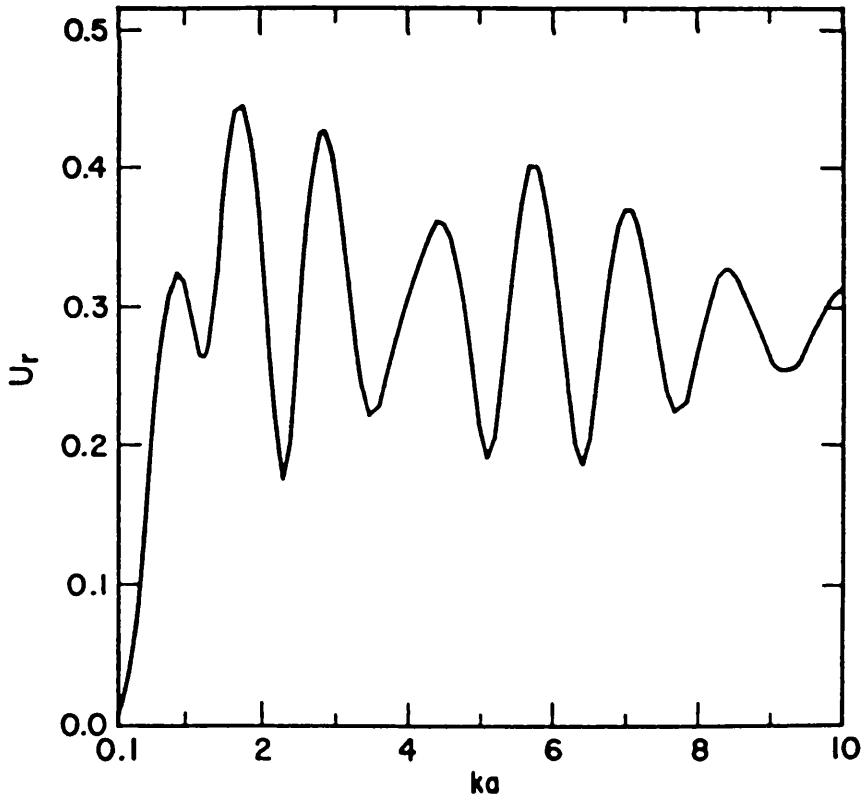

Figure 3.19 (Cont'd) (b) the frequency backscattering amplitude published by Opsal and Visscher [1985]

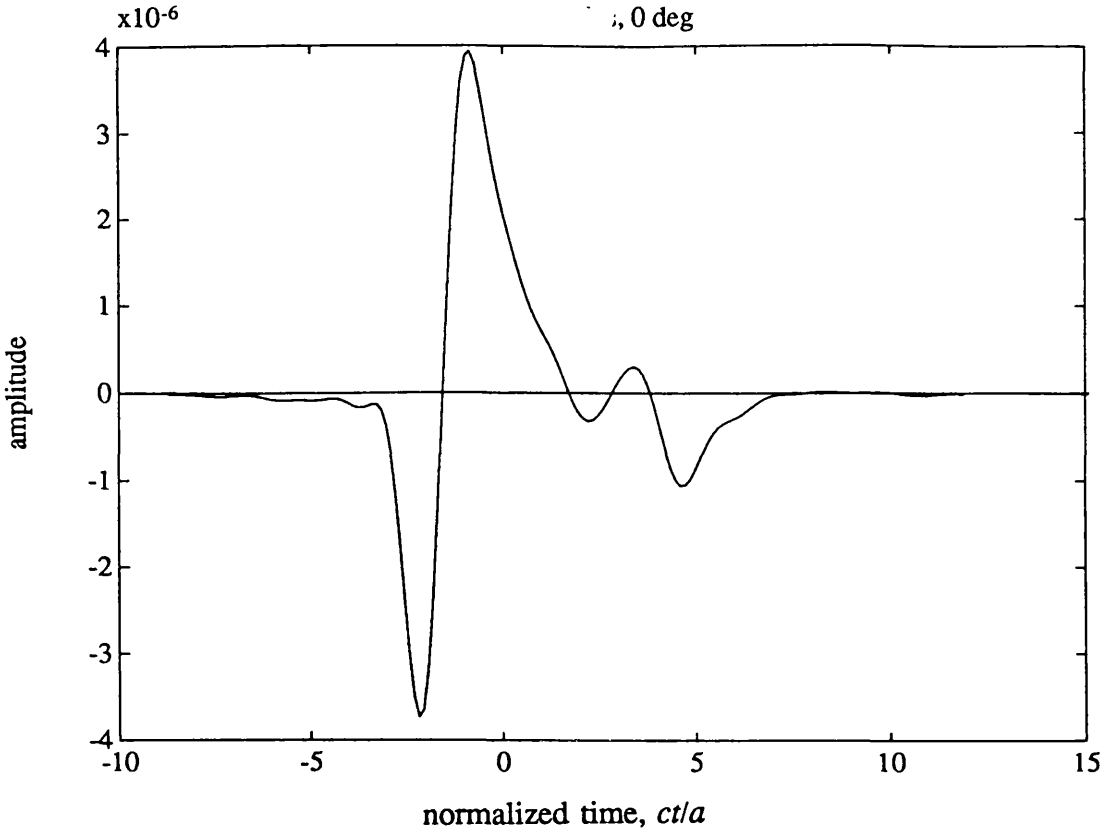

Figure 3.19 (Cont'd) (c) the time domain response from this study

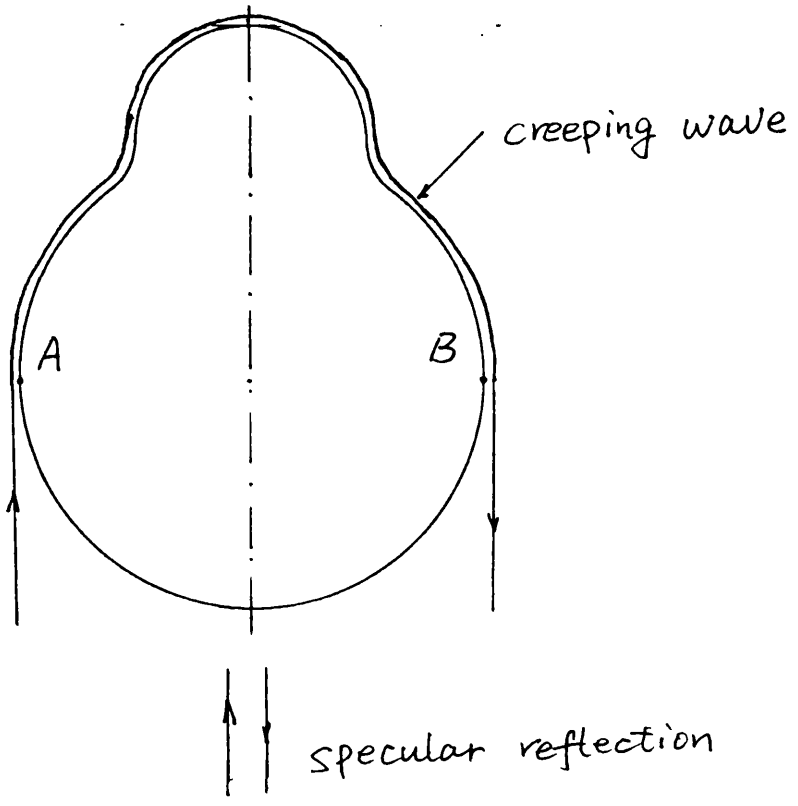

Figure 3.19 (Cont'd) (d) the front surface reflection and the creeping wave

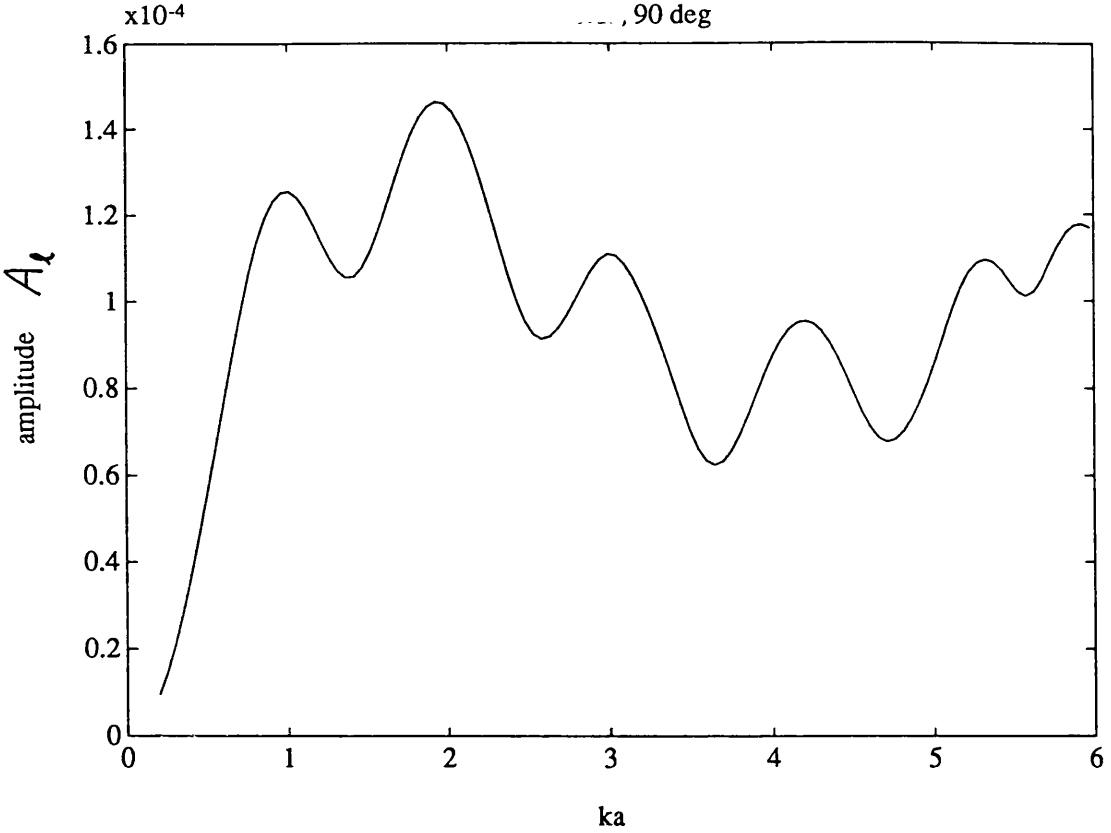

Figure 3.20 Backscattering from the two overlapping voids at $\theta_o=\pi/2$, (a) the frequency domain amplitude from this study

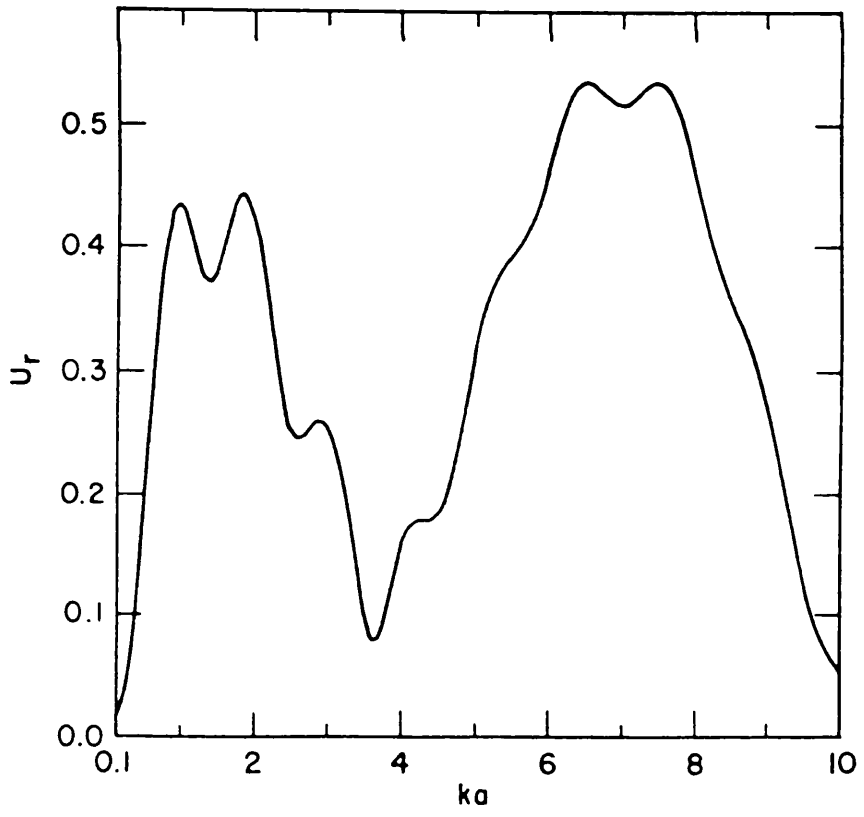

Figure 3.20 (Cont'd) (b) the frequency domain amplitude published by Opsal and Visscher [1985]

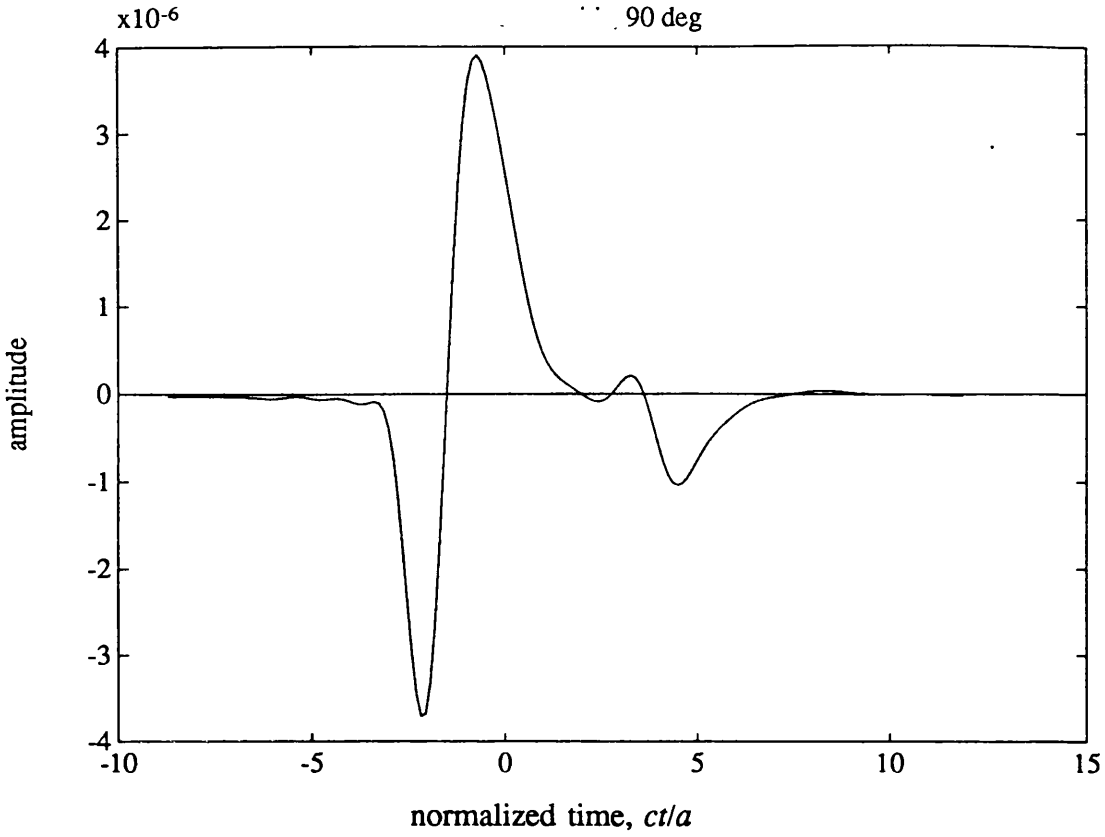

Figure 3.20 (Cont'd) (c) the time domain response obtained from this study

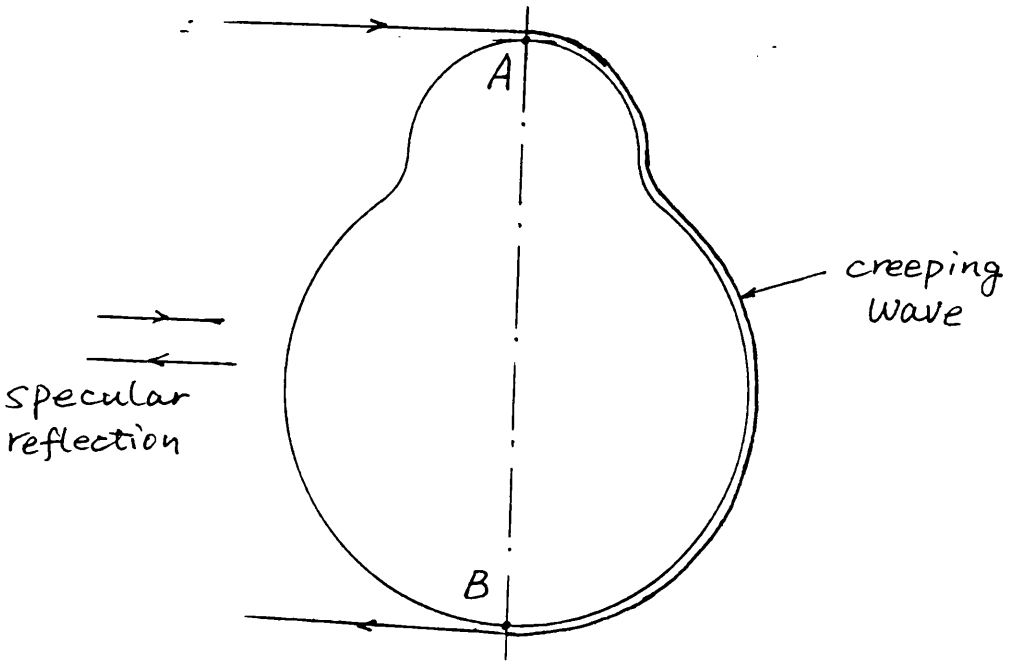

Figure 3.20 (Cont'd) (d) the front surface reflection and the creeping wave

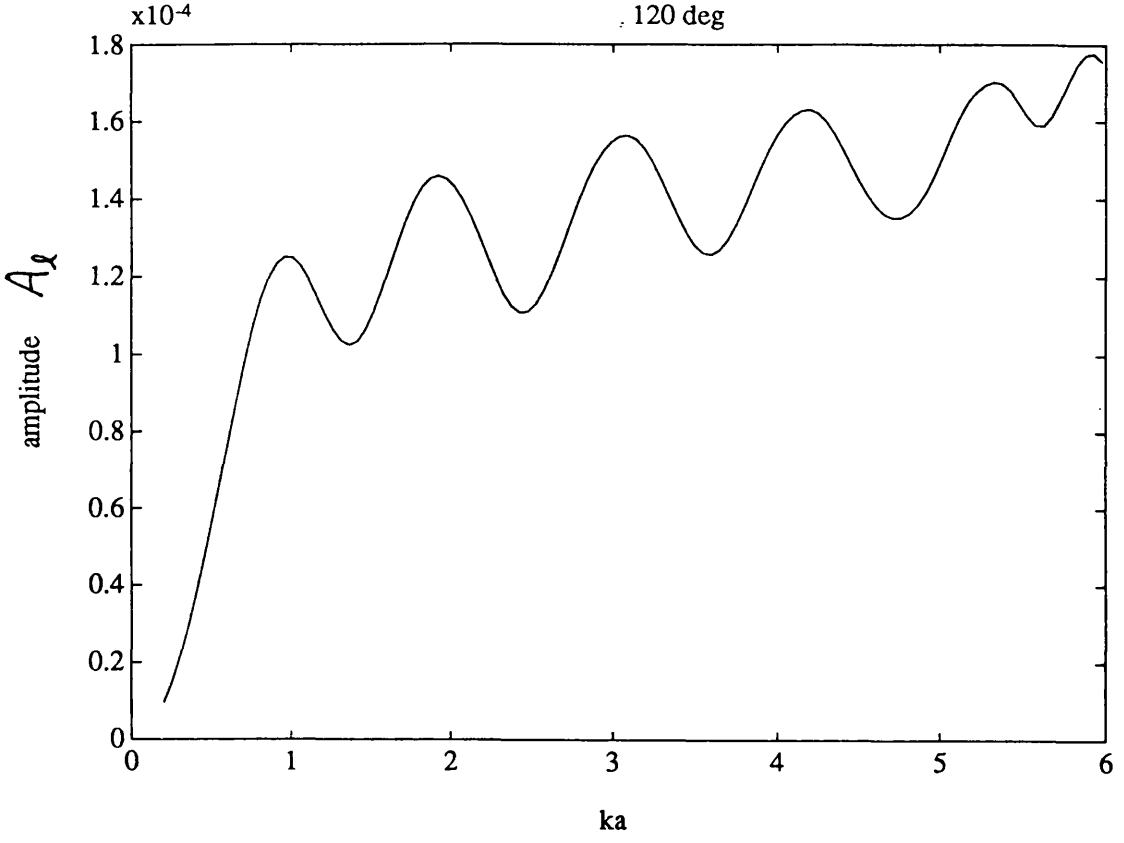

Figure 3.21 Backscattering from the two overlapping voids at $\theta_o=2\pi/3$, (a) the frequency domain amplitude obtained from this study

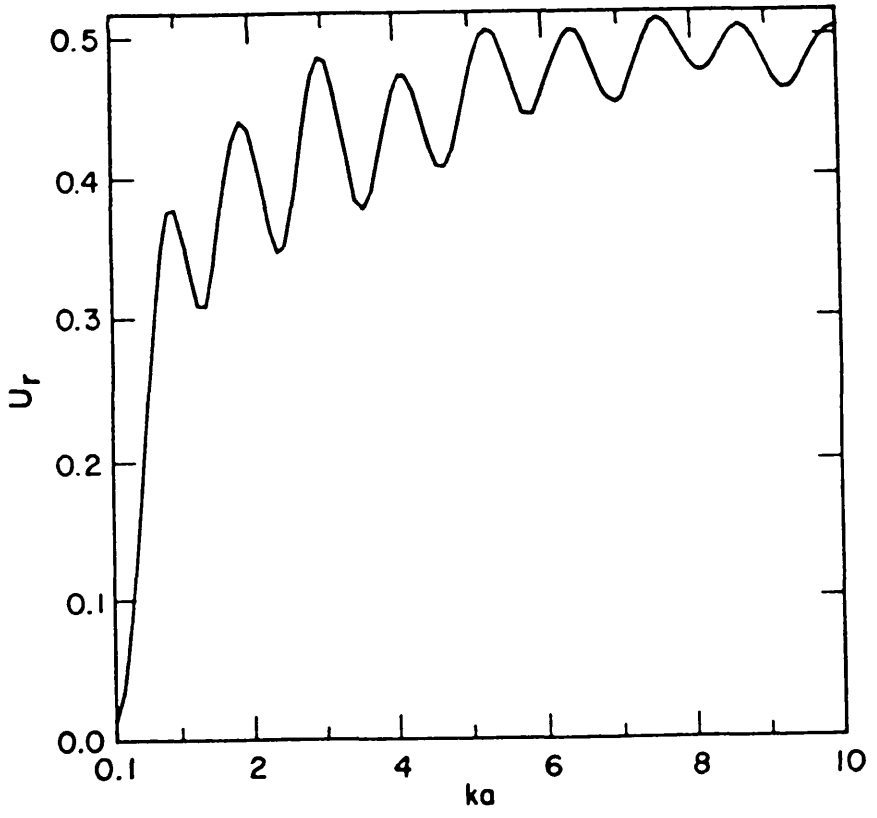

Figure 3.21 (Cont'd) (b) the frequency domain amplitude published by Opsal and Visscher [1985]

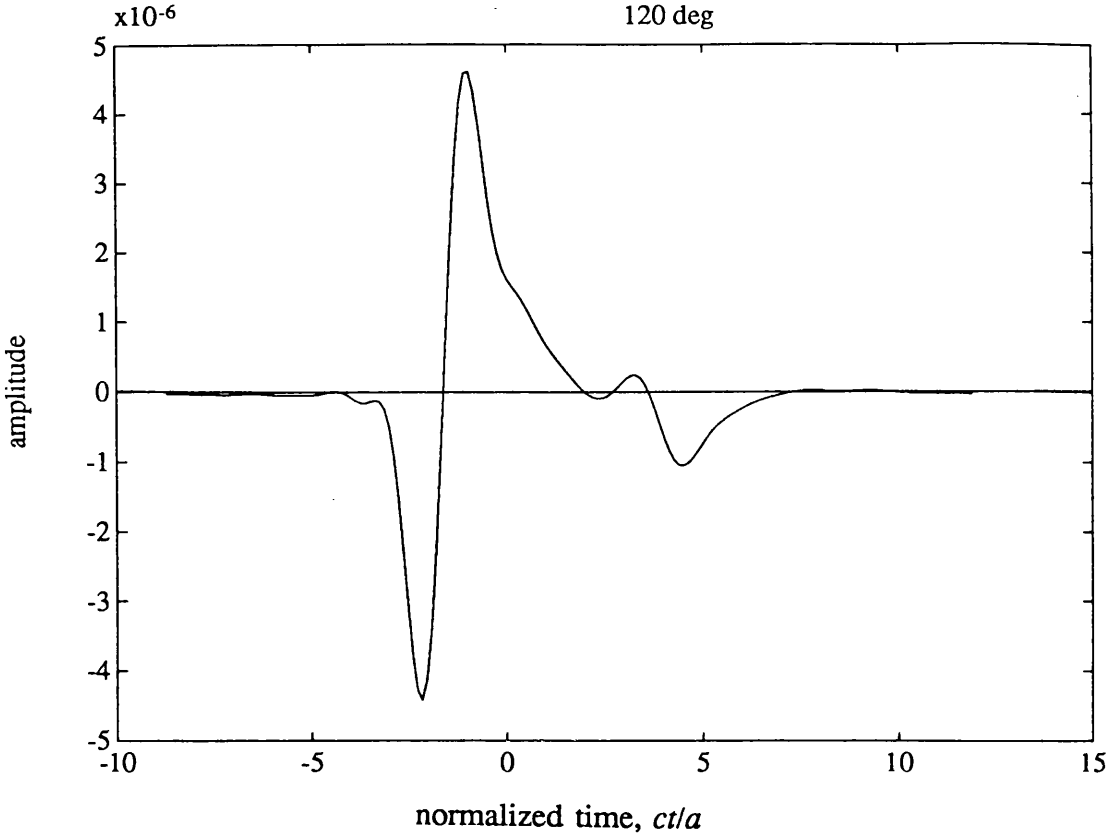

Figure 3.21 (Cont'd) (c) the time domain response obtained from this study

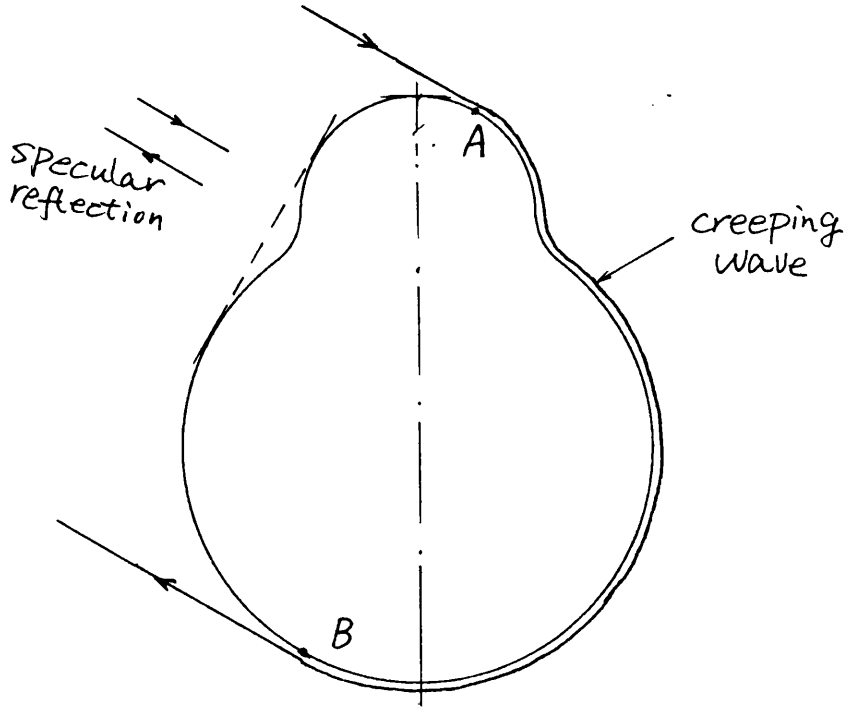

Figure 3.21 (d) the front surface reflection and the creeping wave

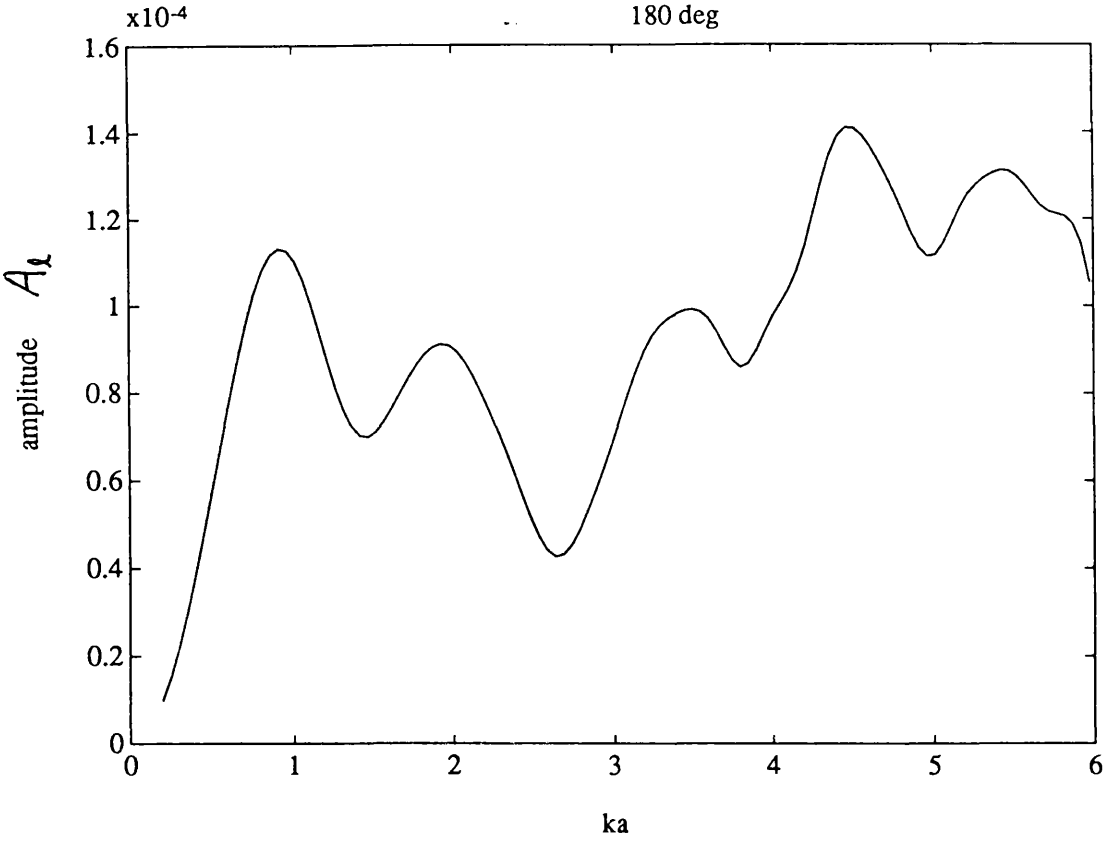

Figure 3.22 Backscattering from the two overlapping two voids at $\theta_o=\pi$, (a) the frequency domain amplitude from this study

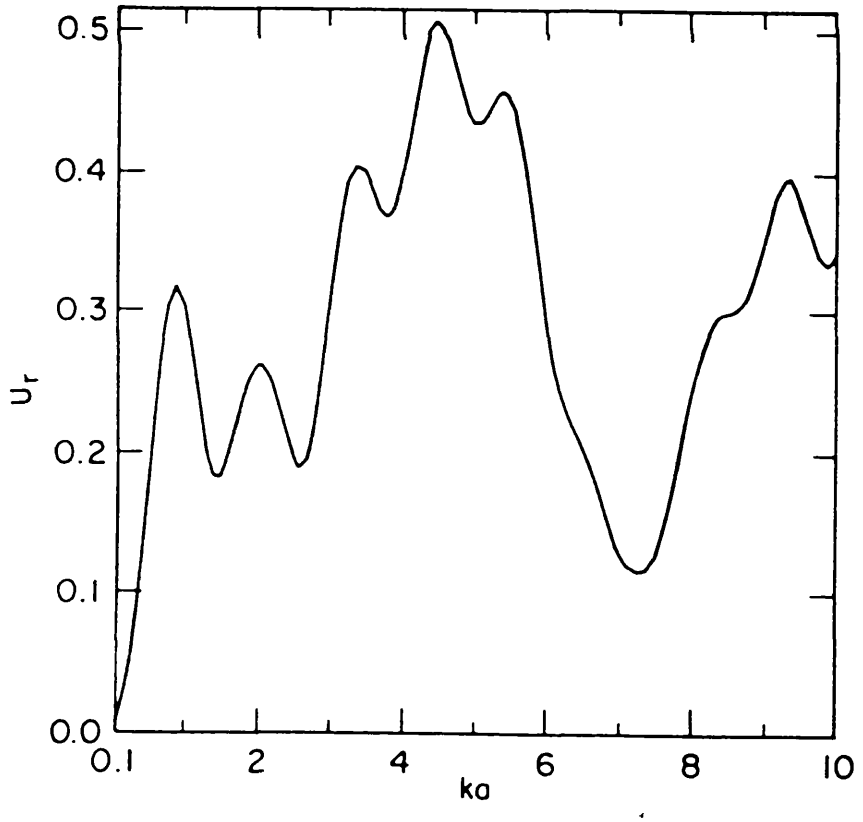

Figure 3.22 (Cont'd) (b) the frequency domain amplitude from Opsal and Visscher [1985]

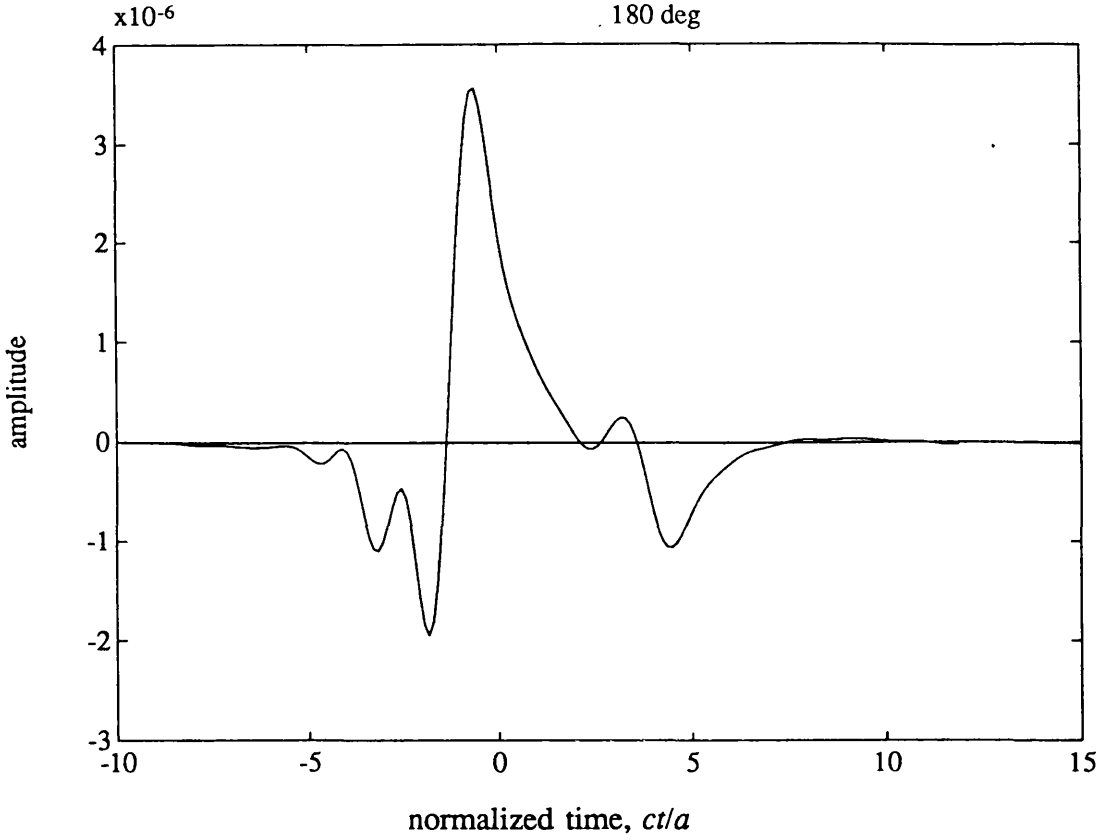

Figure 3.22 (Cont'd) (c) the time domain response from this study

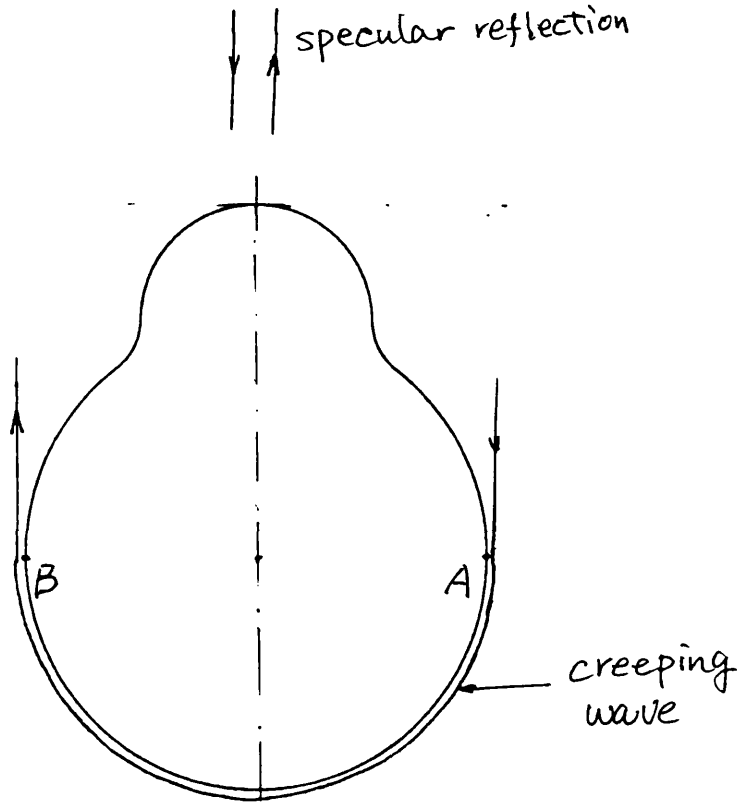

Figure 3.22 (Cont'd) (d) the front surface reflection and the creeping wave

3.5 Discussions

The simulated backscattering results for a variety of voids have been presented in both the time and frequency domains. Some of the results in the frequency domain have been compared with the published results if available, and they compare well. The scattering results from the ovate void, a more general shaped void, are not found in the literature.

The time domain results are band-limited to the same frequency ranges as the frequency domain results. The physical significance of some scattering features has been discussed. All the results presented here can be explained using a simple physical model, i.e. a leading front surface specular reflection followed by a creeping wave which travels around the circumference at a velocity close to that of a longitudinal wave. In most cases, the transit times (between the specular reflections and the creeping waves) measured from the numerical time domain responses agree very well with the simple physical analysis. This, on one hand, justifies the physical analysis. On the other hand, it also indicates that the numerical calculations are reliable.

The backscattering results presented in this chapter are used to test the inverse sizing technique developed in the next chapter.

The computer model is based on the idea of MOOT, which involves a partial wave expansion, and therefore cannot be used in practice for very short wavelength incident waves [Albach, 1989; Visscher, 1980b].

Appendix 3A
NUMERICAL TREATMENTS OF THE SURFACE TRACTION COMPONENTS

The implementation of equation (3-20) into a computer program requires first to calculate the surface traction components, $\vec{t}_{plm}$. This appendix deals with numerical treatments of the surface traction components. The most of the basic equations can be found in many classic books and publications. The following equations were compiled from Visscher [1980b] with references to Pao and Mow [1973] and Morse and Feshbach [1953].

To calculate the surface traction components, one needs the displacement components and their derivatives. The following equations are the components of the displacement in spherical coordinates for the basis functions, $\vec{u}_{plm}$. u^+ is obtained with $z_l=h_l^{(1)}$, and u^- is obtained with $z_l=j_l$.

$$u_{r\ 1lm}=\frac{dz_l(kr)}{d(kr)}Y_{lm}(\theta,\phi) \tag{A.1}$$

$$u_{\theta\ 1lm}=\frac{z_l(kr)}{kr}\frac{\partial Y_{lm}(\theta,\phi)}{\partial\theta} \tag{A.2}$$

$$u_{\phi\ 1lm}=\frac{im}{kr\sin\theta}z_l(kr)Y_{lm}(\theta,\phi) \tag{A.3}$$

$$u_{r\ 2lm}=0 \tag{A.4}$$

$$u_{\theta\ 2lm} = -\frac{im}{\sin\theta} z_l(\beta r) Y_{lm}(\theta,\phi) \tag{A.5}$$

$$u_{\phi\ 2lm} = z_l(\beta r) \frac{\partial Y_{lm}(\theta,\phi)}{\partial\theta} \tag{A.6}$$

$$u_{r\ 3lm} = -\frac{l(l+1)}{\beta r} z_l(\beta r) Y_{lm}(\theta,\phi) \tag{A.7}$$

$$u_{\theta\ 3lm} = -\frac{1}{\beta r} \frac{d[\beta r z_l(\beta r)]}{d(\beta r)} \frac{\partial Y_{lm}(\theta,\phi)}{\partial\theta} \tag{A.8}$$

$$u_{\phi\ 3lm} = -\frac{im}{\sin\theta} \frac{1}{\beta r} \frac{d[\beta r z_l(\beta r)]}{d(\beta r)} Y_{lm}(\theta,\phi) \tag{A.9}$$

Their derivatives in spherical coordinates are as follows.

$$u_{r\ 1lm,r} = k \frac{d^2 z_l(kr)}{d(kr)^2} Y_{lm}(\theta,\phi) \tag{A.10}$$

$$u_{\theta\ 1lm,r} = k \frac{d}{d(kr)} \left[\frac{z_l(kr)}{kr} \right] \frac{\partial Y_{lm}(\theta,\phi)}{\partial\theta} \tag{A.11}$$

$$u_{\phi\ 1lm,r} = k \frac{im}{\sin\theta} \frac{d}{d(kr)} \left[\frac{z_l(kr)}{kr} \right] Y_{lm}(\theta,\phi) \tag{A.12}$$

$$u_{r\ 1lm,\theta} = \frac{dz_l(kr)}{rd(kr)} \frac{\partial Y_{lm}(\theta,\phi)}{\partial\theta} \tag{A.13}$$

$$u_{\theta\ 1lm,\theta} = k\frac{z_l(kr)}{(kr)^2} \frac{\partial^2 Y_{lm}(\theta,\phi)}{\partial\theta^2} \tag{A.14}$$

$$u_{\phi\ 1lm,\theta} = k\frac{im}{(kr)^2} z_l(kr) \frac{\partial}{\partial\theta}\left[\frac{Y_{lm}(\theta,\phi)}{\sin\theta}\right] \tag{A.15}$$

$$u_{r\ 1lm,\phi} = k\frac{im}{kr\sin\theta} \frac{dz_l(kr)}{d(kr)} Y_{lm}(\theta,\phi) \tag{A.16}$$

$$u_{\theta\ 1lm,\phi} = k\frac{im}{kr\sin\theta} \frac{z_l(kr)}{kr} \frac{\partial Y_{lm}(\theta,\phi)}{\partial\theta} \tag{A.17}$$

$$u_{\phi\ 1lm,\phi} = k\left(\frac{im}{kr\sin\theta}\right)^2 z_l(kr) Y_{lm}(\theta,\phi) \tag{A.18}$$

$$u_{r\ 2lm,r} = 0 \tag{A.19}$$

$$u_{\theta\ 2lm,r} = -\beta\frac{im}{\sin\theta} \frac{dz_l(\beta r)}{d(\beta r)} Y_{lm}(\theta,\phi) \tag{A.20}$$

$$u_{\phi\ 2lm,r} = \beta \frac{dz_l(\beta r)}{d(\beta r)} \frac{\partial Y_{lm}(\theta,\phi)}{\partial \theta} \tag{A.21}$$

$$u_{r\ 2lm,\theta} = 0 \tag{A.22}$$

$$u_{\theta\ 2lm,\theta} = -\beta \frac{im}{\beta r} z_l(\beta r) \frac{\partial}{\partial \theta}\left[\frac{Y_{lm}(\theta,\phi)}{\sin\theta}\right] \tag{A.23}$$

$$u_{\phi\ 2lm,\theta} = \beta \frac{z_l(\beta r)}{(\beta r)} \frac{\partial^2 Y_{lm}(\theta,\phi)}{\partial \theta^2} \tag{A.24}$$

$$u_{r\ 2lm,\phi} = 0 \tag{A.25}$$

$$u_{\theta\ 2lm,\phi} = -\beta \frac{(im)^2}{\beta r (\sin\theta)^2} z_l(\beta r) Y_{lm}(\theta,\phi) \tag{A.26}$$

$$u_{\phi\ 2lm,\phi} = \beta \frac{im}{\sin\theta} \frac{z_l(\beta r)}{\beta r} \frac{\partial Y_{lm}(\theta,\phi)}{\partial \theta} \tag{A.27}$$

$$u_{r\ 3lm,r} = -\beta\, l(l+1) \frac{d}{d(\beta r)}\left[\frac{z_l(\beta r)}{\beta r}\right] Y_{lm}(\theta,\phi) \tag{A.28}$$

$$u_{\theta\ 3lm,r} = -\beta \frac{d}{d(\beta r)}\left(\frac{1}{\beta r}\frac{d[\beta r z_l(\beta r)]}{d(\beta r)}\right)\frac{\partial Y_{lm}(\theta,\phi)}{\partial\theta} \tag{A.29}$$

$$u_{\phi\ 3lm,r} = -\beta \frac{im}{\sin\theta}\frac{d}{d(\beta r)}\left(\frac{1}{\beta r}\frac{d[\beta r z_l(\beta r)]}{d(\beta r)}\right)Y_{lm}(\theta,\phi) \tag{A.30}$$

$$u_{r\ 3lm,\theta} = -\beta\, l(l+1)\frac{z_l(\beta r)}{(\beta r)^2}\frac{\partial Y_{lm}(\theta,\phi)}{\partial\theta} \tag{A.31}$$

$$u_{\theta\ 3lm,\theta} = -\beta \frac{1}{(\beta r)^2}\frac{d[\beta r z_l(\beta r)]}{d(\beta r)}\frac{\partial^2 Y_{lm}(\theta,\phi)}{\partial\theta^2} \tag{A.32}$$

$$u_{\phi\ 3lm,\theta} = -\beta \frac{im}{(\beta r)^2}\frac{d[\beta r z_l(\beta r)]}{d(\beta r)}\frac{\partial}{\partial\theta}\left[\frac{Y_{lm}(\theta,\phi)}{\sin\theta}\right] \tag{A.33}$$

$$u_{r\ 3lm,\phi} = -\beta\, l(l+1)\frac{z_l(\beta r)}{(\beta r)^2}\frac{im}{\sin\theta}Y_{lm}(\theta,\phi) \tag{A.34}$$

$$u_{\theta\ 3lm,\phi} = -\beta \frac{im}{(\beta r)^2\sin\theta}\frac{d[\beta r z_l(\beta r)]}{d(\beta r)}\frac{\partial Y_{lm}(\theta,\phi)}{\partial\theta} \tag{A.35}$$

$$u_{\phi\ 3lm,\phi} = \beta \frac{m^2}{(\beta r\sin\theta)^2}\frac{d[\beta r z_l(\beta r)]}{d(\beta r)}Y_{lm}(\theta,\phi) \tag{B.5}$$

The above derivatives are the results in spherical coordinate system, and the following relations are employed,

$$u_{,r} = \frac{\partial u}{\partial r}$$
$$u_{,\theta} = \frac{1}{r}\frac{\partial u}{\partial \theta} \qquad \text{(A.37)}$$
$$u_{,\phi} = \frac{1}{r\sin\theta}\frac{\partial u}{\partial \phi}$$

From the above equations, the surface traction components for the basis functions can be obtained from equation (3-13). The easiest way is to express $\vec{t}$ in terms of its components in a coordinate system of the surface $\in$. Shown as figure A.1, this Cartesian coordinate system is in general different for each point on $\in$, and is defined by three mutually perpendicular unit vector $\hat{n}$ (outward normal to $\in$), $\hat{\phi}$ (which lies in the surface $\in$ because of the assumed axial symmetry) and $\hat{p}$ (in the surface perpendicular both to $\hat{n}$ and $\hat{\phi}$). In this $(\hat{n},\hat{p},\hat{\phi})$ coordinate system, the components of the surface traction (equation (3-13)) are

$$t_n = 2\mu u_{n,n} + \lambda \nabla \cdot \vec{u} \qquad \text{(A.38)}$$

$$t_p = \mu(u_{n,p} + u_{p,n}) \qquad \text{(A.39)}$$

$$t_\phi = \mu(u_{n,\phi} + u_{\phi,n}) \qquad \text{(A.40)}$$

The u symbols here are the components of the displacements (and their derivatives) in the $(\hat{n},\hat{p},\hat{\phi})$ coordinate system. They can be computed from equations (A.1) to (A.36).

If the surface $\in$ is expressed as

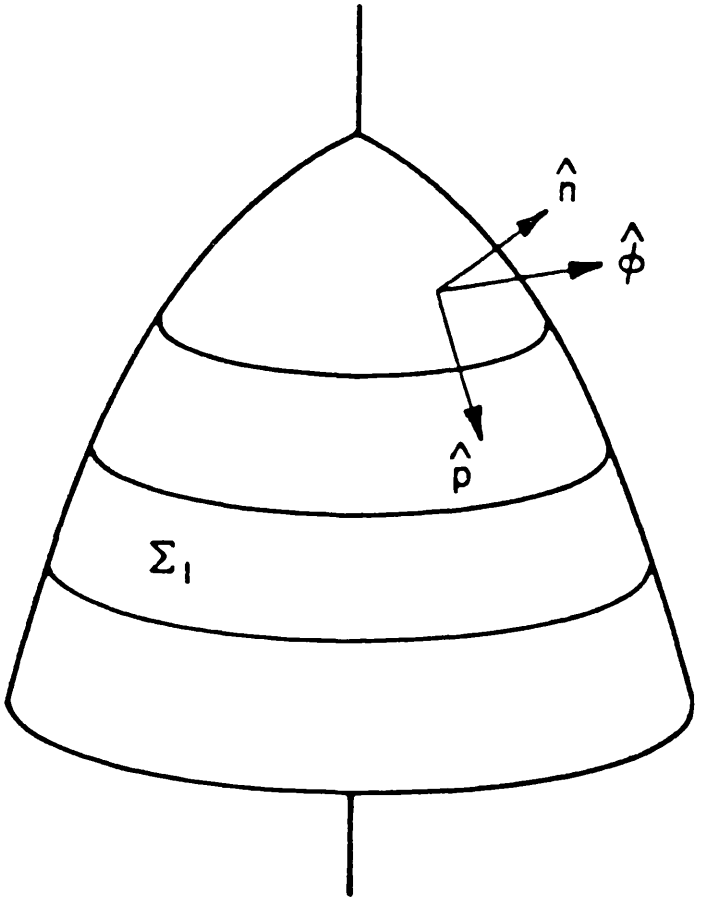

Figure A.1 Cartesian coordinate system of the surface ϵ. $\hat{\phi}$ lies in the surface ϵ; $\hat{n}$ is normal to ϵ; $\hat{\rho}$ is normal both to $\hat{n}$ and $\hat{\phi}$.

$$r = R(\theta) \tag{A.41}$$

then in the $(\hat{n},\hat{p},\hat{\phi})$ coordinate system the components of $\vec{u}$ are

$$\begin{aligned} u_n &= u_r \cos\xi - u_\theta \sin\xi \\ u_p &= u_r \sin\xi + u_\theta \cos\xi \end{aligned} \tag{A.42}$$

where

$$\xi = \arctan\left[\frac{R'(\theta)}{R(\theta)}\right], \quad -\frac{1}{2}\pi < \xi < \frac{1}{2}\pi \tag{A.43}$$

The components of the derivatives of $\vec{u}$ in $(\hat{n},\hat{p},\hat{\phi})$ coordinate system are

$$u_{n,n} = u_{r,r}\cos^2\xi + \left(u_{\theta,\theta} + \frac{u_r}{r}\right)\sin^2\xi + \sin\xi\cos\xi\left(\frac{u_\theta}{r} - u_{r,\theta} - u_{\theta,r}\right) \tag{A.44}$$

$$u_{p,n} = \left(u_{r,r} - u_{\theta,\theta} - \frac{u_r}{r}\right)\cos\xi\sin\xi + u_{\theta,r}\cos^2\xi - \left(u_{r,\theta} - \frac{u_\theta}{r}\right)\sin^2\xi \tag{A.45}$$

$$u_{n,p} = \left(u_{r,r} - u_{\theta,\theta} - \frac{u_r}{r}\right)\cos\xi\sin\xi - u_{\theta,r}\sin^2\xi + \left(u_{r,\theta} - \frac{u_\theta}{r}\right)\cos^2\xi \tag{A.46}$$

$$u_{n,\phi} = u_{r,\phi}\cos\xi - u_{\theta,\phi}\sin\xi - \frac{u_\phi}{r\sin\theta}\sin(\theta - \xi) \tag{A.47}$$

$$u_{\phi,n} = u_{\phi,r}\cos\xi - u_{\phi,\theta}\sin\xi \tag{A.48}$$

$\nabla\cdot\vec{u}$ in equation (A.38) can be simplified as follows:

For the longitudinal wave, when p=1

$$\nabla\cdot\vec{u}_{1lm} = k^{-1}\nabla^2\phi = -k\phi = -kz_l(kr)Y_{lm}(\theta,\phi) \tag{A.49}$$

For the transverse waves, when p=2 or 3

$$\nabla\cdot\vec{u}_{plm} = 0 \tag{A.50}$$

When these equations are substituted into equations (A.38) to (A.40), the components of the surface traction for the basis functions can be evaluated. The formulas are

$$t_{n\,plm} = 2\mu\left[u_{r\,plm,r}\cos^2\xi + \left(u_{\theta\,plm,\theta} + \frac{u_{r\,plm}}{r}\right)\sin^2\xi + \sin\xi\cos\xi\left(\frac{u_{\theta\,plm}}{r} - u_{r\,plm,\theta} - u_{\theta\,plm,r}\right)\right] + \lambda\nabla\cdot\vec{u}_{plm}$$

$$t_{p\,plm} = \mu\left[\sin 2\xi\left(u_{r\,plm,r} - u_{\theta\,plm,\theta} - \frac{u_{r\,plm}}{r}\right) + \cos 2\xi\left(u_{r\,plm,\theta} + u_{\theta\,plm,r} - \frac{u_{\theta\,plm}}{r}\right)\right] \tag{A.52}$$

$$t_{\phi\,plm} = \mu\left[\cos\xi(u_{\phi\,plm,r} + u_{r\,plm,\phi}) - \sin\xi(u_{\phi\,plm,\theta} + u_{\theta\,plm,\phi}) - \frac{u_{\phi\,plm}}{r\sin\theta}\sin(\theta-\xi)\right] \tag{A.53}$$

Appendix 3B:
BESSEL FUNCTIONS AND SPHERICAL HARMONICS

In evaluation of the displacements and surface traction components, spherical Bessel functions, spherical harmonics, and their first and second derivatives are needed. These special functions and their properties can be found in many classic mathematics books. Here some useful equations were compiled from Korn and Korn [1961], Jackson [1963], Press *et al* [1986], and Visscher [1980b].

Spherical Bessel functions

$z_l(x)$ is used to express any of the spherical Bessel functions $j_l(x)$, $y_l(x)$, $h_l^{(1)}(x)$ or $h_l^{(2)}(x)$. The spherical Bessel functions satisfy the following relations

$$z_{l+1}(x) = \frac{2l}{x} z_l(x) - z_{l-1}(x) \tag{B.1}$$

$$z_l'(x) = -z_{l+1}(x) + \frac{l z_l}{x} \tag{B.2}$$

$$z_l'' = -\frac{2z_l'}{x} - \left[1 - \frac{l(l+1)}{x^2}\right] z_l(x) \tag{B.3}$$

where

$$z_l'(x) = \frac{dz_l(x)}{dx}, \quad z_l''(x) = \frac{d^2 z_l(x)}{dx^2} \tag{B.4}$$

Spherical harmonics

Mathematically, the spherical harmonics are related to associated Legendre polynomials by the equation

$$Y_{lm}(\theta,\phi)=\sqrt{\frac{2l+1}{4\pi}\frac{(l-m)!}{(l+m)!}}\;P_l^m(\cos\theta)e^{im\phi} \tag{B.5}$$

The spherical harmonics have the following properties

$$Y_{l,-m}(\theta,\phi)=(-1)^m Y_{lm}^*(\theta,\phi) \tag{B.6}$$

$$\int_0^{2\pi}d\phi\int_{-1}^{1}d(\cos\theta)Y_{l'm'}^*(\theta,\phi)Y_{lm}(\theta,\phi)=\delta_{l'l}\delta_{m'm} \tag{B.7}$$

$$\sin\theta\,Y_{lm}'(\theta,\phi)=-(l+1)\cos\theta Y_{lm}(\theta,\phi)+\sqrt{\frac{(2l+1)(l+1+m)(l+1-m)}{2l+3}}\;Y_{l+1m}(\theta,\phi) \tag{B.8}$$

$$Y_{lm}''(\theta,\phi)=-\frac{\cos\theta}{\sin\theta}Y_{lm}'(\theta,\phi)+\left[\frac{m^2}{\sin^2\theta}-l(l+1)\right]Y_{lm}(\theta,\phi) \tag{B.9}$$

$$\int d\Omega\left[Y_{lm}^*(\theta,\phi)Y_{l'm}(\theta,\phi)\left(\frac{m^2}{\sin^2\theta}\right)+Y^*(\theta,\phi)Y_{l'm}'(\theta,\phi)\right]=l(l+1)\delta_{ll'} \tag{B.10}$$

where

$$Y'_{lm}(\theta,\phi)=\frac{\partial Y_{lm}(\theta,\phi)}{\partial\theta},\qquad Y''_{lm}(\theta,\phi)=\frac{\partial^2 Y_{lm}(\theta,\phi)}{\partial\theta^2} \tag{B.11}$$

Due to the occurrence of the terms $sin^{-1}\theta$ and $sin^{-2}\theta$, some equations for the surface traction are, in the numerical sense, singular at $\theta=0$ and π, if they are evaluated directly from these equations. They are however, not singular in the analytical sense, since they describe physical phenomena that are continuous in space. It can be shown that, if proper limiting procedures are applied, these equations are finite at $\theta=0$ and π. For the limiting procedure, the following properties of the Legendre polynomials have to be employed. They can be found in Albach [1990] and Stratton [1941].

$$\frac{mP_l^m(\cos\theta)}{\sin\theta}=\frac{\cos\theta}{2}\left[(l-m+1)(l+m)P_l^{m-1}(\cos\theta)+P_l^{m+1}(\cos\theta)\right] + m\sin\theta P_l^m(\cos\theta) \tag{B.12}$$

$$\frac{\partial P_l^m(\cos\theta)}{\partial\theta}=\frac{1}{2}\left[(l-m+1)(l+m)P_l^{m-1}(\cos\theta)-P_l^{m+1}(\cos\theta)\right] \tag{B.13}$$

Chapter 4

INVERSE SCATTERING TECHNIQUE: SIZING VOLUMETRIC FLAWS USING THE AREA FUNCTIONS

4.1 Introduction

This chapter reports the theoretical and numerical model studies for a new technique used to determine the size of the void in structural materials, by the inversion of the backscattered ultrasonic signal using the area function formula. Experimental work will be described in Chapter 5. The formulation of this method is based on a weak scattering approximation (the Born approximation), but this sizing technique is shown to work well for voids which are clearly strong scatterers. The area function has been widely used as a method to determine the position of the flaw centroid, assisting implementation of some inversion algorithms, such as inverse Born approximation (IBA) [Rose, 1989; Chaloner and Bond, 1987].

The sizing scheme described in this chapter involves a direct inversion of the backscattered signal, obtained in a single pulse-echo measurement, to reconstruct the cross-sectional area of the flaw, from which the flaw size is extracted. The technique is sensitive to intermediate frequency information making it potentially useful for materials with a high attenuation response.

The plan of this chapter is as follows. In Section 4.2, the time domain Born approximation is reviewed. In Section 4.3, the formulation of the area function is given. Section 4.4 discusses the area function for a spherical void, and the method of extracting the radius of a spherical void from the area function. In Section 4.5, the ultrasonic transducer bandwidth requirements of the area function sizing scheme are discussed. In Section 4.6, this technique is extended to the sizing of non-spherical voids, and the numerical results for the

reconstructions of several non-spherical voids are presented. Finally, in Section 4.7, conclusions are given.

4.2. The Time Domain Born Approximation

The weak scattering limit yields one of the simplest theories of elastic wave scattering. For cases of interest to NDE, Gubernatis *et al* [1977b] have studied systematically the weak scattering limit in terms of the Born approximation. Their work was carried out in the frequency domain, and considerable intuitive understanding of the problem resulted. Despite its simplifying assumption, the frequency domain Born approximation has been widely used in NDE studies. Further, it led to the development of the inverse Born approximation [Rose and Krumhansl, 1979].

Later, Rose and Richardson [1982] formulated the weak scattering theory in the time domain using the Born approximation. The time domain formulation is also rich in its own insights and intuitions, and its picture gives rise to simple transparent formulas for the scattering problem, which allow the solutions of many problems by inspection. The scattering amplitude for more complicated problems can be easily estimated in an intuitive way. The importance of the time domain Born approximation in this study is that it is the basis for the derivation of the area function formula which relates the cross-sectional area of the flaw with the scattering amplitude in a simple way.

As reviewed in Chapter 2, in order to solve the scattering equation, one may express it in integral form and then iterate to develop an infinite perturbation series. When only the leading term in the series is considered, the solution is called the Born approximation [Gubernatis *et al*, 1977b]. Here, Rose and Richardson's [1982] approach is followed in describing the time domain Born approximation.

Consider a longitudinally polarized impulse incident upon an isotropic homogeneous inclusion with material parameter ρ_f, λ_f, and μ_f embedded in an isotropic homogeneous host material with constant material parameter ρ_0, λ_0, and μ_0. Here ρ is the density, and λ and μ are the Lamé parameters. The incident impulse is described by

$$\vec{u}_o(\vec{r},t) = u_0 \hat{e}_o \delta(t - \frac{\hat{e}_o \cdot \vec{r}}{c}) \tag{4-1}$$

where $\hat{e}_o$ is the direction of incidence, t represents time, c is the longitudinal velocity in the host medium, u_0 determines the magnitude of the impulse, $\vec{r}$ is the position, and δ is a delta function. According to the Born approximation, the longitudinal impulse response function of the flaw $(\vec{R}_l(t,\hat{e}_o,\hat{e}_s))$ is given as [Rose and Richardson, 1982]

$$\vec{R}_l(t,\hat{e}_o,\hat{e}_s) = f(\hat{e}_o,\hat{e}_s)\hat{e}_s \frac{1}{c^2}\frac{d^2}{dt^2}\int d^3\vec{r}\,\gamma(\vec{r})\delta(t - \frac{(\hat{e}_o - \hat{e}_s)\cdot\vec{r}}{c}) \tag{4-2}$$

Where $\hat{e}_s$ represents the direction of scattering, and $\gamma(\vec{r})$ is known as the characteristic function of the flaw, which is defined as one inside the flaw and zero elsewhere. The function $f(\hat{e}_o,\hat{e}_s)$ depends on the properties of the host and the flaw materials, as well as on the relative angle between $\hat{e}_o$ and $\hat{e}_s$. It is given by Gubernatis *et al.* [1977b] as

$$f(\hat{e}_o,\hat{e}_s) = \frac{1}{4\pi}\left(\frac{\delta\rho}{\rho_0}\hat{e}_o\cdot\hat{e}_s - \frac{\delta\lambda + 2\delta\mu(\hat{e}_o\cdot\hat{e}_s)^2}{\lambda_0 + 2\mu_0}\right) \tag{4-3}$$

Here $\Delta\rho$, $\Delta\lambda$, and $\Delta\mu$ are the deviations of the flaw's material parameters, which are defined as $\Delta\rho=\rho_f-\rho_0$, $\Delta\lambda=\lambda_f-\lambda_0$, and $\Delta\mu=\mu_f-\mu_0$.

$\vec{R}_l(t,\hat{e}_o,\hat{e}_s)$ (equation (4-2)) in the time domain and $\vec{A}_l$ (equation (2-14)) in the frequency domain (or k domain) are a Fourier transform pair. They have been normalized and do not depend either on the intensity of the incident pulse

or on the distance at which the asymptotic scattering is measured.

In this study, only the backscattering situation is considered, where $\hat{e}_s$=-$\hat{e}_o$, and equation (4-3) becomes

$$f(\hat{e}_o, -\hat{e}_o) = -\frac{1}{4\pi}\left(\frac{\delta\rho}{\rho_0} + \frac{\delta\lambda + 2\delta\mu}{\lambda_0 + 2\mu_0}\right) \tag{4-4}$$

In this case, $\vec{R}_I(t,\hat{e}_o,\hat{e}_s)$ becomes $\vec{R}_I(t,\hat{e}_o,-\hat{e}_o)$ which is expressed as $\vec{R}_I(t)$ for simplicity. Thus

$$\vec{R}_I(t) = -\frac{f(\hat{e}_o, -\hat{e}_o)\hat{e}_o}{c^2}\frac{d^2}{dt^2}\int d^3\vec{r}\,\gamma(\vec{r})\,\delta(t - \frac{2\hat{e}_o\cdot\vec{r}}{c}) \tag{4-5a}$$

There is a simple geometrical interpretation of $\vec{R}_I(t)$: the integral in equation (4-5a) corresponds to the cross-sectional area, $S(t)$, of the flaw intersected by a plane defined by

$$z = \frac{ct}{2} \tag{4-6}$$

where z is the position along the axis of propagation. This plane defines the locus of points in the flaw which has a constant travel time from the transducer. The simple planar form of this locus results from the plane wave approximation and from the weak scattering assumption that the incident impulse travels at the velocity of the host inside the flaw [Rose and Richardson, 1982]. Figure 4.1 shows the backscattering geometry.

So, equation (4-5a) can be rewritten as

$$\vec{R}_I(t) = -\frac{f(\hat{e}_o, -\hat{e}_o)\hat{e}_o}{c^2}\frac{d^2S(t)}{dt^2} \tag{4-5b}$$

It is seen from equation (4-5b) that the backscattered impulse response of a

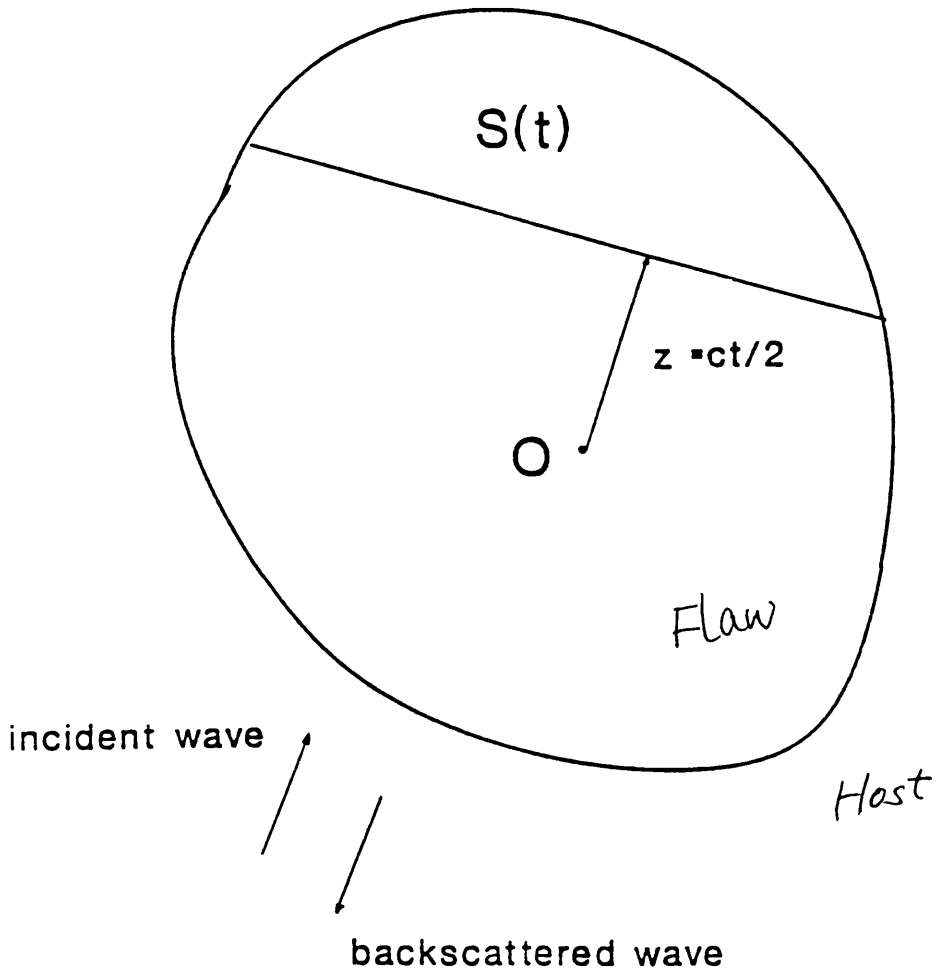

Figure 4.1 Backscattering geometry, where *S(t)* is the cross-sectional area, o is the origin of the coordinates.

flaw is proportional to the second derivative of the cross-sectional area of the flaw. Determination of $\vec{R}_f(t)$ therefore reduces to finding the cross-sectional area, $S(t)$, of the flaw and its second derivative, $S''(t)$, which makes the problem straightforward and simple. Figure 4.2 shows the backscattering from a weak scattering spherical flaw as an example. Figure 4.2b is the cross-sectional area ($S(t)$) of the flaw, which has a parabolic shape with maximum at the flaw centroid. Figure 4.2c represents the second derivative of $S(t)$ and also the time domain impulse response of the flaw. The sign of the delta function in figure 4.2c depends on the material properties of the flaw relative to those of the host.

4.3 Area Function

The relationship between the impulse response function ($\vec{R}_f(t)$) and the cross-sectional area ($S(t)$) is now considered in the opposite way. According to equation (4-5b), if $\vec{R}_f(t)$ is known, $S(t)$ can be reconstructed by double integration of $\vec{R}_f(t)$

$$Reconstructed\ S(t) = AF(t) = -\frac{c^2}{f(\hat{e}_o, -\hat{e}_o)} \iint R_f(t)\, d^2t \qquad (4\text{-}7)$$

where $R_f(t)=\hat{e}_o \cdot \vec{R}_f(t)$; $AF(t)$ represents the reconstructed cross-sectional area, which is defined as the area function for the flaw in order to distinguish it from the original true cross-sectional area, $S(t)$.

Equation (4-7) therefore provides the basis for an inversion scheme that uses the ultrasonic backscattering data to reconstruct the cross-sectional area of the flaw, from which the flaw size can be extracted.

In practice, however, evaluation of $AF(t)$ by direct double integration of $R_f(t)$ is not desirable, since the backscattered response is inevitably convolved with the finite transducer bandwidth and system noise. As a result, a direct

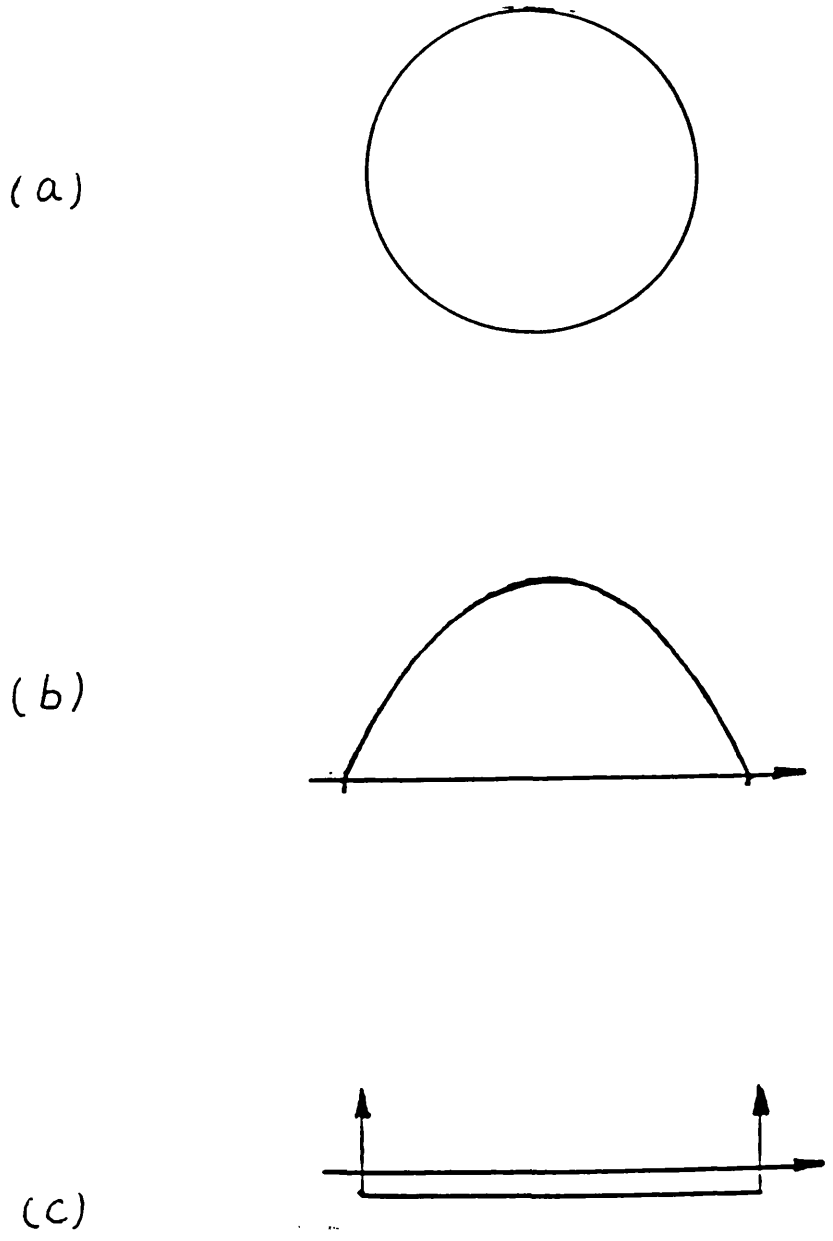

Figure 4.2 Backscattering from a weak scatterer, (a) a spherical flaw; (b) the cross-sectional area, *S(t)*; (c) second derivative of *S(t)*, and impulse response of the flaw.

time-domain deconvolution of the system response from the measured signal is vulnerable to instabilities [Koo *et al*, 1990]. Instead, it is better to do the signal processing in the frequency domain, where it is possible to make specific corrections (e.g. using Wiener filter [Kino, 1987]) in order to desensitize the results to the presence of noise. It is therefore more practical and desirable to evaluate $AF(t)$ in the frequency domain. This can be done by using the Fourier integral theory [Papoulis, 1977] to process equation (4-7). According to the Fourier integral theory, the double integration of a spatial signal is equivalent to the inverse transform of its Fourier transform divided by the factor $-f^2$, where f is frequency. Equation (4-7) can then be expressed in the frequency domain as

$$AF(t) = \frac{c^2}{f(\hat{e}_o,-\hat{e}_o)} \frac{1}{(2\pi)^2} \int_0^\infty \frac{1}{f^2} e^{i2\pi ft} A_l df \qquad (4\text{-}8)$$

where A_l is the Fourier transform of $R_l(t)$. In the following sections, all the area functions considered are evaluated in the frequency domain using equation (4-8), rather than in the time domain through equation (4-7). In equations (4-7) and (4-8), the term $c^2/f(\hat{e}_o,-\hat{e}_o)$ is a constant. Since the absolute value of the magnitude of the area function is not the interest of this study, this term is ignored in the evaluation of the area function. The area function evaluated without this term is simply normalized for presentation in such a way that its maximum is one.

It is clearly understood from equation (4-8) that in order to exactly evaluate the area function, an infinite frequency spectrum of the scattering data is needed. However, all the ultrasonic equipments, especially the transducers, are band-limited. That is to say there is only a limited range of frequency information available. The simple truncation of a certain length of spectrum from an infinite one can be regarded as the multiplication of the original infinite spectrum by a rectangular window function which has a much shorter length. There are other window functions which can be used in signal processing, such as, Hanning, Hamming, Bartlett functions [Papoulis, 1977]. No

matter which window function is used, the distortion of the area function in one way or another is inevitable. In the following discussions of the numerical evaluation of the area function and the sizing technique, it is first concentrated on the usage of the simplest window function - a rectangular window function. The effects of using other window functions on the sizing results are then compared with the results from using a rectangular window function.

Figure 4.3 shows the area function (solid line) for a 200 μm radius ideal weak scattering sphere in titanium. The input data A_I was obtained by using the frequency domain Born approximation formula [Gubernatis *et al*, 1977b] which is

$$A_I(k) = const. \frac{\sin(ka) - ka\cos(ka)}{k} \qquad (4\text{-}9)$$

where a is the radius of the sphere, f is the frequency and k is the wave number defined as $k=2\pi f/c$. A_I was band-limited in the frequency range of $0 \leq ka \leq 6.5$. The dashed line in the figure represents the true cross-sectional area. It can be seen that agreement between the area function and the true cross-sectional area is very good except for some minor differences due to the cut-off of the high frequency information.

4.4 Spherical Void and Radius Estimation

The formulation of the area function (equation (4-8)) is based on the weak scattering approximation, however, many naturally occurred flaws in structural materials are strong scatterers including voids. Previous research by Gurbernitis *et al* [1977b] has shown that for voids in elastic media the Born approximation describes well the scattering when the wavelength of the incident wave is approximately an order of magnitude larger than the scatterer and when the scattering is viewed in the backscattered direction. In this section, the validity of the area function formula for voids is investigated. A new sizing

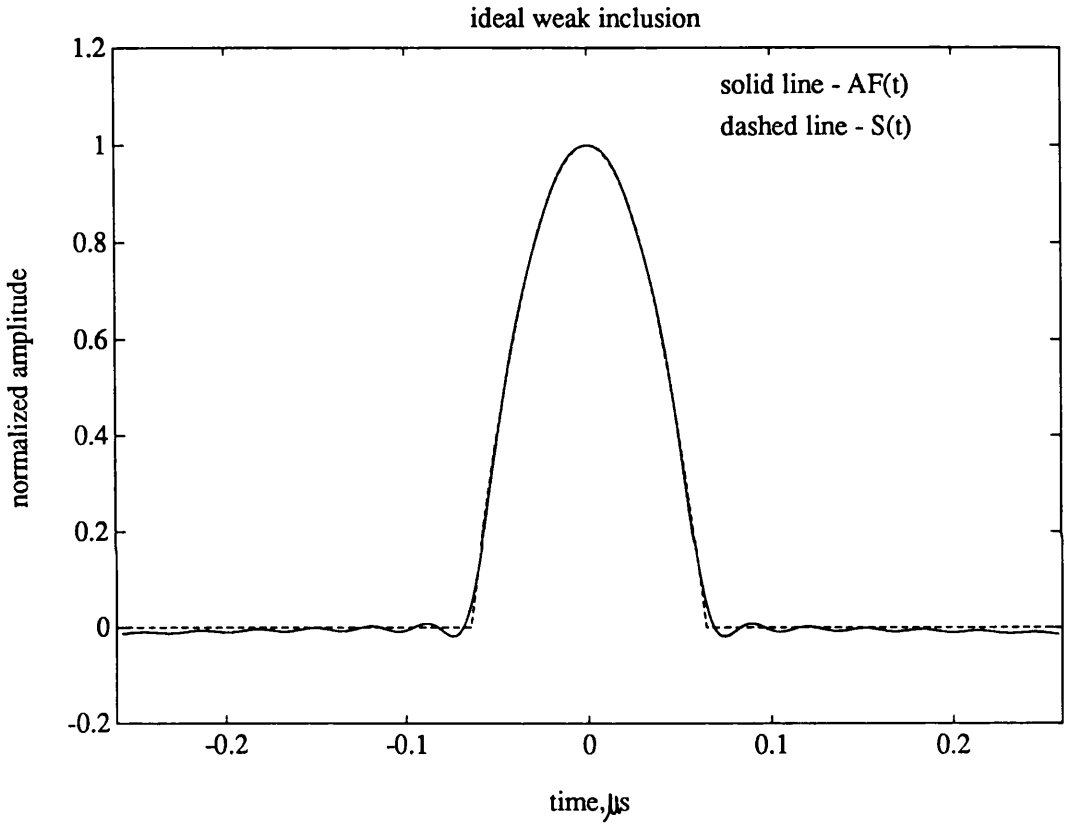

Figure 4.3 *AF(t)* and *S(t)* for a 200 μm radius weak scattering inclusion in titanium (c=6.20 *km/s*, c_t=3.125 *km/s*)

scheme using the area function is developed. We start from the simplest case, the spherical void.

The series solutions of Ying and Truell [1956] were employed to simulate the backscattering data A_l from spherical voids. Figure 4.4 represents the frequency domain backscattering amplitude from a 200 μm radius spherical void in titanium. Figure 4.5 shows the calculated area function, *AF(t)*, and the true cross-sectional area, *S(t)*, for the void. The input backscattering amplitude A_l for the evaluation of *AF(t)* was in the frequency range of $0 \leq ka \leq 6.5$, where a represents the radius of the void. It is impossible to input all the high frequency data. Fortunately, equation (4-8) (the factor $1/f^2$) suggests that high frequency data plays much less significant role than low frequency data. Effects of loss of high and low frequency data will be discussed in Section 4.5.

In figure 4.5, both *AF(t)* and *S(t)* have been normalized so that their maxima are one. It is observed from figure 4.5 that the early arrival of the area function (*AF(t)*) agrees very well with that of the true cross-sectional area (*S(t)*), while in the later parts the agreement is less good. This is not a surprise, because the area function formula is derived from a weak scattering approximation, and the void is a strong scatterer.

Figures 4.6a and 4.6b compare the similarities and the differences between the impulse response for an ideal weak scattering spherical inclusion and the impulse response for a spherical void in titanium. It is seen that the early arrivals of the two impulse responses agree with each other well, and the later parts diverge. For both weak and strong scattering, there is a common feature, a delta-function spike, which occurs at a time determined by tangency of the incident pulse and the flaw surface. Research by Chen [1987] gives a theoretical explanation for these similarities and differences. Applying the elastodynamic ray theory to an arbitrary void in an isotropic and homogeneous

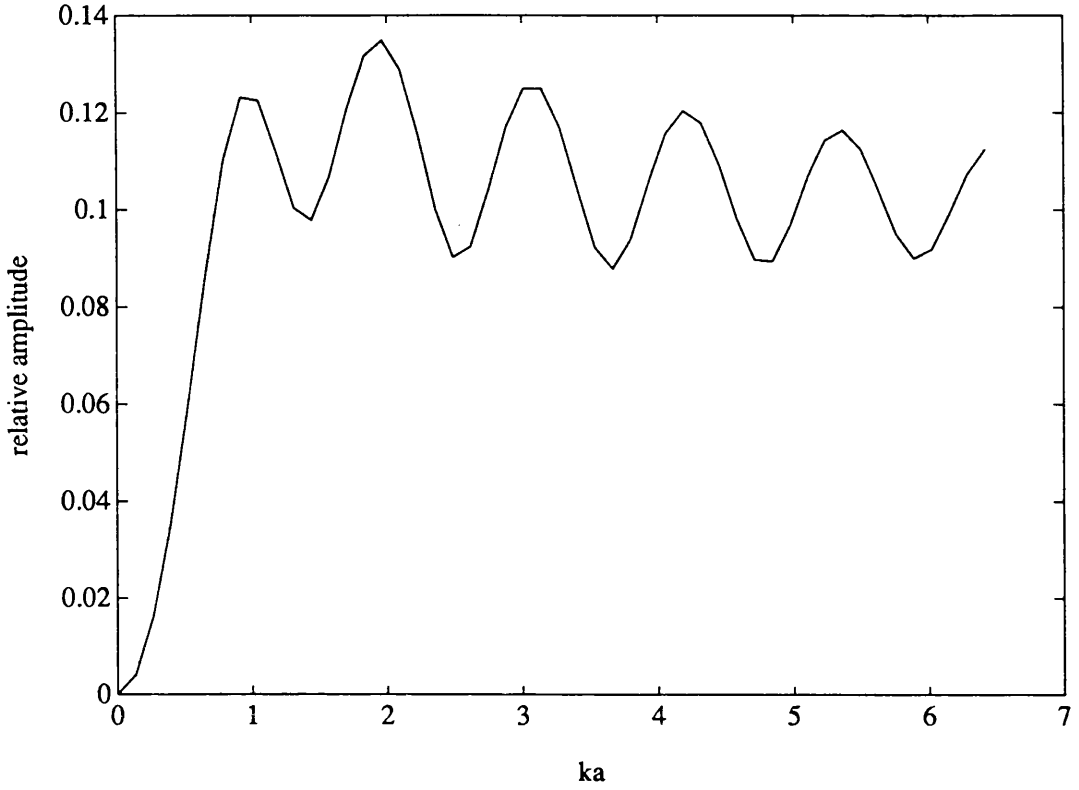

Figure 4.4 Backscattering amplitude from a 200 μm radius spherical void in titanium

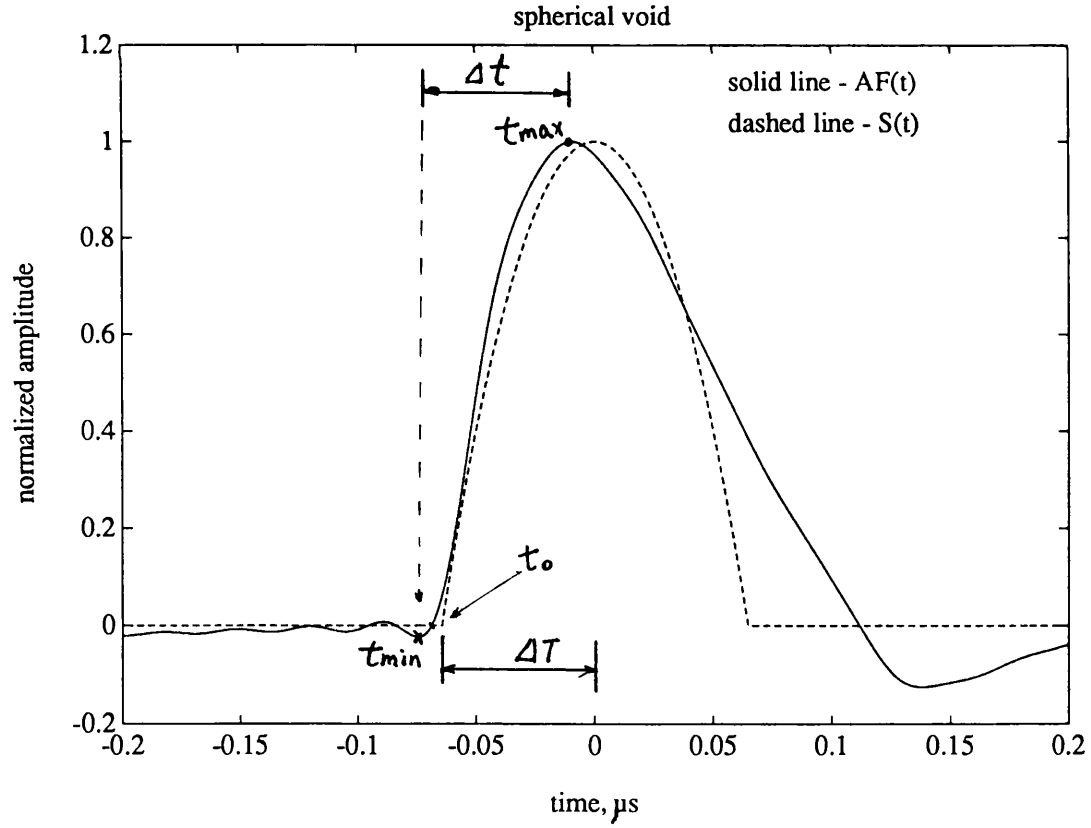

Figure 4.5 The area function, *AF(t)*, and the cross-sectional area, *S(t)* for a 200 μm radius spherical void.

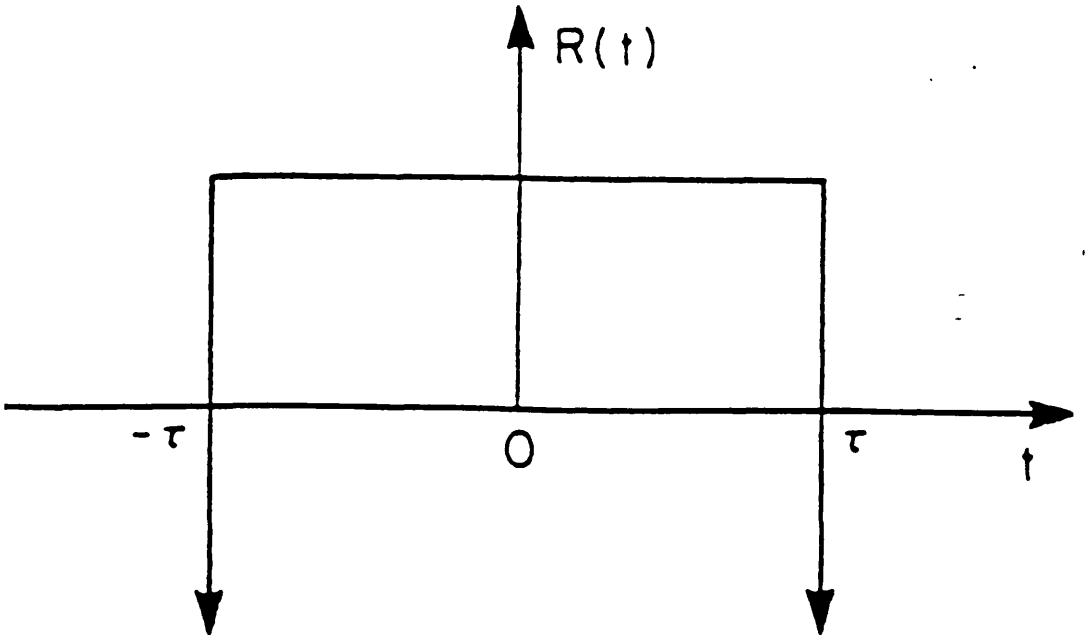

Figure 4.6a The impulse response function for an ideal weak scattering spherical inclusion. The down arrows denote delta functions, where $\tau=2a/c$ *[Kogan et al, 1985].*

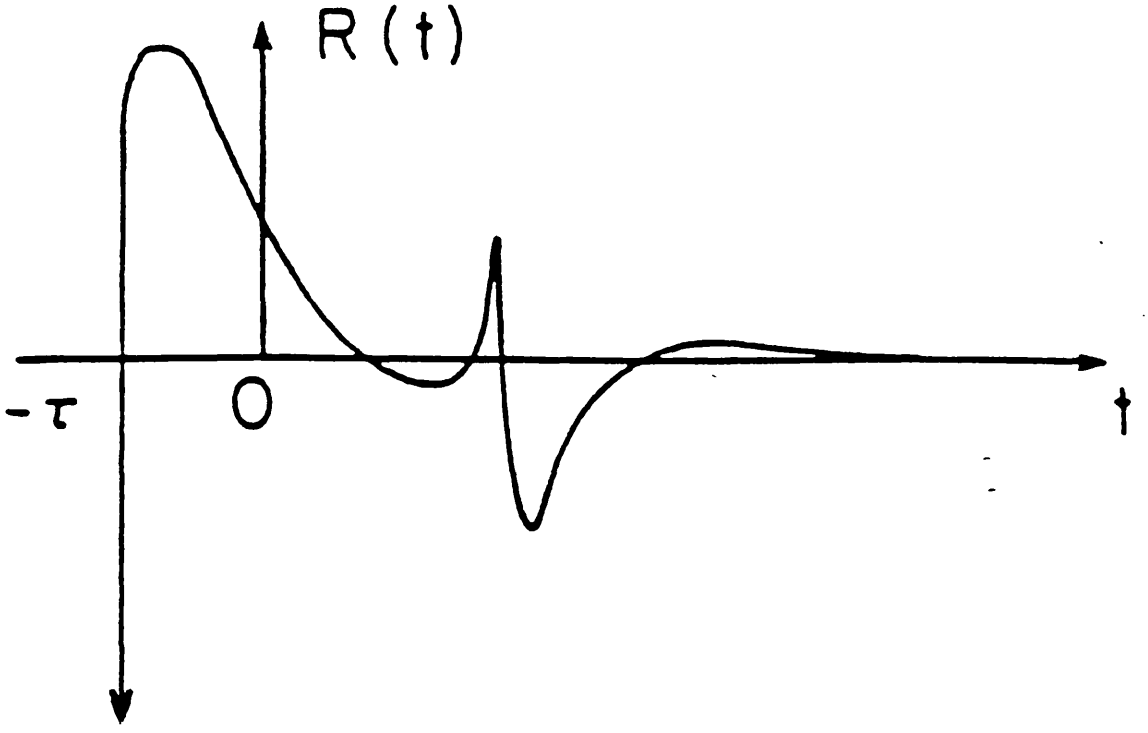

Figure 4.6b The impulse response function for a spherical void in an otherwise isotropic and homogeneous elastic medium. The down arrow denotes a delta function, where $\tau=2a/c$. [Kogan et al, 1985]

medium, he found that for the host material having a Poisson ratio 1/3, which is true for most structural materials, the early arrival of the backscattered signal from a void is expected to agree with the Born prediction.

From the above observation and analysis, the early arrival of the area function for a spherical void may therefore be used to extract the radius of the void. In figure 4.5, t_{max} represents the time at which $AF(t)$ reaches it maximum value, and t_{min} represents the time when $AF(t)$ has the last valley point before the time t_{max}. It is seen from figure 4.5 that the maximum value of $AF(t)$ occurs a little before the maximum value of $S(t)$, at which the incident wave passes through the centre of the void. The minimum value of $AF(t)$ (the last one before t_{max}) occurs a little before $S(t)$ starts rising from zero, at which the incident wave starts touching the void. The time difference (Δt) between the values where $AF(t)$ starts from minimum (t_{min}) and reaches maximum (t_{max}) therefore can be regarded as an approximation to the time difference (ΔT) between the times at which the incident wave starts touching the void and when it passes through the centre of the void. Given the relationship between the position, z, and the time, t, in the backscattering geometry as shown in equation (4-6), the radius of the void can therefore be estimated using Δt by the relation

$$a = \frac{c\Delta t}{2} \tag{4-10}$$

Thus, equations (4-8) and (4-10) provide a simple sizing technique, the area function sizing scheme. The data in figure 4.5 was used to estimate the radius in this way. The resulting radius estimation is 204 μm, which is just 2% over the true radius.

Although the time origin used in figure 4.5 was chosen to be at the centre of the void, the choice of time origin has no effect on the shape of the

area function. Equation (4-7) indicates that $AF(t)$ moves with the shift of time origin, but its shape remains unchanged and neither does Δt change. Thus, the estimated radius is not affected by the choice of time origin in the time domain signal.

4.5 Bandwidth Requirements

In practice, the bandwidth of a transducer is usually not as wide as that used in the calculation of $AF(t)$ shown in figure 4.5 ($0 \leq ka \leq 6.5$). The bandwidth effects are investigated here. Figure 4.7 shows the shape change in the area function for a 200 μm radius spherical void in titanium, with respect to the changing bandwidth of the input data A_I, which varies from $0 \leq ka \leq 6.5$ to $1 \leq ka \leq 2$. There are two important observations to be made from this figure. First, while narrowing the bandwidth of the input data seriously distorts the shape of the area function, t_{max} and t_{min} remain remarkably stable. This observation is the basis for the practical applicability of this sizing technique. The second observation from figure 4.7 is that the time at which $AF(t)$ is zero (represented by t_0) is not as stable as the time t_{min}, with respect to the changing bandwidth. This second observation is the reason why we use t_{min}, rather than t_0.

Radius estimations obtained using simulated scattering data for a spherical void in titanium with limited bandwidth are shown in figure 4.8, where the normalized radius represents the ratio of the estimated radius to the true radius. The "o" curve in figure 4.8 shows how the radius estimates are affected when the minimum ka value present in the data is raised from 0 to 1.8, while the maximum ka value is fixed at 6.5. The curve indicates a general trend that insufficient low frequency data cause underestimate of the radius. If an error of less than 20% is required, a loss of low frequency information to $ka \geq 1$ can be tolerated. The "*" curve in figure 4.8 shows the effects of lowering

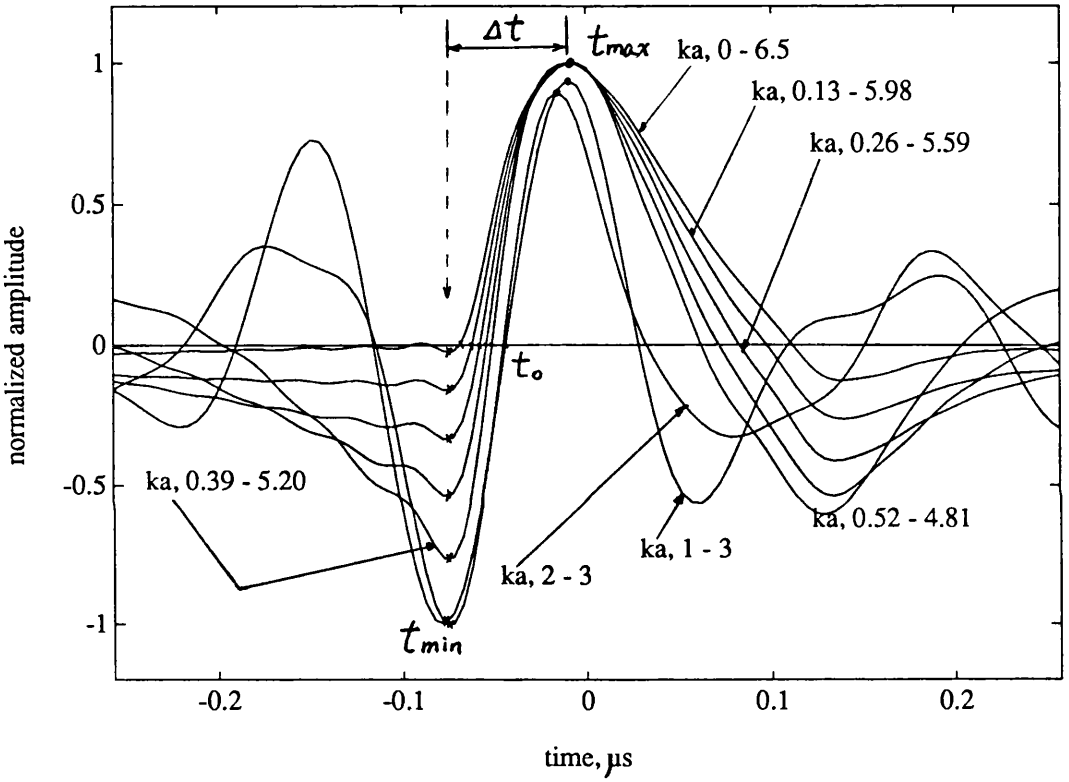

Figure 4.7 The area function for a 200 μm radius void in titanium, with different bandwidth for the input data

the maximum *ka* value present in the data, while the minimum *ka* value is fixed at 0. The general trend is that a loss of high frequency data leads to overestimate of the radius. If an error of less than 20% is required, a loss of high frequency data to $ka \leq 3$ can be tolerated.

From the above simplified analysis of bandwidth effects on radius estimates, it is concluded that a minimum bandwidth of $1 \leq ka \leq 3$ is adequate to obtain radius estimates accurate to within 20%. In practice, the bandwidth requirements can be less restrictive, because the errors caused by loss of low and high frequency data have opposite effects on the sizing results. A bandwidth of $1 \leq ka \leq 2$ for a void of 200 μm radius was tested using simulated data (the corresponding *AF(t)* is shown in figure 4.7), the radius estimate obtained is 216 μm, which is 8% over the true radius.

However, in real measurements, the radius (*a*) of a void is not known *a priori*, so the transducer which can be used in practice should have a wide bandwidth so that it is able to cover a wide range of expected flaw sizes. The effect of the match between flaw sizes and transducer bandwidth properties is shown as figure 4.9. The figure shows the normalized radius vs the centre wave-number k_c of a transducer, multiplied by the flaw radius *a*. Each curve is for a transducer of different relative bandwidth, expressed in terms of the ratio of the maximum frequency f_{max} of the transducer to the minimum frequency f_{min}. It can be found out from this figure that for a f_{max}:f_{min}=8:1 transducer, measurements will be accurate to within 20% for a 3:1 range of flaw sizes; for a f_{max}:f_{min}=4:1 transducer and the same level of accuracy, the range flaw sizes is about 1.6:1. Curves for transducers with other bandwidth properties can be calculated and presented in the same way. Figures like figure 4.9 can be used as a guide for selecting a transducer to match a particular range of flaw sizes.

A good broadband commercial transducer might typically have an 8:1

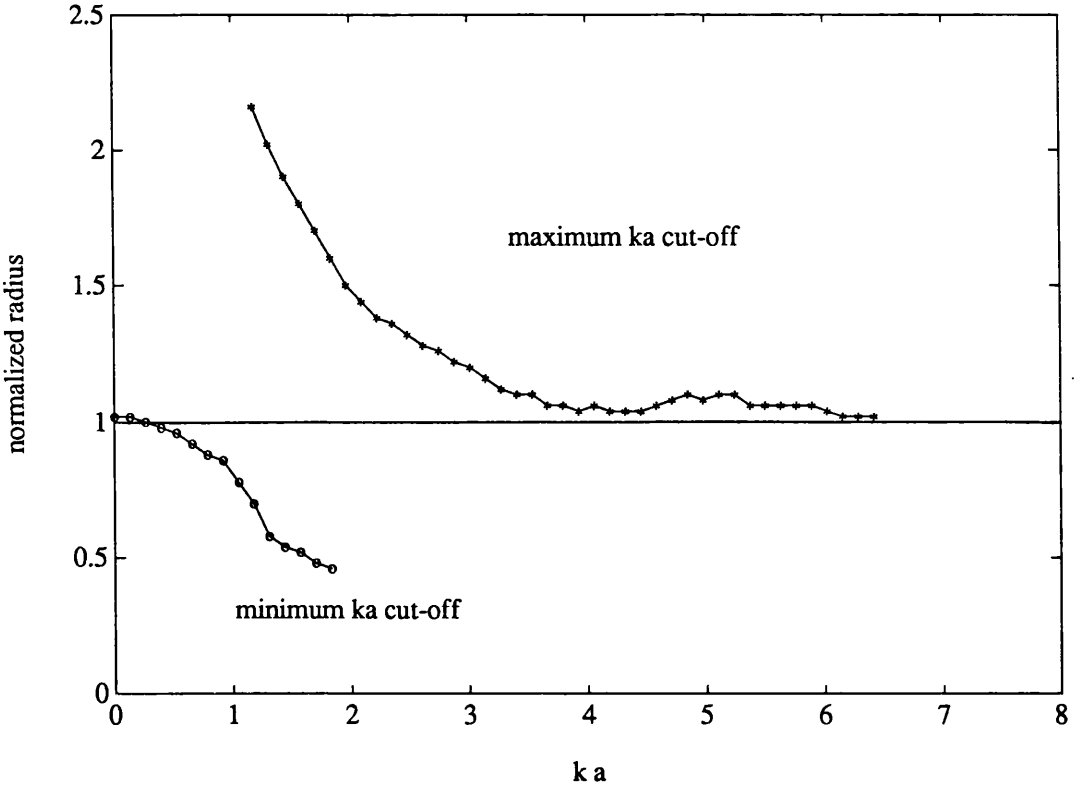

Figure 4.8 Effect of limited bandwidth on the accuracy of the area function sizing technique

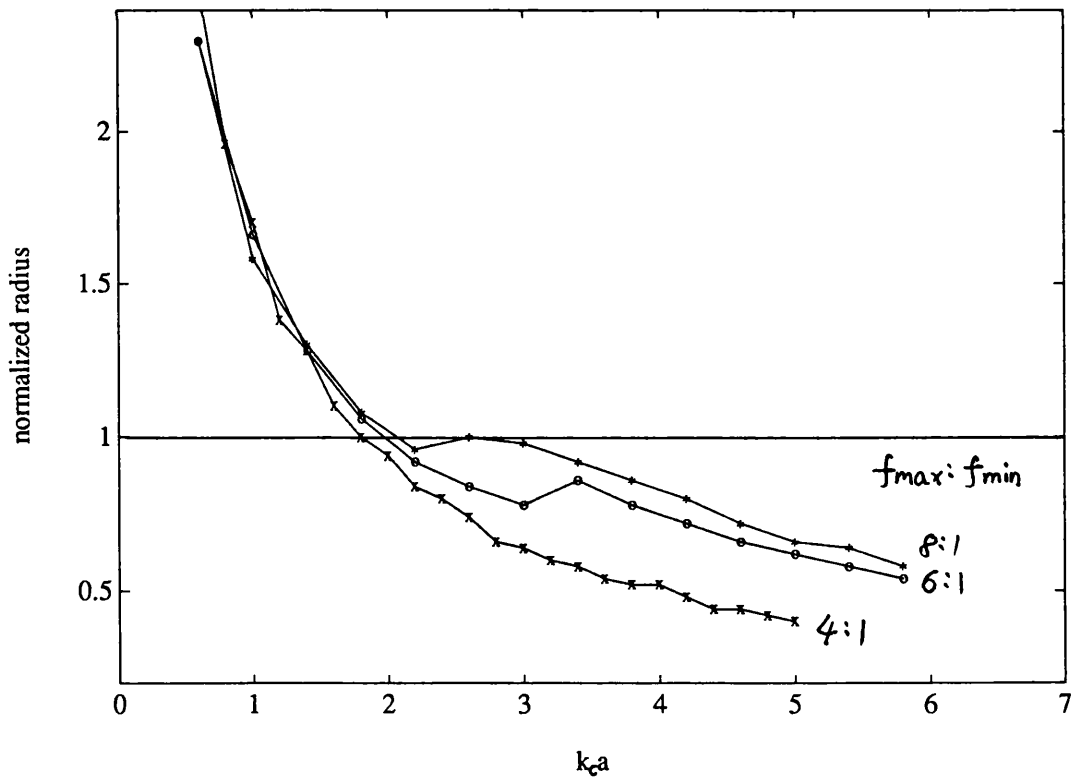

Figure 4.9 Accuracy of the area function sizing method vs transducer centre frequency and bandwidth

range of usable frequency. As an example, according to figure 4.9, a transducer with a centre frequency of 7.5 MHz, f_{min}=1.7 MHz, and f_{max}=13.3 MHz (f_{max}:f_{min}=8:1) would be capable of measuring radii of voids in titanium in the range of 200 μm to 600 μm to an accuracy of 20% using the area function sizing scheme.

Comparing figures 4.8 and 4.9 with the results of the bandwidth effects on the accuracy of the IBA published by Elsley and Addison [1980] and Addison *et al* [1982] (they are shown as figures 4.8a and 4.9a), it is found that the general trends of bandwidth requirements for these two techniques are very similar, however, the bandwidth requirements of the area function sizing technique are less severe than those of the IBA. According to Rose [1989], the IBA requires a minimum bandwidth of $0.5 \leq ka \leq 2.5$ in order to give radius estimates accurate to within 20%, while the area function technique requires a bandwidth of $1 \leq ka \leq 3$ to give the same level of accuracy.

Effects of using other window functions

As mentioned early, rectangular window function is not the only function which can be used to select a segment of an infinite spectrum. In signal processing, other kinds of window functions are usually used to reduce the side lobe characteristics of a rectangular window to improve the results [Papoulis, 1977]. Here, effects of imposing the Hanning window function, one of the most commonly used window functions in spectrum analysis, on the flaw sizing results are investigated. The Hanning function is defined as [Papoulis, 1977]

$$w(n) = \frac{1}{2}\left(1 + \cos\left(\frac{\pi n}{n_{\max}}\right)\right) \qquad (4\text{-}11)$$

where n is the data point.

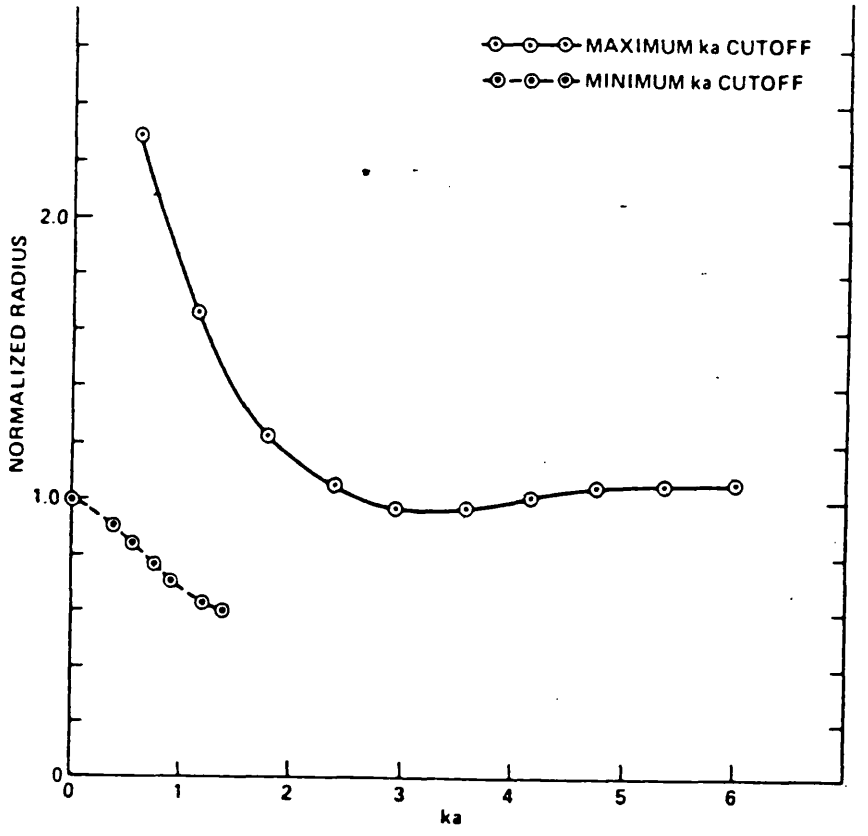

Figure 4.8a Effect of limited bandwidth on the accuracy of the IBA [Elsley and Addison, 1980]

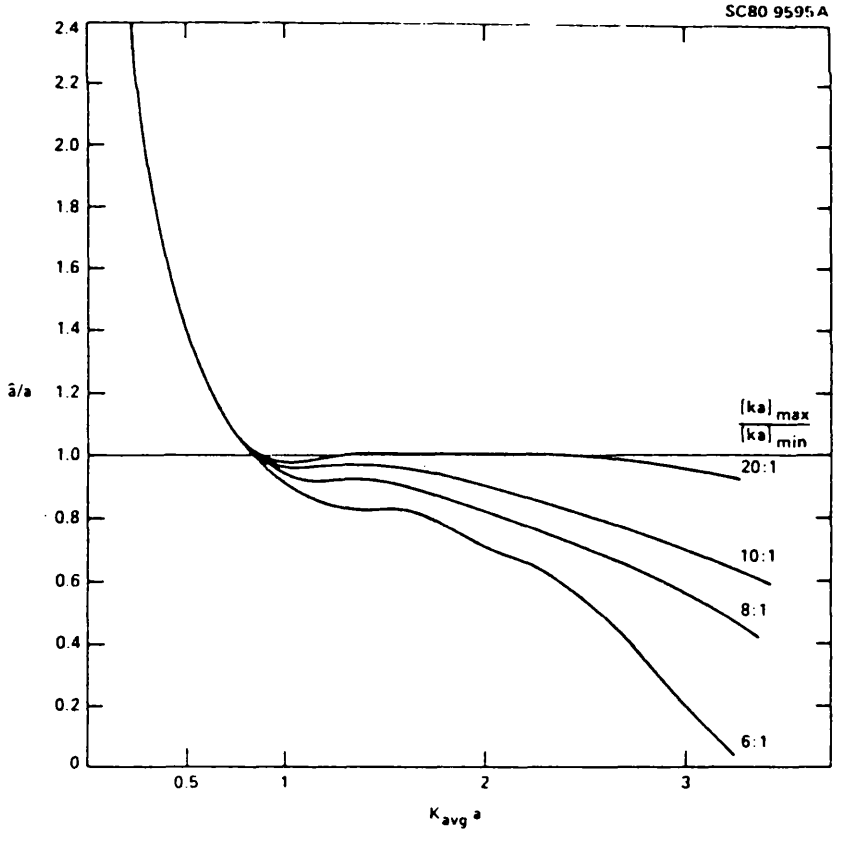

Figure 4.9a Accuracy of the IBA vs transducer centre frequency and bandwidth [Elsley and Addison, 1980]

Figure 4.10 compares the effects of imposing a Hanning and a rectangular window function to the scattering spectrum on the accuracy of the area function sizing technique. The solid lines are for the rectangular window, the dashed lines are for the Hanning window. Same as figure 4.8, the "o" curves show how the radius estimates are affected when the minimum *ka* value present in the data is raised from 0 to 1.8, while the maximum *ka* value is fixed at 6.5. The "*" curves show the effects of lowering the maximum *ka* value, while the minimum *ka* value is fixed at 0. The figure clearly reveals that using a Hanning window function does not improve the accuracy of the area function sizing technique, and using a rectangular window generates much better results. In the following study, a rectangular window function is used for the evaluation of the area functions.

4.6 Non-Spherical Voids

In this section, the area function sizing technique is applied to non-spherical voids. The case of centre-symmetric void is first considered, and then the more general case of non-centre-symmetric void is considered.

4.6.1 A spheroidal void

A 2:1 (252×126 μm) oblate void in titanium is taken as an example. The void is shown as figure 4.11.

The backscattering data were simulated using MOOT in Chapter 3, and shown as figure 3.11. The scattering data in the frequency range of 0 to 20 MHz ($0 \leq ka \leq 5.0$, where a is the longer semiaxis of the oblate void) were used to calculate the area functions. Figures 4.12a to 4.12c show the resulting area functions and the true cross-sectional areas for three incident directions of

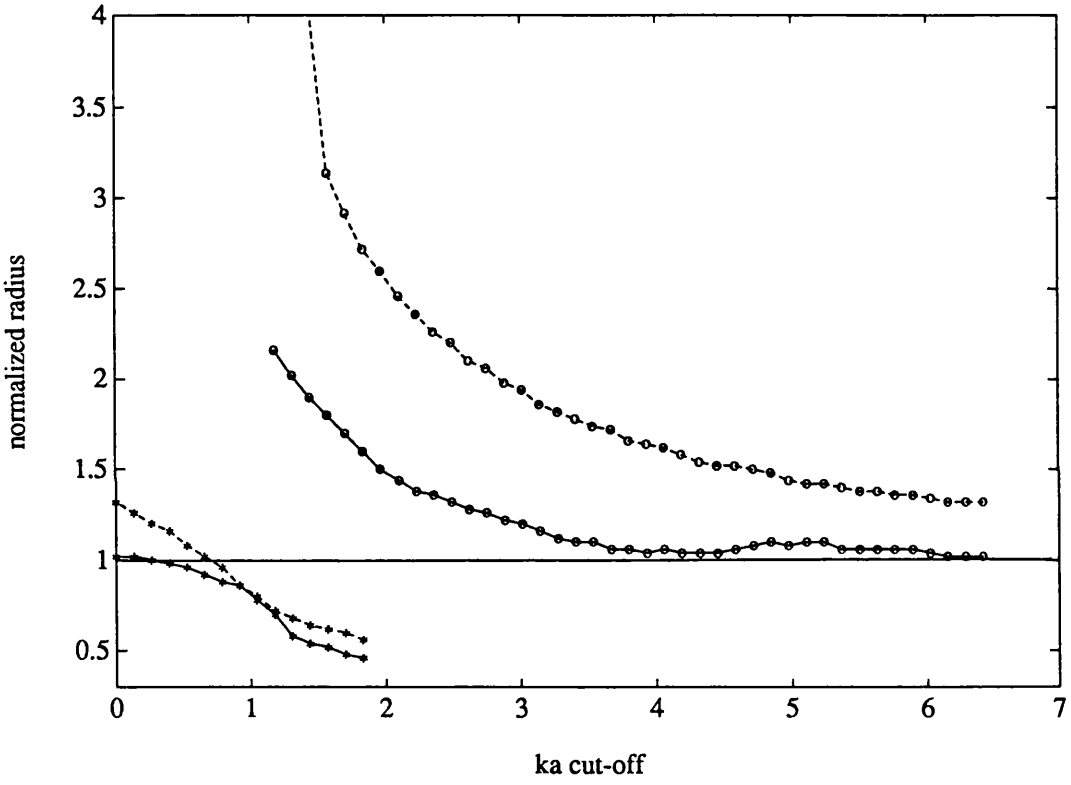

Figure 4.10 Effects of using Hanning window on the sizing accuracy

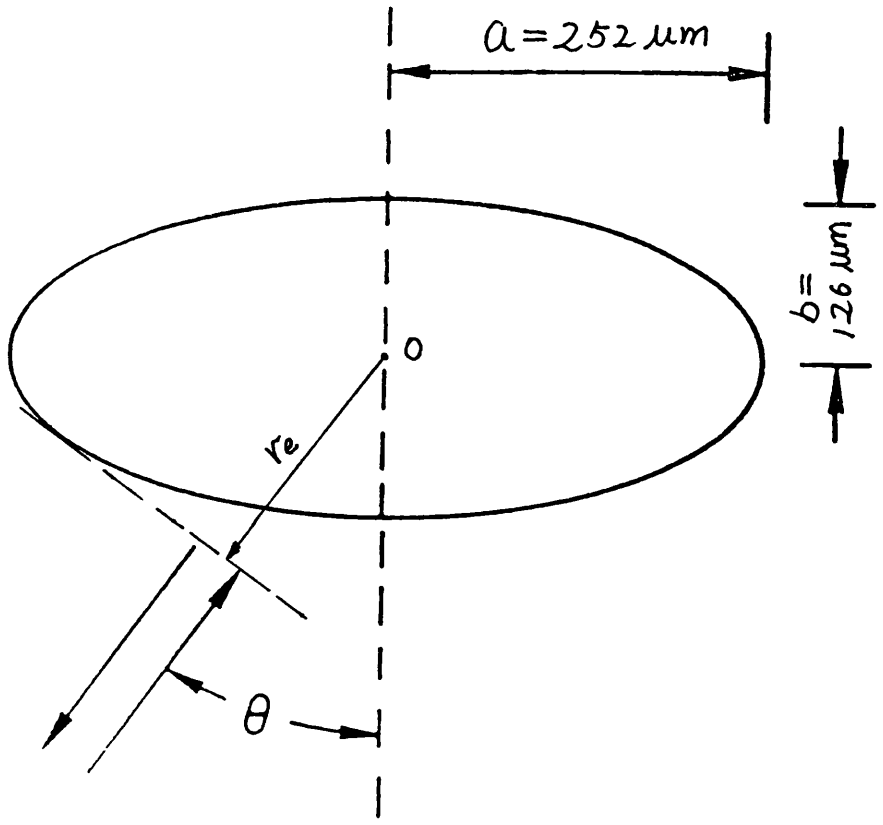

Figure 4.11 Backscattering geometry for the 2:1 oblate, where r_e is the tangent plane distance

(a)

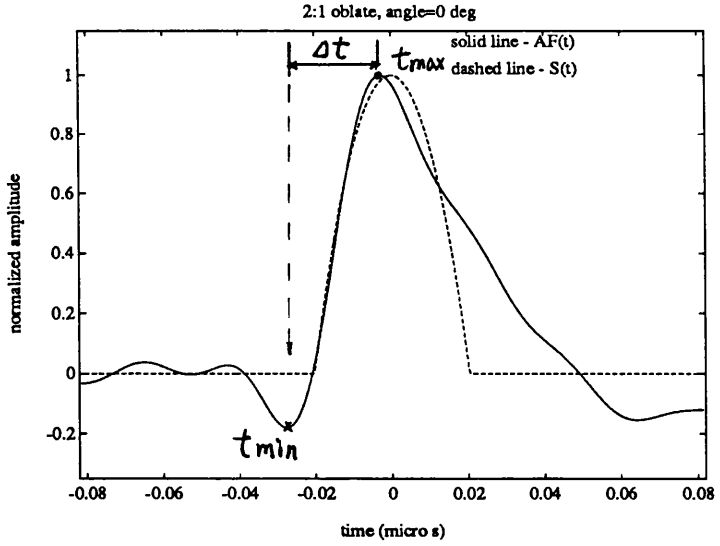

(b)

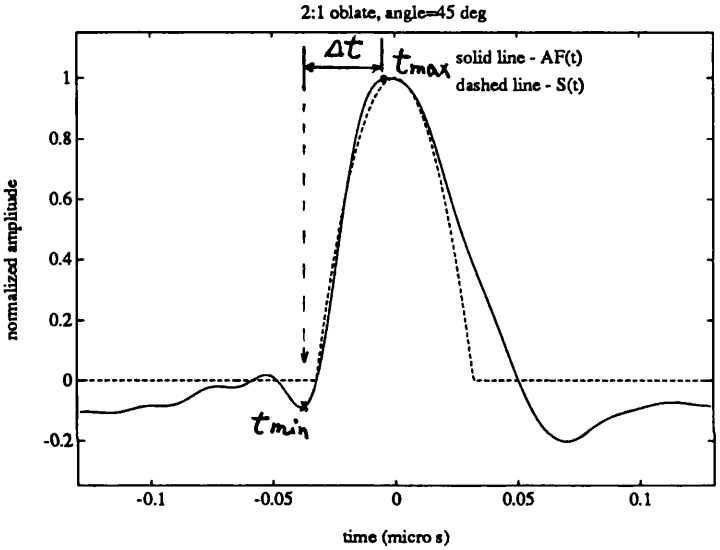

(c)

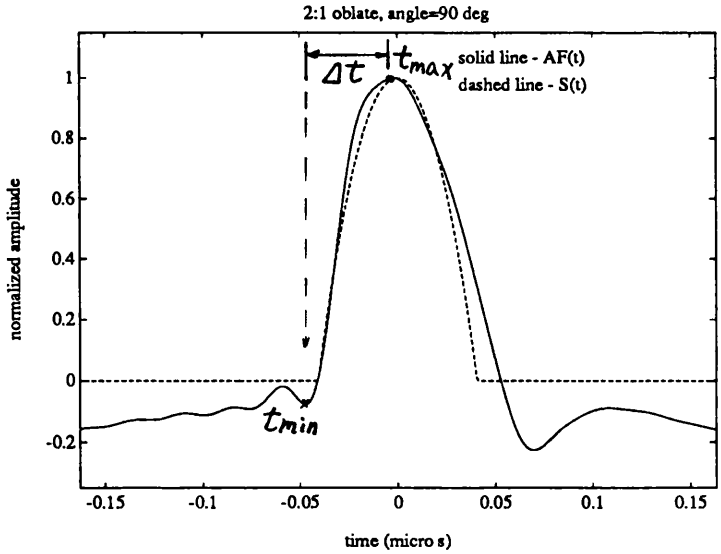

Figure 4.12 *AF(t)* and *S(t)* for the 2:1 oblate void at three directions: (a) θ_o=0; (b) θ_o=π/4; (c) θ_o=π/2.

θ_o=0, π/4 and π/2, where the angle θ_o is measured from the symmetry axis (see figure 4.11).

It is seen from figures 4.12 that as in the case of spherical void, the first part of *AF(t)* in each incident direction predicts *S(t)* very well. The time difference, Δt, between the times where *AF(t)* starts from minimum (t_{min}) and reaches maximum (t_{max}) may therefore be used to estimate the tangent plane distance in the incident direction in the same way that it extracts the radius of a spherical void, by the relation

$$r_e(\theta) = \frac{c\Delta t}{2} \tag{4-12}$$

The backscattering data (A_l) in the frequency range of 3 to 20 MHz ($0.74 \leq ka \leq 5.0$, which can be met by a good transducer in practice) were used to evaluate the area functions for several incident directions, to estimate the tangent plane distances using equation (4-12). The results are shown in Table 4.1 and figure 4.13. Because of the symmetry of the void, only the results in the range of $0 \leq \theta_o \leq \pi/2$ are shown in the table.

Table 4.1 and figure 4.13 show that all the estimated tangent plane distances, $r_e(\theta_o)$, are in good agreement with the true values of $r_e(\theta_o)$. The largest error is less than +18% of the true value. For all the directions, the same frequency range was used, so the relative bandwidth $kr_e(\theta_o)$ was different for each direction, changing from $0.37 \leq kr_e(\theta_o) \leq 2.5$ at θ_o=0 to $0.74 \leq kr_e(\theta_o) \leq 5$ at θ_o=π/2. This is believed to be the reason why the error for each direction is so different.

If the tangent plane distances are estimated for a number of directions, the boundary of the void can be reconstructed using a nonlinear least-squares

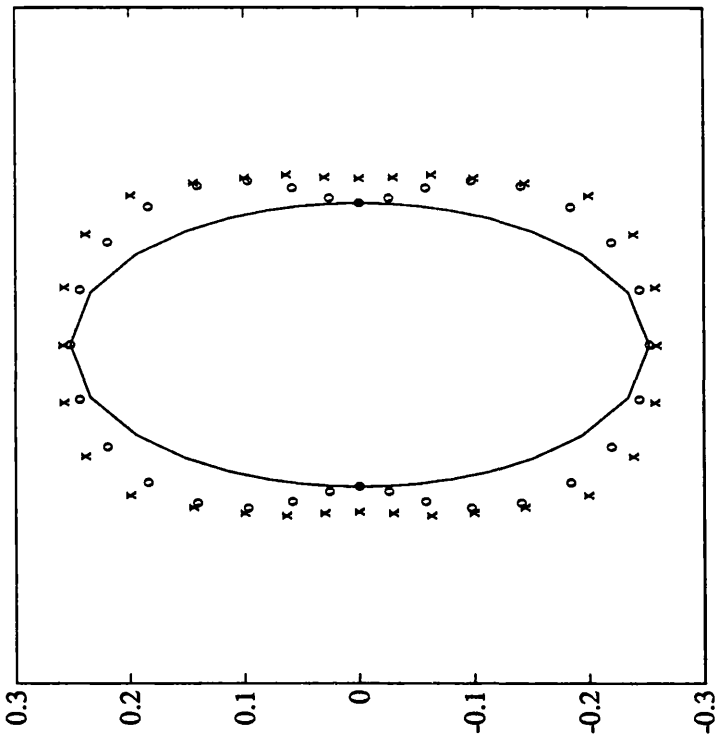

Figure 4.13 Reconstructed r_e for the 2:1 oblate void, where the solid line represents the boundary of the void; "o" is the true r_e, and "x" is the estimated r_e.

Table 4.1 Ture and estimated tangent plane distance for the 2:1 oblate void

θ_o	true r_e (μm)	kr_e	estimated r_e (μm)	error (%)
0	126	0.37~2.50	148	17.5
π/16	133	0.39~2.64	152	14.3
π/8	151	0.44~3.00	164	8.6
3π/16	175	0.51~3.47	179	2.3
π/4	199	0.58~3.95	204	2.5
5π/16	221	0.65~4.38	240	8.6
3π/8	238	0.70~4.72	258	8.4
7π/16	248	0.73~4.92	262	5.6
π/2	252	0.74~5.00	258	2.4

fitting procedure [Schmerr *et al*, 1989; Hsu *et al*, 1984]. However, it is not the interest of this study.

4.6.2 An ovate void

This is a case of non-centre-symmetric void. The backscattering amplitudes for an ovate void in titanium have been studied in Chapter 3, and they are used in this section to study the area functions for the void. Figure 3.13 (also shown in the next page as figure 4.14) depicts the shape and dimensions of the void, and the backscattering amplitudes for several incident directions can be found in figures 3.14 to 3.16.

These backscattering data in the frequency range of 0 to 20 MHz ($0 \leq ka \leq 4.5$) were used to evaluate the area functions. Figures 4.15a to 4.15e show the calculated area functions and the true cross-sectional areas for five directions: θ_o=0, $\pi/4$, $\pi/2$, $3\pi/4$ and π. As in the cases of spherical and spheroidal voids, the first part of each *AF(t)* agrees very well with that of the corresponding *S(t)*. The time difference (Δt) between t_{max} and t_{min} therefore can be regarded as an approximation to the time difference (ΔT) between the times at which the incident wave starts touching the void and when it passes through the position with the maximum cross-sectional area. Here, to assist the discussion, the term local radius is defined as the distance from the position where the flaw's cross sectional area has the maximum value to a plane (perpendicular to the propagation direction) tangent to the front surface of the flaw (see the void's geometry in figure 4.14). The local radius is represented as r_l. Thus, the local radius r_l can estimated by the value of $c\Delta t/2$.

Because of the complexity of the void's geometry, only three special directions (θ_o=0, $\pi/2$, π) are considered for flaw sizing. For θ_o=0, r_l=*b*; for θ_o=$\pi/2$, r_l=*a*; for θ_o=π, r_l=*d* (*b, a, d* are shown in figure 4.14). The backscattering data in a practical frequency range of 2 to 17 MHz ($0.45 \leq ka \leq 3.82$) were used to evaluate the area functions and to estimate the local radii for these three directions. The sizing results are listed in Table 4.2. It can be seen

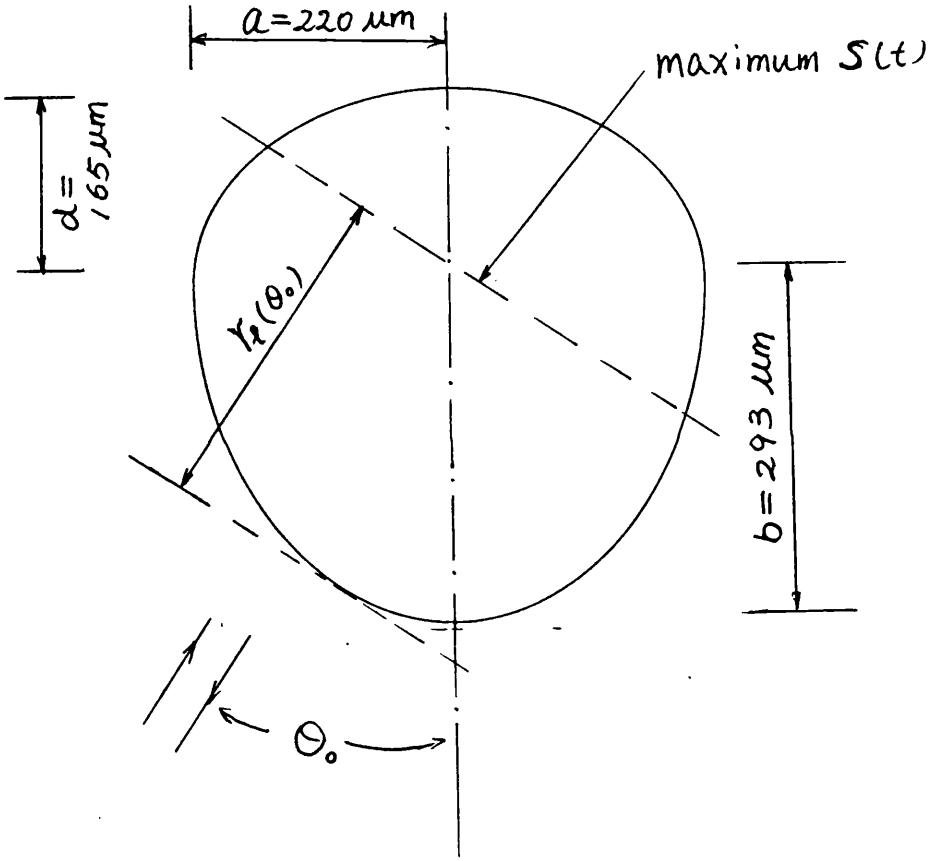

Figure 4.14 The geometry of the ovate void, r_l is the local radius

(a)

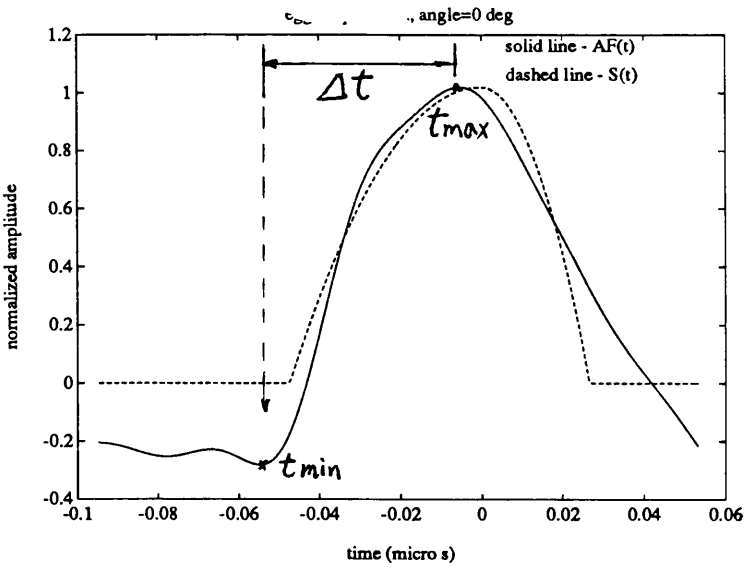

(b)

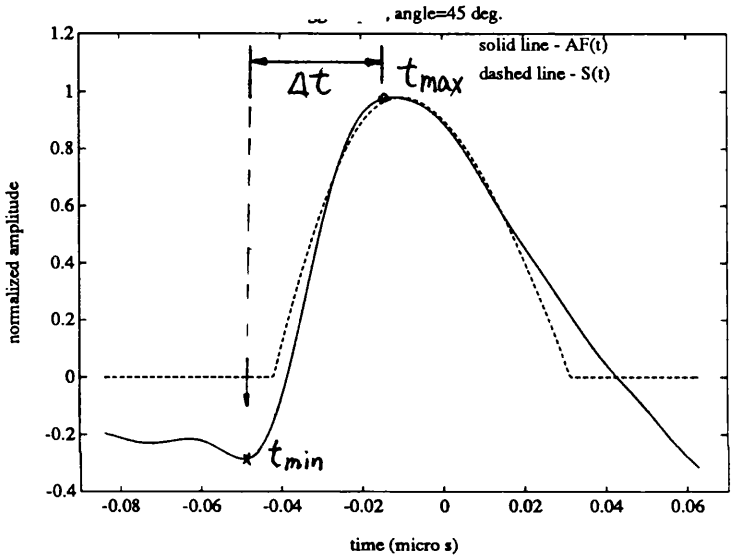

(c)

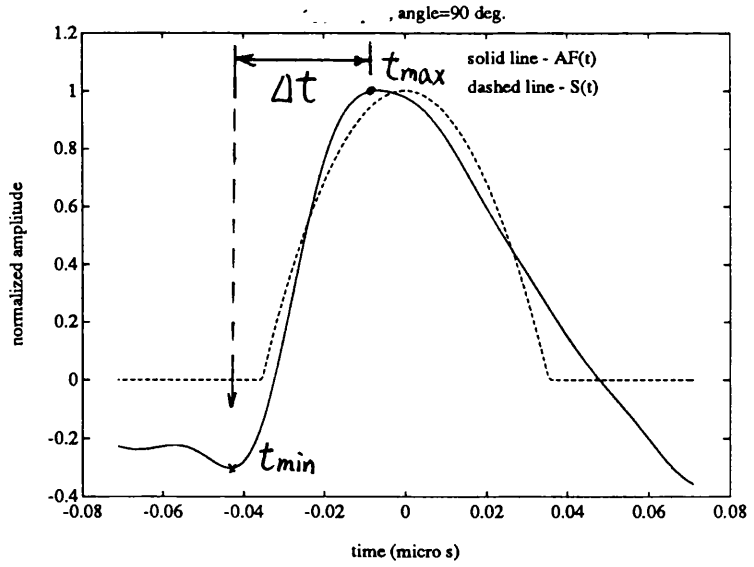

Figure 4.15 *AF(t)* and *S(t)* for the ovate void at five directions: (a) θ_o=0; (b) θ_o=π/4; (c) θ_o=π/2;

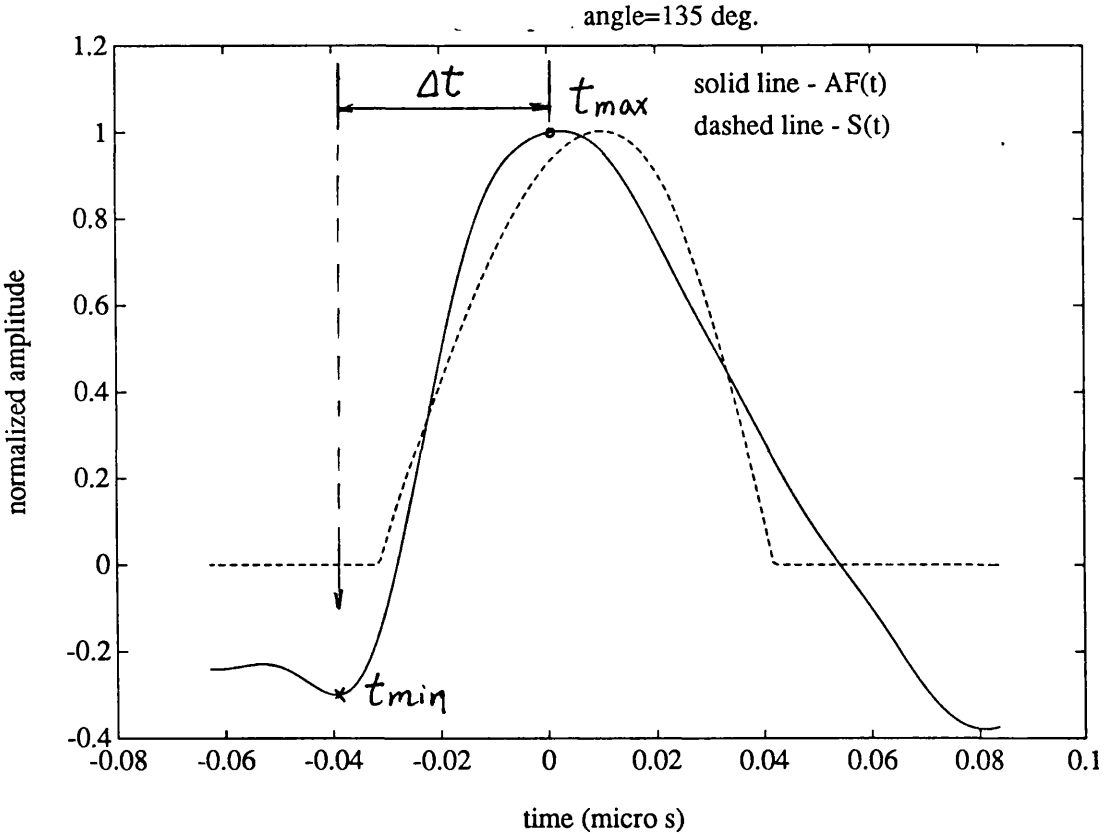

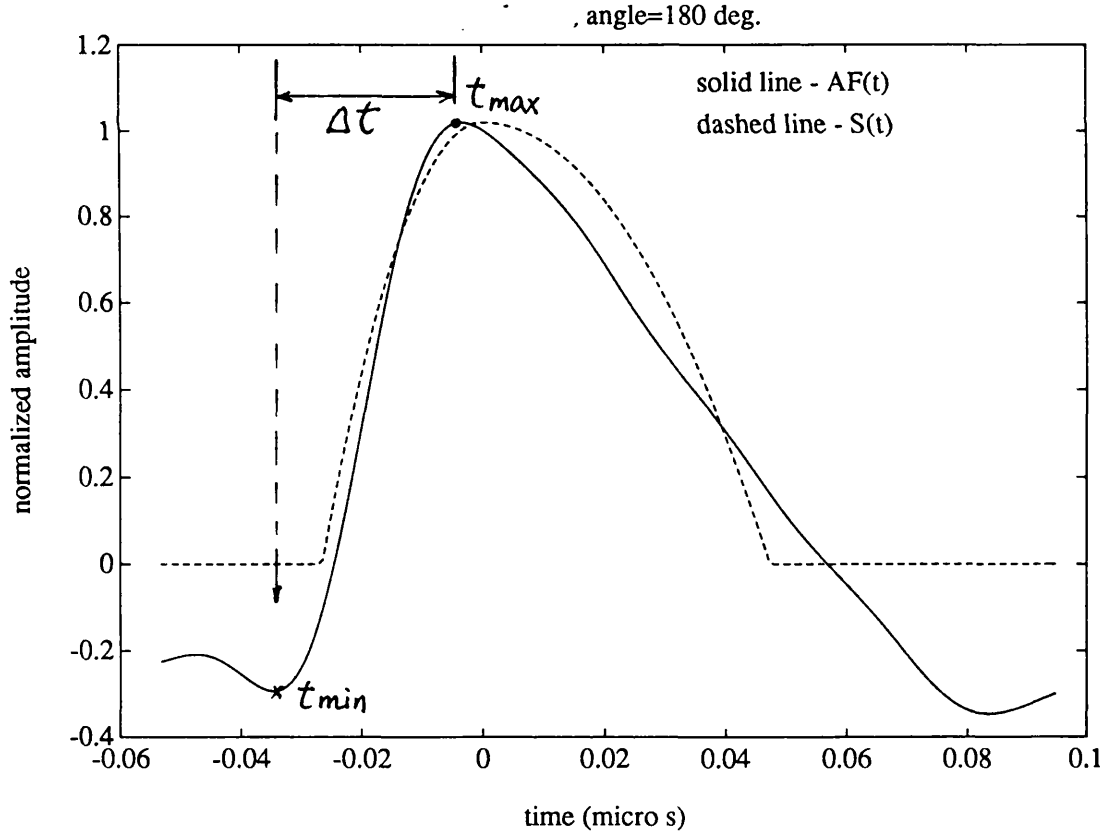

Figure 4.15 (Continued) (d) $\theta_o=3\pi/4$; (e) $\theta_o=\pi$

that $c\Delta t/2$ estimates the local radius very well. All the errors are within 16%. The same frequency range was used for all the incident directions, while the dimension of the void is different for each direction. As a result, the relative bandwidth *ka*, *kb* and *kd* were in different range. This may be a reason why the errors for these three directions are so different.

Table 4.2 The true and estimated local radii for the ovate void

θ	true local radius r_l (μm)	kr_l range	estimated local radius (μm)	error (%)
0	293	$0.60 \le kb \le 5.09$	308	5.5
π/2	220	$0.45 \le ka \le 3.82$	216	-2.7
π	165	$0.34 \le kd \le 2.86$	193	15.8

4.6.3 Two overlapping spherical voids

This is another example of more complicated non-centre-symmetric voids. The shape and dimensions of the void have been illustrated in Chapter 3 and shown as figure 3.17 (also shown here in the next page as figure 4.16). The backscattering results were discussed in Chapter 3. The simulated scattering data in frequency range of 0 to 29.6 MHz ($0 \leq ka \leq 6$, where a represents the radius of the larger sphere) were used to calculate the area functions of the void. Figures 4.17 show the area functions and the true cross-sectional areas for two incident directions of $\theta_o=0$ and π. As the cases discussed before, in each direction the agreement between the first part of $AF(t)$ and that of $S(t)$ is observed to be good. The result at direction of $\theta_o=\pi$ deserves more attention, where the area function has also clearly reconstructed the small sphere. This means that the area function has potential to reconstruct the fine details of the flaw shapes.

At direction of $\theta_o=0$ or $\pi/2$, the local radius is just the radius of the larger sphere. As discussed in the last case, Δt (between t_{max} and t_{min}) measured from the area function can be used to estimate the local radius and therefore the radius of the larger sphere, by the relation $r_l=c\Delta t/2$. At $\theta_o=\pi$, the local radius is the addition of the radii of the two spheres (represented as a^+), so the value of $c\Delta t/2$ can be used to estimate a^+. In any other direction, the geometry becomes very complicated, and sizing is not performed here.

The frequency range of the input scattering data for the evaluation of the area functions was limited in a practical frequency range of 2 to 17 MHz ($0.41 \leq ka \leq 3.41$) to size the void for the incident directions of $\theta_o=0$, $\pi/2$, and π. The sizing results are listed in Table 4.3. The difference between the estimated and the true values are all less than 6%.

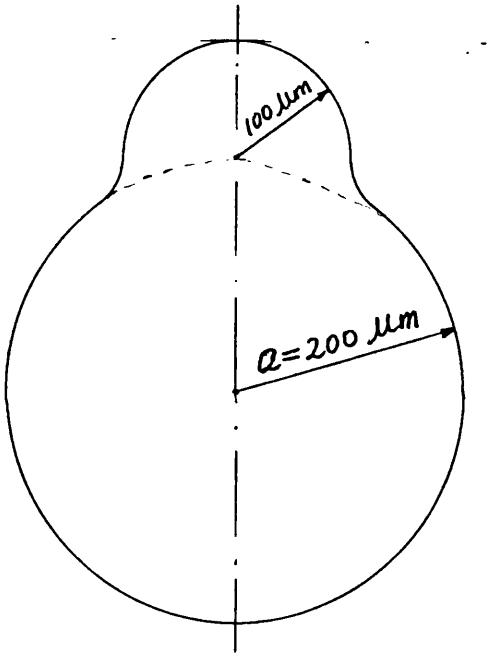

Figure 4.16 The geometry of the two overlapping voids

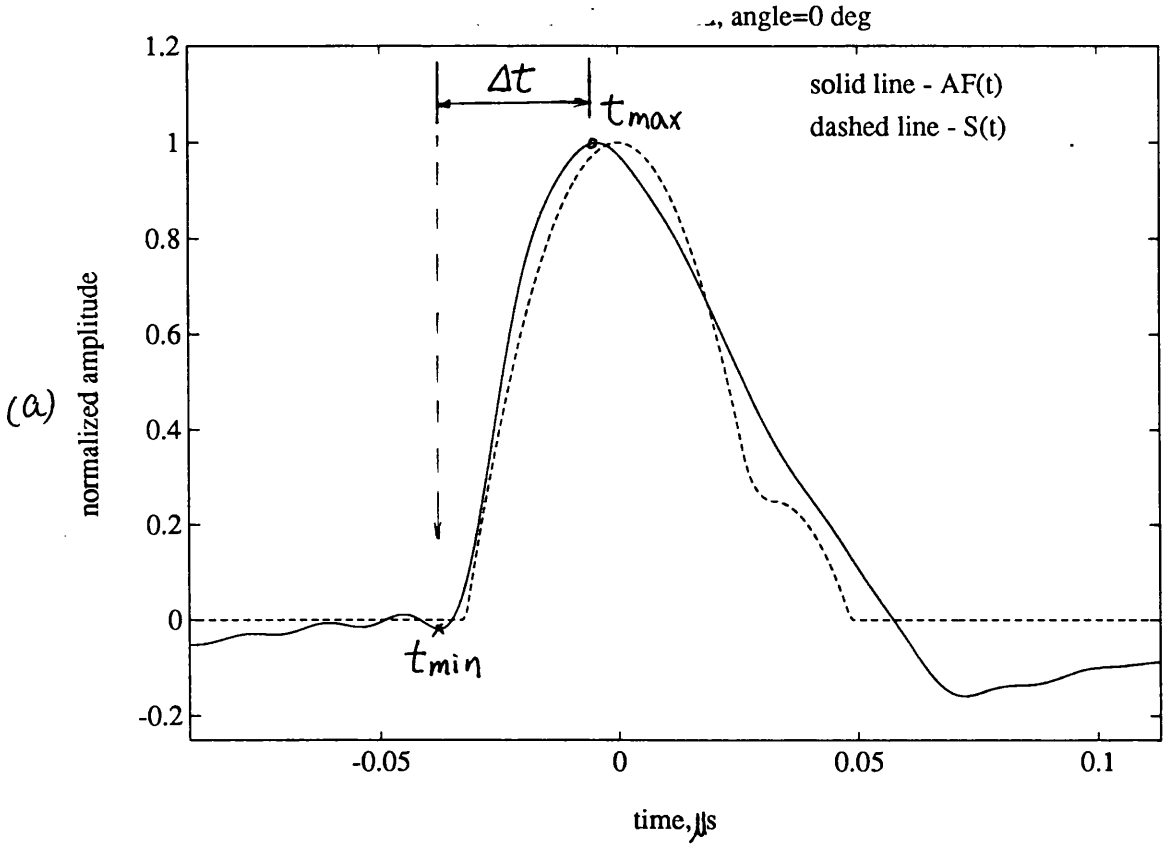

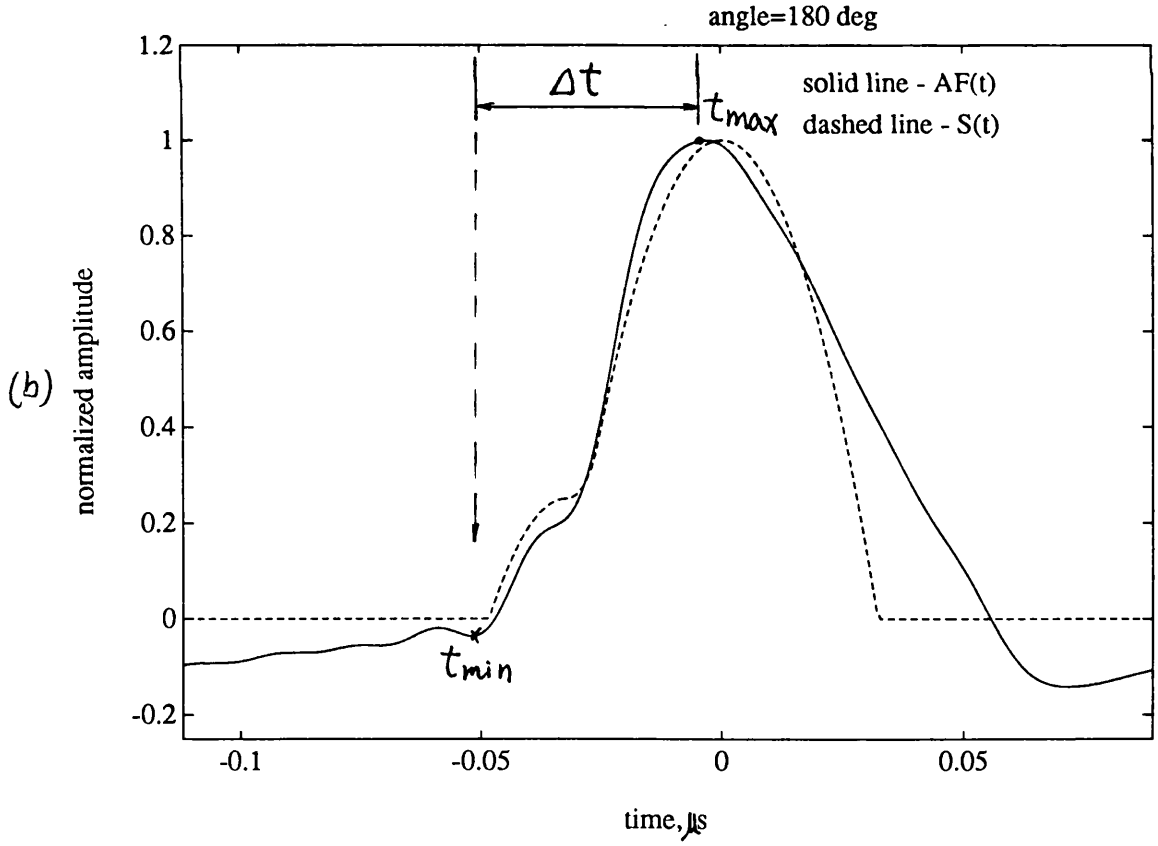

Figure 4.17 *AF(t)* and *S(t)* for the two overlapping voids in the directions: (a) θ_o=0; (b)θ_o=π

Table 4.3 The true and the estimated local radii for the overlapping voids at three directions

θ	true local radius (μm)	kr_l range	estimated local radius (μm)	error (%)
0	200	$0.41 \le ka \le 3.41$	205.5	2.8
$\pi/2$	200	$0.41 \le ka \le 3.41$	208.5	4.3
π	300	$0.62 \le ka^{+} \le 5.12$	315.8	5.3

4.7 Discussions and Conclusions

It has been shown numerically that the area function formula based on the Born approximation provides a simple inversion technique which can be used to determine the size and shape of voids in structural materials. For spherical voids, the radii (a) can be estimated; for non-spherical voids, the tangent plane distances (r_e) (for centre-symmetric voids) or the local radii (r_l) (for non-centre-symmetric voids) can be estimated. The technique has certain bandwidth/flaw size match requirements, however, a good transducer can cover a useful range of flaw sizes. All the sizing results in this chapter were obtained by processing the simulated scattering data in some practical frequency ranges which can be met by commercial transducers.

There are some similarities between this sizing scheme and the IBA. First of all, they share the same theoretical basis - the Born approximation. Secondly, the bandwidth requirements follow the same trends - insufficient low frequency data causes underestimate of the flaw size and lack of high frequency data leads to overestimate of the flaw size.

However, the area function sizing technique has two distinguished advantages over the IBA:

(1) The area function sizing scheme does not require to determine the flaw centroid. The IBA has to be supplemented by another method to locate the flaw centroid and shift the time domain signal so that the time origin is at the flaw centroid (zero-of-time problem), before the algorithm can be implemented. This is one of the main objections to the use of the IBA for defect sizing. Even though there have been some advances in solving this problem [Chaloner and Bond, 1987; Bond *et al*, 1988; Addison *et al*, 1981], to date, determination of the flaw centroid in

ultrasonic reconstruction of flaws remains an unresolved fundamental problem [Koo *et al*, 1990]. In fact, the area function algorithm has been used by some scientists [Koo *et al*, 1990; Chaloner and Bond, 1987] as an interim algorithm in the IBA to locate the flaw centroid. Even if the zero-of-time problem were perfectly solved, implementing the IBA would require more signal processing work than implementing the area function technique.

(2) The bandwidth requirements for the area function sizing technique are less severe than those of the IBA. In order to give radius estimates accurate to within 20%, the area function sizing scheme requires a bandwidth of $1 \leq ka \leq 3$, while the IBA requires a bandwidth of $0.5 \leq ka \leq 2.5$.

Cohen-Tenoudji and Tittmann [1982] formulated an inversion algorithm based on the Kirchhoff approximation, which gives anoutput function $A(t)$. The algorithm is very similar to the area function algorithm in the frequency domain. However, they sized the flaws in a different way. In their study, the radius of the sphere and the semi-axis of the ellipsoid were obtained by using the time difference between the value where the function $A(t)$ crosses zero and t=0. There are two problems in their method: (1) the position of the flaw centroid must be estimated (as the IBA), and therefore zero-of-time needs to be solved first; (2) the time t_0 where the function $A(t)$ crosses zero is used, while it has been shown in figure 4.7 that t_0 is much less stable than t_{min} with respect to the changing bandwidth.

The applicability of the area function sizing technique to strong scattering inclusions has not yet been studied. Given the conclusion by Gubernatis *et al* [1977b] that for elastic inclusions where the properties of defect and host differed by 20-40%, the Born approximation is very good for

all angles and even at short wavelengths, it is expected that this sizing technique will be able to be applied to some types of strong scattering inclusions.

Chapter 5
EXPERIMENTAL RESULT

5.1 Introduction

This Chapter describes the experimental implementation of the area function sizing scheme and the results obtained. Section 5.2 is a description of the experimental system. Section 5.3 describes the experimental procedures and the signal pre-processing techniques used to obtain the isolated flaw signal. Section 5.4 gives the experimental sizing results obtained with several simple flaws. Section 5.5 is the discussions of the experimental results.

5.2 Experimental System

The experiment system is shown schematically in figure 5.1. The experiments can be performed in either immersion or contact testing mode.

In immersion testing experiments, the transducers are scanned mechanically using a XYZ scanning frame fixed on a water tank. The stepping motor drives can move the slides (and therefore the transducers installed on them) by 2.5 μm increments.

The pulse-receiver used in the experiments is a Panametrics 5052PR, which excites the transducers by a sharp voltage spike of about -200 to -380 volts. The resistive load presented to the transducer by the pulse-receiver can be altered between 50 to 250 ohms for optimum matching. Data acquisition is performed using a GOULD Biomation model 4500 digital oscilloscope at a sampling rate of 100 MHz with 8 bit resolution [Saffari, 1986]. The sampled time domain signal is then transferred to an IBM-PC via an IEEE 488 data bus for processing. The PC is also linked to UCL (University College London)

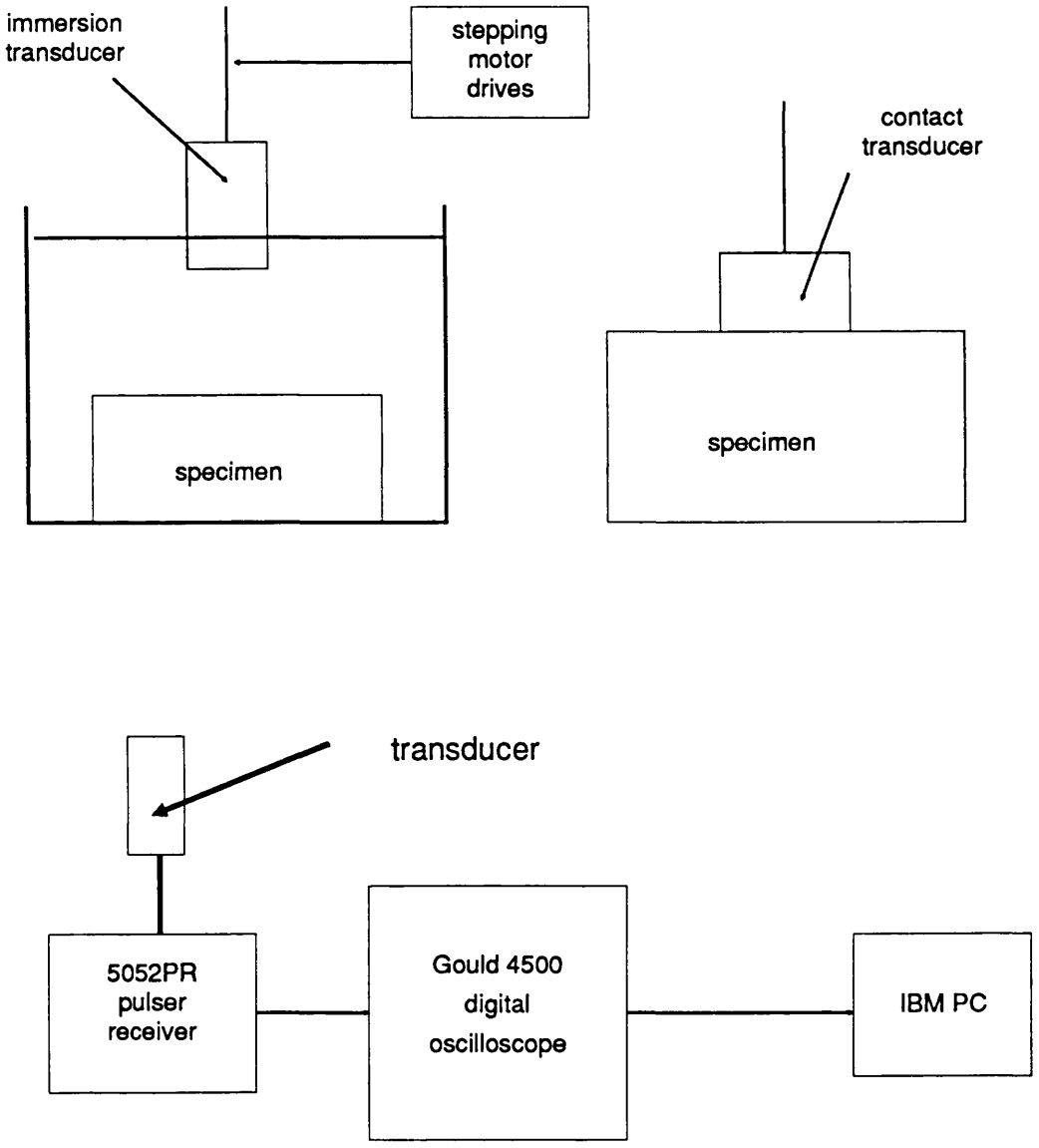

Figure 5.1 Schematic diagram of the experiment set up

Data Exchange, through which the computing facilities of ULCC (University of London Computer Centre) and Bloomsbury Computer Consortium can be accessed.

The transducers used are various commercial broadband piezoelectric transducers, with different frequency characteristics. These transducers are listed in Table 5.1.

Table 5.1 Transducers used in the experiments

Transducer	Centre frequency	Mode	Element diameter	Near field or focal length
Ultran XL 50-5-P3	5 MHz	immersion (focused)	12 mm	77 mm in water (focal length)
Krautkrämer 5KB 53051	5 MHz	contact	10 mm	19.2 mm in steel
Harisonic CRO208	2.25 MHz	contract	10 mm	9 mm in aluminium

The characteristics of a transducer are very complicated. Some of its basic properties can be understood by modelling the transducer as a simple piston source which sits on an ideal baffled surface [Krautkrämer and Krautkrämer, 1983]. The radiation pattern produced by any ultrasonic transducer is composed of two zones, knows as (1) the Fraunhofer Zone or "far-field", and (2) the Fresnel Zone or "Near-field". Figure 5.2 (after Krautkrämer and Krautkrämer [1983]) shows the theoretical axial pressure variations with distance for a normal flat transducer.

All contact and immersion flat transducers have a natural "focus". The

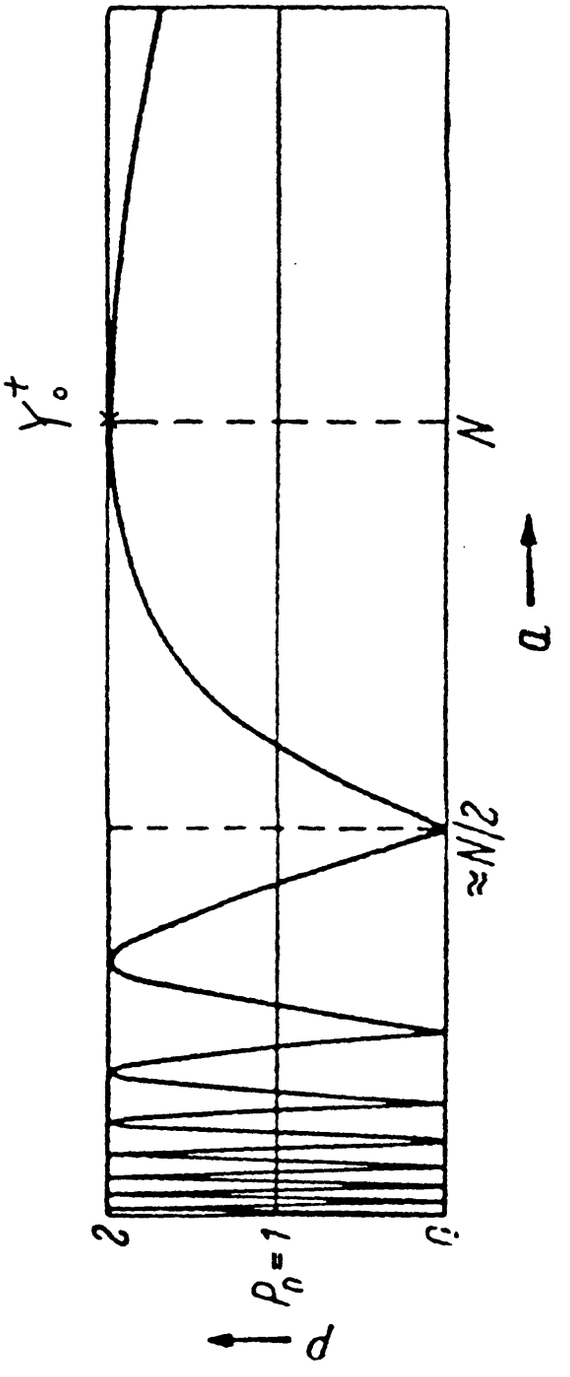

Figure 5.2 Axial pressure variation with distance for a normal transducer [Krautkrämer and Krautkrämer, 1983]

pressure peak in an axial beam profile at the point of the natural focus is given the symbol Y_o^+ in figure 5.2. The natural focus corresponds to the transition from the near field to the far-field. This transition distance is the near-field length which is represented by *N*. The most commonly used approximate expression for calculation of the near-field length is [Krautkrämer and Krautkrämer, 1983]

$$N \approx \frac{1}{4}\frac{D^2}{\lambda} \tag{5-1}$$

where *D* is the element diameter of the transducer, and λ is the wavelength in the material transmitting the sound. All the experiments reported in this thesis were conducted in the far fields of the transducers.

Focused immersion transducers employ acoustic lenses to manipulate the pattern of the sound beam. Through the use of acoustic lenses, it is possible to shift the position of Y_o^+ towards the transducer. The Y_o^+ point then becomes the focus of the transducer. Focused transducers are usually used in the experiments to improve the sensitivity and signal-to-noise ratio when the flaw is very small or the scattering is very weak. The first transducer in Table 5.1 is a point focused transducer.

The samples considered in the investigation are listed in Table 5.2. The properties of the materials are also listed in the table.

5.3 Experimental Procedures and Pre-Signal Processing

The procedures for experimental implementation of the area function sizing scheme are summarised in figure 5.3. The steps 1 to 5 are referred to as signal pre-processing; the steps 6 and 7 are the implementation of the area function sizing algorithm.

Table 5.2 Samples and material properties

Samples used in the experiments

	Material	Block dimensions (mm)	Defect type	Defect dimensions (mm)	Location
1	Buehlers "Transoptic"	Disk 30 dia 13 thick	Spherical polystyrene inclusion	0.8 dia	10 mm from block centre
2	Titanium	Rectangular 55X35X24	Bored cylinder	0.53 dia	1.5 mm from surface
3	Maraging steel	Rectangular 100X100X45	Spherical void	0.6 dia	Block centre
4	Aluminum	Rectangular 200X100X35	Bored cylinder	1.45 dia	7.5 mm from surface

Properties of the materials

Material	Longitudinal velocity (m/s)	Transverse velocity (m/s)	Density (g/cm^3)
Titanium	6200	3125	4.35
Buehler's "Transoptic"	2690	1340	1.18
Polystyrene	2350	1200	1.06
Maraging steel	5700	3120	8.0
Aluminium	6320	3130	2.7

The properties for Buehler's "transoptic", polystyrene and maraging steel were obtained from Chaloner [1988] where she used the same samples. The properties for titanium and aluminium were obtained from Krautkrämer and Krautkrämer [1983].

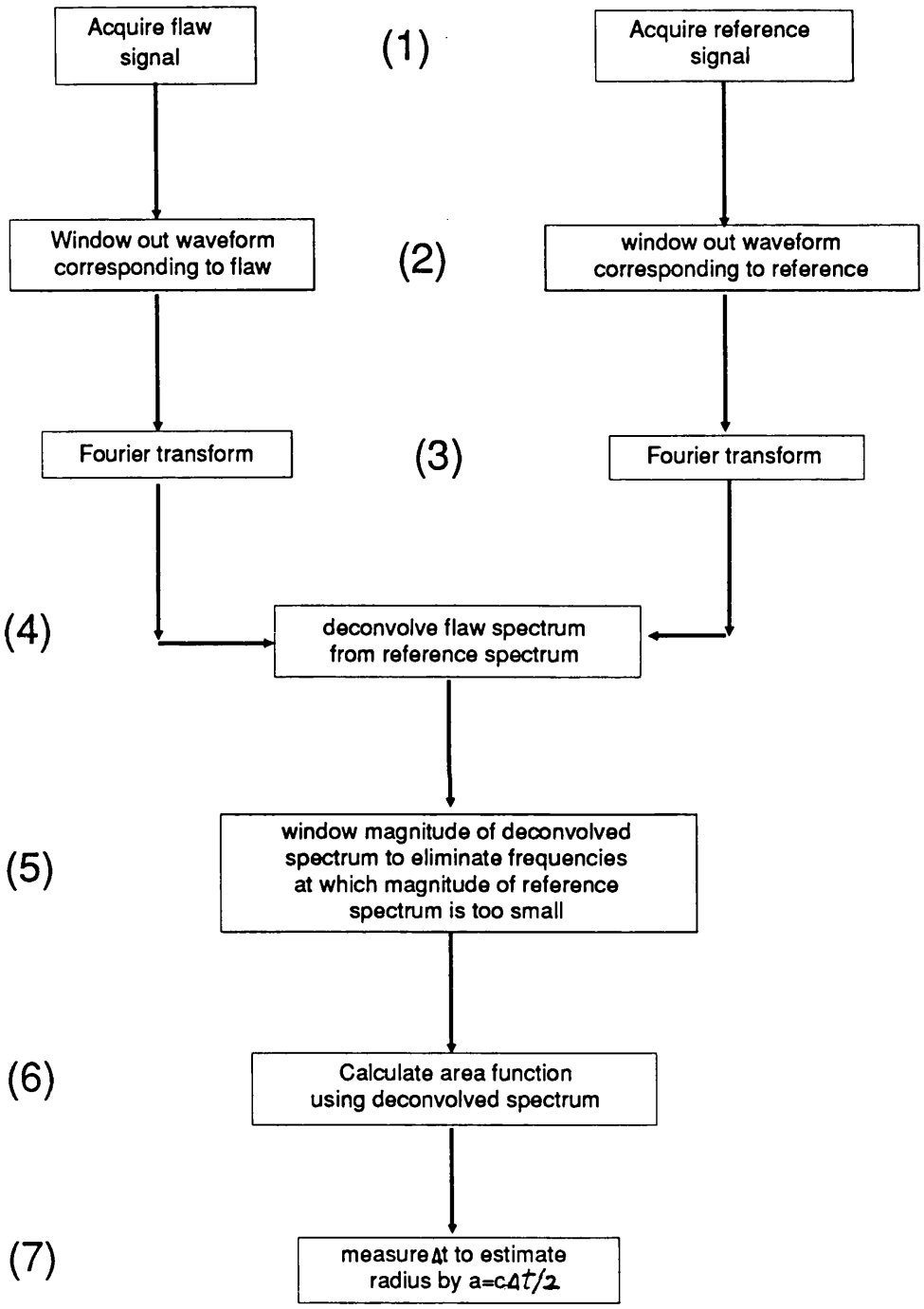

Figure 5.3 Procedures for measuring the flaw sizes using the area functions

The main objective of the signal pre-processing is to isolate the flaw signal. In ultrasonic measurements, a measured signal is always convolved with system and material effects that are not flaw related, such as pulser-receiver, oscilloscope circuit characteristics and material attenuation. To isolate the signal scattered from the flaw, these effects must be removed. The process of isolating the flaw response from the effects of the rest of the testing system is often referred to as deconvolution [Fitting and Alder, 1977].

Experimentally, the first problem is the detection of the flaw signal in the received waveform. This is usually done simply by noting points at which the signal rises significantly above the background level. Because the flaw is usually small, the return amplitude from the flaw is very sensitive to the probe/flaw alignment and it requires a degree of patience to optimise the signal.

It is desirable to obtain as high a signal-to-noise ratio as possible. The signal-to-noise ratio can be enhanced by either increasing the signal level or decreasing the noise level. The major noise sources in a flaw signal are either thermal noise generated in the electronic components, grain scattering noise in the material, or tail signals from the front face of the part under investigation [Addison *et al*, 1982].

To increase the signal level, one may simply increase the output of the transducer. However, this will not improve the signal to grain-scattering-noise ratio, since the amplitude of the grain scattering noise rises in proportion to the strength of the incident wave. Another way to increase the signal level is to use focused transducers. Focusing is an effective way of increasing the echo amplitude from small reflectors at the focus. In this study, a focused transducer has been used on two small scatterers.

Decreasing the noise level is another approach to improve the signal to

noise ratio. The thermal noise can be reduced by the time averaging of a large number of signals captured at different moments. The tail of a front surface echo noise can be reduced by subtraction of a measured signal from a flawless region of the same or a similar part [Addison *et al*, 1982]. However, these noise-reducing measures are not taken in this study in order to make the experiments as simple as possible. Another reason is that in practical applications, these measures may not be easily incorporated, or even after these measures being taken, the signals are usually not as good as the signals obtained in laboratory without these treatments. It is also one of the intentions to see how well this sizing scheme works with a low signal-to-noise ratio.

The choice and acquisition of the reference signal (in step 1) will be discussed in detail in the sub-section "deconvolution techniques".

In step 2, the portion of the acquired waveform containing the flaw signal or the reference signal is separated by multiplying the waveform by a window function whose length and position are selected by the operator. A shaped window such as a Hanning window is often a good choice in spectrum analysis. However, using such windows distorts the late-arriving creeping wave (which is an essential part of the scattering signal from a void), therefore a rectangular window function is used in this study.

The next step (Step 3) is to perform FFT to obtain the spectrum of the time domain signal. In order to increase the frequency domain resolution, before the FFT is performed, the signal is padded with zeros at the end to give a total of 1024 or 2048 points. FFT is performed using the signal processing software, MATLAB.

The deconvolution algorithm used in step 4 will be discussed in the subsection "deconvolution techniques".

In step 5, the deconvolved spectrum is examined to eliminate frequencies at which the magnitude of the reference spectrum is too small, usually around less than 10% - 20 % of the peak amplitude of the reference spectrum [Addison *et al*, 1982].

With the isolated raw flaw spectrum in a certain frequency range, the area function is evaluated using equation (4-8) in step 6.

Finally, in step 7, the time t_{max} and t_{min} are found from the resulting area function and the time difference Δt between t_{max} and t_{min} is measured and used to estimate the radius by the relation $a=c\Delta t/2$ (equation (4-10)).

Deconvolution techniques

Before a proper deconvolution procedure can be established, the experimental system must be analyzed. A generalized ultrasonic spectroscopic system is depicted as figure 5.4 which is from Fitting and Adler [1977]. An electrical waveform generated by the transmitter is applied to the transmitting transducer to producer an acoustic pulse. Since it is very difficult in conventional NDT to transfer energy from an ultrasonic probe into a specimen via an air gap, some form of coupling material should be provided. For contact testing, this can be done by smearing a layer of coupling gel onto the specimen surface. For immersion testing, the whole inspection can be carried out in a water bath, where the water serves as the coupling material. Other liquids also can be used as coupling materials. As the acoustic wave propagates through the material being studied, interactions of the acoustic energy with the material alter the amplitude, phase and direction of the wave. A receiving transducer then captures the acoustic energy and converts the mechanical signal to an electrical signal. An amplifier is usually needed to increase its amplitude. The signal is then recorded and processed in an analysis system, which is usually

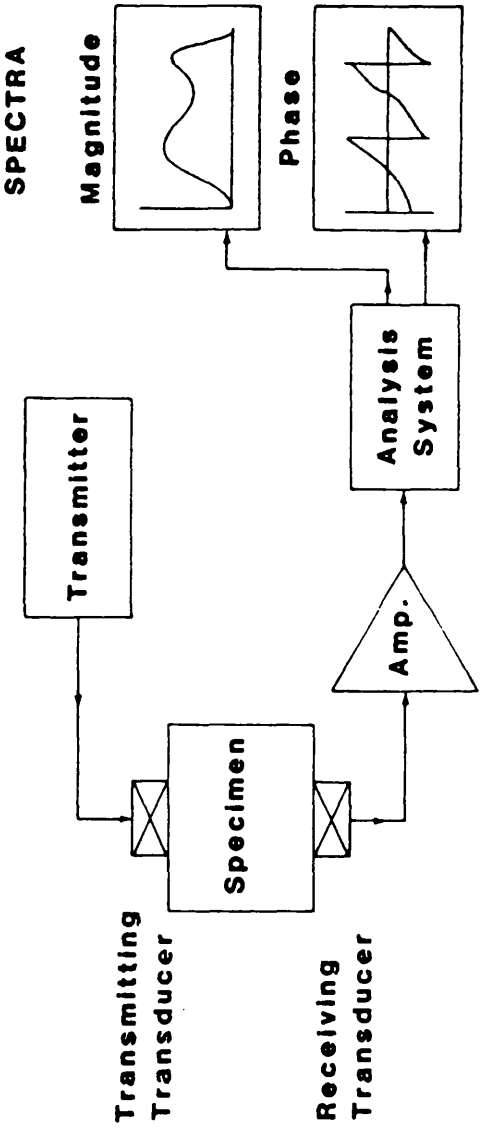

Figure 5.4 A generalized ultrasonic spectroscopy system (after Fitting and Adler[*] [1977])

done using a computer nowadays.

In the ultrasonic system analysis, each component of the system depicted in figure 5.4 can be reasonably assumed as a linear time-invariant (LTI) system [Frederick and Seydel, 1973]. Although such an assumption may not be always appropriate, generally it reflects reality and does provide a good basis for assessing the performance of system components [Fitting and Adler, 1977].

The behaviour of a LTI system can be completely described by its impulse time response or its equivalent frequency response. These two responses are a Fourier transform pair. Figure 5.5 displays a block diagram of the ultrasonic testing system with references to Fitting and Alder [1977] and Koo [1987]. The time domain response and the frequency domain response are shown with symbols at the left and right sides of the figure respectively. Among them, $\alpha(\omega)$ is the attenuation coefficient which is dependent on the frequency (the attenuation is caused mainly by absorption and dispersion); d_1 represents the distance of the acoustic path between the transmitting transducer and the flaw, and d_2 is the distance of the acoustic path between the flaw and the receiving transducer.

Hence, from figure 5.5, if the noise is neglected, the output time domain response is

$$v_o(t) = r(t) * x_2(t) * c_2(t) * m_2(t) * f(t) * m_1(t) * c_1(t) * x_1(t) * p(t) * v_i(t) \qquad (5\text{-}2)$$

The corresponding output frequency response is

$$V_o(\omega) = R(\omega) X_2(\omega) C_2(\omega) e^{-\alpha(\omega) d_2} F(\omega) e^{-\alpha(\omega) d_1} C_1(\omega) X_1(\omega) P(\omega) V_i(\omega) \qquad (5\text{-}3)$$

In this study, only the backscattering direction (pulse-echo) is considered, where a single transducer is used to transmit and receive acoustic

Impulse Time Response		Impulse Frequency Response
$v_i(t)$	Input voltage	$V_i(\omega)$
$p(t)$	Pulser	$P(\omega)$
$x_1(t)$	Transmitting transducer	$X_1(\omega)$
$c_1(t)$	Mechanical Coupling	$C_1(\omega)$
$m_1(t)$	Material attenuation	$exp(-\alpha(\omega)d_1)$
$f(t)$	Flaw	$F(\omega)$
$m_2(t)$	Material attenuation	$exp(-\alpha(\omega)d_2)$
$c_2(t)$	Mechanical coupling	$C_2(\omega)$
$x_2(t)$	Receiving transducer	$X_2(\omega)$
$r(t)$	Receiver	$R(\omega)$
$v_o(t)$	Output Voltage	$V_o(\omega)$

Figure 5.5 Elements of an ultrasonic testing system model as a linear, time-invariant system

waves, in which case

$$\begin{aligned} C_1(\omega) &= C_2(\omega) = C(\omega) \\ X_1(\omega) &= X_2(\omega) = X(\omega) \\ d_1 &= d_2 = d_0 \end{aligned} \tag{5-4}$$

Thus, according equation (5-3), the backscattering output frequency response is

$$V_o(\omega) = R(\omega)X^2(\omega)C^2(\omega)e^{-2\alpha(\omega)d_0}P(\omega)V_i(\omega)F(\omega) \tag{5-5}$$

In principle, all the responses plus the input and output voltages can be measured and therefore the backscattering flaw response can be obtained by direct deconvolution

$$F(\omega) = \frac{V_o(\omega)}{R(\omega)X^2(\omega)C^2(\omega)e^{-2\alpha(\omega)d_0}P(\omega)V_i(\omega)} \tag{5-6}$$

However, it is impractical. In practice, a reference signal representing the spectrum of the complete interrogating system is sought. This can be done by obtaining an reflection from the back surface of a flawless specimen as a reference signal [Addison *et al*, 1982; Chaloner and Bond, 1987]. This specimen should be made of the same material as the flawed specimen, and its back surface should be made at the same distance from the front surface as the flaw. Here is an analysis to explain why this signal can be used as a reference signal. Figure 5.6 shows the flawed specimen and the flawless reference specimen. Replacing the term $F(\omega)$ in equation (5-5) with the term $R_{back}(\omega)$, the reflection function for the back surface, one can obtain the frequency response of the signal reflected from the back surface of the flawless specimen

$$V_{back}(\omega) = R(\omega)X^2(\omega)C^2(\omega)e^{-2\alpha(\omega)d_0}P(\omega)V_i(\omega)R_{back}(\omega) \tag{5-7}$$

It is well known that for a flat surface, $R_{back}(\omega)$ is a frequency-independent coefficient constant which depends on the properties of the specimen material and the material loading the surface. When the wave coming from an

(a) a flawed sample

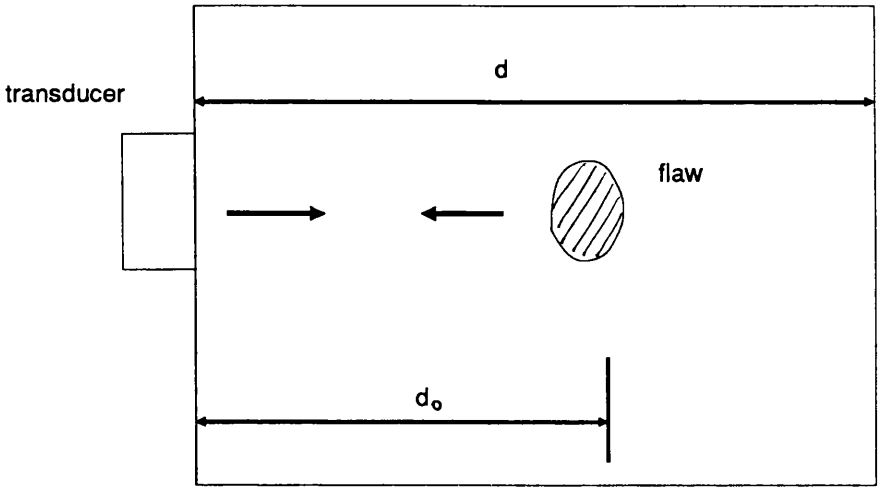

(b) a flawless reference sample

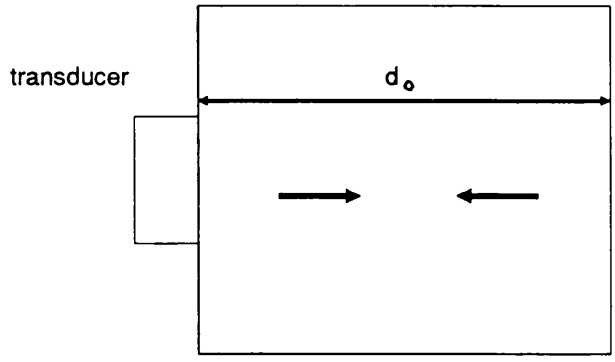

Figure 5.6 Acquiring a reference signal

acoustically harder material (e.g. titanium) strikes an acoustically softer material (e.g. water or air), $R_{back}(\omega)$ is a negative constant [Krautkrämer and Krautkrämer, 1983]

$$R_{back}(\omega) = -|E| \tag{5-8}$$

where the negative sign indicates the reversal of the phase relative to the incident wave, and $|E|$ is a constant.

Comparing equation (5-7) with equation (5-5), one can obtain the flaw response through the following deconvolution algorithm using a back surface reflection as the reference signal

$$F(\omega) = \frac{V_o(\omega)}{V_{back}(\omega)}\left(-|E_{back}|\right) = \frac{V_o(\omega)}{-V_{back}(\omega)}|E| \tag{5-9}$$

In this study, only relative scattering amplitude information is needed, so the frequency-independent constant factor $|E|$ can be discarded without affecting the relative scattering amplitude. The deconvolution process can therefore be rewritten as

$$F(\omega) = \frac{V_o(\omega)}{V_{ref}(\omega)} \tag{5-10}$$

Where $V_{ref}(\omega)$ represents the reference spectrum, and is taken as

$$V_{ref}(\omega) = -V_{back}(\omega) \tag{5-11}$$

Bear in mind that the flaw scattering amplitude obtained from equation (5-10) has only relative meaning with an unknown normalization factor.

To simplify the problem further, we do not use another flawless specimen, instead, the reference signal is obtained from the back surface of the

flawed specimen itself (see figure 5.6). In this case, the spectrum of the back-surface reflection is

$$V_{back}(\omega) = R(\omega)X^2(\omega)C^2(\omega)e^{-2\alpha(\omega)d}P(\omega)V_i(\omega)(-|E|) \qquad (5\text{-}12)$$

where d is the distance from the front surface to the back surface of the flawed specimen. If the reference spectrum is still taken as equation (5-11), the corresponding deconvolution procedure should therefore be corrected by the factor $exp(-2\alpha(\omega)(d-d_0))$ (compare equations (5-12) and (5-7)):

$$F(\omega) = \frac{V_o(\omega)}{V_{ref}(\omega)} e^{-2\alpha(\omega)(d-d_0)} \qquad (5\text{-}13)$$

The value of $exp(-2\alpha(\omega)(d-d_0))$ is dependent on the frequency. However, as $(d-d_0)$ is usually small, the factor $exp(-2\alpha(\omega)(d-d_0))$ is ignored in this study, and the deconvolution procedure is still expressed as equation (5-10).

In immersion testing mode, the reflection from the front surface of a specimen also contains all the characteristics of the testing system and can be used as a reference signal. In this case, since the wave coming from an acoustically softer material strikes an acoustically harder material, the incident and reflected waves are in phase. So

$$V_{ref}(\omega) = V_{front}(\omega) \qquad (5\text{-}14)$$

and the corresponding deconvolution procedure is

$$F(\omega) = \frac{V_o(\omega)}{V_{ref}(\omega)} e^{2\alpha(\omega)d_0} \qquad (5\text{-}15)$$

As in equation (5-13), since d_0 is usually small, the factor $exp(2a(\omega)d_0)$ in equation (5-15) is ignored, and the deconvolution procedure is still expressed as equation (5-10).

The deconvolution procedure expressed in equation (5-10) neglects the

noises. However, at two ends of the reference spectrum where the signal-to-noise ratio is low, such operation is unstable. Thus, equation (5-10) must be modified to handle this situation. The Wiener filter [Muradami *et al*, 1978; Kino, 1987] has been successfully employed to desensitizes the deconvolution process.

The Wiener filter desensitized deconvolution can be expressed as [Mradami *et al*, 1978],

$$F(\omega) = \frac{V_o(\omega)}{V_{ref}(\omega)} W(\omega) \tag{5-16}$$

where $W(\omega)$ is the Wiener filter and is defined as

$$W(\omega) = \frac{|V_{ref}(\omega)|^2}{|V_{ref}(\omega)|^2 + Q^2(\omega)} \tag{5-17}$$

where $Q(\omega)$ is known as the desensitization term and usually taken to be a non-optimally chosen, frequency independent constant [Neal *et al*, 1992]. The most commonly used value for Q has been 10% of the maximum value of the reference magnitude [Neal *et al*, 1992; Neal and Thompson, 1986],

$$Q = 0.1 \, |V_{ref}(\omega)|_{\max} \tag{5-18}$$

To test how well this deconvolution model works, an experiment was performed on Sample 1, a Buehlers "Transoptic" disc containing a 400 μm (obtained from optical measurement) radius polystyrene spherical inclusion. The sample was manufactured at Ames Laboratory, Iowa State University, USA. The transducer used was the Ultran XL 50-5-P3, a point focused transducer. Its centre frequency was about 4.6 MHz and its bandwidth at 14 dB below the peak amplitude was approximately 0.8 - 8.4 MHz. The measurement was performed in a water immersion tank. The experimental results are displayed in

figures 5.7 to 5.10.

The transducer was first focused at the front surface of the sample to obtain a reference signal in the time domain. Figures 5.7a and 5.7b show the reference signal and its spectrum. The transducer was then focused at the depth where the inclusion was known to be located, and scanned around the inclusion until the transducer and flaw aligned properly and the maximum reflection signal was obtained. Figure 5.8a shows the measured time domain flaw signal, and figure 5.8b is its spectrum.

Equation (5-16) was then used to deconvolve the flaw signal from the reference signal. The desensitising Wiener filter term Q was set at 10% of the maximum value of the reference magnitude. The result was found to be insensitive to small changes in the filter level (the value of Q). The spectrum of the resulting raw flaw signal is shown as the solid line in figure 5.9. This result is compared with the numerical simulation result which is shown as the dashed line in figure 5.9. The simulation result was calculated by employing Ying and Truell [1956] series solutions. Both the experimental data and the calculated data are normalized so that their maxima are one in order to be compared. It is seen that the scattering features shown in these two curves, such as the frequencies where peaks and valleys occur, agree very well.

The raw flaw frequency response was then transformed back to the time domain as shown in figure 5.10. Two signals in figure 5.10 are apparent. The first reflection is from the front face of the inclusion, and the second reflection is assumed to be from the back face of the inclusion. The transit time (τ) between these two reflections can be calculated approximately as

$$\tau \simeq \frac{2d}{c} \simeq \frac{2\times 0.8}{2.35} \simeq 0.68\,\mu s \qquad (5\text{-}19)$$

where d is the diameter of the inclusion, and c is the longitudinal velocity in

the inclusion. The transit time measured from figure 5.10 is 0.72 ± 0.01 μs, which is in good agreement with the calculation using equation (5-19).

The interference of these two reflections gives rise to the characteristic oscillating pattern in the frequency domain shown in figure 5.9. The separation between peaks or valleys should be about

$$\Delta f = \frac{1}{\tau} \approx 1.47 \ MHz \tag{5-20}$$

This value is close to what is observed in figure 5.9.

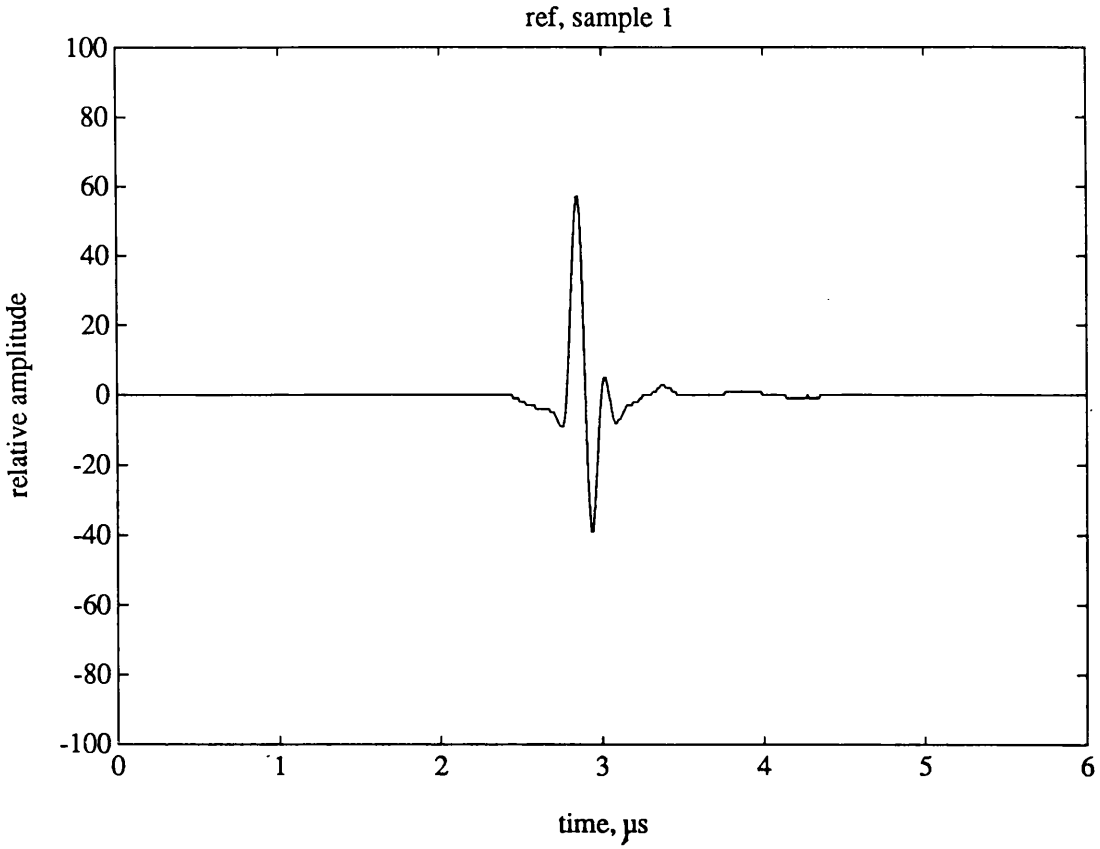

Figure 5.7a Reference time domain signal obtained from the front surface of the plastics sample

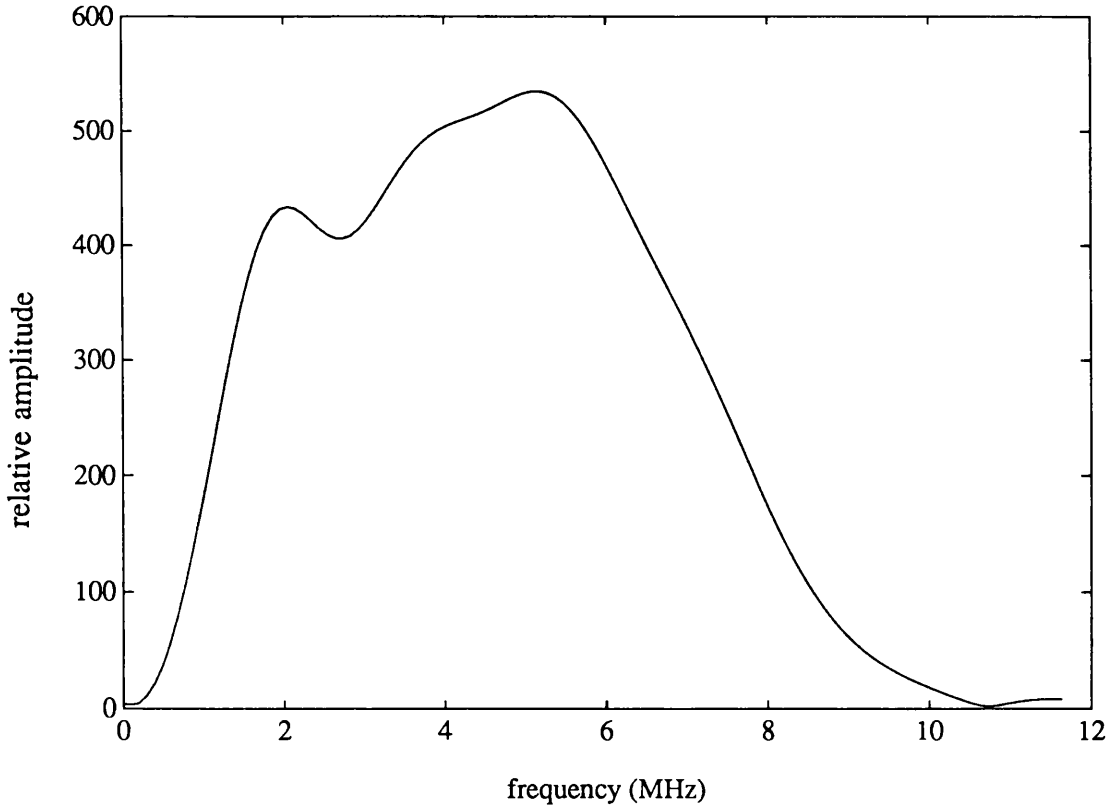

Figure 5.7b Frequency spectrum of the above reference signal

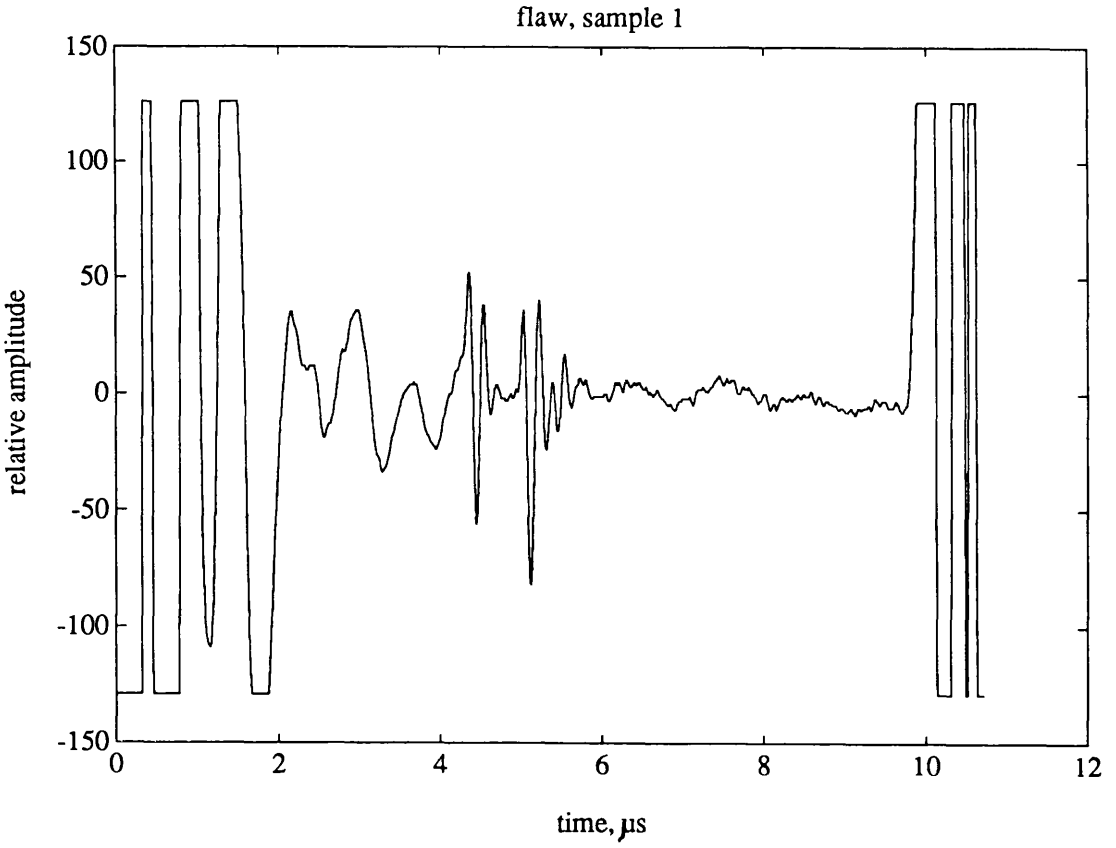

Figure 5.8a Flaw time domain signal from the 400 μm radius polystyrene inclusion in the plastics sample

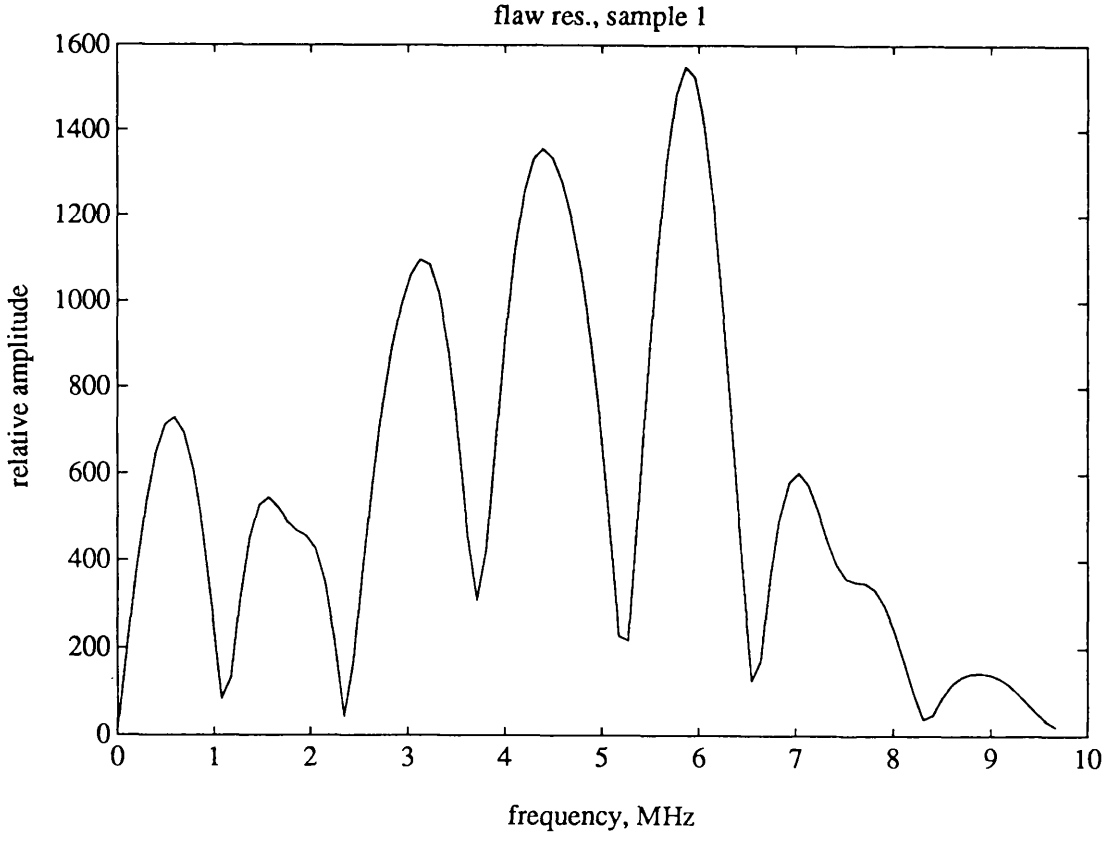

Figure 5.8b Frequency spectrum of the above flaw signal

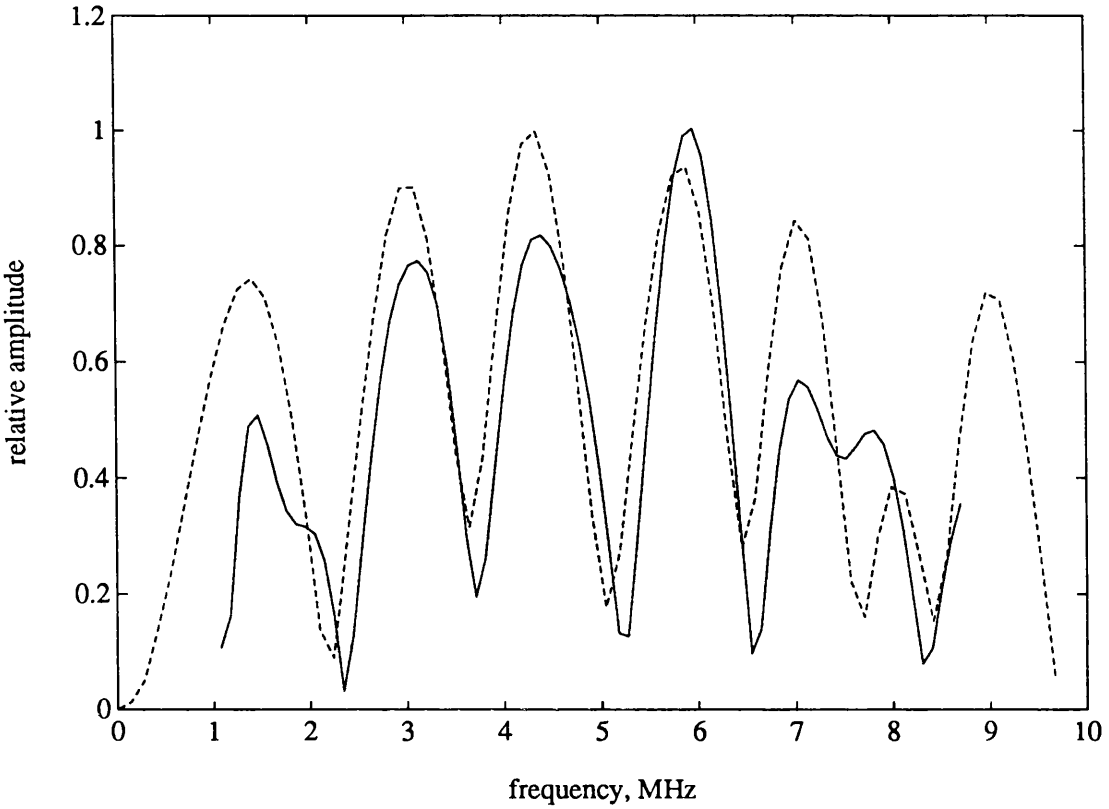

Figure 5.9 Deconvolved frequency spectrum for the 400 μm radius polystyrene inclusion. Solid line: experimental result; Dashed line: numerical calculation

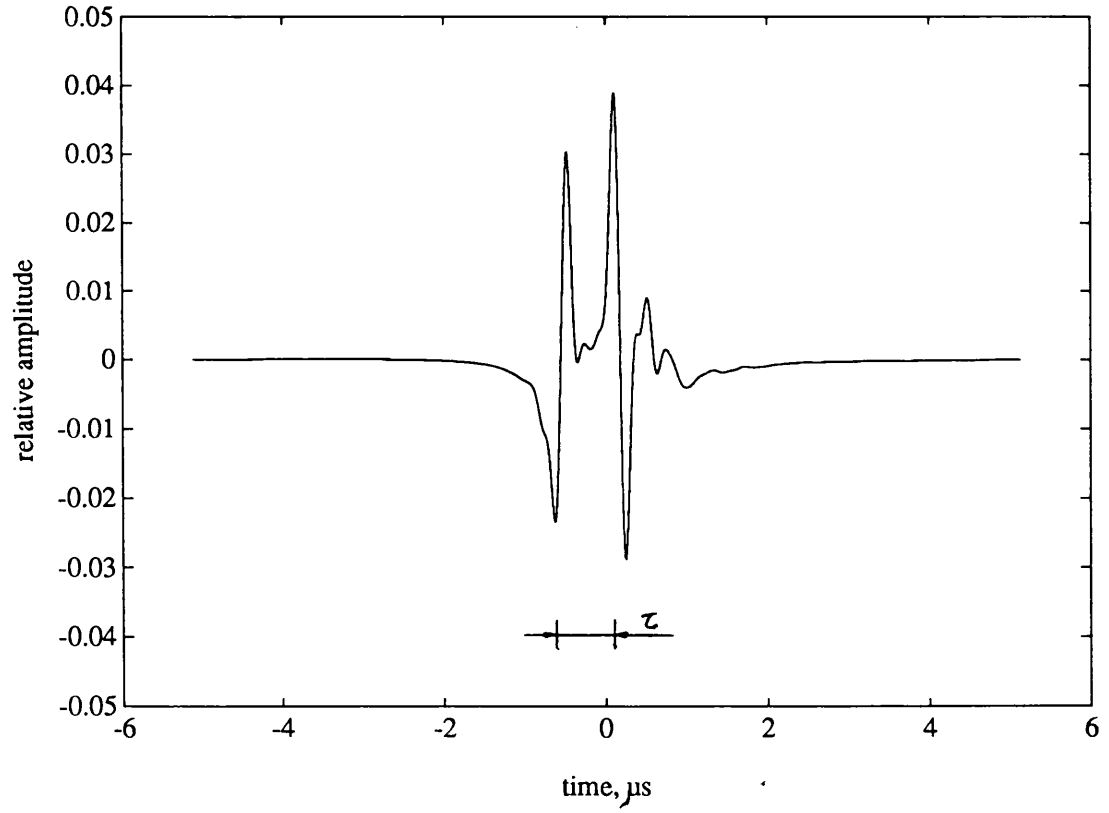

Figure 5.10 Deconvolved flaw time domain signal transformed from the spectrum in figure 5.9

5.4 Experimental Results

Using the signal pre-processing techniques illustrated in the last section, experiments were performed on several samples. The area functions were evaluated using the experimentally measured scattering data and then used to estimate the sizes of the scatterers.

5.4.1 A small cylindrical hole (r=265 μm)

The sample used was a titanium block containing a 265 μm radius (obtained by optical measurement) circular cylindrical hole about 1.5 mm from and parallel to a surface of the block. Figure 5.11 shows the position at which the experiment was performed.

The experiment was performed in immersion mode. The transducer used was the Ultran XL 50-5-P3. The centre frequency of the transducer was about 6.5 MHz and its bandwidth at 14 dB below the peak amplitude was approximately 3 - 11 MHz. The transducer was first focused at the front surface to obtain a reflection as the reference signal. Since the hole is much nearer to the front surface than to the back surface, by choosing the signal from the front surface as the reference rather than that from the back surface, the differences caused by variation in the travelling distances of the reference and the flaw signals are smaller. The time domain reference signal is shown as figure 5.12a, and its spectrum is shown as figure 5.12b. The transducer was then focused at the depth where the hole was known to be located to obtain the time domain flaw signal which is shown as figure 5.13a. Its spectrum is displayed as figure 5.13b.

Deconvolution was then performed using Equation (5-16) (the desensitization term Q was set at 10% of the maximum reference magnitude),

and figure 5.14 shows the resulting raw flaw spectrum. The raw flaw response in the frequency range of 3 to 11 MHz ($0.81 \leq ka \leq 2.95$) was then used to evaluate the area function using equation (4-8). The resulting area function is shown as figure 5.15. From this figure, the time t_{max} at which the area function has its maximum (point *A*) was found and measured. Then the last valley before t_{max} was found and the time t_{min} was measured. The time difference (Δt) between t_{max} and t_{min} was calculated to give the estimate for the radius of the hole, using the relation $a=c\Delta t/2$ (equation (4-10)). The radius estimate is 255 ± 15 μm, which is in excellent agreement with the optically measured radius of 265 μm (this value was reported in Som [1991]).

Som [1991] measured the radius of the same hole using high frequency (up to 50 MHz). The method he used was Satellite Pule Observation Technique (SPOT) [Gruber, 1980]. The diameter estimation was given by him as 513 ± 10 μm, which compares well with the result obtained from this study.

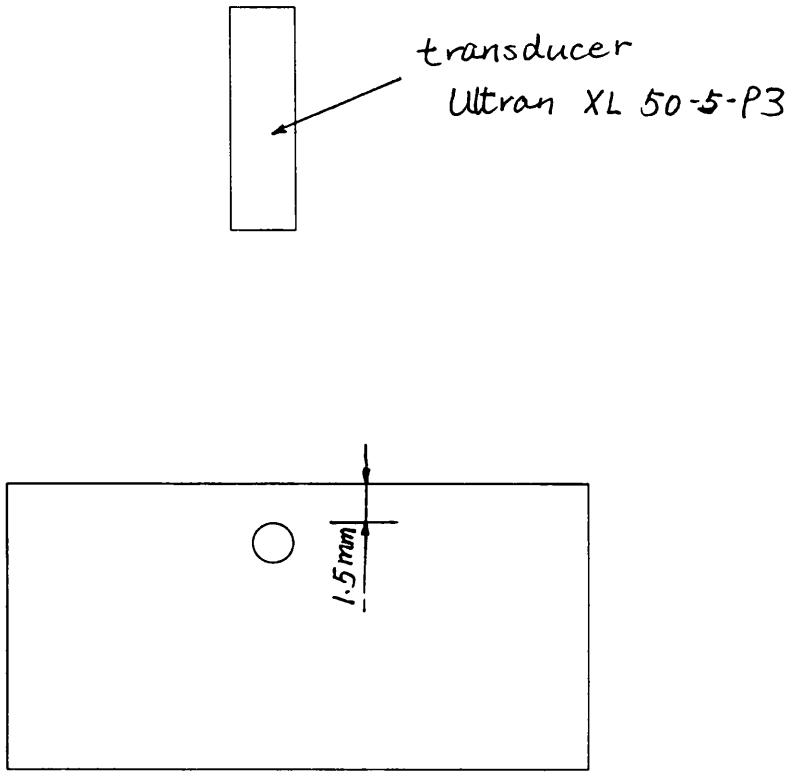

Figure 5.11 The position for the experiment on the titanium block containing a small cylindrical hole

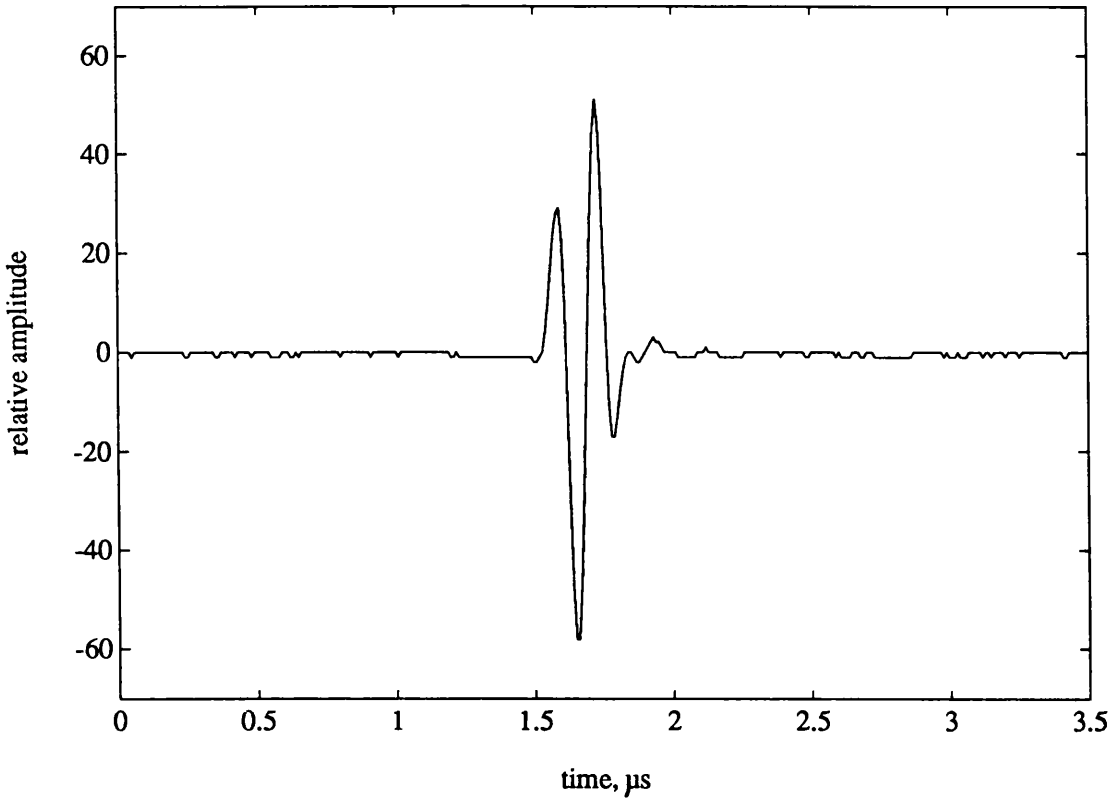

Figure 5.12a Reference time domain signal obtained from the front surface of the titanium sample

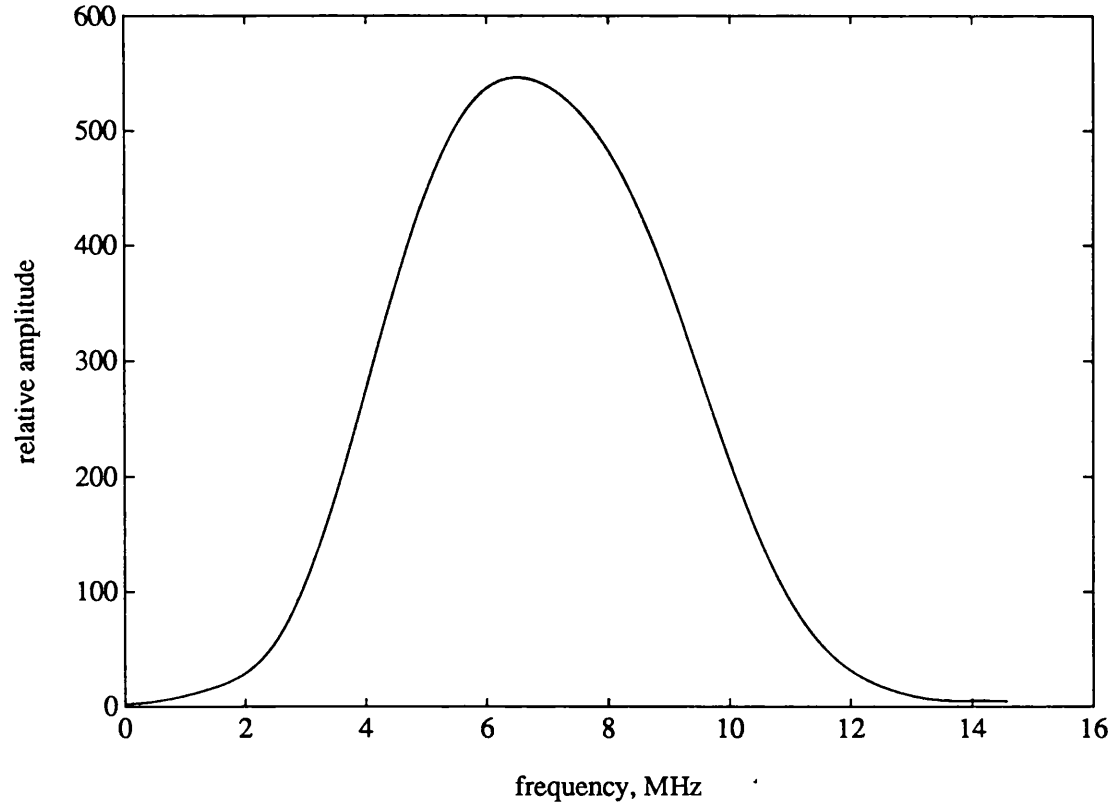

Figure 5.12b Frequency spectrum of the above reference signal

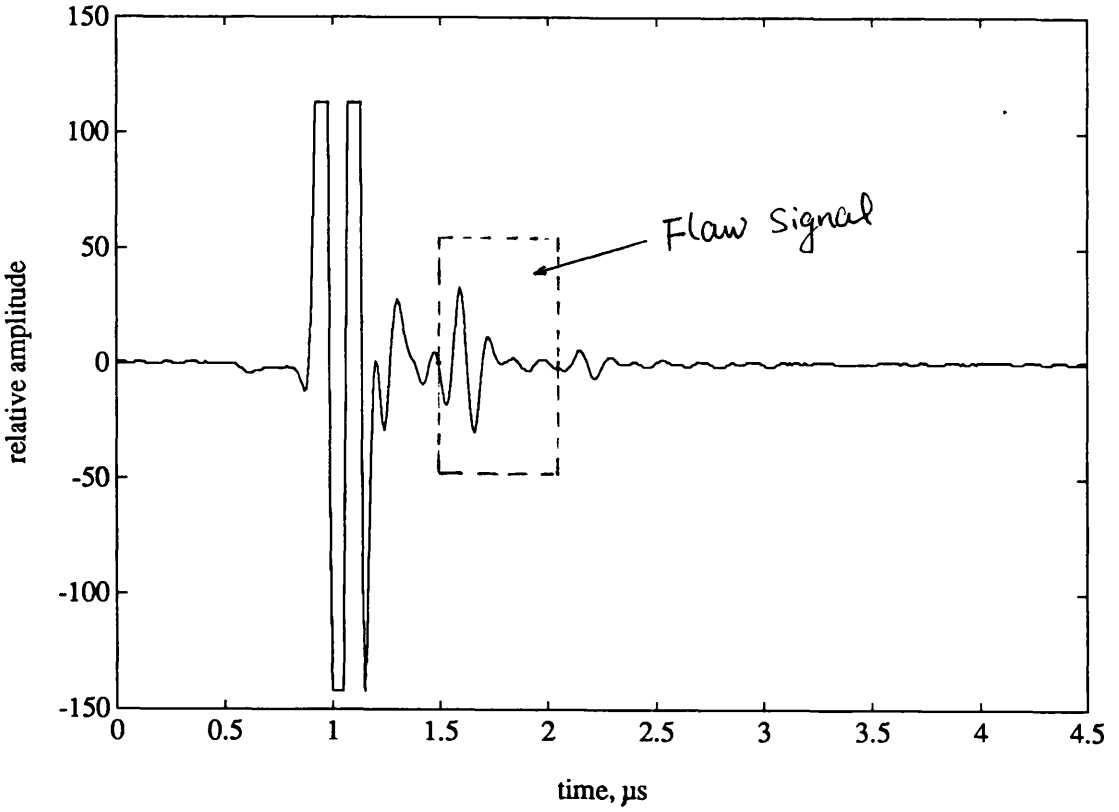

Figure 5.13a Flaw time domain signal from the 265 μm radius cylindrical hole in the titanium block

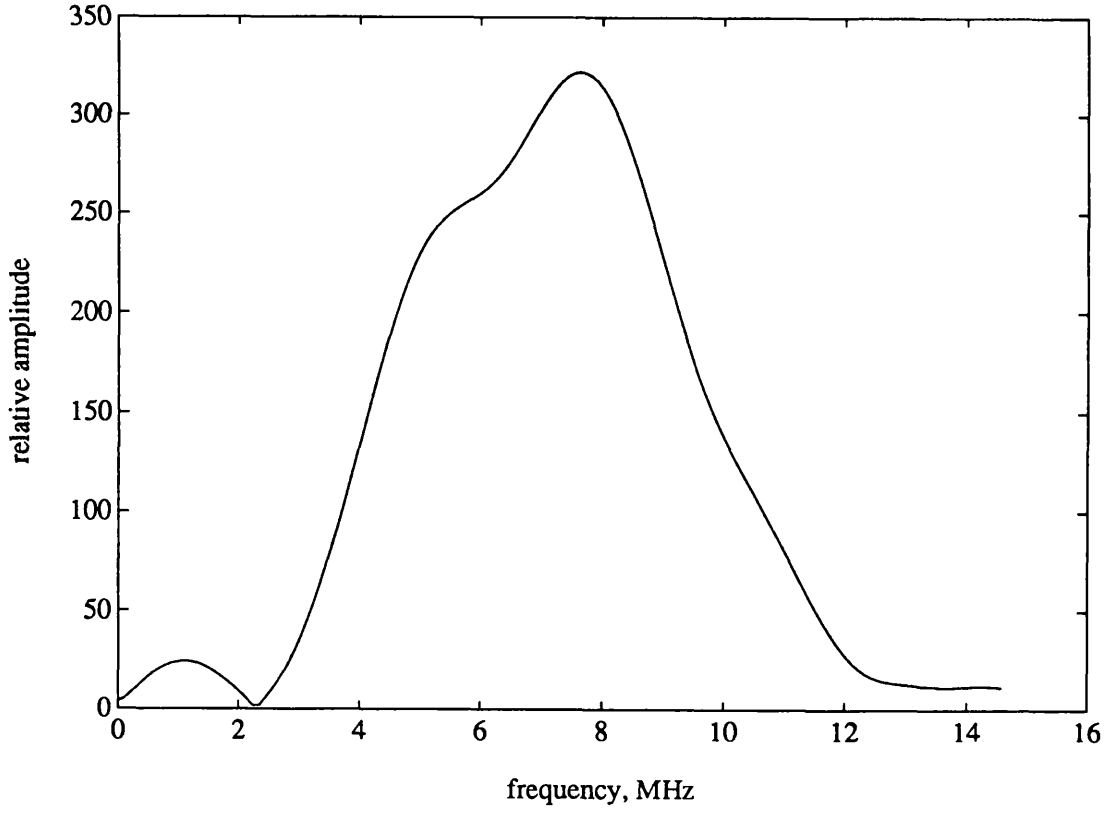

Figure 5.13b Frequency spectrum of the above flaw signal

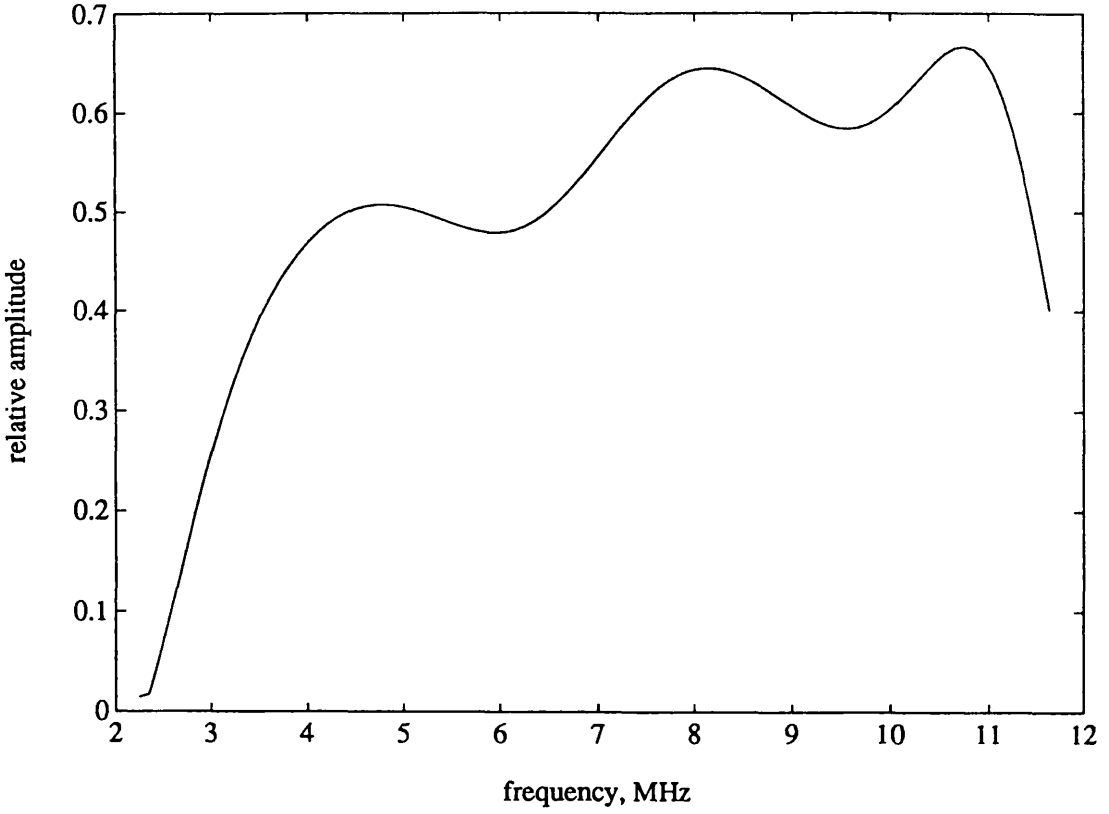

Figure 5.14 Deconvolved frequency spectrum for the 265 μm radius cylindrical hole

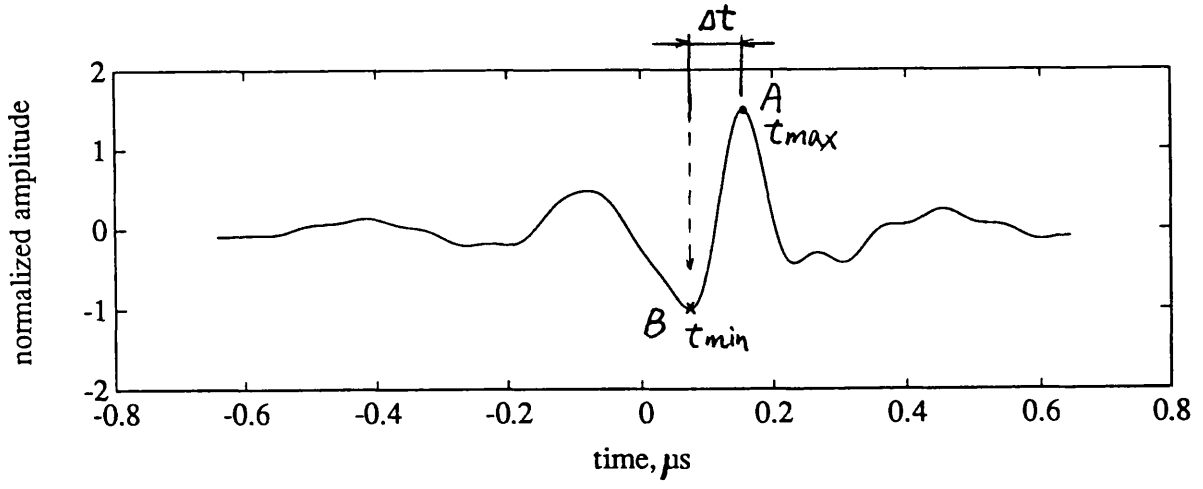

Figure 5.15 The area function for the small cylindrical hole, obtained from the scattering data shown in figure 5.14

5.4.2 A spherical void

The sample was a maraging steel block containing a 300 μm radius spherical void in the block centre. The sample was made by diffusion bonding, manufactured at Royal Ordnance plc. Figure 5.16 depicts the position of the experiment. The experiment was performed in contact mode, and the transducer used was the Krautkrämer G5KB 53051. The experiment was made difficult due to a high level of grain scattering from the host material and the interferences from the bonding line. Results were easier to obtain and contained fewer anomalous contributions along the bonding line rather than normal to it despite the increase in grain scattering.

In contact testing, the state of the coupling is one of the most difficult experimental parameters to control. It is found that measurements are extremely sensitive to the thickness and uniformity of the coupling material [Saffari, 1986]. As shown in figure 5.5 and equation (5-5), a frequency dependent coupling factor, $C(\omega)$, is included in the linear system model. Great care was taken in the experiment to ensure that the coupling factors were not too different in the acquisition of the reference signal and in the acquisition of the flaw signal. However, by no means it could be maintained exactly same.

The centre frequency of the transducer was about 4.5 MHz and its bandwidth at 14 dB below the peak amplitude was approximately 2 - 7 MHz.

The reference signal was obtained from the back surface of the sample. It is shown as figure 5.17a, and its spectrum is shown as figure 5.17b. The time domain flaw signal is shown as figure 5.18a, and figure 5.18b is its spectrum. Deconvolution was performed using equation (5-16), and the resulting raw flaw spectrum is shown as figure 5.19. The desensitization term Q was chosen to be 15% of the maximum value of the reference magnitude, higher than that used

in the last experiment because of a low signal-to-noise ratio in this experiment.

The scattering data in the frequency range of 2 to 7 MHz ($0.67 \leq ka \leq 2.33$) was used to evaluate the area function which is shown as figure 5.20. The time difference Δt between t_{max} and t_{min} (see figure 5.20) was then measured from the resulting area function and used to estimate the flaw radius using the relation $a=\Delta tc/2$ (equation (4-10)). The radius estimate is 336 ± 15 μm. The nominal radius of the void was recorded as 300 μm [Chaloner, 1988]. The difference is about 12%. The less accurate sizing result was probably caused by that the flaw signal was seriously contaminated by the noises due to a high degree of grain scattering and less desirable bonding quality. Some errors also occurred in the deconvolution process due to ignored factor $exp(-2\alpha(\omega)(d-d_0))$ (see equation (5-13)). In this experiment, this factor was more significant than that in the last experiment, because the distance $d-d_0$ was much larger (50 mm) and the $\alpha(\omega)$ was larger due to a high degree of grain scattering of the material.

Chaloner [1988] reported the sizing results for the same sample using the IBA. The radius estimations in her study were in the range of 253 - 271 μm.

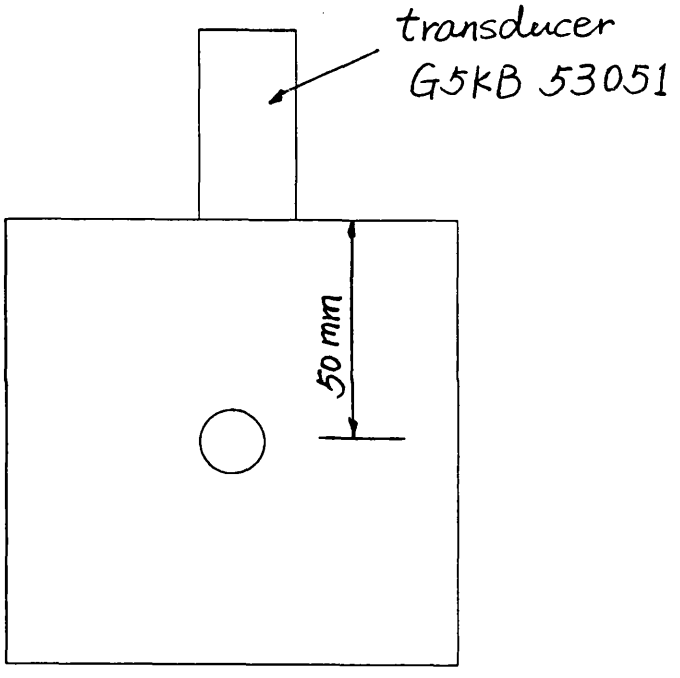

Figure 5.16 The position for the experiment on the maraging steel block containing a spherical void

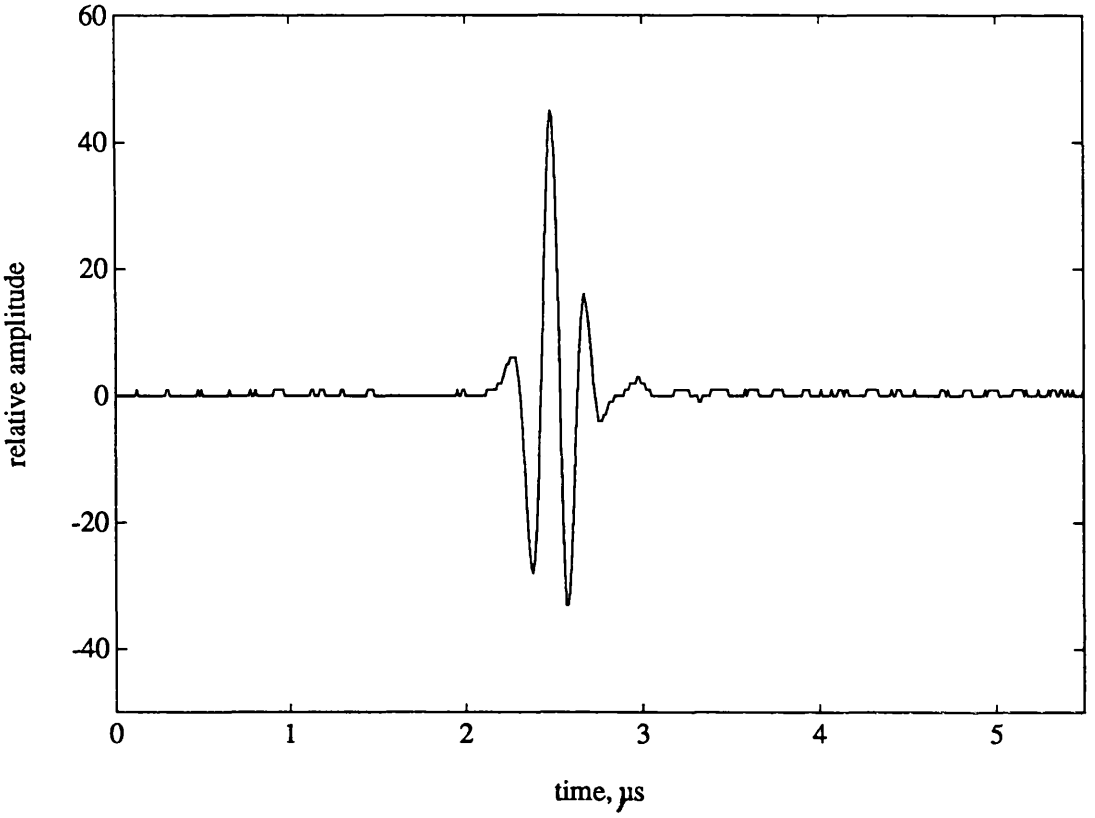

Figure 5.17a Reference time domain signal obtained from the back surface of the maraging steel block

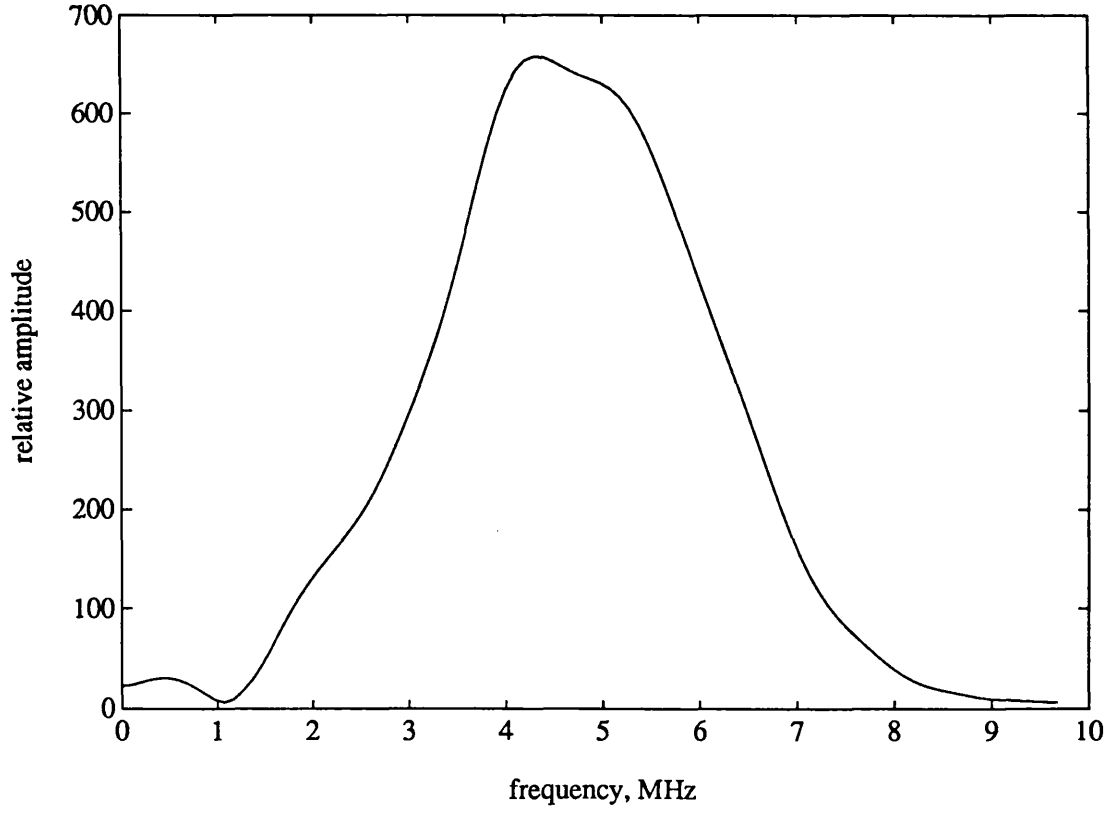

Figure 5.17b Frequency spectrum of the above reference signal

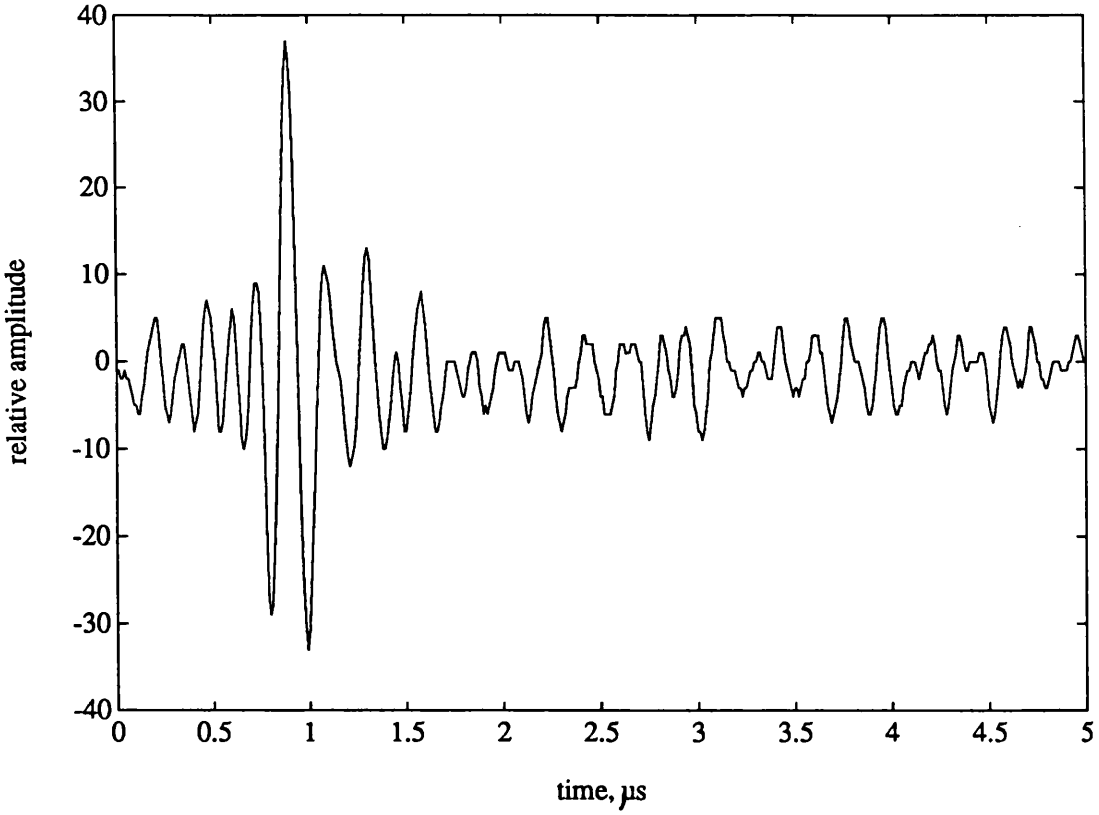

Figure 5.18a Flaw time domain signal from the 300 μm radius spherical void in the maraging steel block

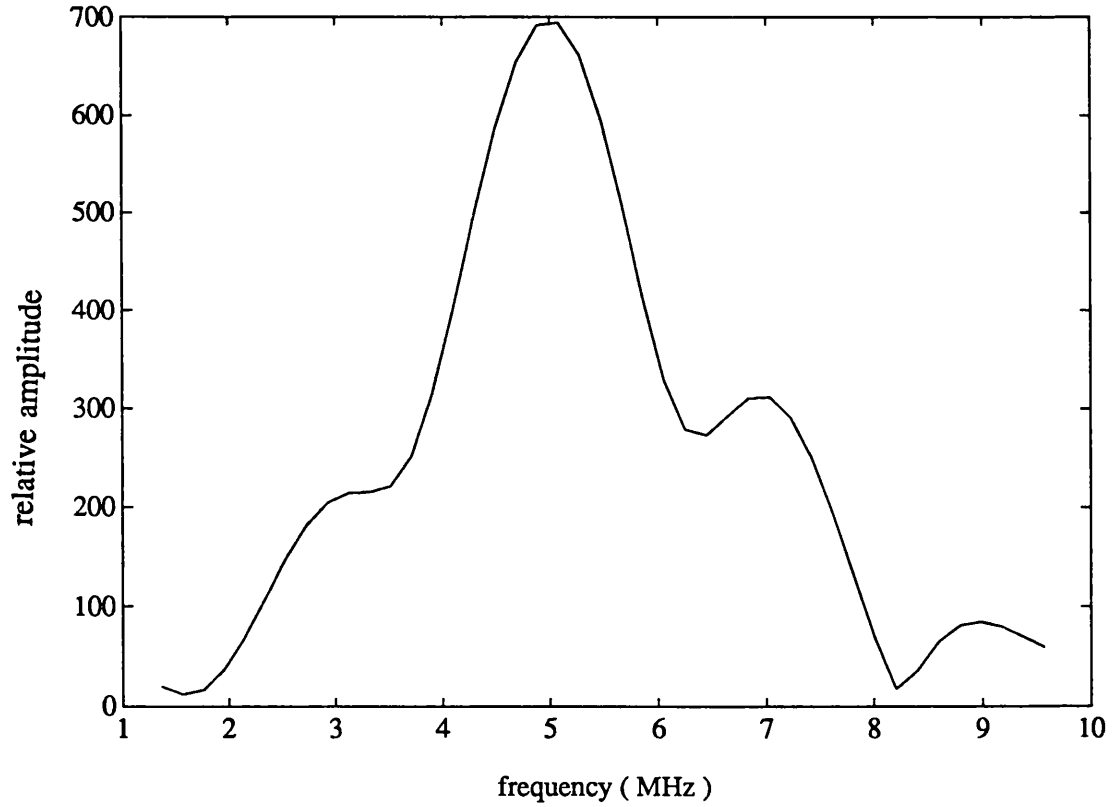

Figure 5.18b Frequency spectrum of the above flaw signal.

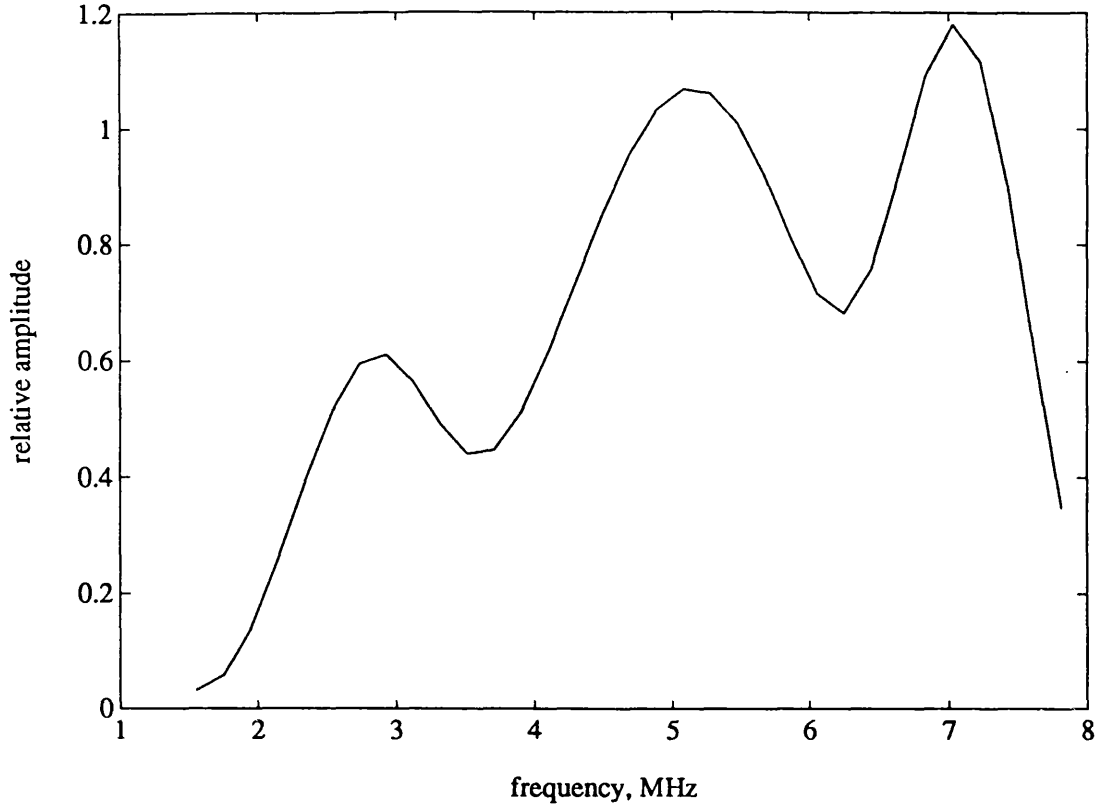

Figure 5.19 Deconvolved frequency spectrum for the 300 μm radius spherical void

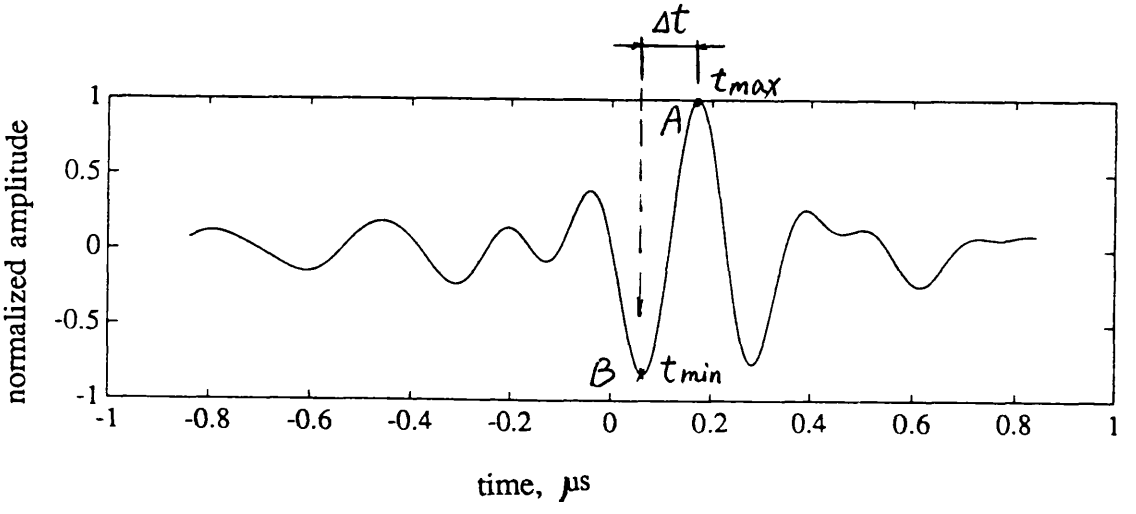

Figure 5.20 The area function for the 300 μm spherical void, obtained from the scattering data shown in figure 5.19

5.4.3 A large cylindrical cavity

The sample used was an aluminum block containing a 725 μm radius circular cylindrical hole which is 7.5 mm from and parallel to a surface of the block. The experiment was performed in contact mode. The position for the experiment is displayed as figure 5.21. The transducer used was the Harisonics CRO208. The centre frequency of the transducer was about 3.5 MHz and the its bandwidth at 20 dB below the peak amplitude was approximately 1.2 - 5 MHz.

The reference signal was obtained from the back surface. The time domain reference signal and its spectrum are shown as figures 5.22a and 5.22b respectively. The time domain flaw signal was then captured and it is shown as figure 5.23a. Figure 5.23b is the spectrum of the flaw signal. Equation (5-16) was then used to perform deconvolution (the desensitization term was set as: $Q=0.1|V_{ref}(\omega)|_{max}$), and figure 5.24 shows the deconvolved flaw spectrum.

As in the last experiment, great care was needed in this experiment to ensure that the coupling factors were not too different in the acquisition of the reference signal and in the acquisition of the flaw signal. The flaw signal in this experiment was much cleaner compared with that in the last experiment, because the level of the grain scattering in the aluminum block was much weaker than that in the maraging steel block, and there was no bonding line influence in this experiment. The errors occurred during the deconvolution process due to the ignored factor $exp(-2\alpha(\omega)(d-d_0))$ (equation (5-13)) was smaller in this experiment, as $(d-d_0)$ was much smaller (7.5 mm compared to 50 mm in the last experiment) and $\alpha(\omega)$ was smaller as well due to a lower degree of grain scattering.

The deconvolved flaw scattering data in the frequency range of 1.2 to

4.6 MHz ($0.85 \leq ka \leq 3.3$) was then used to evaluate the area function using equation (4-8). The resulting area function is shown as figure 5.25, from which Δt between t_{max} and t_{min} was measured and the radius was estimated using equation (4-10) ($a=c\Delta t/2$). The estimated radius is 696 ± 15 μm which is 4% less than the nominal radius of 725 ± 25 μm.

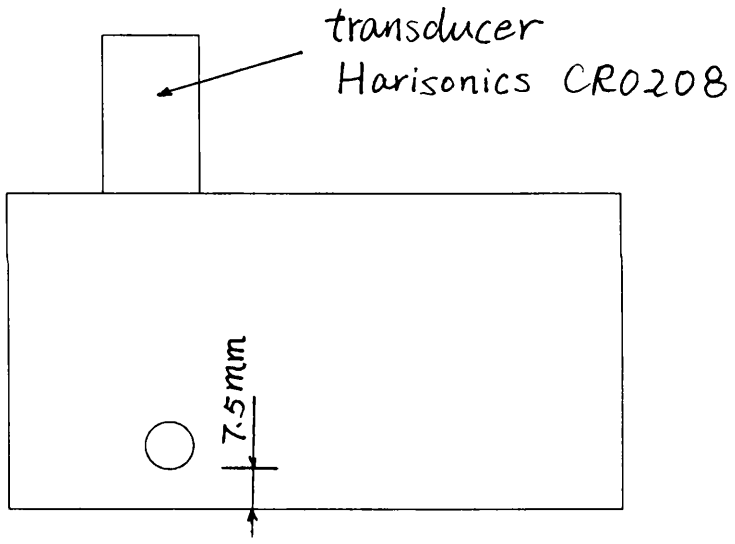

Figure 5.21 The position for the experiment on the aluminum block containing a cylindrical hole

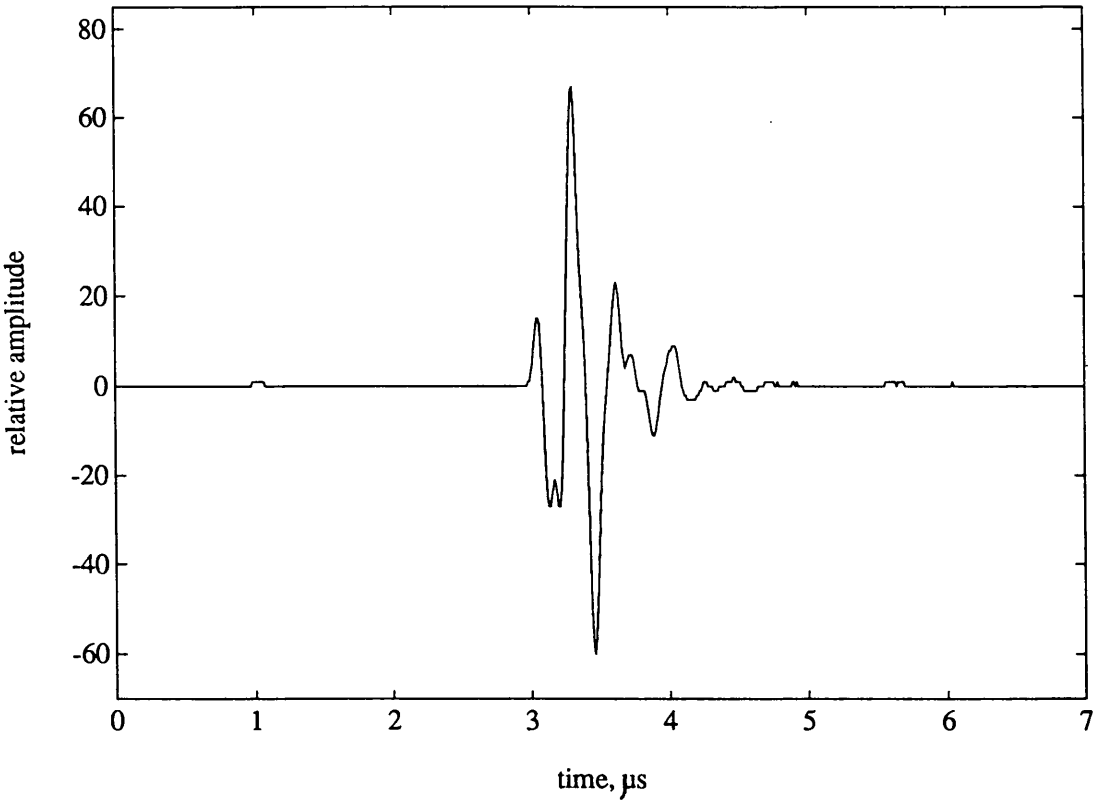

Figure 5.22a Reference time domain signal obtained from the back surface of the aluminium sample.

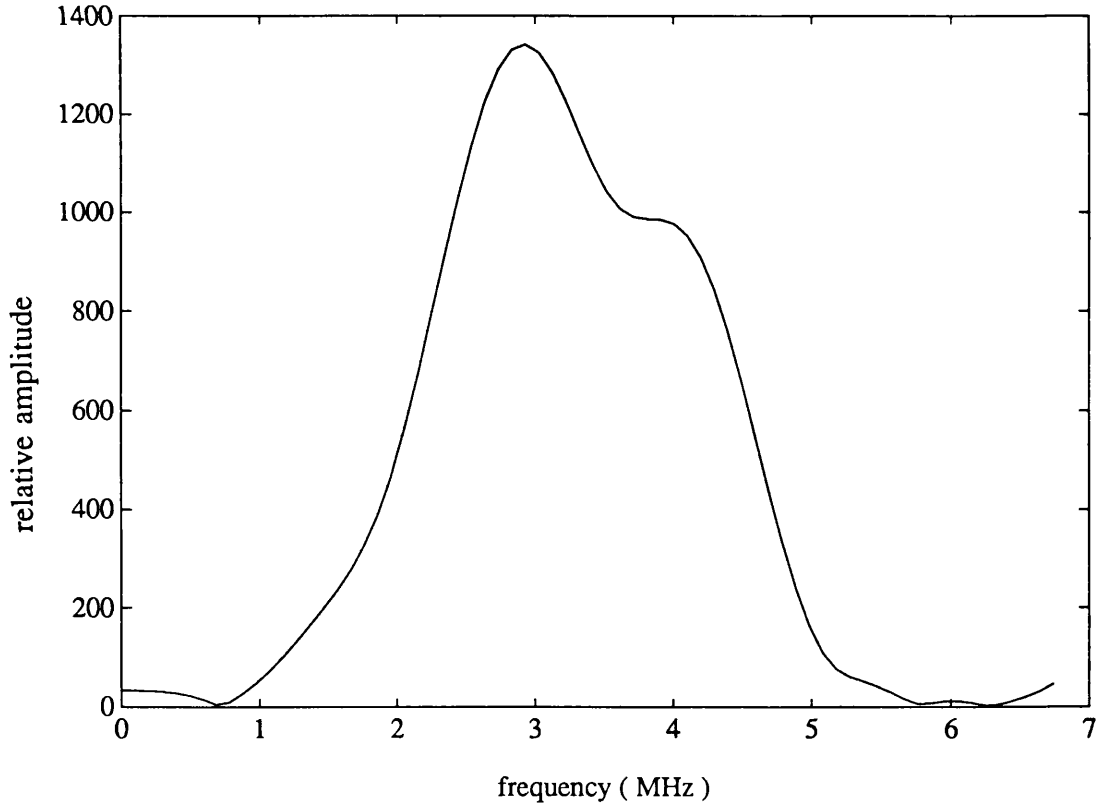

Figure 5.22b Frequency spectrum of the above reference signal

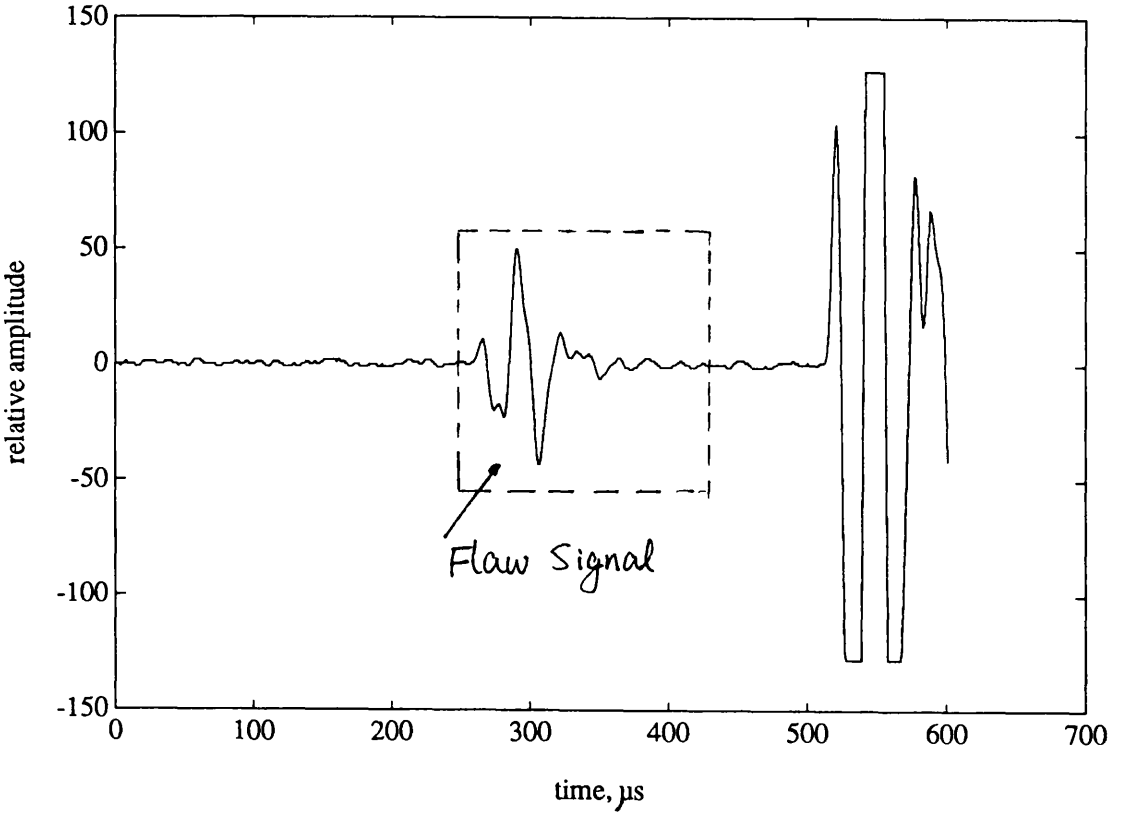

Figure 5.23a Flaw time domain signal from the 725 μm radius cylindrical hole in the aluminium block

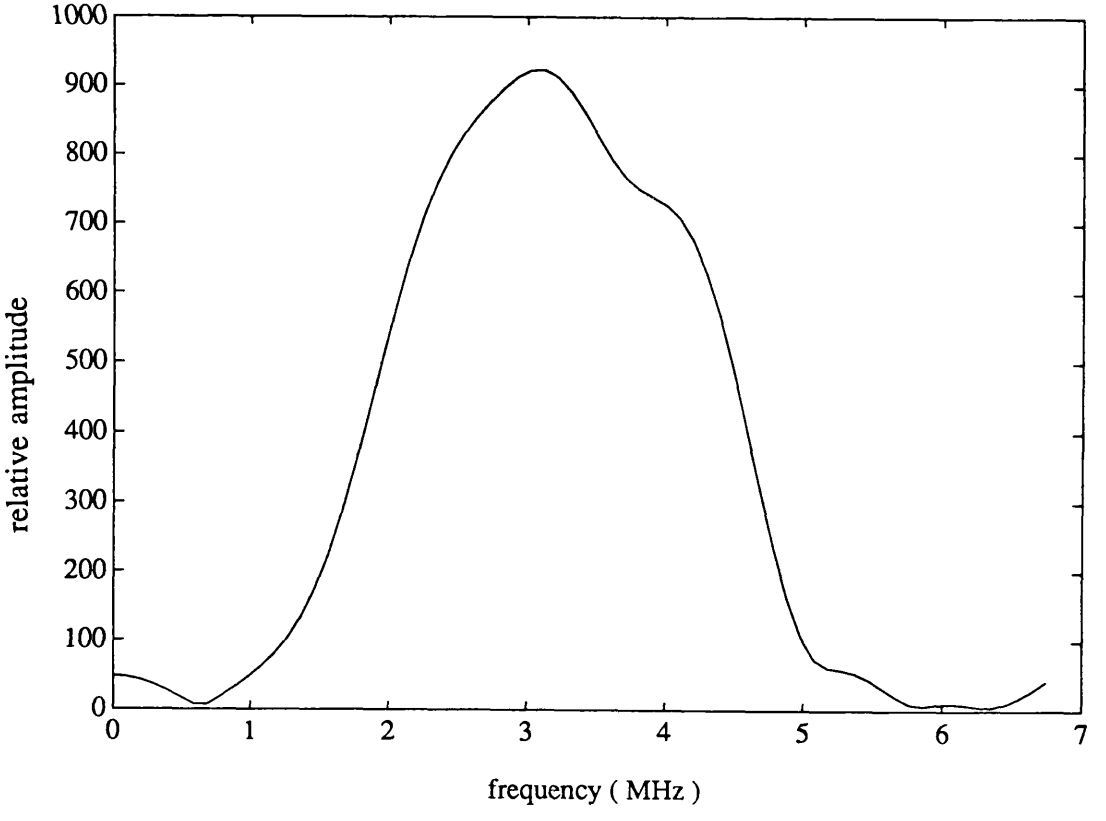

Figure 5.23b Frequency spectrum of the above flaw signal

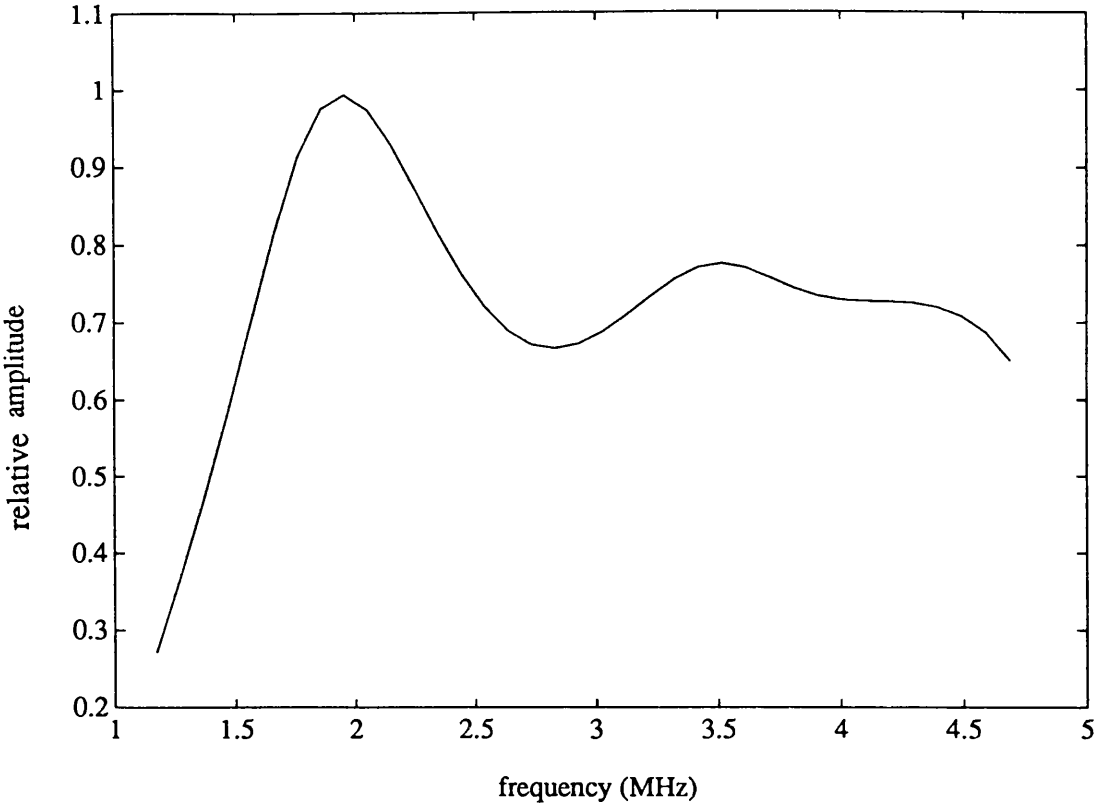

Figure 5.24 Deconvolved frequency spectrum for the 725 μm radius cylindrical hole.

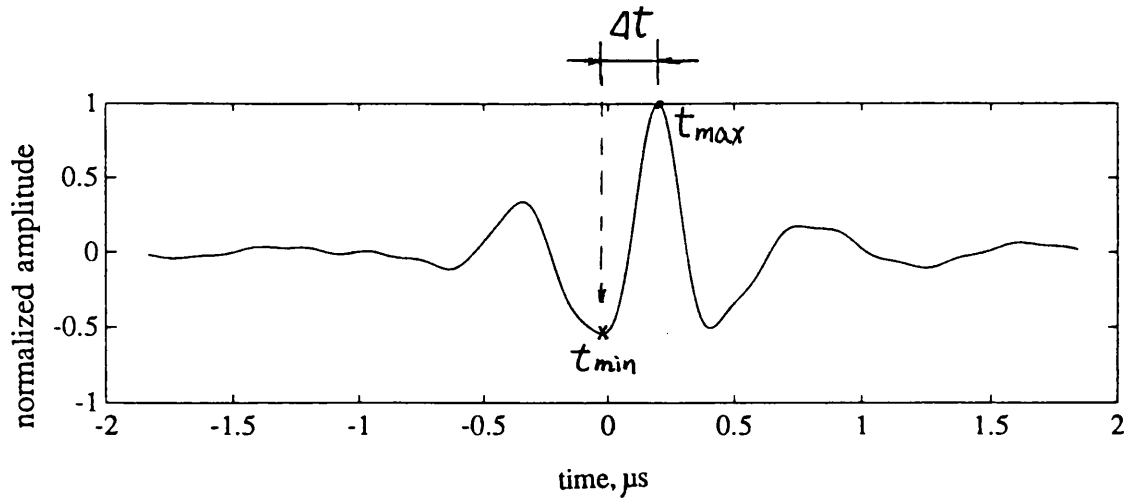

Figure 5.25 The area function for the 725 μm radius cylindrical hole, obtained from the scattering data shown in the above figure

5.5 Discussions

The ultrasonic flaw sizing algorithm using the area function has been tested experimentally for three cases, (1) a small cylindrical hole (r=265 μm) in a titanium block, (2) a spherical void (r=300 μm) in a maraging steel block, and (3) a large cylindrical hole (r=725 μm) in an aluminum block.

In all these three experiments, although the area functions evaluated from the experimental data are seriously distorted, compared with the corresponding true cross-sectional areas, all the sizing results are in good agreement with the optically or mechanically measured flaw sizes. The experimental results have verified the conclusions made in the last chapter based on the simulation results. The experimental results have shown that the algorithm can be applied to estimate the sizes of voids to an acceptable accuracy, provided proper transducers are used. A guide for selecting transducers has been discussed in Chapter 4 (see figure 4.9). In general, if adequate bandwidth is available, the results agree with the nominal sizes of the defects to within 10% and often better.

Although none of the tests were strictly speaking "blind", since in each case the approximate flaw radius was known, the optical measurement value of the 265 μm radius cylindrical hole and the mechanical measurement value of the 725 μm radius cylindrical hole were obtained after the ultrasonic measurements.

The surface finish of the defect in the diffusion bonded maraging steel is unknown, but it is expected that some surface roughness may be present due to the spark erosion process [Chaloner, 1988]. This might be one of the reasons why the sizing result with this sample is less accurate.

The flaw signal from the spherical void in maraging steel block was seriously corrupted by noises. Some sources of the noise could have been compensated for in signal processing. However, this was not done in order to keep the experiment as simple as possible, and more important to see how well this sizing scheme performs with a highly contaminated flaw signal. Even though the sizing result is not as good as the other two cases, it is still very acceptable in practical application which is very encouraging.

All the defects used in the experiments have the greatest dimension less than 1.5 mm. This is because, in the majority of materials, flaws of greater dimension can be adequately and accurately described by conventional imaging methods and more specialised techniques are not necessary.

No samples with more complicated defect geometries are available. However, the simulation studies in Chapter 4 suggests that the method can be applied to some other shaped voids.

The comparisons between the area function sizing technique and the IBA have been made in Chapter 4.

Chapter 6
CONCLUSIONS

6.1 Summary of the Results

This thesis reports a theoretical and experimental study of ultrasonic scattering from volumetric flaws in structural materials and ultrasonic inversion techniques for sizing such flaws.

For forward scattering problems, the Method Of Optimal Truncation (MOOT) has been studied and used to generate forward scattering data. MOOT has been widely applied in the study of the elastic wave interactions with various scatterers. It has been found accurate and reliable.

In this study, a large general purposed computer model was developed, based on MOOT. The computer model can be used to simulate ultrasonic scattering from different shapes and sizes of voids, with only minor changes to specify the size and shape of the void considered. Backscattering amplitudes for a number of voids (including spheroidal voids, an ovate void, and two overlapping voids) were calculated and presented both in the frequency and time domains. These results were used to provide understanding of basic physical mechanism of scattering by voids. A simple physical model, which assumes a leading front surface specular reflection followed by a creeping wave which travels around the circumference of the void at a velocity close to that of longitudinal wave, was extended and shown to apply to ovate and some more complex voids. The transit times between the specular reflections and the creeping waves were measured from the numerical time domain responses for several voids, and they are in good agreement with the analytical results from the physical model.

For inverse scattering problems, the study has addressed only one aspect of the flaw characterisation problems, the determination of the flaw's geometric features. Other aspects of the flaw characterisation, such as flaw classification and determination of the flaw's material properties, are not specifically addressed.

In this study, a new ultrasonic sizing technique, the area function sizing scheme, has been developed for sizing isolated volumetric flaws in structural materials. The method determines the size of a flaw by the inversion of the backscattered ultrasonic signal using the area function formula. The area function formula is derived from a weak scattering approximation, the Born approximation, but it has been demonstrated by numerical and experimental results that the sizing scheme works well for voids which are clearly strong scatterers.

This area function sizing technique can be formulated and used in either the time or the frequency domain. It is easier to understand in the time domain, in terms of relating it to specific flaw geometric features. However, it is easier and more stable to do signal processing in the frequency domain. Following the time domain analysis, the work in this study was therefore performed in the frequency domain.

The area function sizing technique has been tested to reconstruct geometric features of several regular and irregular shaped voids using the numerical backscattering data in some practical frequency ranges which can be met by commercial transducers. The technique has also been tested to size several simple flaws experimentally. The experiments and numerical studies have demonstrated that, provided sufficient spectral bandwidth is available (at least about $1 \leq ka \leq 3$), the simple shaped voids can be accurately sized normally to within 10% using the area function sizing technique. Satisfactory

sizing result has been observed with a low signal-to-noise-ratio signal (Section 5.4.2).

The area function sizing scheme shares much of its theoretical basis with the IBA [Rose, 1989]. It also shares some of the attractive features of the IBA which were summarised in Chaloner's Ph.D thesis [1988]. These are:

(1) The area function technique does not require absolute amplitude measurement, which makes it much easier for the method to be applied in practice. Accurate absolute amplitude is very difficult to measure in practical applications, even in laboratory. It is very dependent on the scattering situation, location, coupling material and equipment etc..
(2) The evaluation of the area function (equations (4-7) and (4-8)) involves an integration of the experimental data which has the effect of desensitising the inversion to random noise.
(3) Low frequency data is highly weighted which means that the effects of noise due to grain scattering (which increases with the fourth power of frequency in elastic materials) are minimised.

However, this study has shown that the area function sizing scheme has several distinguished advantages over the IBA. These advantages have been discussed in Chapter 4, and they are summarised as follows:

(1) The area function sizing technique does not require to locate the flaw centroid in the time domain signal to assist the implementation of the algorithm. The difficulty of solving the zero-of-time problem is therefore avoided, and this avoids one of the main obstacles encountered when the IBA is applied. Even if the zero-of-time problem were perfectly solved, implementing the IBA would require more signal processing procedures than implementing the area function sizing technique.

(2) The bandwidth requirements for the area function sizing method ($1 \leq ka \leq 3$) appear to be less severe than those of the IBA ($0.5 \leq ka \leq 2.5$).

The applicability of the area function sizing scheme is at present limited due to simplifying assumptions in its theoretical derivation, which is based on a weak scattering assumption. The results presented in the thesis are for voids. The extension of this technique to strong scattering inclusions has not yet been studied.

Another limitation of the area function sizing scheme is its bandwidth requirements. Each transducer with a certain bandwidth can only be used to size a certain range of the flaw sizes. The broader the transducer bandwidth, the wider range of the flaw sizes that it can be used to size. This limitation can only be eased by the improvement of the bandwidth of the available ultrasonic transducers. This transducer-based limitation are not unique for this inversion technique. They are also shared by the IBA and many other ultrasonic inversion schemes.

In summary, the area function sizing scheme has been shown to be a simple and direct way of inverting ultrasonic scattering amplitudes to obtain the geometric features of isolated flaws in the bulk of a structural material.

6.2 Suggestions for Future Research

This section gives a number of suggestions for future work based on this study. Most of them are direction extensions to the work already performed which should improve experimental results or which should expand the range of application of the technique.

For the forward scattering numerical model, it is worthwhile to expand

the model to deal with inclusions. This should be straightforward. It can be done by replacing the stress free boundary conditions with the boundary conditions for the elastic inclusion.

With the development of the expert system, the indirect inversion techniques become more attractive. The computer model based on MOOT can be used to generate data bases to develop adaptive learning inversion sizing schemes.

For the area function sizing scheme, there are a number of questions which need to be addressed.

Because the formulation of this technique is based on a weak scattering approximation, it is necessary to investigate further the theoretical reason why the technique works so well for voids, which are clearly strong scatterers. This should lead to a better understanding of the physical process. It has been shown that there is a creeping wave present in the backscattering signal from a void. The effects of the creeping wave on the area function sizing technique should be studied further in the next stage study.

The extension of the area function technique to strong scattering inclusions should be studied numerically and experimentally. The Born approximation has been shown to work well for some strong scattering inclusions [Gubernatis *et al*, 1977b]. It is therefore expected that the area function sizing scheme would apply to some types of strong scattering inclusions.

The evaluation of the area function involves an integration and as a result it is insensitive to random noise. (Chapter 5 has shown a very noisy experimental signal, which gave a reasonable sizing result.) However, it is

inevitable that noise affects at least some procedures of the sizing scheme. The effects of noise on sizing results should be studied quantitatively in future research.

The bandwidth requirements of the area function sizing technique are not severe. However, the wider the bandwidth of the transducer, the more accurate the sizing result. All real signal measurements are expected to lose some lower frequency and much of the higher frequency components. For this sizing technique, low frequency data is highly weighted. In future research, some extrapolation methods could be used to reconstruct the low frequency end of a signal, so as to improve the sizing results.

The application of this sizing technique to some complex shaped scatterers has been investigated in Chapter 4 using numerical forward scattering data. However, more work is still needed, especially from the experimental point of view.

So far, the deconvolution has been performed by obtaining a reference signal from either the back-surface or the front surface of a sample, but this can be difficult in practice. Koo [1987] has successfully used the leading pulse of the signal from a flaw itself as the reference for the deconvolution in the experiments. He pointed out that with an impulsive input signal, the output signal from a flaw usually contains a leading pulse plus other later arriving responses. If the scatterer is a volumetric flaw, then the leading pulse is the front surface echo which is the same as from a perfect reflector at the flaw location but normalized by the unknown flaw Gaussian curvature and reflection coefficient. Since this front pulse also contains all the characteristics of the testing system except the flaw, it can be extracted and used as a reference signal in the deconvolution process. This deconvolution process may be used to make the area function sizing technique more easily applied in practical

situations.

The success of implementing this deconvolution process means that sizing can be performed in a single measurement, with no need for another measurement to get the reference signal. Thus, all the procedures needed can be incorporated into a computer software, and the sizing scheme can be developed into a "real-time" method - displaying the sizing result right after a measurement is taken.

REFERENCES

Achenbach, J. D., Gautesen, A. K. and McMaken, H. (1982) *Ray Methods for Waves in Elastic Solids*, Pitman Advances Publishing Program, Boston.

Addison, R. C., Elsley, R. K., and Martin, J. F. (1982) "Test Bed for Quantitative NDE-Inversion Results", Review of Progress in Nondestructive Evaluation, Thompson, D. O. and Chimenti, D. E. eds., Plenum Press, New York, Vol. 1, pp. 251-261.

Albach, P. H. (1988) *The Scattering of Time Harmonic Elastic Waves From Hemispherical Surface Indentations*, M.Phil.-Ph.D Transfer Thesis, University College London.

Albach, P. H. (1989) *Three-Dimensional Scattering of Time Harmonic Elastic Waves from Axisymmetric Surface Indentations in A Half-Space*, Ph.D Thesis, University of London.

Alder, L. and Achenbach, J. D. (1980) "Elastic Wave Diffraction by Elliptical Cracks: Theory and Experiment", J. Nondestr. Eval., Vol. 1, pp. 87-99.

Auld, B. A. (1973) *Acoustic Fields and Waves in Solids*, Vol. 1 & 2, John Wiley, New York.

Bhagat, P. K., Chimenti, D. E., Moran, T. J., and Shimmin, K. D. (1984) "Effects of Deconvolution Procedures on Size Estimates in the Born inversion Algorithm", Review of Progress in Quantitative Nondestructive Evaluation, Thompson, D. O. and Chimenti, D. E. eds., Plenum Press, New York, Vol. 3, pp. 395-403.

Bleistein, N., and Cohen, J. K. (1979) "The Singular Function of a Surface and Physical Optics Inverse Scattering", Wave Motion, Vol. 1, pp. 153-161.

Bleistein, N., and Cohen, J. K. (1980) "Progress on a Mathematical Inversion Technique for Nondestructive Evaluation", Wave Motion, Vol. 2, pp. 75-81.

Bond, L. J. (1989a) "Numerical Techniques and Their Use to Study Wave Propagation and Scattering - A Review", IUTAM Symposium on Elastic Wave Propagation and Ultrasonic Nondestructive Evaluation, Datta, S.K., Achenbach, J.D and Rajapakse, Y.S eds, Elseviser Science Publisher, North-holland, pp. 17 - 28.

Bond, L. J. (1989b) "Born inversion: Application to spherical and spheroidal voids", Proc. Ultrasonics international'89, Butterworth Scientific, Guildford, pp. 768-773.

Bond, L. J., Rose, J. H., and Wormley, S. J. (1987) "Sizing in the Born-Radius/Zero-of-Time Shift Domain", Proc. Ultrasonics international'87, Butterworth Scientific, Guildford, pp. 401-406.

Bond, L. J., Chaloner, C. A., Wormley, S. J., Neal, S. P., and Rose, J. H. (1988) "Advances in Born Inversion", NATO ASI Series, Ed. Chen, C. H., Springer-Verlag Berlin Heidelberg, Vol. F44, pp. 23-37.

Bond, L. J. (1982) "Methods for the Computer Modelling of Ultrasonic Waves in Solids", Research Techniques in NDT, Ed. Sharpe, R. S., Academic Press, London, pp. 107-150.

Brind, R. J., Achenbach, J. D., Gubernatis, J. E. (1984) "High Frequency Scattering of Elastic Waves from Cylindrical Cavities", Wave Motion, Vol. 6,

pp. 41-60.

Chaloner, C. A. (1988) *Inversion Techniques Applied to the Ultrasonic Characterisation of Defects in Elastic Media*, Ph.D Thesis, University of London.

Chaloner, C. A., and Bond, L. J. (1987) "Investigation of the 1-D Inverse Born Technique", IEE Proc. Part A, Vol. 134, pp. 257-265.

Chaloner, C. A., and Bond, L. J. (1986) "Test for 1-D Inverse Born Inversion Data", Electronics Letters, Vol. 22, pp. 171-173.

Chaloner, C.A. and Bond, L.J. (1986) "Ultrasonic signal processing using Born inversion", NDT International, Vol. 19, No. 3, pp.133-140.

Chen, J. S. (1987) "Elastodynamic ray theory and asymptotic methods for direct and inverse scattering problems", Ph.D dissertation, Iowa State Univ., Ames, IA.

Chou, C. H., Khuri-Yakub, B. T., Kino, G. S., and Evans, A. G. (1980) "Defect characterisation in the short-wavelength regime", J. Nondestr. Eval. Vol. 1, pp. 235-247.

Cohen-Tenoudji, F. and Tittmann, B. R. (1982) "Technique for the inversion of backscattered elastic wave data to extract the geometrical parameters of defects with varying shape", Appl. Phys. Lett., Vol. 41, No. 6, pp. 574-576.

Cohen-Tenoudji, F., Ahlberg, L., Tittmann, B. R., Opsal, J. L., Varadan, V. V., and Quentin, G. (1981) "The role of Creep Rays in the Scattering From Spheroidal Cavities and Inclusions in Solids", Ultrasonics Symposium

Proceedings, IEEE, New York, pp. 853-858.

Datta, S. K. and Shah, A. H. (1982) "Diffraction of Medium and Long Wavelength Horizontally Polarised Shear Waves by Edge Cracks", J. Appl. Phys., Vol. 6, No. 8, pp. 374-376.

Davies, J. B. (1973) "A Least-Squares Boundary Residual Method for the Numerical Solution os Scattering Problems", IEEE Trans. Microwave Theory Tech., MTT-22, pp. 99-104.

Elsley, R. K. and Addison, R. C. (1980) "Dependence of the accuracy of the Born inversion on noise and bandwidth", Proc. of the DARPA/AF Review of Progress in QNDE, July 1980, pp. 389-394.

Fitting D. W., and Adler, L. (1981) *Ultrasonic Spectral Analysis for Nondestructive Evaluation*, Plenum Press, New York and London.

Frederick, J. R., and Seydel, J. A. (1973) "Improved Discontinuity Detection Using Computer-Aided Ultrasonic Pulse-Echo Technique", Welding Research Council Bulletin No. 185.

Freedman, A (1962) Acoustica, Vol. 12, No. 10. pp. 95.

Graff, K. F. (1975) *Wave Motion in Elastic Solids*, Clarendon Press, Oxford.

Gruber, G. J. (1980) "Defect identification and sizing by the ultrasonic satellite-pause technique", J. Nondestr. Eval., Vol. 1, No. 4, pp. 263-276.

Gubernatis, J. E. (1979) "Long-wave Approximations for the Scattering of Elastic Waves from Flaws with Applications to Ellipsoidal Voids and

Inclusions", J. Appl. Phys., Vol. 50, No. 6, pp. 4046-4058.

Gubernatis, J. E., Domany, E., and Krumhansl, J. A. (1977a) "Formal Aspects of the Theory of the Scattering of Ultrasound by Flaws in Elastic Materials", J. Appl. Phys., Vol. 48, No. 7, pp. 2804-2811.

Gubernatis, J. E., Domany, E., Krumhansl, J. A., and Huberman, M. (1977b) "The Born Approximation in the Theory of the Scattering of Elastic Waves by Flaws", J. Appl. Phys., Vol. 48, No. 7, pp. 2804-2811.

Harker, H. A. (1988) *Elastic Waves in Solids*, Adam Hiler/British Gas plc, Bristol.

Hudson, J. A. (1980) *The Excitation and Propagation of Elastic Waves*, Cambridge University Press, Cambridge.

Hsu, D. K., Rose, J. H., and Thompson, D. O. (1984) "Reconstruction of Inclusions in Solids Using Ultrasonic Born Inversion", J. Appl. Phys., Vol. 55, No. 1, pp.162-168.

Jackson, J. D. (1963) *Classical Electrodynamics*, Wiley, New York.

Johnson, G. and Truell, R (1965) "Numerical Computations of Elastic Scattering Cross Sections", J. Appl. Phys., Vol. 36, No. 11, pp. 3466-3475.

Kino, G. S. (1987) *Acoustic Waves: Devices, Imaging, and Analog Signal Processing*, Prentice-Hall, Inc., Englewood Cliffs, New Jersey.

Kohn, W. and Rice, J. R. (1979) "Scattering of Long-Wavelength Elastic Waves From Localized Defects in Solids", J. Appl. Phys., Vol. 50, pp. 33-53.

Kogan, V. G., Hsu D. K., and Rose. J. H. (1985) "Characterization of Flaws Using the Zeros of the Real and Imaginary Parts of the Ultrasonic Scattering Amplitude", J. Nondestr. Eval., Vol. 6, No. 2, pp. 57-68.

Koo, L. S., Shafiee, H. R., Hsu, D. K., Wormley, S. L., and Thompson, D. O. (1990) "Two-dimensional ultrasonic tomography in nondestructive evaluation by using area functions", IEEE Trans. UFFC., Vol. 37, No. 2, pp. 148-158.

Koo, L. S. (1987) *Ultrasonic Flaw Classification: An Approach Using Modelling, Signal Processing, and Adaptive Learning*, Ph.D thesis, Iowa State University.

Korn, G. A., and Korn, T. M. (1961) *Mathematical Handbook for Scientists and Engineers*, McGraw-Hill, London.

Krautkrämer, J., Krautkrämer, H. (1983) *Ultrasonic Testing of Materials*, Third edition, Springer-Verlag, London.

Langenberg, K. J., Bruck, D., and Fischer, M. (1982) "Inverse scattering algorithms, New Procedures in Nondestructive Testing", P. Holler, Ed., Springer-Verlag, Berlin, pp. 381-392.

Levy, B. R. and Keller, J. B. (1959) "Diffraction by a Smooth Object", Communications on Pure and Appl. Math., Vol. 12, pp. 159-209

Manolis, G. D. and Beskos, D. E. (1988) *Boundary Element methods in Elasto-Dynamics,* Unwin Hyman, London.

Morse, P. M. and Feshbach, H. (1953) *Methods of Theoretical Physics*, Vols.

I and II, Mcgraw-Hill Book Company, New York, Toronto, London.

Muradami, Y., Khuri-Yakub, B. T., Kino, G. S., Richardson, J. M., and Evans, A. G. (1978) "An Application of Wiener Filtering to Nondestructive Evaluation", Appl. Phys. Lett., Vol. 33, pp. 685-687.

Neal, S. P., Speckman, P. L., and Enright, M. A. (1992) "Error Analysis and Ultrasonic Scattering Amplitude Estimation Using the Wiener Filter with Limited Prior Information", Review of Progress in Quantitative NDE, Vol. 11, Thompson, D. O. and Chimenti, D. E. eds., Plenum Press, New York. (In press)

Neal, S. P., and Thompson, D. O. (1986) "An Examination of the Application of Wiener Filtering to Ultrasonic Scattering Amplitude Estimation", Review of Progress in Quantitative NDE, Vol. 5, Thompson, D. O. and Chimenti, D. E. eds., Plenum Press, New York, pp. 737-745.

Neal, S. P., Thompson, D. O. (1987) "An A priori Knowledge Base Wiener Filtering Approach to Ultrasonic Scattering Amplitude Estimation", Review of Progress in Quantitative NDE, Vol. 6, Thompson, D. O. and Chimenti, D. E. eds., Plenum Press, New York, pp. 807-813.

Opsal, J. L. and Visscher, W. M. (1985) "Theory of elastic wave scattering: Applications of the method of optimal truncation", J. Appl. Phys., Vol. 58, No. 3, pp. 1102-1115.

Opsal, J. L. (1980) "Calculations of Elastic Wave Scattering from Voids and Crack-like Defects by the Method of Optimal Truncation", Proceedings of the DARPA/AFML Review of Progress in Quantitative NDE, pp. 292-299.

Panametrics (1985) *Ultrasonic Products for NDT*, products catalogue.

Pao, Y. H. (1983) "Elastic Waves in Solids", J. Appl. Mech., Vol. 50, pp.1152-1164.

Pao, Y. H. and Mow, C. C. (1973) *Diffraction of Elastic Waves and Dynamic Stress Concentrations*, Adam Hiler, London.

Papoulis, A. (1977) *Signal Analysis*, McGraw-Hill, New York.

Press, W. H., Flannery, B. P., Teukolsky, S. A., and Vetterling, W. T. (1986) *Numerical Recipes*, Cambridge University Press, Cambridge.

Richardson, J. M. (1978) "The Inverse Problem in Elastic Wave Scattering at long Wavelengths", 1978 Ultrasonic Symposium Proceedings, IEEE, New York, pp. 759-766.

Rizzo, F. J., Shippy, D. J., and Rezayat, M. (1985) "A Boundary Integral Equation Method for Radiation and Scattering of Elastic Waves in Three Dimensions", Int. J. Numerical Methods in Eng. Vol. 24, pp. 115-129.

Rose, J. H. (1989) "Elastic wave inverse scattering in nondestructive evaluation", Pure & Appl. Geophy., Vol. 131, No. 4, pp. 715-739.

Rose, J. H. and Opsal, J. L. (1983) "The Inversion Born Approximation: Exact Determination of Shape of Convex Voids", Review of Progress in Nondestructive Evaluation, Vol. 2, Thompson, D. O. and Chimenti, D. E. eds., Plenum Press, New York, pp. 949-959.

Rose, J. H. and Richardson, J. M. (1982) "Time domain Born

approximation", J. Nondestr. Eval., Vol. 3, No. 1, pp. 45-53.

Rose, J. H. and Krumhansl, J. A. (1979) "Determination of Flaw Characteristics from ultrasonic Scattering Data", J. Appl. Phys., Vol. 50, pp. 2951-2952.

Saffari, N. and Bond, L. J. (1987) "Body to Rayleigh Wave Mode-Conversion at Steps and Slots", J. Nondestr. Eval., Vol. 6, No. 1, pp. 1-21.

Saffari, N. (1986) *Characterisation of Surface Defects Using Elastic Waves Mode-Conversions*, Ph.D Thesis, University of London.

Sanchez-Sesma, F. J. (1987) "Site Effects on Strong Ground Motion", Soil Dominicus and Earthquake Eng., Vol. 6, No. 2, pp. 124-132.

Schmerr, L. W., Jr., Sedov, A., and Chiou, C. P. (1989) "A unified constrained inversion model for ultrasonic flaw sizing", Res. Nondestr. Eval. Vol. 1, pp. 77-97.

Som, A. (1991) *The Ultrasonic Characterisation of Solid-State Bonds*, Ph.D thesis, University of London.

Temple, J. A. G. (1987) "European Developments in Theoretical Modelling of NDE for Pipework", Int. J Pres. Ves. and Piping, Vol. 28, pp. 227-267.

Thompson, D. O., Wormley, S. J., and Hsu, D. K. (1986) "Apparatus and Technique for Reconstruction of Flaws Using Model-based Elastic Wave Inverse Ultrasonic Scattering", Rev. Sci. Instrum., Vol. 57, pp. 3089-3098.

Thompson, R. B. and Wadley, H. N. G. (1989) "The Use of Elastic Wave-

Material Structure Interaction Theories in NDE Modelling", Critical Review In Solid State and Material Sciences, Vol. 16, No. 1, pp. 37-89.

Thompson, R. B. and Thompson, D. O. (1985) "Ultrasonics in Nondestructive Evaluation", Proceedings of the IEEE, Vol. 73, No. 12, pp. 1716-1755.

Thompson, R. B. (1983) "Quantitative Ultrasonic Nondestructive Evaluation Methods", J. Appl. Mech., Vol. 50, pp. 1191-1201.

Thompson, R. B., and Gray, T. A. (1983) "A model relating ultrasonic scattering measurements through liquid-solid interfaces to unbounded medium scattering amplitudes", J. Acoust. Soc. Am., Vol. 74, No. 4, pp.1279-1290.

Tittmann, B. R. (1983) "Scattering of Elastic Waves From Simple Defects in Solids, A Review", Wave Motion, Vol. 5, pp. 299-306.

Tittmann, B. R., Domany, E., Opsal, J. L., and Newman, K. E. (1983) "Elastic Wave Scattering from Irregular Voids", J. Appl. Phys., Vol. 54, No. 11, pp. 6079-6085.

Tittmann, B. R., Morris, W. L. and Richardson, J. M. (1980) "Elastic Wave Scattering at Long Wavelengths", Appl. Phys. Lett., Vol. 36, pp. 199-201.

Tsao, S. J., Varadan, V. V., and Varadan, V. K. (1983) "*T*-matrix Approach to Scattering of Elastic (SH-) Waves by An Inclined Surface Void", J. Appl. Mech., Vol. 50, pp. 143-148.

Varadan, V. V., Lakhtakia, A., and Varadan, V. K. (1988) "Comments on Recent Criticism of the *T*-Matrix Method", J. Acoust. Soc. Am., Vol. 84, No.

6, pp. 2280-2284.

Varadan, V. K., and Varadan, V. V. eds (1980) *Acoustic Electromagnetic and Elastic Wave Scattering-Focus on the T-matrix Approach*, Pergamon, New York.

Varadan, V. V. and Pao, Y. H. (1976) "Scattering Matrix for Elastic Waves. I. Theory", J. Acoust. Soc. Am., Vol. 60, No. 3, pp. 556-566.

Varadan, V. V. and Varadan, V. K. (1979) "Scattering Matrix for Elastic Waves. III. APPlication to Spheroids", J. Acoust. Soc. Am., Vol. 65, No. 4, pp. 896-905.

Visscher, V. M. (1981) "Calculation of the Scattering of Elastic Waves from A Penny Shaped Crack by the Method Of Optimal Truncation", Wave Motion, Vol. 3, pp. 49-69.

Visscher, V. M. (1980a) "A New Way to Calculate Scattering of Acoustic and Elastic Waves I, Theory illustrated for Scalar Waves", J. Appl. Phys. Vol. 51, No. 2, pp. 825-834.

Visscher, V. M. (1980b) "A New Way to Calculate Scattering of Acoustic and Elastic Waves II, Application to elastic Waves Scattering from Voids and Rigid Fixed Obstacles", J. Appl. Phys. Vol. 51, No. 2, pp. 835-845.

Waterman, P. C. (1976) "Matrix Theory of Elastic Wave Scattering", J. Acoust. Soc. Am., Vol. 60, No. 3, pp. 567-580.

Waterman, P. C. (1969) "New Formulation of Acoustic Scattering", J. Acoust. Soc. Am., Vol. 45, pp. 1417-1429.

White, R. M. (1958) "Elastic Wave Scattering at a Cylindrical Discontinuity in a Solid", J. Acoust. Soc. Am., Vol. 30, No. 8, pp. 771-785.

Yang, J. (1990) *The Ultrasonic Scattering from Volumetric Flaws and Their Characterisation*, M.Phil - Ph.D Transfer thesis, University College London.

Yang, J. and Bond, L. J. (1991) "Reconstruction of Volumetric Flaws Using Ultrasonic Backscattering Data", Ultrasonics International 91, Le Touquet, France, July 1-4, 1991, Butterworth-Heinemann (In press).

Yang, J. and Bond, L. J. (1991) "Ultrasonic Sizing of Voids Using Area Functions", 18th Review of Progress in Quantitative Non-Destructive Evaluation, Brunswick, Maine, USA, July 29 - August 2, 1991, Vol. 11, Plenum Press, New York (In press).

Yang, J. and Bond, L. J. (1991) "Ultrasonic Technique for Sizing Voids by Using Area Functions", IEE Proceedings Part A (Submitted).

Ying, C. F. and Truell, R. (1956) "Scattering of A Plane Longitudinal Wave by A Spherical Obstacle in An Isotropically Elastic Solid", J. Appl. Phys., Vol. 27, No. 9, pp. 1086-1097.

Zhang, H. and Bond, L. J. (1989) "Ultrasonic Scattering by Spherical Voids", Ultrasonics, Vol. 27, pp. 116-119.